Minéralisations et Circulations péri-granitiques :Modélisation numérique couplée 2D/3D, Applications au District minier de Tighza (Maroc-Central).

Khalifa Eldursi

UNIVERSITE D'ORLÉANS

ÉCOLE DOCTORALE SCIENCES ET TECHNOLOGIES

LABORATOIRE ISTO

THÈSE présentée par :

Khalifa ELDURSI

Soutenue le : **29 mai 2009**

Minéralisations et Circulations péri-granitiques : Modélisation numérique couplée 2D/3D, Applications au District minier de Tighza (Maroc-Central).

Peri-granitic circulations and mineralization: 2D/3D Coupled Numerical Modeling, applications in the Mining District of Tighza (Central Morocco)

pour obtenir le grade de : **Docteur de l'université d'Orléans**

Discipline/ Spécialité : Sciences de la Terre et de l'Atmosphère

THÈSE dirigée par :

Mr. Eric MARCOUX	Professeur, ISTO Université d'Orléans
Mr. Laurent GUILLOU-FROTTIER	Ingenieur-Chercheur, (HDR) BRGM-Orléans

RAPPORTEURS :

Mr. Jean-Jacques ROYER	Ingenieur-Chercheur, ensg-inpl-Nancy
Mr. Michel JEBRAK	Professeur, Université du Québec-Montréal

JURY:

Mr. Bruno SCAILLET	Directeur de recherche, CNRS-ISTO-Orléans (**Président du jury**)-Examinateur
Mr. Michel JEBRAK	Professeur, Université du Québec-Montréal
Mr. Jean-Jacques ROYER	Ingenieur-Chercheur, ensg-inpl-Nancy
Mr. Alain BONNEVILLE	Professeur, IPGP-Paris-Examinateur
Mr. Fabrice FONTAINE	Chargé de recherche, CNRS-IPGP-Paris-Examinateur
Mr. Eric MARCOUX	Professeur, ISTO Université d'Orléans
Mr. Laurent GUILLOU-FROTTIER	Ingenieur-Chercheur, BRGM-Orléans
Mr. Yannick BRANQUET	Maître de conférences, ISTO Université d'Orléans

TABLE OF CONTENTS

LIST OF FIGURES AND TABLES

Acknowledgement
Remerciements

I am deeply indebted to my supervisors Mr. MARCOUX Eric, GUILLOU-FROTTIER Laurent and BRANQUET Yannick for their constructive remarks, availability, assistance and looked closely at the final version of the thesis for English style and grammar, correcting both and offering suggestions for improvement. I also extend my gratitude to the jury's members for their acceptance to judge and evaluate this work.

I would like to express my gratitude to all those who gave me the possibility to complete this thesis (Mr MARTELET Guillaume, CALCAGNO Phillipe, GLOAGUEN Eric, GUMIAUX Charles, VIDAL Max and BURGISSER Alain.

I expand my sincerest gratitude to my family in Libya for their stimulating support, and to my host family (Auberger's family) in Vichy for their hospitality, friendship and assistance during my stay in France. I am grateful to my colleagues in ISTE and ISTO whose offer me helps, stimulating suggestions, support, interesting and valuable hints and encouragement to go ahead all the time of research and writing.

Chapter (I) General Introduction

Résumé français du chapitre (I)

1. Introduction Générale

L'objectif de cette thèse consiste à étudier les systèmes hydrothermaux en tant que processus créé par la mise en place de magma et responsables de la genèse de gisements de minerai. Ce travail adopte une approche qui est basée sur la modélisation numérique pour caractériser le transfert de chaleur et l'écoulement des fluides hydrothermaux dans la croûte. Nous présentons ci-dessous les quatre problèmes principaux liés à cette recherche, ces problèmes seront traités ou au moins abordés par notre approche numérique. Les sections suivantes sont destinées à présenter quelques principes sur la connaissance de la minéralisation, la modélisation numérique et on finit en récapitulant nos objectifs de cette recherche.

1.1 L'origine des fluides hydrothermaux

Depuis le siècle dernier, il a été confirmé que les fluides hydrothermaux étaient responsables de beaucoup de gisements de minerai, mais l'origine de ces fluides reste toujours discutée. Plusieurs hypothèses ont été proposées: 1) l'origine météorique : il a été suggéré que l'eau météorique puisse jouer un rôle significatif dans la composition des fluides hydrothermaux responsables de la formation de minéralisations liées à l'intrusion. Grace à la mise en place de magma, le gradient thermique installe une circulation convective de l'eau dans l'encaissant, et peut être responsable de la formation de minéralisations (Taylor, 1981). En plus, la taille et la forme de quelques dépôts suggèrent que les solutions hydrothermales lessivent un volume très grand de la roche, y compris des roches encaissantes; ainsi la taille de pluton parent reflète que le volume énorme de fluide vient de l'encaissant plutôt que du corps magmatique, ce qui fait que l'origine météorique des fluides est une hypothèse plus réaliste. 2) l'origine magmatique : grâce au rapport spatial qui existe entre beaucoup de dépôts hydrothermaux et de roches magmatiques, une école pense que le magma consolidé est la source de beaucoup (si ce n'est pas tout) de solutions hydrothermales (Khitarov et al. 1982 ; Manning, 1984 ; Strong, 1981). Cameron et Hattori (1987) ont produit des évidences pour la présence des fluides oxydés pendant la formation d'un certain nombre de dépôts canadiens et australiens d'or; ils ont contesté l'hypothèse orthodoxe qui dit que l'origine des fluides peut seulement être magmatique. 3) l'origine mélange (origine météorique-magmatique) : Un des mécanismes hypothétiques célèbres est le mélange entre deux types d'eau, (magmatique et météorique).

Des évidences actuelles prouvent que les mêmes dépôts peuvent être formés par des différents types d'eau. Au moins des eaux de deux origines ont pu avoir joué un rôle important dans la formation de quelques minéralisations.

Notre première question consiste à tester numériquement l'hypothèse de l'origine météorique des fluides hydrothermaux pour former des gisements de minerai. Notre question principale est : l'origine météorique des fluides est-elle suffisante pour former des gisements de minerai?

1.2 Le système de fractures

Il a été suggéré que tous les processus hydrothermaux exigent des perméabilités suffisantes dans l'encaissant qui permettent aux fluides de s'écouler de leur source jusqu'à la place du dépôt minéral. Cette perméabilité a été réalisée par des roches se fracturant sur des échelles microscopiques à des échelles de grandes failles. Ces systèmes sont censés avoir une capacité de faire circuler une grande diversité de composants comprenant les matériaux minéralisateurs (Yardley, 1983 ; Fischer and Paterson, 1985).

La deuxième question vient du rôle des failles ou des systèmes de fracturation où la perméabilité est relativement élevée par rapport à la zone encaissante. Quel est le rôle des failles et/ou des systèmes de fractures? Jouent-ils un rôle de valve pour transporter des constituants de minerai loin de zone chaude (autour du corps magmatique), ou bien jouent-ils également un rôle de piège structural pour les gisements?

1.3 L'âge des gisements et de l'intrusion parent

Brimhall (1979) a démontré qu'il y a deux étapes de minéralisation : pré-principal et principal. La minéralisation pré-principale, composée par de grandes tailles de minéralisations disséminées de cuivre-molybdène du type porphyre, formée entre 600-700°C, pourrait se mettre en place par un *système intrusif plus jeune*. Pendant l'étape principale plus tardive, un système géothermique impliquant les fluides hydrothermaux à des températures entre 200-350°C, redépose une grande partie du cuivre disséminé pour former des veines riches en minéraux. Si nous avons un lien génétique entre une minéralisation et un corps magmatique, pourquoi avons-nous un décalage d'âge entre la minéralisation et le pluton parent ? Dans certains cas la minéralisation serait plus ancienne que le pluton parent? D'ailleurs, pouvons-nous prendre ce phénomène comme un argument pour montrer qu'il n'y a aucun lien génétique entre le pluton et la minéralisation? Et s'il y a plus d'un cycle de minéralisation, combien de cycles pourraient être liés à un corps magmatique, et eux dépendant de quels facteurs ?

1.4 La géométrie du pluton

A partir de différentes études (par exemple White, 1981, et Wallace, 1991), il a été proposé trois morphologies générales de minéralisations dépendant de la morphologie ou de la forme

de l'intrusion. Dans d'autres cas (ex: gisement d'Henderson) la géométrie compliquée de l'intrusion reflète des effets très compliqués sur la morphologie des gisements de minerai. Par conséquent, la question principale concerne le rôle de la géométrie du pluton pour piéger ou localiser des gisements de minerai ?

2. L'application numérique dans les domaines géologiques

Les observations sur le terrain peuvent souvent être insuffisantes pour mesurer l'évolution temporelle des systèmes hydrothermaux. Par conséquent, le développement récent dans le domaine informatique s'est traduit par un progrès dans la modélisation numérique. Les convections hydrothermales liées à des intrusions magmatiques ont été étudiées numériquement par différents auteurs (e.g. Norton and Knight, 1977 ; Cathles, 1977 ; Norton 1979 ; Candela and Holland, 1986 ; Cook et al., 1997 ; Gerdes and Baumgartner, 1998, Barrie et al., 1999 ; Cui et al., 2001 ; Norton and Hulen, 2001 ; Gow et al., 2002 ; Oliver et al., 2006). Ils ont soutenu que la modélisation numérique constitue une méthode valide pour simuler les systèmes hydrothermaux autour des plutons et étudier la probabilité de former des gisements de minerai autour d'eux.

Les questions suivantes sont les objectifs principaux de cette recherche :

Comment l'emplacement de magma peut-il créer une convection hydrothermale?

Comment la géométrie (la forme) de l'intrusion impacte les systèmes convectifs, la distribution de chaleur, et le R^2AI (Restricted Rock Alteration Index, un paramètre développé pour localiser la zone favorable pour la minéralisation)?

Quel est le rôle de la zone perméable (des fractures et des failles) lors de la formation des gisements de minerais?

Comment la modélisation numérique peut-elle aider à expliquer le lien génétique entre l'intrusion et la minéralisation associée et les problèmes de datation?

Pour répondre à ces questions, nous avons divisé notre travail en deux parties principales représentant :

1) L'examen de modèles théoriques de circulations hydrothermales autour d'un pluton, et la compréhension du rôle de différents paramètres tels que la variation de la perméabilité, la variation de la forme des intrusions et le rôle des zones perméables telles que des failles et des systèmes de fracturation.
2) L'application de nos modèles numériques sur des exemples naturels pour interpréter les observations sur le terrain.

1. General Introduction

The objective of this thesis is to study hydrothermal systems as identified processes accompanied magma emplacement and ore genesis. It includes a numerical approach to characterize heat transfers, hydrothermal fluid flow as results of magma emplacement. The thesis also includes a 3D modeling of a hercynian example from Central Morocco. The example was chosen to study the relationships between intrusions and ore deposition. We also present the numerical modeling as a successful method to examine different hypotheses and natural examples concerning intrusion-related ore deposits.

In the 19th century, a debate on the source of metals has been launched. Hydrothermal deposits have shown that the source can be derived from either purely magmatic solutions or pure meteoric solutions. It is also during this century that J.A. Phillips introduced the concept of mixtures of fluids and the difficulty of determining various contributions.

Later, some scientists have recognized that meteoric and magmatic fluids could both play a role in the mineralization process, and that metals could come from various sources as solutions could move over large distances. At the middle of 20th century, the fact that several sources could coexist in fluids and dissolved species was finally accepted. Definitive proof of this multiplicity has been given by the analysis of radiogenic and stable isotopes allowing to track the source of fluids. Finally, the process of mineralization was defined as a result of a combination of different factors interacting with each other. The main mechanisms include: tectonic deformation, fluid flow, chemical reactions involving mineral dissolution, transport of ions, and precipitation and mixtures of different fluid sources.

In addition, changes in temperature or pressure could be a cause of chemical reactions and precipitation of mineralization too. For example, temperature changes are responsible for changes in fluid density which may lead to the hydrothermal fluid flow where chemical reactions dominate between the rock and hydrothermal solution.

To study these processes, many approaches were proposed; one of these methods deals with numerical simulations which have helped to understand fluid circulation, heat transfer and the zones where chemical reactions can occur. Numerical studies have been varied from simple models, in which the authors observe only one variable such as temperature variation, to complicated models such as coupled models in which the authors observe different variables such as temperature, pressure, fluid velocity and so on. However, numerical modeling was as a key to solve different geological problems in different domains, for example in hydrology (Wu et al., 2002; Garavito et al., 2006; Peratta and Popov, 2006 ; Yin et al., 2007) where models simulate hydraulically and chemically driven fluid and solute transport to calculate

stresses and pressure flow changes and transient solute transport in fractured porous media. In geochemistry field, the numerical modeling of Ondrak and Möller (1999) of coupled heat and mass transport was applied to simulate the temporal and spatial evolution of temperature and quartz precipitation in a hydrothermal vein system. In detail, their computer model simulates the time-dependent temperature evolution of a shear zone and its vicinity by convective and conductive heat transport. They attempted to distinguish zones of precipitation and dissolution of vein minerals due to flow-controlled mass transport. Polyansky and Poort (2000) have proposed 2D modelling study of sedimentation, fluid flow and heat flow in the Baikal rift basin undergoing flank uplift and basin subsidence. It has been performed in order to understand the impact of these processes on the surface heat flow and hydrothermal anomalies. Their model suggests that fluid flow in the sedimentary basin combined with a topographically driven heat advection in the surrounding basement is a sufficient mechanism to account for the increased heat flow within the basin and the main features of the hot springs distribution. Garven et al., (2003) modeled brine migration and heat transport in the Kuna Basin, to evaluate flow patterns and heat transport in faulted rift basins and the effects of buoyancy-driven free convection on reactive flow and ore genesis. Moreover, Schardt et al., (2003) simulated numerically seafloor hydrothermal systems based on the Lau back-arc basin. They investigate conditions that lead to the formation of economic massive sulfide ore deposits in seafloor environments. Kühn et al., (2006) have investigated the 3D geological architecture around the Mount Isa lead–zinc–silver and copper deposits to study fluid flow patterns due to free thermal convection in permeable rock masses. Ma et al., (2006) have carried out a numerical model to investigate hydrothermal fluid flow in the Wabamun Group, Parkland field, northeastern British Columbia, Canada. Their numerical results indicate that faults play the most critical role in controlling hydrothermal fluid flow. Zhu and Yang (2006) introduced their 2D numerical conceptual model to represent the volcanic facies architecture of part of the submarine Mount Read Volcanic successions in western Tasmania. Their numerical results reveal that a synvolcanic fault strongly controls fluid migration paths.

The pumice and volcanic breccias are also important, focusing on hydrothermal fluid circulation and implying that alteration and mineralization may occur preferentially in such facies. In addition, the syn-volcanic intrusion significantly alters the preexisting regime of fluid flow and temperature distribution. They proposed that vigorous fluid circulation is initiated near the intrusion and then shifts to the more permeable host facies (Zhu & Yang, 2006). Furthermore, Yang (2006) presented the first fully 3D numerical modeling of fluid flow and heat transport in the McArthur Basin, and reveals that fluid flow tends to circulate

within more permeable fault zones and form a series of planar convection cells over the fault plane rather than in less permeable host rocks.

In geothermal studies, Wisian and Blackwell (2004) have attempted to construct their basic model of extensional geothermal systems that include structure, heat input, and permeability distribution. Their two-dimensional simulation models were used to evaluate the effect of permeability and structural variations in the Basin and Range geothermal system of the western U.S. They have concluded that a permeable fault in one valley can induce flow if there are no equally good upflow paths in the adjacent valleys. Similarly, when bulk permeability is high enough, additional deep circulation cells develop in adjacent valleys, diverting heat and fluid from the fault and consequently reducing temperatures in the fault itself. Guillou-Frottier et al. (2000) simulated porphyry-type ore deposits hosted by ash-flow calderas, using a thermo-mechanical model of upper crustal and study magmatic system behavior during the pre- and post-caldera formation stages. They have shown that in the presence of regional extension, the development of caldera border faults may be suppressed to the advantage of deep-seated fractures, and clustered above the central part of the magma chamber, thus forming favorite conditions for the formation of porphyry-type ore deposits. Stimac et al. (2001) have used 2D numerical model for complex host rocks and multiple emplacements of magma to simulate conductive and convective heat transport around magma bodies, they concluded that high conductive thermal gradients are enhanced locally by fault-controlled zones of convective heat (geothermal fluid) transport. Dobson et al. (2004) and McKenna and Blackwell (2004) characterized a reservoir by utilizing several parameters, including temperature along the producing fault and the predicted surface heat flow. Time scales are on the order of 0.1 Myr for development of maximum reservoir temperatures.

They explained that young faults are frequently associated with extensional geothermal systems. Harcouët et al., (2007) computed pressure–temperature paths, compared to thermobarometric data of the area of the Ashanti belt southern Ghana in West Africa. Zhao et al, (1998) presented finite element simulations of temperature gradient driven rock alteration and mineralization in fluid saturated porous rock masses. They explored the significance of production/annihilation terms in the mass balance equations and the dependence of the spatial patterns of rock alteration upon the ratio of the roll over time of large scale convection cells to the relaxation time of the chemical reactions. Special concepts such as the gradient reaction criterion or rock alteration index (RAI) were used, (Ondrak and Möller, 1999 ; Guillou-Frottier et al., 2000 ; Collin et al., 2002 ; Garven et al., 2003 ; Regenauer-Lieb and Yuen, 2004 ; Oliver et al., 2006 ; Yang, 2006 ; Ma et al., 2006). In ore exploration, numerical

modelling was mostly applied in volcanic systems and sedimentary basins (Papale, 1999 ; Yasukawa et al., 2003 ; Simms and Garven, 2004 ; Ma et al., 2006 ; Oliver et al., 2006 ;Gerya and Burq, 2007).

From all the works mentioned above, it is clear that numerical modeling is widely used because of rapid progression of computer technology to solve complicated problems. For that reason, numerical simulation is chosen to answer the following subtitles which represent some questions concerning hydrothermal fluid flow and ore genesis which are not yet clarified enough.

1.1 The origin of hydrothermal fluids related ore deposits

As mentioned above, in the last century, it has been definitively confirmed that hot aqueous solutions have played a part in the formation of many different types of mineral and ore deposits, for example veins, stockworks of various types, volcanic-exhalative deposits and others. Such fluids are usually called hydrothermal solutions and many lines of evidence attest to their important role in carrying a wide variety of materials and of depositing these to form minerals as diverse as gold and muscovite. One of the main arguments faces geologists is the origin of hydrothermal fluids. It was difficult in different sites of ore deposits to determine the origin of hydrothermal fluids, i.e. their meteoric or magmatic origin.

However, homogenization of fluid inclusion in minerals from hydrothermal deposits and other geothermometers have shown that the depositional range for all types of deposit is approximately 50-650°C.

Analysis of the fluid has shown water to be the common phase (Skinner, 1979). Different geochemical studies propos different sources for the origin of hydrothermal fluids (Evans, 1997):

1) Surface and ground water, referred to by geologists as meteoric water.
2) Oceanic water.
3) Formation and deeply penetrating meteoric water.
4) Metamorphic water.
5) Magmatic water.

Three hypotheses were proposed to reconstruct the scenario of the origin of hydrothermal fluids based on geochemical data:

1.1.1 The first hypothesis (magmatic origin)

Based on a spatial relation between many hydrothermal deposits and magmatic activities, a strong team of geologists hold that consolidating magmas are the source of many hydrothermal solutions. The fluids were considered as low temperature residual fluids left

over after pegmatite crystallization. Different scenarios were proposed by different authors based on field and laboratory studies, who flow to the same postulate, propose that magma may be the main source of water, the metals and other elements, as well as, the heat to drive the mineralizing system (Strong, 1981 ; Manning, 1984). More evidences come from stable isotope investigations (Sheppard, 1977). The precise analysis of Bowman et al. (1987) on the Bingham Canyon, Utah deposit demonstrates that the hydrothermal fluids that formed the potassic and propylitic alteration there were magmatic in origin. In addition, Bowman et al. (1987) have used carbon isotope data from Archaean gold vein and shear zone systems Hollinger-McIntyre in Canada and the golden Mile in Western Australia, to sustain the hypothesis of a magmatic origin of the mineralizing solutions. In contrast, Cameron & Hattori (1987) offered an evidence to confirm the presence of oxidized fluids during the formation of Canadian and Australian Archaean gold deposits; they contended the hypothesis that the magmatic origin is the unique source of fluids to form ore deposits.

1.1.2 The second hypothesis (meteoric origin)

In contrast, another school of thought supposed that geothermal systems form where a heat engine (usually magmatic) at depths of a few kilometres sets deep ground waters in motion figure (I.1a). These waters were supposed to be meteoric in origin but in some systems formation or other saline waters may be present. The different kinds of a hydrothermal system are demonstrated in figure (I.1a). Where meteoric water sinking to deep into a zone of high temperature, it absorbs heat and rises into one or a succession of permeable zones (A, B & D). Outflows in (C) depend on the permeability of surrounded rocks and the pressure at the top of the zone (BD). One of the most interesting types is the emplacement of magma, where pluton are the main heat source to boiling water, and consequently, the development of convection currents (convective cells) in the water. Figure (I.1b) illustrates the structure of a geothermal system in a volcanic terrain (aupo Volcanic zone, New Zealand). In figure (I.1c, d) geothermal systems are assumed to be responsible of forming vein tin and copper mineralization in and adjacent to the Land's End Granite in south-west England. In figure (I.1e) we have a wide picture, with geothermal systems being responsible of some of the different types of mineralization in south-west England (Evans, 1998). This general example shows how the meteoric water and the geothermal systems can be a plausible mechanism to form ore deposits. Another point we need to think about, the most striking characteristic of porphyry copper deposits comparing with other hydrothermal ore deposits is their massive dimensions. The size and shape of these deposits imply that the hydrothermal solutions rise from large volumes of rock, counting host rocks, as well as the parent intrusion. This

supposes that the large volume of hydrothermal fluid comes from the host rocks than from intruded body which makes the meteoric origin of hydrothermal fluids more realistic.

Furthermore, out of intrusions, thermal perturbations made by magma emplacement set up a convective circulation of water in the country rocks, and this may be responsible for the propylitic alteration (diorite model conditions), as Taylor (1981) has shown for the diorite model deposit of Bakirçay, Turkey. In this study, he used Sr isotopes to demonstrate that fluids that formed the potassic alteration were magmatic-hydrothermal and those that caused the propylitic alteration were meteoric-hydrothermal, but he did not show the mechanism of convective circulation or how this can be related to fluid forming ore deposits. Previous works have shown that estimating water concentrations in felsic magmas vary from 2.5 to 6.5 wt%, at depths around 4.5 km fluid remains in liquid case in melts due to high containing pressure (> 0.1GPa), (Evans, 1998). As magmas crystallize to form anhydrous minerals, a huge volume of water can be released by a cooling magma,1km^3 of felsic magma with 3% water could exsolve approximately 100Mt (10^{11} l), (Brimhall & Crerar, 1987). Whether any granitic magma can create economic ore deposits under good conditions, or whether the ability to release a significant amount of mineralizing fluids is dependent on the source of magma itself to have high concentrations of metals, is today under active debate (Evans, 1998).

In addition, during the cooling phase of intruded magma, the meteoric fluids may mix with magmatic system and leading to the development of low temperature minerals: sericite, pyrophyllite and clay minerals. Taylor & Fryer (1982, 1983) have used geochemical analysis to demonstrate that the meteoric-hydrothermal fluids had the potential to remobilize and reconcentrate copper and molybdenum at both Bakirçay and Santa Rita, New Mexico. Moreover, Nesbitt et al. (1989) and Madu et al. (1990) discussed and produced isotopic evidence for regarding these mineralizing fluids as evolved meteoric water that had gained hydrogen and oxygen isotopic values close to those of magmatic and metamorphic water by interaction with sedimentary rocks. A cross section shows the formation of Carlin deposits is given in figure (I.2).

Berger & Bagby (1991) and other authors favor intrusion-driven hydrothermal convection cells as the mineralizing mechanism. They suggest that meteoric fluid is the responsible to form gold deposits. Fluid inclusion work proposes that boiling phase was not an important precipitation process, and perhaps, a mixing with cooler meteoric water having a different chemical composition was the mechanism of ore formation.

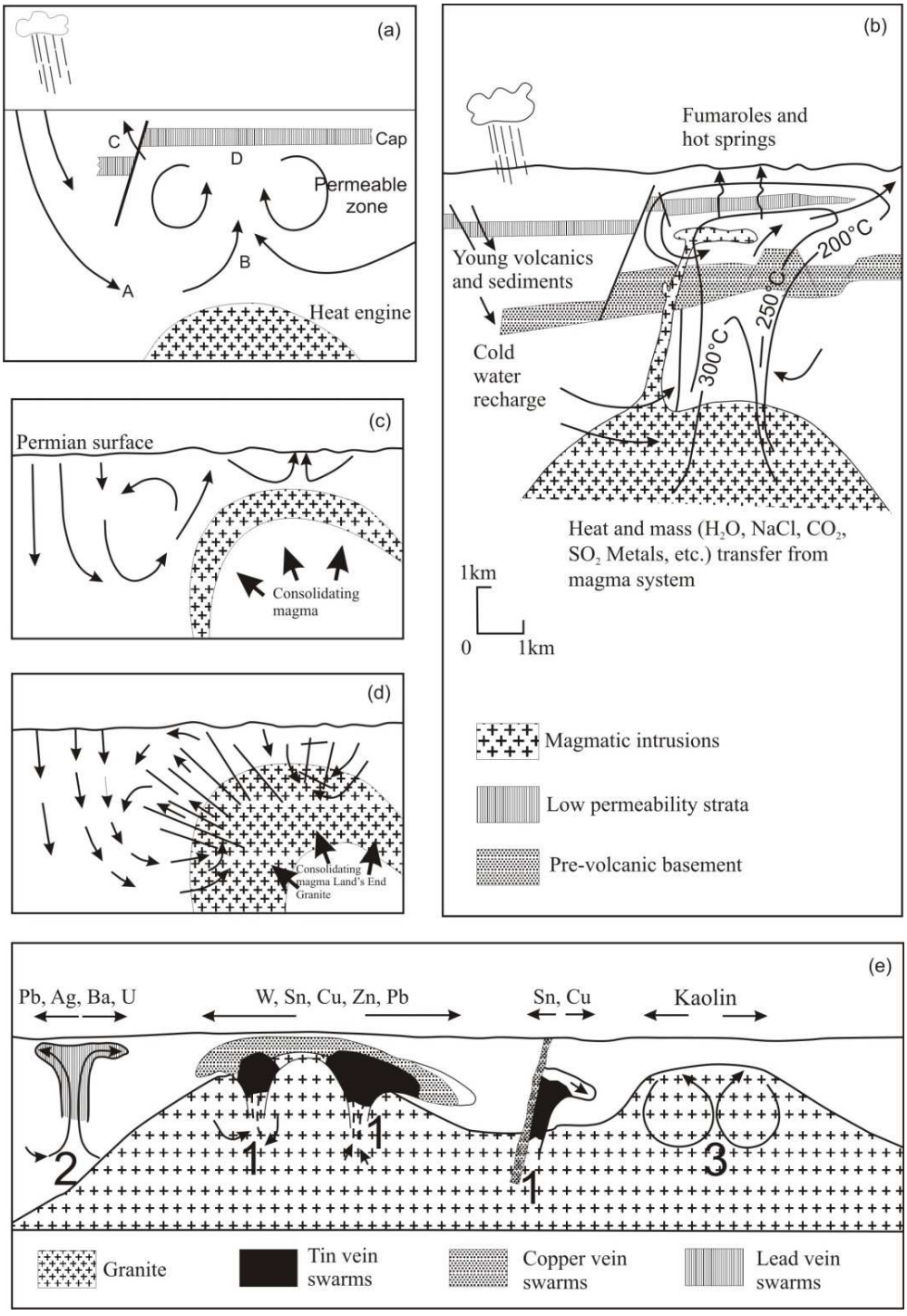

Figure (I.1) (a) Some features of a geothermal system. (b) structure of a geothermal system like that of the Taupo volcanic zone, NZ. (after Henley & Ellis 1983.) (c and d) evolution of some of the mineralization in a flank of the Land's End Granite; (e) (after Moore 1982) possible fossil geothermal systems associated with the granite batholith of south-west England, illustrating the different types and settings of mineralization in that region, and the district zoning developed there. (1) Dines (1956) type emanative canters. (2) cross course mineralization (succinctly described by Alderton 1978). (3) Kaolin deposits (weathering may have played a part in their formation).

1.1.3 The third hypothesis (meteoric and magmatic origin)

One of the famous hypothetical mechanisms is the mixing of waters, e.g. magmatic and meteoric waters. Recent evidence confirms that some deposits can be created by different types of fluids. Those fluids with at least two different parentages may have played a major role in the formation of some ore deposits.

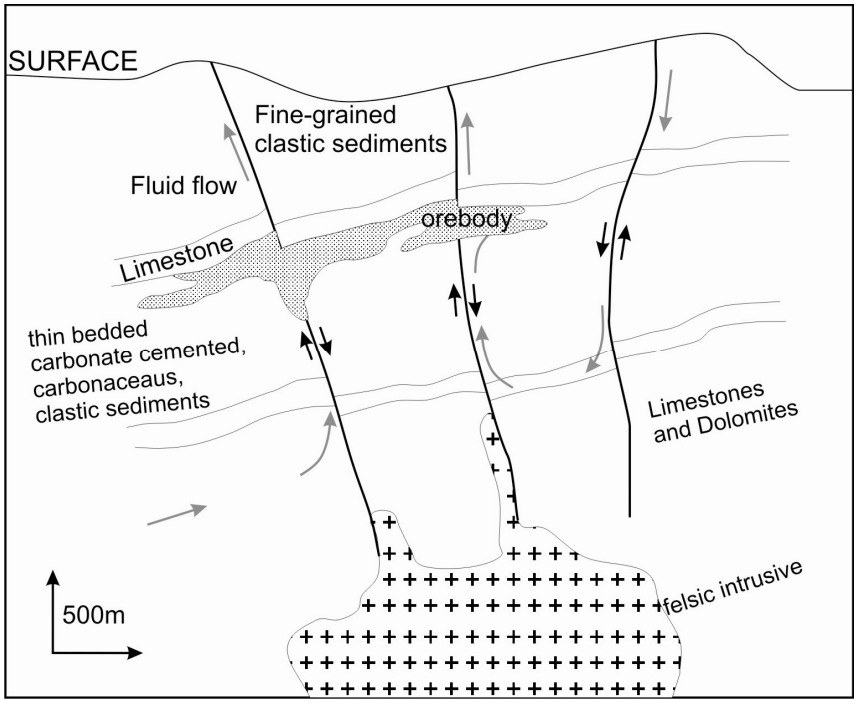

Figure (I.2) Formation of Carlin-type deposits, (modified after Sawkins 1984).

The meteoric origin has been proposed of different fluids, but the reaction and long burial give them different chemical characters. Moreover White (1974) has proposed a meteoric origin for both metamorphic and formation fluids but chemical reactions between rock and fluids may change the chemical character.

The mixture fluid was also shown in different natural examples, where intrusions were only interpreted as the main heat source to provide the driving force for the circulation of fluids. Silver veins of the Hualgayoc district, Peru, were discussed by MacFarlane & Petersen (1990); their investigations showed that intrusions were the main heat source in the ore-forming solutions, but the source of fluid was mixed between meteoric, magmatic and metamorphic origin. Plimer (1985) has also postulated a mixed source for metals in huge Broken Hill orebodies of New South Wales. As well as, Hall (1990) demonstrates that some ore deposits Cornish deposits such as boron, lithium and tin in were derived from the granites, whereas the copper and sulphur was leached from the country rocks. A similar scenario was proposed by Cathelineau (1982) to explain the epigenetic uranium mineralization of the Variscan Metallogenic Province of western Europe.

Ore geology, like in other topics of earth sciences, we study and model the evidence and data collected in the field and from lecture survey and try to reconstruct the story, but in many analytical studies the evidences and results are sometimes partial and open to a variety of interpretations. Therefore, a worth further research concerning the best investigated deposits and their modes of genesis are still modified continually.

Based on the lecture survey, we can here introduce our first series of questions: what are the most important, meteoric or magmatic fluids? Are the meteoric fluids enough to form ore deposits or do we need magmatic fluids to create them? What is the role of magmatic body in the generation of ore deposits, is it a genetic or a structural role?

Newberry et al. (1990) contended that a major factor controlling metallogeny is the *depth of emplacement*?

How could the circulation of hydrothermal fluid be around magmatic bodies during and after emplacement?

1.2 Hydraulic fracturing

It was suggested that any hydrothermal process requires the development of sufficient rock permeability to permit the mineralizing solutions to flow far from their source to the depositional zones. Therefore, for flow to take place in such systems regional permeability must be developed. This permeability is realized by fractures on micro scales to major crustal faults. Additionally, under such conditions such as shear zones or fractures, ore constituents may be accumulated in zones of low pressure. In this way, the assemblages of many gold veins may have been formed (Saager et al., 1982). Much of the fracturing is due to the solutions themselves, it is now well known that fluids under high pressure can dramatically influence the mechanical behaviour of the crust (Phillips, 1972) and develop sites for precipitation of material held in solution. The fracturing of rocks by water under high pressure is known as hydrofracturing or hydraulic fracturing. These systems were supposed to have a capacity to leach a wide range of components including ore-forming materials from a very large volume of crust (Yardley, 1983 ; Fischer & Paterson, 1985).

It is now known that major roles in enhancing rock permeability are played by the development of fracture systems on very different scales. Such a model, and variations of it, has been used to explain the formation of a number of gold deposits (see, Kerrich & Fryer (1979), Phillips et al. (1984), Shepherd & Allen (1985), Annels & Roberts (1989) and Williams (1990).

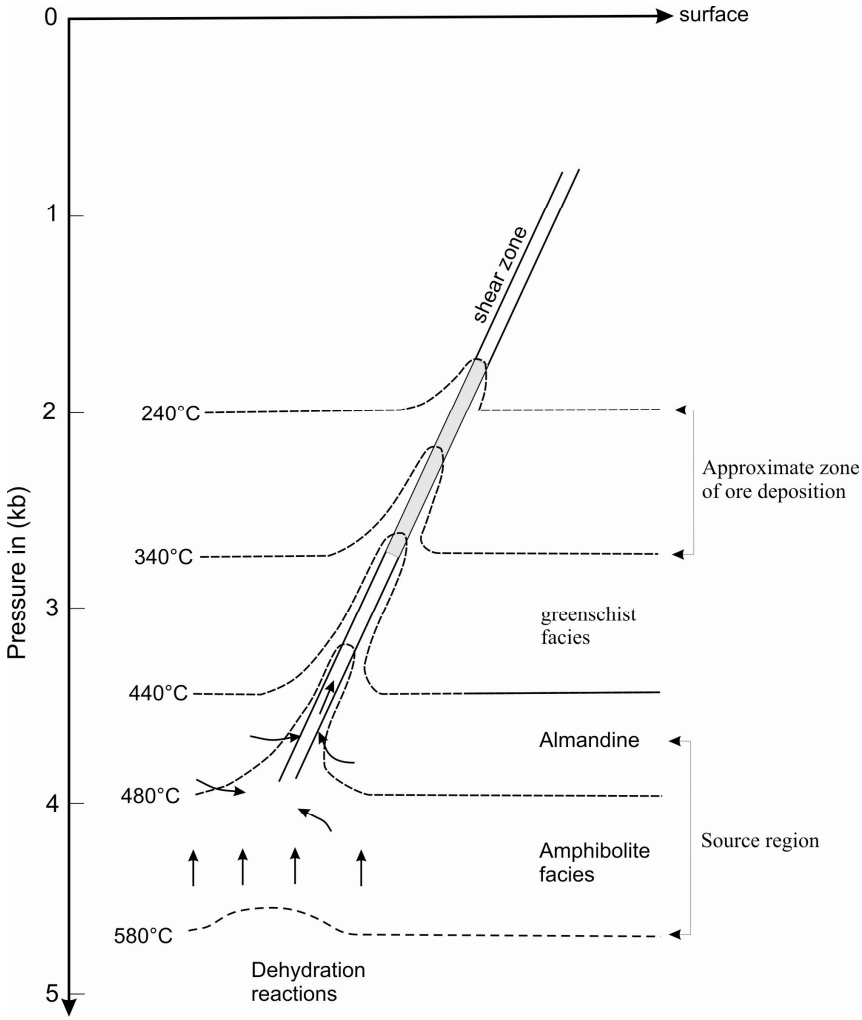

Figure (I.3) Diagram of a shear zone where metamorphic water from a large volume of rock is rising to higher levels. (modified after Fyfe & Henley 1973).

Some of these and other authors have advanced the results of isotopic studies in support of their models. Based on the discussion above, hydraulic fracturing plays an important role in the circulation of fluids in the zone around intrusions. Consequently, it leads to the formation of veins in which may host different economic deposits, figure (I.3).

The second series of questions then comes from the role of fracture systems or faults where the permeability is relatively high comparing to the surrounding zone.

What is the role of faults and/or fracture systems? Do they play a role of valve to transport ore constituents far from hot zone (around intruded body) or do they also play a role of structural trap for ore deposits?

1.3 Age dating of ore deposits

When orebodies represents part of a stratigraphical succession, like the Mesozoic ironstones of north-western Europe, their age is absolutely defined. On other hand, syn-genetic deposits are sometimes difficult to date, especially when there are evidences that many of them may

have formed from polyphase mineralization, with epochs of depositions being separated by intervals of several Myr.

Brimhall (1979) has shown that there are two mineralization cycles: pre-main and main. The mineralization of the pre-main cycle consisted of mineralization formed at 600-700°C, and possible set in motion by a *younger intrusive system*. During the main cycle, relating to hydrothermal fluids, achieved temperature of 200-350°C and leached much of the disseminated copper, to form the rich vein ore deposits.

Hayba et al. (1986) and Heald et al. (1987) have classified these types of deposits into two groups: acid sulphate and adularia-sericite. Heald et al. (1987) proposed that these two groups of deposit reflect their distance from their main heat source; the acid sulphate type being spatially and temporally related to a shallow hydrothermal system Figure (I.4a). Conversely, the adularia-sericite deposits are later than the magmatic activity. Consequently, it becomes spatially unrelated to intrusive volcanic and have formed above a deeper heat source, (figure I.4b).

A third series of questions thus arises: if we have a genetic link between mineralization and intruded bodies, why do we have a gap in age between mineralization and parent pluton, is that related to the period of emplacement? Why the mineralization appears to be older than parent pluton in certain cases?

Moreover, can we take this phenomenon as an argument to prove that there is no genetic link between the pluton and mineralization? Furthermore, if there is a long period of deposition, on which factor(s) does it depend?

1.4 Intrusion geometry

Sillitoe (1973) showed that porphyry copper deposits that occur in a subvolcanic environment associated with stocks (apexes). Christie & Braithwaite (1986) and other workers have pointed out that apexes or high portions of intrusive body may be responsible for the formation of epithermal gold mineralization. In porphyry copper deposits, different evidences suggest that porphyry is connected to an equigranular intrusion of similar composition with much larger dimensions.

Within this complicated form, the mineralization (development of oligoclase and actinolite) has been trapped because of pluton's form (Carten, 1986). After Carten et al. (1988), Seedorff (1988) has shown that the existence of 12 stocks related to three intrusive bodies is the responsible of forming of different hydrothermal alteration assemblages in numerous cycles in Henderson deposits. Each apex was surrounded by an ore shell. Moreover, from different studies (e.g. White 1981, and Wallace, 1991), three general orebody morphologies were

recognized and may depend on the morphology or the shape of related intrusion, figures. (I.5 & I.6). From the data mentioned above, the fourth question is what is the role of pluton geometry in trapping or localizing ore deposits?

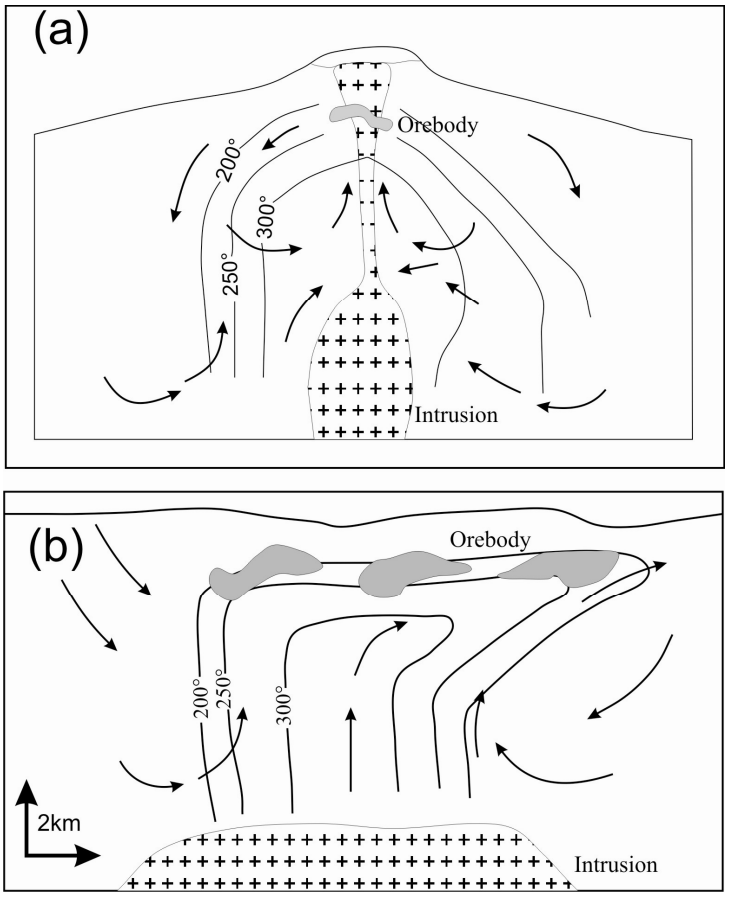

Figure (I.4) the formation of two types of epithermal deposits in a volcanic system, based on Heald et al (1987) with modifications from Henley (1991). (a) acid sulphate type. (b) Adularia-sericite type. The heat source is represented by an intrusion several kilometers below the mineralized zone. (a) is drawn at the same scale as (b).

We presented above the main four problems concerning this research which will be answered or at least more clarified by our numerical approach. The following sections are to present some of principle knowledge in mineralisation classifications in order to show the diversity of ore deposits. Then we focus our interest in ore related igneous activity and more precisely in ore felsic association because it is considered economically as one of the main purposes in ore geology.

2. Classifications of ore deposits

Many classifications were made by different authors to classify ore deposits. The first classification was proposed by Lindgren's in 1913 and improved in 1933. The classification was based on the type of process forms ore deposits:

1. Deposits formed by mechanical processes.

2. Deposits formed by chemical processes of concentration.

(A) In surface waters: (i) by reactions (between solutions), and (ii) by evaporation (of solutions).

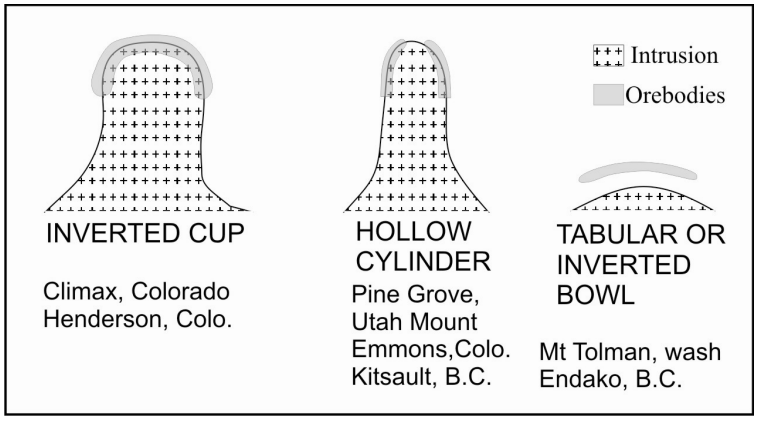

Figure (I.5) Porphyry orebody morphologies. Modified after (Evans, 1998).

After that we present the major concepts in numerical modelling and finished by summarizing our aims of research.

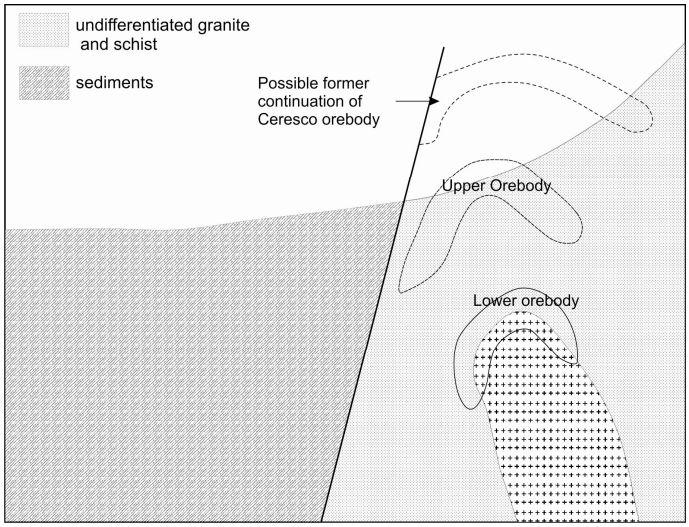

Figure (I.6) Generalized geological section through the Climax mine, Colorado (modified from Hall et al. 1974).

(B) in bodies of rock: (i) by concentration of substances contained within rocks by (a) weathering, (b) ground water and (c) metamorphism; (ii) by introduced substances (a) without igneous activity, and (b) related to igneous activity by (I) ascending hydrothermal waters, i.e. epithermal, mesothermal and hypothermal deposits, and (II) by direct igneous emanations, i.e. pyrometasomatic and sublimate deposits.

(C) In magma by differentiation: (i) magmatic deposits, and (ii) pegmatites.

Epigenetic hydrothermal deposits are classified according to their depth and temperature of formation: 1) hydrothermal deposits correspond to deep-high temperature deposits; 2) mesothermal deposits formed at low temperatures and medium depths, 3) epithermal deposits formed near surface, 4) leptothermal deposits located in the transitional zone between

mesothermal and epithermal and 5) telethermal deposits correspond to very low temperature deposits formed far from the source of the hydrothermal solutions.

In addition, Stanton (1972) classified ores as rocks; he recognized seven important worldwide associations as follows:

1) Ore in igneous rocks:
   (A) Ores of mafic with ultramafic associations.
   (B) Ores of felsic association.
2) Iron concentrations of sedimentary affiliation.
3) Manganese concentrations of sedimentary affiliation.
4) Stratiform sulphides of marine and marine-volcanic association.
5) Strata-bound ores of sedimentary affiliation.
6) Ores of vein association.
7) Ore deposits of metamorphic affiliation.

Finally, another classification was proposed by (Jébrak & Marcoux, 2008), where ore deposits were arranged based on their environment to:

1) Ores associated to plutons: a) mafic and ultramafic, b) felsic, c) alcalan plutons and d) in metamorphic settings.
2) Ores associated to volcanic activities (Marin and continental volcanic activities).
3) Ores in sedimentary basins
4) Ores related to continental hydrothermalism.

In this research, we focus on ore deposits associated to felsic intrusions.

3. Peri-granitic Mineralization (ore related to igneous activity)

The mineralizations associated to granitic plutons are the main types of mineral deposits on our planet, figure (I.7). This type is a major supplier of metals such as Au, W, Ag, Pb, Zn., Through many types of deposits (porphyry copper, pre-granitic veins, skarns ...). It is therefore of major economic targets.

Thompson et al. (1999), Thompson & Newberry (2000) and Lang & Baker (2001) have attempted to identify the following characteristics in ore-related intrusions:

1) Granitoids which are spatially associated to gold mineralizations are predominantly poor in calcium and metaluminous to peraluminous.

2) In a geodynamic frame, these granitoids are located on active continental margins.

3) These intrusions are late-orogenic.

4) The mineralization is located in the granitoids, and / or their *edges* in both intrusions and *host rock*.

5) The morphology of the mineralization is highly variable: it occurs most often in the form of quartz veins, parallel to each other or stockwork. However, the mineralization is also present in both veins and disseminated in the granite (Fig. I.8), as breccia (Kidston, Australia,), in the form of Greisen (Salavas, Spain, (Harris, 1980)) or as a skarn contact.

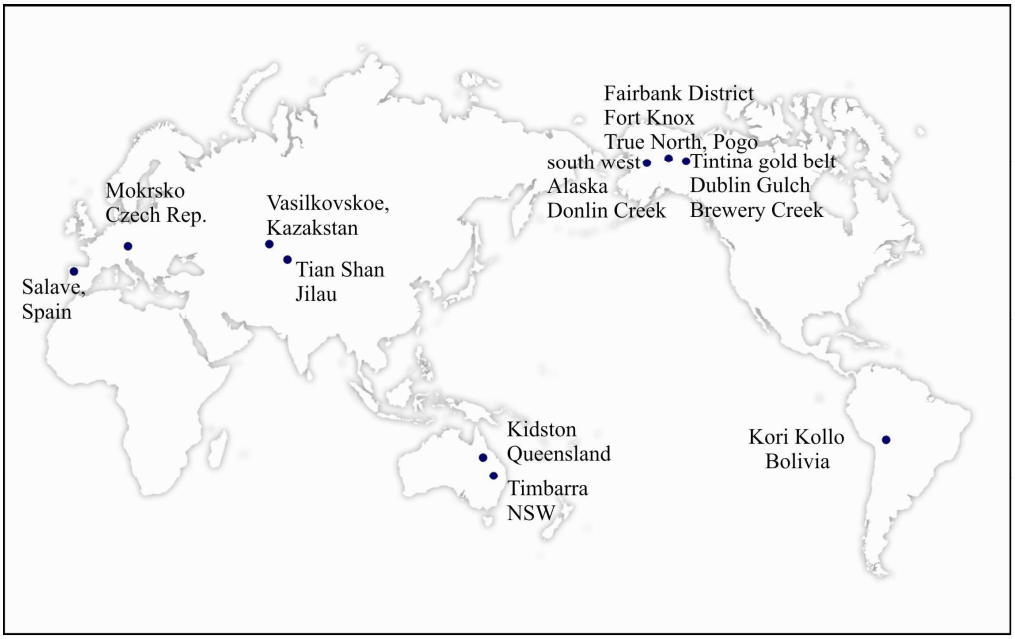

Figure (I.7) Some examples of ore deposits associated to intrusions of gold deposits. Modified after Thompson et al. (1999), Thompson & Newberry (2000) and Lang & Baker (2001).

6) The amount of sulphide represented in mineralization is always low (less than 3%), they occur frequently as an identical metal characterized by the presence of arsenic, tungsten, tin, bismuth, tellurium, gold, silver and antimony. Quantitatively, pyrite and / or arsenopyrite are dominant. The gold is in the form of electrum or maldonite with bismuthinite and bismuth.

7) The alterations associated to the mineralization are marked by the appearance, in varied proportions qualitatively and quantitatively of quartz, potassium feldspar, albite, sericite, carbonates.

8) The composition of fluids is mainly low salinity-CO_2 dominant, (Thompson et al., 1999).

Some of these points are not included in our models, where geochemical model is needed to verify them. In contrast, the physical relationship between mineralization and pluton can be simulated using our approach. Later, we will attempt to verify also the points (4 and 5) by observing the spatial relation between intrusion and ore deposits (where and when could they be formed comparing with emplacement period of magma), the morphology of ore deposits as a consequence of pluton geometry, these points and the questions mentioned above will be

answered, either by hypothetical and/or field observations of natural examples where pluton related ore deposits is still debated.

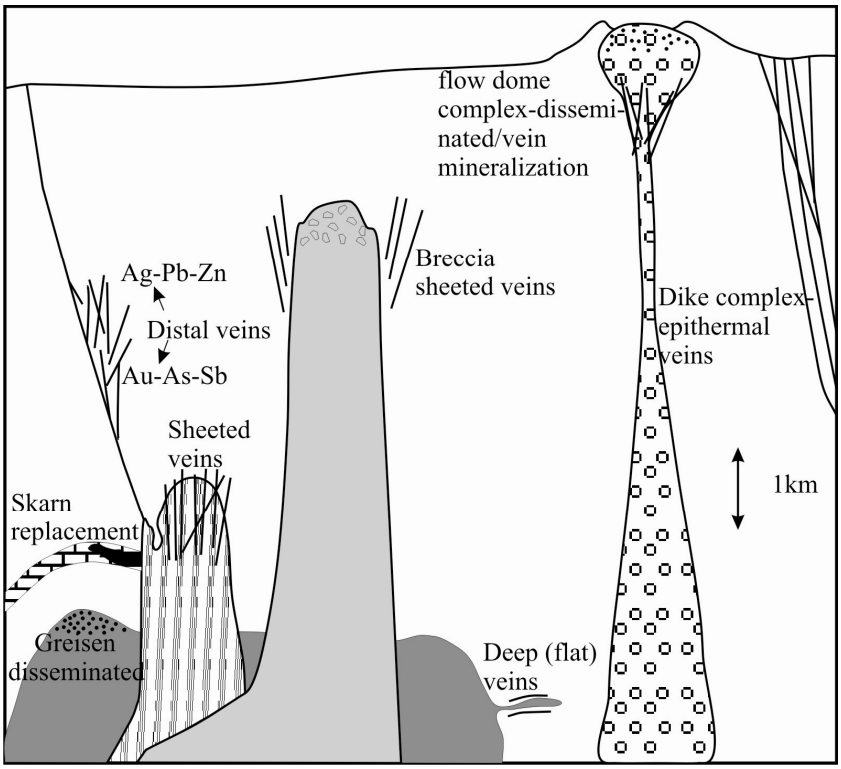

Fig. (I.8) The different mineralization styles spatially associated to intrusions. (modified after Thompson & Newberry 2000).

4. Numerical modeling

During the nineteenth century, scientists started to use simple models that were essentially mechanical (analogical modeling) to simulate and study the regional deformations in the upper crust. In twentieth century, the computer science arises, and the numerical modeling invaded almost all the scientific domains, because it resumes time, effort and gives more detailed results with simple modifications.

The principal role of numerical modeling is that if the laws of a new phenomenon have the same form with those of another which has already been studied, then the consequences of the latter can be transferred to the new phenomena. Therefore, examining physical laws with simple models is necessary to understand the simple consequences. Afterward, the validation of the model by simulate a physical phenomena and published models are also essential to verify that the model is able to reproduce the same results and bring insights that can often be answers or explanations about real complicated models. For that reason, progression and attempt to find an explanation for numerical solutions each time and simple case is essential before taking a step again forward the physical complexity.

However, to construct any numerical model four distinct steps should be followed:

Formulation:

In this part, the modeler tries to express the physical problem in mathematical form.

Numerical implementation:

During this period, the mathematical model is ready for solution. An algorithm solution is appropriate for implementation by the computer.

Computation:

This part includes the coding of the solution algorithm by using a computer language. Long and a complicated code may be involved here. thus, the code must be considered carefully at this stage.

Validation:

Simplifications and approximations are the foundations of numerical modeling. As a result, unacceptable errors may be introduced in numerical solution. Thus, it is essential to verify and compare the numerical results with studied physical phenomena.

In this research, which is focused on a single modeling method, it is not possible to present in detail all aspects of numerical modeling. However, by a systematic approach to model building, the basic processes inherent in many similar methods will be presented with numerical procedures and simplification in the next chapter.

5. Numerical application in geological fields

The classical methods such as geochemical analysis may often be insufficient to quantify the temporal evolution of hydrothermal systems. For example, what we observe in the field is a result of numerous coupled processes such as fluid flow, water–rock interaction, and fluid evolution which have taken a long time periods to form an observed mineralization, and at the end the samples bring often the traces of last periods, mixed with deformed traces of previous periods.

Based on this introduction, the development in numerical modelling may brings the answer to separate different processes and examine the duration and controlling factors of a hydrothermal circulation. In one hand, an oversimplification of the system by decoupling different processes included in vein mineralization makes the numerical modelling too far from the reality. In the other hand, nonlinearities of the coupled system make analytical solutions difficult or even impossible. For that reason, numerical models simulating coupled heat and mass transport may be the reasonable method to obtain a better understanding in time scales at which hydrothermal vein deposits form. Even though some models decrease the complexity of real systems and replaces them by principal geological units, physical processes and chemical reactions, the solution of running numerical models (in previous works)

emphasises that the numerical results bring insights to better understanding different physical phenomena.

Hydrothermal convections related magmatic intrusions have been studied numerically by different authors (e.g. Norton and Knight, 1977 ; Cathles, 1977 ; Norton, 1979 ; Candela and Holland, 1986 ; Cook et al, 1997 ; Gerdes and Baumgartner, 1998 ; Barrie et al., 1999 ; Cui et al., 2001 ; Norton and Hulen, 2001 ; Gow et al., 2002 ; Oliver et al., 2006). They sustained that the numerical modelling is a valid method to simulate hydrothermal systems around plutons and studying the probability of forming ore deposits around them.

Barrie et al. (1999) reviewed a variety of models simulating active and fossil hydrothermal systems, in different geological settings and concluded that the geometry and depth of the intrusion, the permeability of the host rock and hydrothermal system during and after the emplacement are the four critical factors in determining the style and pattern of alteration and mineralization. More recently, Schardt et al. (2005) investigated the effect of magma intrusion on the genesis of the ore deposit in Western Australia. However, there have been fewer papers dealing with the mechanisms of fluid flow, from metal source regions, transport through a fracture network, to the deposition sites (see Large et al., 2005; Leach et al., 2005; Oliver et al., 2006 and Beaudoin et al., 2006).

We present here our models as a hydrothermal coupled model which has the capacity to be closer to the reality by: 1) varying numerous physical parameters such as viscosity, density, heat capacity and thermal conductivity of fluid and rock which varied with temperature. As well as the pressure and permeability which are varied with depth. These parameters have not been varied together before 2) studying the hydro-thermal behaviour before, during and after magma emplacement to examine active and fossil hydrothermal systems 3) arguing different models with varied pluton's shapes and depth of emplacement 4) dealing with the mechanisms of fluid flow, from metal source regions, transport through a fault or fracture network, since it is increasingly recognised as an important mechanism for fluid flow and mass transport in hydrothermal systems (see Zhao et al., 2003, Large et al., 2005; Leach et al., 2005; Oliver et al., 2006) 5) applying RAI (alteration rock index) in our models and use it as an indicator to sites of ore deposits 6) attempting to simulate and simplify natural examples and compare our result with field observations.

6. Aims of this research

Numerical modelling is a method to quantify hydrothermal fluid flow, and to examine the factors that control the hydrothermal circulation induced by magmatic intrusions. Thus, our work is focused on the prospective effects of the geometry of intruded body, depth of

emplacement and the role of apexes and permeable zones (such as fractures and/or faults) in hydrothermal systems *during and after emplacement*.

The aim of this work is to provide a theoretical background for the interpretation of hydrothermal data showing indications of fluid circulation and heat transfer. The system investigated here is simplified to discuss the relationships between temperature and fluid physical parameters; we acknowledge here that our hydrothermal systems and their equations of enthalpy are lacking for more complex systems. Hereunder, we attempt to simulate and simplify different natural examples by studying only the fluid circulations in the porous media without taking into account the chemical alternation /interactions between meteoric and magma fluids.

Investigation of mineralization in a particular area should begin by considering the following five questions:

1. What is the architecture of the mineralizing system?

2. What is its geotectonic history?

3. What processes were driving fluid flow on the scale of the system?

4. What was the nature of the fluids associated with the mineralization?

5. What was the mechanism for alteration and precipitation of the ore?

Qualitative answers to these questions lead the way to conceptual models, which in turn provide a framework for quantitative, numerical models.

The objective behind this part is to examine the effects of the pluton geometries and the heterogeneous permeability distributions on fluid circulation, heat transfer and subsequently localizing (R^2AI), within some different known geological settings, in order to estimate the possible position of ore deposits.

The following questions are the main aims of this research:

1. How does intruded magma affect and/or create a hydrothermal convection?
2. How does the geometry (shape) of intruded body impacts on convective patterns, thermal distribution and R^2AI?
3. What is the role of permeable zone (fractures and faults) in forming ore deposits?
4. How does the numerical modelling explain the genetic link between intruded magma and related mineralization and the age dating problems as well?

To answer these questions, we divided our work into two main parts representing:

1) Examine theoretical cases of hydrothermal circulation around a pluton, and study the effects of different parameters such as permeability, shape of intruded bodies and permeable zones (e.g. faults and fracture systems).
2) Applying numerical models to natural cases to compare numerical results with field observations.

Chapter (II) Numerical modeling and physical properties of magma

Résumé français du chapitre (II)

Dans cette partie de la thèse, nous essayons d'expliquer brièvement les paramètres physiques du magma qui jouent un rôle important pour le transfert de chaleur et l'écoulement de fluide. Puis nous décrivons la construction du modèle et nous terminons avec la validation de notre modèle avant les applications.

1. Paramètres physiques

L'évolution de la distribution de la température en n'importe quelle structure est régie par les propriétés thermiques du matériel, en particulier par la capacité calorifique et la conductivité thermique.

1.1 Conductivité thermique

C'est la propriété d'un matériel qui indique sa capacité à transférer la chaleur de façon conductive. La conductivité thermique ($W.m^{-1}.K^{-1}$) varie inversement avec la température. Ainsi des mesures de conductivité thermique en fonction de la température montrent généralement que la conductivité thermique diminue avec l'augmentation de température, jusqu'environ à 1000-1200°C (Clauser, 1988). Les équations suivantes expriment la conductivité thermique en fonction de la température pour les roches magmatiques, métamorphiques, sédimentaires et l'eau :

$$\lambda_{\text{roches magmatiques}} = -0.0016(T) + 2.6842 \quad \text{(II.1)}$$

$$\lambda_{\text{roches métamorphiques}} = -0.0023(T) + 3.1138 \quad \text{(II.2)}$$

$$\lambda_{\text{roches sédimentaires}} = -0.0044(T) + 4.0276 \quad \text{(II.3)}$$

$$\lambda_{\text{l'eau}} = 0.0012(T) + 0.2557 \quad \text{(II.4)}$$

où T est la température en K.

1.2 La capacité calorifique

Également connu en tant que *chaleur spécifique*, c'est la quantité de chaleur qu'il faut fournir à un système pour élever sa température d'un kelvin. Dans le Système International d'unités, la capacité calorifique s'exprime en joules par kelvin ($J.K^{-1}$). Comme nous avons fait pour la conductivité thermique, nous essayons de trouver un rapport mathématique simple expriment la relation entre la capacité calorifique et la température:

$$C_{P\ \text{roches magmatiques}} = 0.6169(T) + 626.32 \quad \text{(II.5)}$$

$$\mathbf{C_{P\ roches\ métamorphiques}} = 0.5915(T) + 636.14 \quad \text{(II.6)}$$

$$\mathbf{C_{P\ roches\ sédimentaires}} = 0.5814(T) + 683.07 \quad \text{(II.7)}$$

$$\mathbf{C_{P\ l'eau}} = 16.782(T) + 2013.2 \quad \text{(II.8)}$$

1.3 Densité

Elle est définie comme le quotient de la masse *m* et du volume v d'un matériel. ($\rho = m*v^{-1}$), l'unité de SI pour la densité est $kg{\cdot}m^{-3}$. La densité de n'importe quel matériel change avec la température. La diminution de la densité avec la température jusqu'à 1000°C est entre 11- 13 %.

L'équation qui exprime la variation de densité par rapport aux changements de température pour obtenir la convection thermique est:

$$\rho = \rho_0 \left(1 - a_v \left(T - T_0\right)\right) \quad \text{(II.9)}$$

Où ρ est la densité à T_0 et α_v est le coefficient volumétrique de dilatation thermique.

1.4 Viscosité

Elle mesure de la facilité de l'écoulement d'un liquide et de la mobilité des ions; elle représente une mesure de la résistance à l'écoulement. Une relation mathématique qui exprime la relation entre la viscosité et la température est nécessaire pour la simulation numérique qui étudie la mise en place de magma et la circulation hydrothermale. Le rapport entre la viscosité et la température peut être exprimé par une équation d'Arrhénius :

$$\mu = C * e^{\left(Ea/RT\right)} \quad \text{(II.10)}$$

où μ est la viscosité, C c'est une constante, Ea est l'énergie d'activation, égale à 30 $K*J*mole^{-1}$ et R la constante de gaz universelle, égale à 8.314472 $J*K^{-1}*mol^{-1}$.

1.5 La perméabilité et la pression du fluide

La perméabilité est la capacité d'un matériel à transmettre le fluide; l'unité SI pour la perméabilité est en mètres carrés; ce paramètre est un paramètre géologique critique car la migration de fluides joue un rôle fondamental dans le processus de minéralisation.

Ingebritsen et Manning, (2003) ont proposé un rapport exponentiel entre la perméabilité et la profondeur, basé sur des études et des évaluations géothermiques de flux de fluide métamorphique:

$$Log\left(K\right) \approx -14 - 3.2\log\left(z\right) \quad \text{(II.11)}$$

où K est la perméabilité et le z est la profondeur (km).

La pression du fluide peut réduire la force de roche et provoquer une rupture fragile par la tension efficace principale en profondeur (z). Donc, la pression du fluide par rapport à la tension verticale s'exprime par l'équation suivante:

$$\sigma_v' = \left(\sigma_v - P_f\right) = \rho_R g z (1 - \lambda_v) \quad \text{(II.12)}$$

où le σ_v est la pression efficace, P_f la pression du fluide, ρ_R la densité de la roche, z la profondeur, g l'accélération de la gravité et λ_v est le facteur de fluide de pore.

Pour estimer l'influence de l'advection thermique, nous avons utilisé le nombre de Péclet qui décrit le rapport entre l'advection et la diffusion thermique. Le nombre de Péclet est un nombre sans dimensions de la vitesse moyenne de l'écoulement et permet de comparer l'advection à la diffusion. On le lie aux paramètres sans dimensions Re (le nombre de Reynolds) et Pr (nombre de Prandtl), Le nombre de Péclet peut être écrit comme:

$$\mathrm{Pe} = u\, R / \underline{\kappa} \quad \text{(II.13)}$$

Où u est le vecteur de vitesse du fluide, R est la dimension caractéristique de l'objet étudié en (m) et $\underline{\kappa}$ est la diffusivité thermique.

2. La construction du modèle

L'équation principale qui calcule la température dans la partie thermique de nos modèles (et qui inclut le transfert de chaleur par de convection et conduction) est exprimée comme:

$$S.C_{eq}\left(\frac{\partial T}{\partial t}\right) + \nabla\left[-\lambda_{eq}\nabla T + C_L \vec{u} T\right] = Q \quad \text{(II.14)}$$

Où S est le terme de stockage, C_{eq} dénote la capacité de chaleur volumétrique efficace ; le λ_{eq} définit la conductivité thermique efficace ; et le C_L est la capacité de chaleur volumétrique du fluide mobile. Le côté droit de l'équation (Q) correspond à la source de chaleur générale.

Quand ce qui contrôle le mouvement de fluide dans le milieu poreux est le gradient de potentiel hydraulique, la loi de Darcy s'applique. Selon cette loi, le flux net qui traverse une surface poreuse est :

$$u = -K/\mu\,(\nabla P + \rho_f g \nabla z) \quad \text{(II.15)}$$

Où u est la vitesse de Darcy, K est la perméabilité du milieu poreux, μ est la viscosité dynamique du fluide.

La continuité de la loi de Darcy est exprimée par:

$$\partial P / \partial t + \nabla.\left[-K/\mu(\nabla P + \rho_f g \nabla z)\right] = Q_s \quad \text{(II.16)}$$

Où S est le terme de stockage,

Les modèles ont été divisés en deux types : un type de modèles théoriques où nous avons simulé les modèles hypothétiques pour examiner les effets de la profondeur de la mise en place, de la forme de pluton ou des zones perméables. Il a été également inclus dans cette

partie la simulation de différents exemples, tous étant faits en 2D. Le deuxième type de modèles a été construit pour simuler un exemple particulier venant du Maroc Central avec une géométrie plus compliquée et plus réaliste du pluton; cette partie a été faite en 3D.

Enfin la validation de nos modèles a été réalisée pour simuler deux modèles publiés (Rabinowicz et al 1998, et modèles de Gerdes et al., 1998) et pour comparer l'observation de terrain de certains exemples normaux avec nos modèles numériques équivalents (pour plus de détails voir ci-dessous).

1. The code:

COMSOL is a general purpose reactive-transport code developed for a variety of scientific problems, thermal and earth sciences problems are one of them. Simulations can be solved for coupled fluid flow, heat transfer and water-rock interactions, as well as the ability to solve these functions individually. To solve the PDEs (partial differential equations), COMSOL Multiphysics uses the *finite element method (FEM)*. For example a PDE will involve a function u(**x**) defined for all **x** in the domain with respect to some given boundary condition. The purpose of the method is to determine the function u(**x**). The method requires the discretisation of the domain into subregions or cells. For example a two-dimensional domain can be divided by a set of triangles (the cells). On each cell the function is approximated by a characteristic form. For example u(**x**) can be determined by a linear function on each triangle. The software runs the finite element analysis together with adaptive meshing and error control using a variety of numerical solvers.

In numerical modeling, the discretization of the model into small subdomains (primitives hexahedra and tetrahedra in 3D and quadrilaterals and triangles in 2D) is fundamental to facilitate the calculation. The governing equations are then solved inside each of these subdomains, with an assurance to keep the continuity of solution across the common interfaces between two subdomains. So, the solution inside each portion can be a part of the main picture of fluid flow in the entire model. Those subdomains are called cells, and all elements or cells together are called a mesh or grid. The process of obtaining an appropriate mesh (or grid) is termed mesh generation (or grid generation).

Comsol multiphysics was made to solve different physical problems such as heat transfer, electromagnetics, fluids dynamics, structural mechanics and others, in addition to earth sciences. It was used to valid or study different phenomena. Comsol-multiphysics is upgraded frequently and its validation is carried out each year by an international conferences and published papers which are made especially for Comsol-Multiphysics applications.

2. Parameters and free convection mode

Fluids are produced in the earth's crust by different mechanisms such as devolatilization reactions (organic matter, H_2O and CO_2 during diagenesis and metamorphism) and fluid release during crystallisation of magmas. However, infiltration of meteoric waters and migration of fluids between distinct reservoirs can disturb these initial fluid compositions and temperatures by mixing processes. Fluid flows are driven by several driving mechanisms, including: (1) Topography- or gravity driven flow; (2) compaction-driven flow during basin subsidence; (3) seismic pumping and tectonically driven flow; and (4) buoyancy driven flow

(Kühn et al., 2006). Migration of fluids outside their initial reservoir and/or production zone results necessarily in fluid mixing. This process is especially developed in environments where fluid circulation is active such as sea floor hot springs and numerous geothermal systems (e.g. Fournier, 1977; Fournier, 1973; Dubois et al., 1994). The conclusion of Gessner et al. (2006) suggests that thermally driven flow or free convection is one possible mechanism.

2.1 Physical Parameters

The basic mechanism for heat transport is heat conduction. Heat conduction responds to gradients of temperature. However, additional heat transfer will also be accomplished by advection due to the movement of the three phases: solid, liquid and gas. The latent heat inherent to phase changes may also have significant thermal effects. The evolution of the temperature distribution in any structure is governed by the thermal properties of the material, particularly heat capacity and heat conductivity. In the case of intruded magma, it is hard to determine these properties because of the numerous phenomena that occur simultaneously within the magma, and they can not be separated easily. These effects include in particular the evolution of the porosity, water content, type and amount of crystallization, changes in the chemical composition (Vosteen et al., 2003). Therefore, in this section, we will try to illustrate the thermal properties.

2.1.1 Thermal Conductivity (λ)

Thermal conductivity as a function of high temperature is isotropic for many volcanic and plutonic rocks; in contrast, thermal conductivity of some sedimentary and many metamorphic rocks may be strongly anisotropic and difficult to measure due to the influence of many petrophysical parameters such as the evolution of the porosity and moisture content (in sediments and volcanic rocks), the dominant mineral phase (in metamorphic and plutonic rocks), and the anisotropy (in sediments and metamorphic rocks) (Clauser and Huenges, 1995).

2.1.1.1 The influence of porosity and the dominant mineral phase

Clauser and Huenges (1995), provided experimental evidence to prove that thermal conductivity varies inversely with porosity, this role is applicable for volcanic rocks, high porosity distribution is clearly skewed towards low conductivities.

Because plutonic and metamorphic rocks display a much smaller and similar porosity, the dominant mineral phase controls different conductivity distributions. For plutonic rocks, the feldspar content is the main mineral dominant, therefore high feldspar content (more than 60%) biases the distribution towards low conductivities. In contrast to that, quartz content

presents the dominant mineral phase in metamorphic rocks, low conductivity part is made up of rocks with low quartz content; the high conductivity portion consists of quartzite only.

2.1.1.2 The influence of surrounding temperature

The thermal conductivity reduction due to the temperature is marked clearly for materials except some amorphous or fused materials such as obsidian but they aren't discussed here. Thermal conductivity varies inversely with temperature, thus measurements of thermal conductivity as function of increasing temperature generally show initially a decrease with temperature, until around 1000-1200 °C (Clauser, 1988). Volcanic glasses and rocks with a small iron content increase in thermal conductivity for temperatures above 800-1000°C. Above around 900°C, the decrease of thermal conductivity with temperature is quite different, depending on the feldspar content: while there is no significant decrease (roughly 10%) in conductivity up to 300°C for rocks that are rich in feldspar, rocks that are poor in feldspar decrease by more than 40%. For metamorphic rocks, the decrease of thermal conductivity with temperature depends on the content in a dominant mineral phase. In rocks poor in quartz the decrease in conductivity amounting to about one third of the room temperature value up to 200°C, then it remains roughly constant up to 500°C (Clauser, 1988; Clauser and Huenges, 1995; Vosteen and Schellschmidt, 2003).

In our numerical modelling, detailed search was made to obtain experimental data available in the literature; often data on thermal conductivity is available for room temperature conditions only. Therefore some empirical relationships have been proposed for extrapolation on the basis of data measured at quite elevated temperature. Figure (II.1a,b and c) gives one of these databases for thermal conductivities (Vosteen and Schellschmidt, 2003). The thermal conductivity was varied with temperature by using the following linear relations:

$$\lambda_{\text{magmatic rocks}} = -0.0016(T) + 2.6842 \quad \text{(II.1)}$$

$$\lambda_{\text{metamorphic rocks}} = -0.0023(T) + 3.1138 \quad \text{(II.2)}$$

$$\lambda_{\text{sedimentary rocks}} = -0.0044(T) + 4.0276 \quad \text{(II.3)}$$

$$\lambda_{\text{water}} = 0.0012(T) + 0.2557 \quad \text{(II.4)}$$

Where λ is thermal conductivity in ($W.m^{-1}.K^{-1}$) and T is temperature in K.

The expressed property equations developed in this work are theoretically derived from empirical data. To simplify the experimental data we assumed that the relation between the thermal conductivity and temperature is always linear, and the effects of the water and gas content and porosity are negligible.

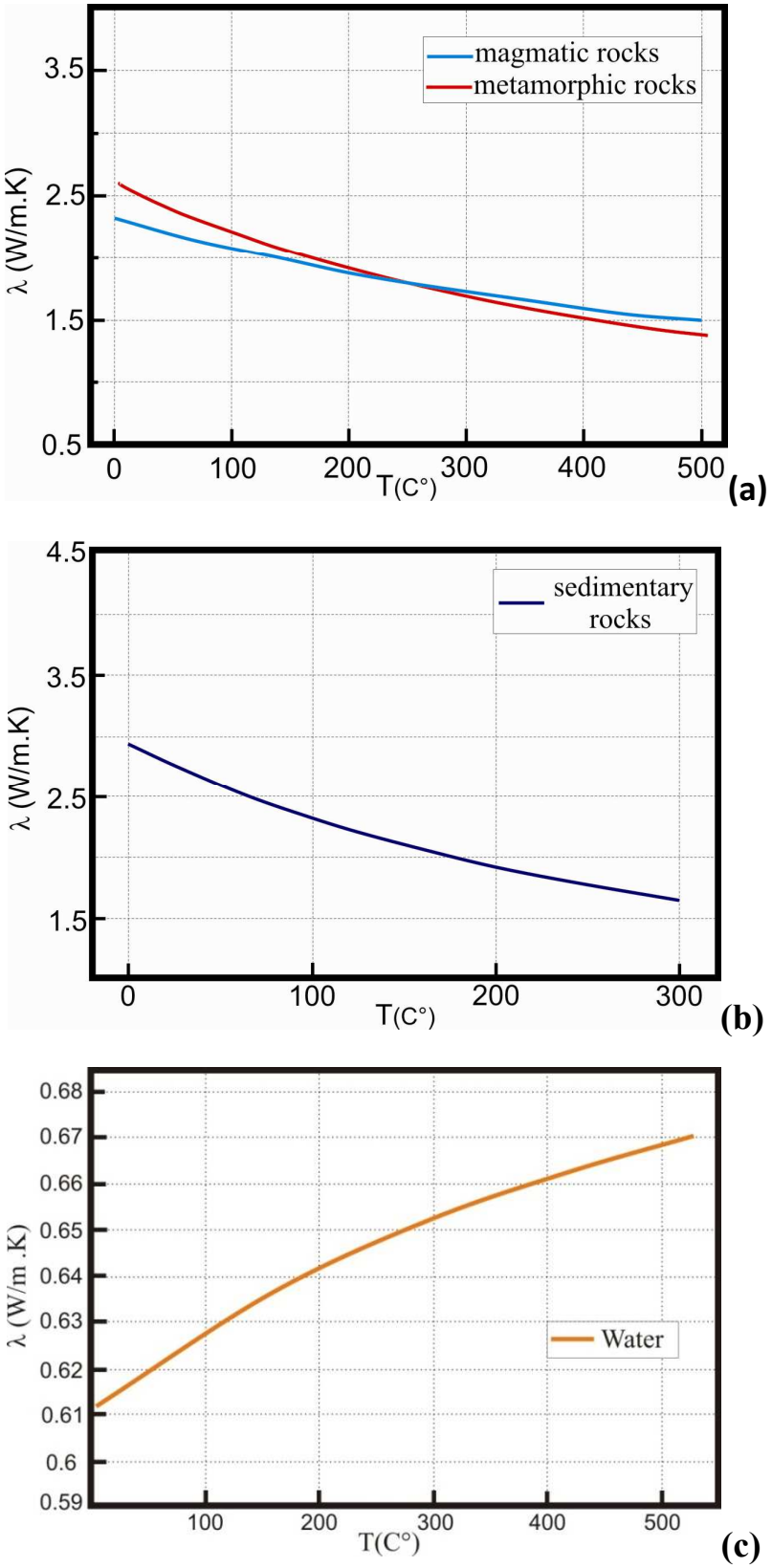

Figure (II.1): Thermal conductivity of water and different types of rocks, a) for magmatic and metamorphic rocks, b) for sedimentary rocks, c) for water (modified after Vosteen and Schellschmidt 2003).

Based on the previous lecture survey, this simplification is acceptable because the maximum temperature applied in our models was 700 C°, for this thermal limit, the assumption of linear relationship between temperature and thermal conductivity is likely acceptable.

2.1.2 Specific Heat Capacity (c_P)

It is notice that the measurements of specific heat capacity on rock materials are more rarely than thermal conductivity. Nevertheless, heat capacity ($J.kg^{-1}.K^{-1}$) is defined as the amount of heat required to raise the temperature of the unit mass (1 kg) of a substance by a unit temperature increase (1 K). The heat capacity designated by c_p, may be expressed as follows (Schaërli & Rybach, 2000):

$$c_p = \left(\frac{\partial H}{\partial T}\right)_p \qquad \text{(II.5)}$$

Where H is enthalpy (in J).

Specific heat capacity is fundamentally important in geothermal calculations because its value is reated to the amount of material in the object, the thermal conductivity λ ($W.m^{-1}.K^{-1}$) and the thermal diffusivity κ ($m^2.s^{-1}$) by the equation:

$$\kappa = \left(\frac{\lambda}{C_p * \rho}\right) \qquad \text{(II.6)}$$

where ρ is density $kg.m^{-3}$.

Values for the specific heat capacity of gases, fluids and solid materials such as metals, some rocks or other substances are reported in the literature. The specific heat of gases and fluids plays a role in porous rocks. In most cases the pore filling is water, and sometimes air, oil or mixtures of the three. A large number of data on specific heat capacities of elements and rocks or minerals are reported by Vosteen and Schellschmidt (2003).

As we have done for the thermal conductivity, we attempt to find a simple mathematic relationship expressing the relation between specific heat capacity and temperature based on literature data. Figure (II.2a, and b) summarize the empirical results done by Vosteen and Schellschmidt (2003).

The following linear relationships show the temperature-dependance laws for heat capacity of different type of rocks and water:

$$\mathbf{c_{P\ magmatic\ rocks}} = 0.6169(T) + 626.32 \qquad \text{(II.7)}$$

$$\mathbf{c_{P\ metamorphic\ rocks}} = 0.5915(T) + 636.14 \qquad \text{(II.8)}$$

$$\mathbf{c_{P\ sedimentary\ rocks}} = 0.5814(T) + 683.07 \qquad \text{(II.9)}$$

$$\mathbf{c_{P\ water}} = 16.782(T) + 2013.2 \qquad \text{(II.10)}$$

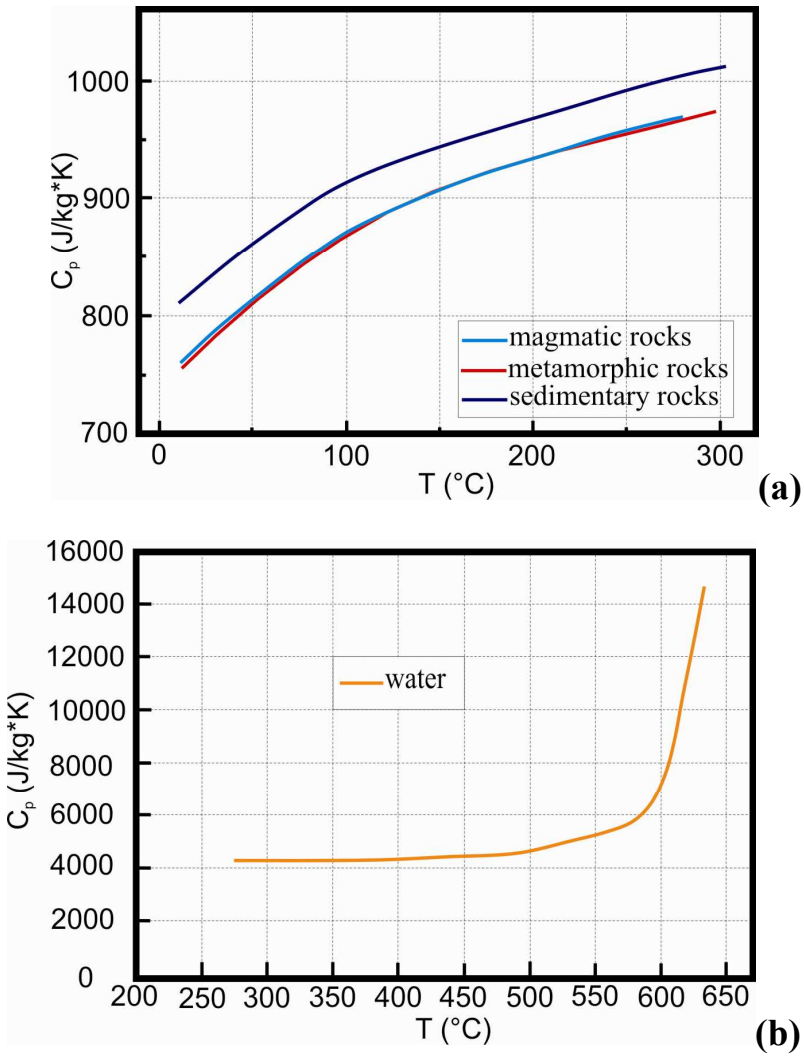

Figure (II.2): Specific heat capacity varies with temperature for a) magmatic, metamorphic, sedimentary rocks, b) and water (modified Vosteen and Schellschmidt 2003).

2.1.3 **Density**

Density (ρ) is defined as the quotient of the mass *m* and the volume V of a material. $\rho = m.v^{-1}$. The SI unit for density is $kg \cdot m^{-3}$. The density of any material changes with temperature. The relative decreasing of density with temperature up to 1000°C is between 11-13 %. When a fluid or rock is heated, its density generally decreases (for rock too especially when we deal with the geological time scale) because of thermal expansion.

Figure (II.3) shows that fluids heated from below or within become gravitationally unstable, because the cold part tends to sink while the hot part rises. This phenomenon called thermal convection (Turcotte and Schubert, 2002).

Chemical composition and specially water included are important parameters affecting on the density of liquids such as melts. Figure (II.4) shows that the variation of density based on chemical composition could be small or large over a range of several hundreds of degrees

Celsius, such as between melts of contrasting major-element composition (between basalt and rhyolite) (Best, 2001).

The thermal convection that driven by buoyancy forces is essentially depends on density variations. To take into account the buoyancy forces, we must take into our account small density variations in vertical force balance:

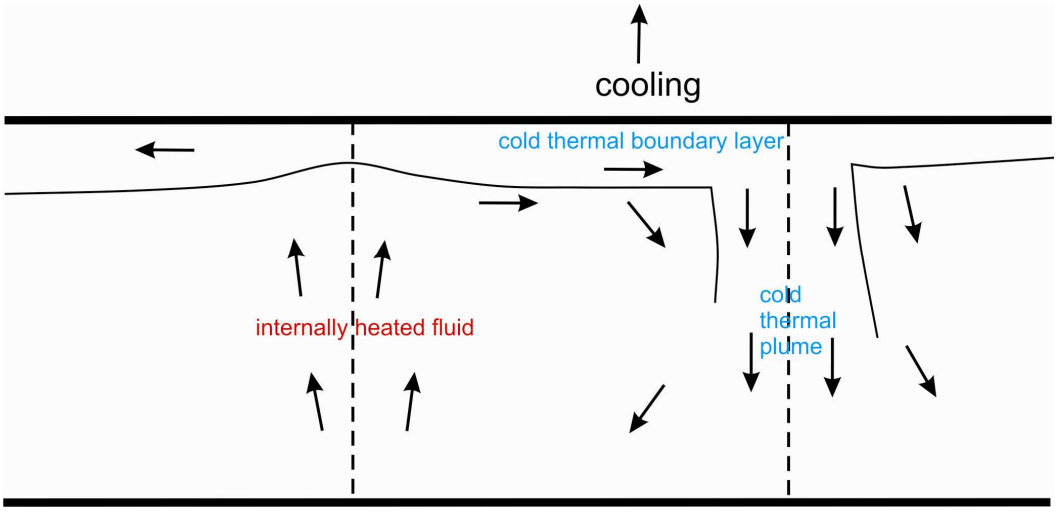

Figure (II.3): The idea of thermal convection in a fluid layer heated from within and cooled from above. (modified after Turcotte and Schubert, 2002).

$$\rho = \rho_0 + \rho' \qquad \text{(II.11)}$$

Where $\boldsymbol{\rho_0}$ is a reference density and ρ' is a density varied with temperature.

Specific densities at constant P and T can be calculated at another P and T by using compressibility and thermal expansion data for rocks and melts (Lange & Baker, 2001).

The coefficient of isothermal compressibility β, expresses the change in volume or density as P changes with depth in the earth at constant T:

$$\beta = -\left(1/V\right)\left(dV/dP\right)_T = -\left(1/\rho\right)\left(d\rho/dP\right)_T \qquad \text{(II.12)}$$

Where V is the molar volume.

Because dV/dP is negative β is positive; it has units of reciprocal pressure. For crystalline solids (Lange & Baker, 2001), β = 1-2 $*10^{-11}$ Pa^{-1}, for melts, β ~ $7*10^{-11}$ Pa^{-1} and water 1.7 Pa^{-1}. The volumetric coefficient of thermal expansion $\boldsymbol{\alpha_v}$, expresses the change in volume or density as T changes at constant P.

$$a_v = -\left(1/V\right)\left(dV/dT\right)_P = -\left(1/\rho\right)\left(d\rho/dT\right)_P \qquad \text{(II.13)}$$

α_v has units of reciprocal degrees. Most minerals and rocks have a thermal expansion in the range of 1-$5*10^{-5}$ deg^{-1}, for many silicate melts, α_v ~ $3*10^{-5}$ deg^{-1} and for water $4.7*10^{-4}$ deg^{-1}.

The densities of natural melts depend mostly on their chemical composition; especially the concentration of water and its changes during crystallization is more dramatic.

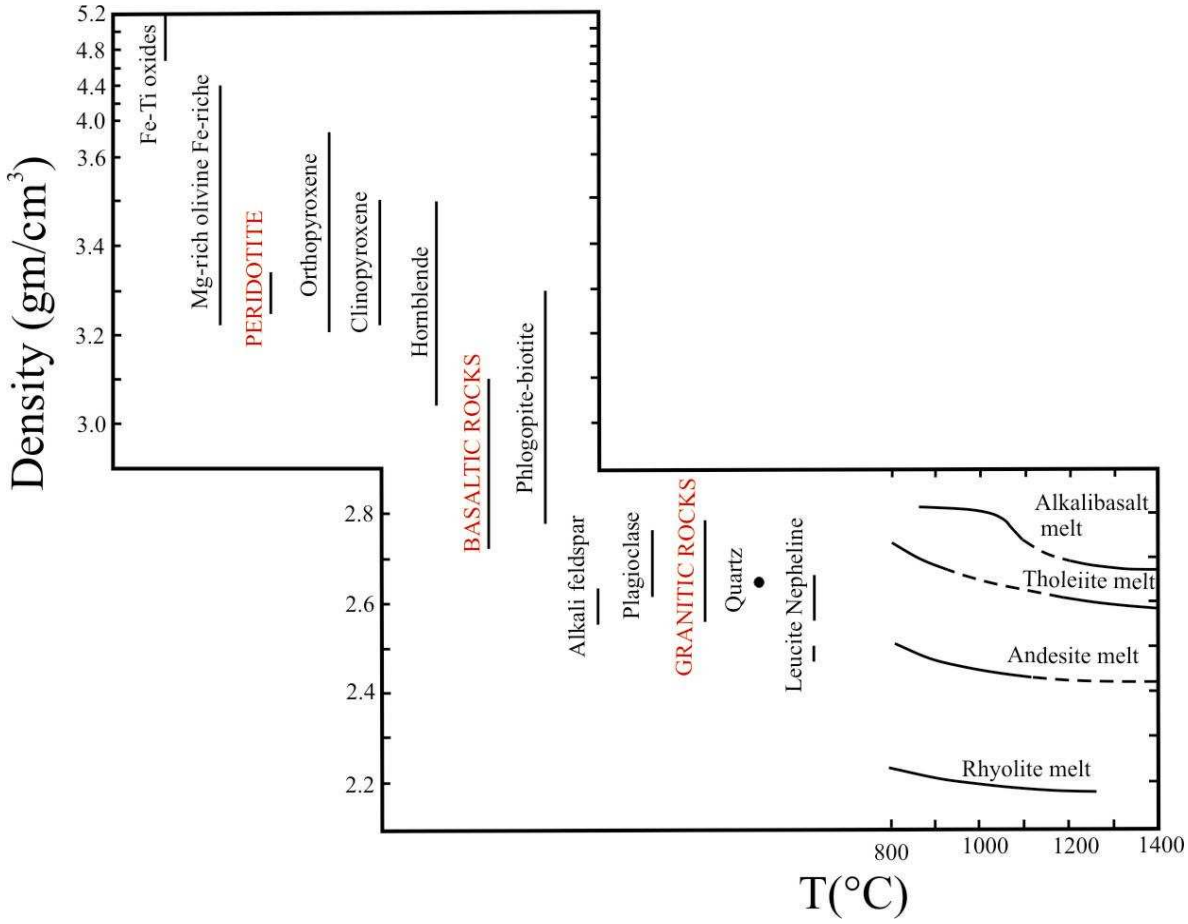

Figure (II.4): Densities of common rock-forming minerals and rocks at atmospheric P and T and melts at 1 atm. Higher densities for mafic solid-solution silicates are Fe-rich end members; lower densities are Mg-rich end members. Note change in density scale in upper left. Experimentally measured densities for crystal-free melts. (modified after Murase and McBirney, 1973).

For example, dissolving only 0.4 wt.% water in a basalt melt at 1200°C and 700 bars has the same effect on density as increasing T by 175°C or decreasing P by 2300 bars (Ochs and Lange, 1997). Following to our simplification, we once again introduce a relation between temperature and density to create thermal convection as we consider the variation of density with pressure is small and then negligible. The density variations caused by temperature changes are given by Turcotte and Schubert (2002):

$$\rho' = -\rho_0 a_v (T - T_0) \tag{II.14}$$

By substitution of equation [II.13] into equation [II.10], we obtain:

$$\rho = \rho_0 (1 - a_v (T - T_0)) \tag{II.15}$$

Equation [II.15] is our expression for density variation with temperature changes, to create and obtain thermal convection.

2.1.4 Viscosity

Viscosity is a measure of the ease of flow of a melt and the mobility of ions, or is a measure of the resistance to flow. Thus, viscosity is a manifestation of mobility. In other words, fluidity is the term used to express the contrast of viscosity.

The unit of viscosity is the Pa s (Pascal*second) or the poise (10 poise = Pa s). Viscosity is the most important property of melts that controls the dynamic behaviour of magmas. Segregation of partial melts in upper mantle and lower crustal sources, magma ascent to shallower depths, intrusion, extrusion as lavas or as explosive fragments, and crystallization all depend on the viscosity of the melt. To demonstrate the importance of viscosity in the mobility of fluids, we take the tar (asphalt) as an example. Tar at 24°C is more viscous than honey, which is more viscous than water. One principal factor governing viscosity of fluids is their temperature. For any melt or fluid composition, higher T reduces the viscosity by losing the melt or fluid structure through the increased kinetic energy of the atoms; ionic mobility is enhanced. Figure (II.5) illustrates the strong dependence of melt viscosity on T and composition. (Best, 2003). For example, the dependence on T is shown by the fact that between 700°C and 1000°C the viscosity of a water-free rhyolite melt decreases by six orders of magnitude, from about 10^{15} to 10^{9} Pa s (Murase and McBirney, 1973; Webb and Dingwell, 1990; Dawson et al., 1990).

Briefly, based on the previous paragraphs, a mathematic relation expresses the relation between viscosity and temperature is necessary to be accounted for in the numerical simulation which studies the hydrothermal coupling pre—syn and post-magma emplacement. Based on Turcotte and Schubert (2002), viscosity dependence temperature can be expressed by Arrhenius equation:

$$\mu = C * e^{\left(Ea/RT\right)} \qquad \text{(II.16)}$$

Where μ is viscosity, C is a constant, Ea is activation energy, equal to 30 K*J/mole and R is universal gas constant, equal to 8.314472 J/K*mol.

This equation is applicable for both melts and fluids because both of them have a Newtonian behaviour. Where Newtonian fluid is a fluid behaves like water-its shear stress is given by:

$$\tau = \mu * \left(\frac{\partial u}{\partial x}\right)$$

Where τ is the shear stress exerted by the fluid, μ is the fluid viscosity and ∂u/∂x is the velocity gradient perpendicular to the direction of shear.

The viscosity of a Newtonian fluid is the constant of proportionality between shear stress and strain rate. The constant C can be eliminated by referencing the viscosity to its value at the upper boundary μ_0, the variation of viscosity of water with temperature then can be determined by the following equation (Kestin et al., 1978):

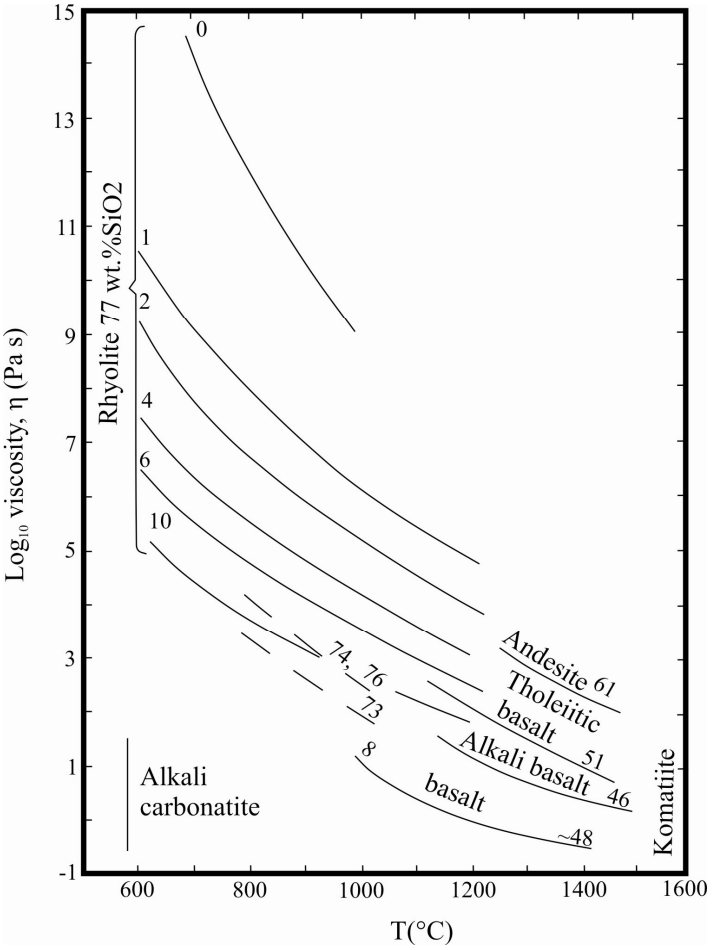

Figure(II.5): Newtonian viscosities of some crystal and melts as a function of T at 1 atm. P dependences are negligible. Concentrations of silica in weight percentage are indicated as well as of water in weight percentage at low-T end of curves, (modified after Murase and McBirney, 1973).

$$\mu = 2.414 * 10^{-5} * 10^{\left(\frac{247.8}{(T+133)}\right)} \qquad \text{II.17)}$$

2.1.5 Permeability and fluid pressure

Permeability is the capacity of a material to transmit fluid, the SI unit for permeability is square meter; it is a critical geological parameter because migrating fluids play a fundamental subsurface role in ore deposition, hydrocarbon maturation and migration, seismicity, and metamorphism.

The majority of significant ore deposits exist because of the advective solutes and heat by fluid circulation, transport, and deposition of chemical species are all linked to fluid flow, and

the thermal effects of fluid flow can explain the emplacement of certain types of ore deposits **(**Ingebritsen and Manning, 1999). Numerical modelling in different geological environments shows that permeability is the most important factor in fluid flow which occurs throughout the continental crust, from the surface to at least 15km depth (Famin et al., 2004). However, it is difficult to determine exactly a relation for permeability related depth, because the permeability is varying with time by different processes such as dissolution-precipitation reactions, compaction, fracturing and poroelastic response. For this reason, we can say that permeability is a parameter that depends on depth and time, which means, the permeability's value changes with different depths at fixed time and it is also varying with time at constant depth, especially when we deal with long time intervals like geological time periods. To simplify our models, we assumed that permeability is constant with time and varies only with depth. Another problem makes the mathematic expression of permeability related depth more difficult is that at the zone of brittle-ductile transitional zone, permeability decreases and varies strongly (Ingebritsen and Manning, 2003 ; Famin et al., 2004).

However, Ingebritsen and Manning (2003) proposed based on geothermal studies and estimates of metamorphic fluid flux a quasi-exponential decay of permeability (K in m²) with depth (z in km) of:

$$Log(K) \approx -14 - 3.2\log(z) \qquad \text{(II.18)}$$

Figure (II.6) shows permeability as function of depth in continental crust, based on geothermal and metamorphic data. This equation was used in our models to vary permeability with depth starting from 100m as we consider the upper 100m of the crust represented by quaternary deposits.

Fluid pressure may reduce rock strength and causes brittle failure through the principle of effective stress, at depth (z); it is convenient to defined fluid pressure with reference to vertical stress (overburden pressure) by

$$\sigma_v' = (\sigma_v - P_f) = \rho_R g z (1 - \lambda_v) \qquad \text{(II.19)}$$

Where σ_v' is effective overburden pressure, σ_v overburden pressure, P_f is fluid pressure, ρ_R is rock density, z is depth, g is gravitational acceleration and λ_v is pore fluid factor.

Pore fluid factor is the variable which controls which type of fluid pressure dominates with depth, and we can calculate it by using the following equation:

$$\lambda_v = \rho_w / \rho_R \qquad \text{(II.20)}$$

Where ρ_W is water density.

Fluid overpressuring may arise through the following: 1) compaction, especially in areas of rapid sedimentation; 2) diagenetic and metamorphic dehydration processes aided by organic maturation; 3) igneous intrusion into fluid saturated crust; and perhaps 4) direct linkage to zones of mantle degassing, as recently postulated for San Andreas Fault system (Sibson, 2001).

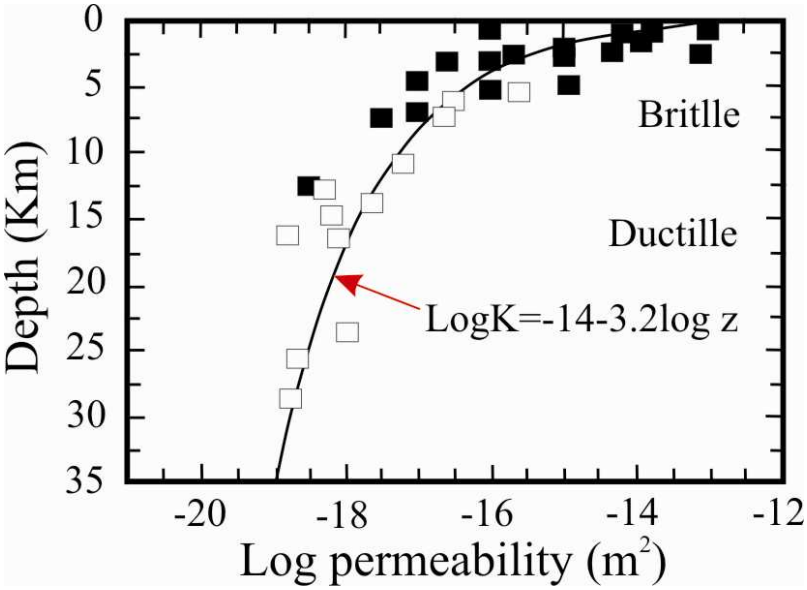

Figure (II.6): Permeability related depth curve based on geothermal data (solid squares), and metamorphic systems (open squares), (modified after Ingebritsen and Manning, 2003).

At few kilometres depth, fluid pressure is abutting to hydrostatic values (with $\lambda_v < 0.4$), with increasing depth to be more than several kilometers λ_v's values exceed hydrostatic pressure and being adjacent to lithostatic values ($\lambda_v \rightarrow 1.0$); fluid pressure levels are assumed to be near-lithostatic pressure ($\lambda_v \approx 1.0$ with $P_f \approx \sigma_v$) where the prograde metamorphism is dominated figure (II.7), (Etheridge et al., 1984; Sibson, 2001).

2.2 Free convection theory

A porous medium heated from below has an unstable situation, because cool fluid tends to sink and hot fluid tends to rise. This situation leads to free thermal convection as soon as viscous forces are not too high (Kühn et al., 2006).

On the one hand, Rayleigh convection occurs when Rayleigh number (non dimensional number representing the ratio between driving and resisting forces to fluid flow), exceeds a critical value (Eq. (II.21) & Figure (II.8)). If the thermal gradient (or any of variable parameters of the deriving buoyancy force such as permeability and density contrast) is less than some critical value, the fluid remains motionless and heat is transferred by conduction only. The non-horizontal isotherms are able to make fluids flow, without taking into account if the Rayleigh number is less or higher than its critical value. This so-called non-Rayleigh

convection is characterized by very slow fluid flow velocities, compared to Rayleigh convection.

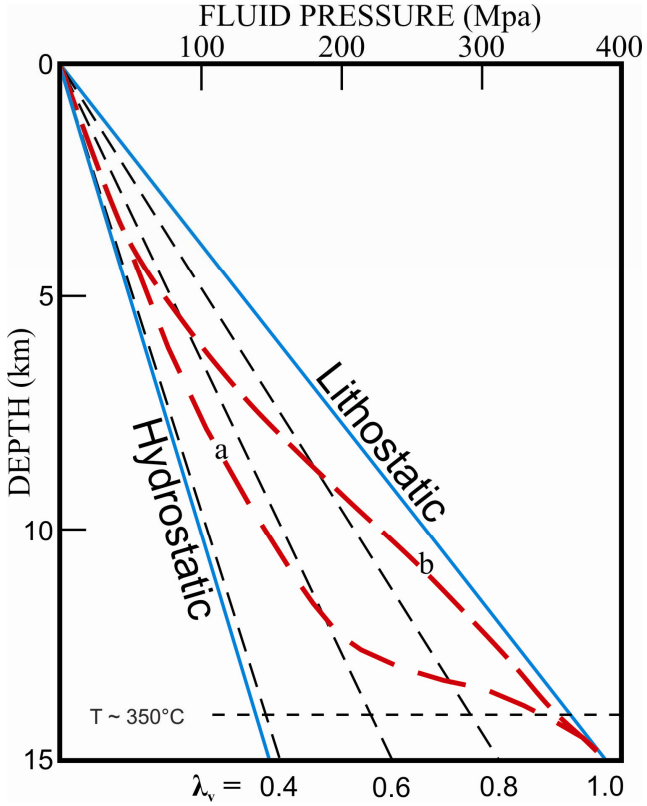

Figure (II.7): Hypothetical fluid pressure profiles, red dashed lines (a,b) represent two progressions from hydrostatic to near lithostatic fluid pressures (modified after Sibson, 2001).

2.2.1 Rayleigh Number

The dimensionless Rayleigh number (Ra) represents the ratio of the buoyant forces and the viscous forces, inhibiting fluid flow (Kühn et al, 2006). Turcotte and Schubert (2002) show linear stability analysis in a fluid saturated porous layer heated from below yields the dimensionless Rayleigh number:

$$Ra = \alpha_f g \rho^2{}_f Cp_f Kz \frac{(T - T_0)}{(\mu\lambda)} \qquad \text{(II.21)}$$

Where subscript f = fluid which is equivalent to water for our case, $(T\text{-}T_0)$ is the temperature difference and g is the gravity ($m.s^{-1}$). The critical value of the Rayleigh number Ra_{cr} marks the onset of convection. If $Ra < Ra_{cr}$, disturbances will decay with time; if $Ra > Ra_{cr}$, perturbations will grow exponentially with time. The critical Rayleigh number is a function of the wavelength of the disturbance. Figure (II.8) shows how Ra_{cr} depends on $2\pi z/\lambda$ where b is the depth. If the Rayleigh number and wavelength lie in the zone above the curve, the convection dominates; if the point lies below the curve, convection cannot occur.

In the case shown in figure (II.8), the value of wavelength corresponding to the critical Rayleigh number is:

$$\lambda = 2*(2)^{1/2}*z, \text{ hence } \min(Ra_{cr}) = 4\pi^2 = 39.4784 \qquad \text{(II.22)}$$

Therefore buoyancy forces can be strong enough to overcome the viscous resistance, (Turcotte and Schubert, 2002).

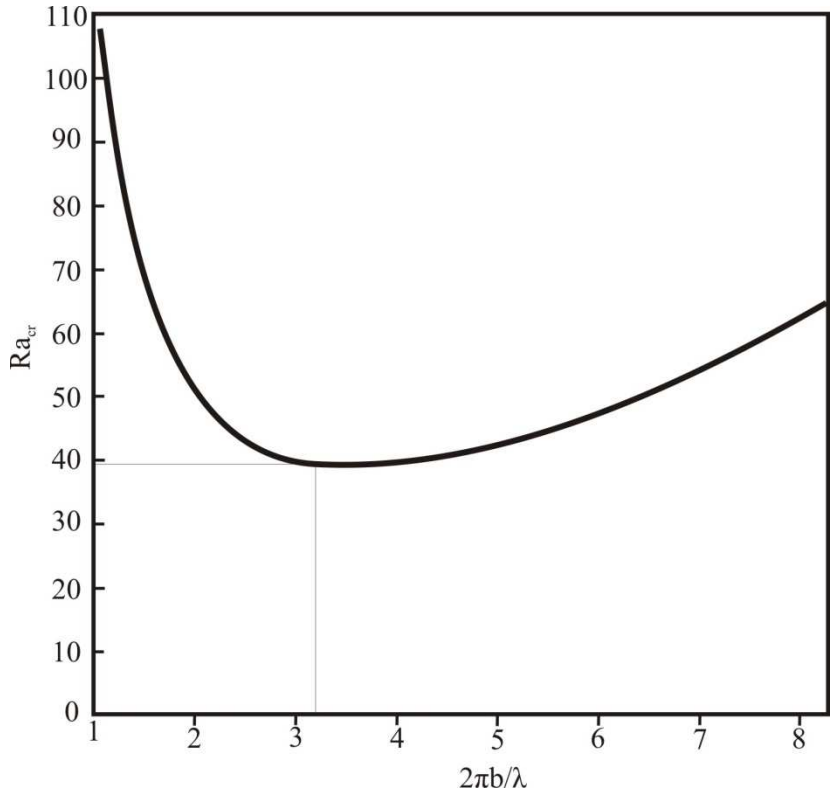

Figure(II.8): critical Rayleigh Number for the onset of convection in a layer of porous material heated from below as a function of dimensionless wave number 2Πz/λ ***(****modified after Turcotte and Schubert, 2002****).***

2.2.2 Peclet Number

The Péclet number is a dimensionless measure of the mean velocity of flow and comparing advection versus diffusion. Pe number can be written as:

$$Pe = u\,R/\kappa \qquad \text{(II.23)}$$

Where u is the velocity vector, R is a characteristic length in (m) and κ is the thermal diffusivity.

To estimate the zone of thermal advection, we have used the Peclet number which is defined as a ratio between advection and thermal diffusion. In fact, Peclet number *Pe* derived from the measured maximum velocities. Thus, when the Peclet number is small, the influence of heat advection is small because of the slow velocity. Therefore, we can say that the vertical velocity increases as the Peclet number increases and the vice versa. There is a critical Peclet

number above which the heat advection becomes efficient (Alduncin, 1993; Friedhelm & Igel 1999; Holzbecher, 2005), this critical value is (*Pe)* >1, indicative of the dominance of advection over diffusion.

2.2.3 Heat Transfer

Heat transfer involves two parts, temperature, and heat flow, where heat flow characterizes the movement of thermal energy. On a microscopic scale, thermal energy is related to the kinetic energy of molecules. It is natural for regions of high thermal energy to transfer this energy to regions with less thermal energy (∇ T). Physical properties of the medium help or avoid the transferring of thermal energy two regions at differing temperatures. Some of these physical properties are thermal conductivities, specific heats, material densities, fluid velocities, fluid viscosities, and more.

From both laboratory and theoretical studies, the rheology of mantle rocks (as they are treated as semi-viscous or semi-solid in behavior) is partly related to the temperature as a function of depth. Therefore, it is important to know the way in which heat can be lost from the interior to the surface. There are three mechanisms for the transfer of heat: conduction, convection and radiation.

2.2.3.1 Conduction

Heat transfer by conduction is performed by vibrating atoms in any material. The rate at which heat is conducted over time from a unit surface area, called the heat flux or heat flow, is the product of the thermal gradient and the thermal conductivity, or

$$\textit{Heat flow} = \textit{thermal conductivity} * \textit{thermal gradient}$$

$$(W*m^{-2}) \qquad (W*m^{-1}*K^{-1}) \qquad (K*m^{-1})$$

The governing equation to express the conductive heat transport is Fourier's law:

$$q = -\lambda * \left(\frac{\partial T}{\partial z} \right) \tag{II.24}$$

Where λ is the coefficient of thermal conductivity and z is the coordinate in direction of the temperature variation. The minus sign is to explain that heat flows in the direction of decreasing temperature, (Best, 2001).

2.2.3.2 Convection

Convection is a movement caused by a density contrast which is a consequence of temperature differences; where less dense material moves upward and more dense moves downward. Convection includes advection, in which mass or heat is transported by the currents or motion in the fluid.

2.2.3.3 Advection

A good example of advection is transport of plate tectonics to a subduction zone, the motion of the heat mantle carries the plate down to the mantle. Another common advected substance is heat, and here fluids may be water, air, or any other heat-containing fluid material. Any substance or conserved property (such as heat) can be advected, and treated mathematically as a scalar concentration of substance and the fluid as a vector field.

2.2.3.4 Radiation

It represents the transfer of electromagnetic energy from the surface of a hot body into the surrounding zone. An example of this way of transfer is the heat transferred from a hot lava into the atmosphere. In a vacuum, this energy moves at 299,800 km/s.

2.2.3.5 Production

We deal with radiogenic heat production which comes from radioactive decay as a specific value for each type of rock or lithological formation as showed in the table below. Heat production is an important way as many types of granite in Australia localized ore deposits cause of high heat production, (McLaren et al., 1999).

Granite	**9.3**
peridotite	**0.020**
Average continental upper crust	**3.9**
Alkali basalt	**1.9**

*Table (II.1): Radiogenic heating per mass of some rock types in (10^{-10} W*kg^{-1}), (after* Fowler, 2001).

2.3 Free convection in numerical view

2.3.1 Heat Transfer

The main equation which calculates temperature in the thermal part includes the convection and conduction heat transfer is expressed as:

$$C_{eq}\left(\frac{\partial T}{\partial t}\right)+\nabla\left[-\lambda_{eq}\nabla T+C_L\vec{u}T\right]=Q \qquad \text{(II.25)}$$

Where C_{eq} denotes the effective volumetric heat capacity; λ_{eq} defines the effective thermal conductivity; and C_L is the volumetric heat capacity of the moving fluid. The total fluid velocity $\vec{u}$ is a vector of directional velocities u, v and w in case of model 3D. The terms on the right hand of the equation Q denote general heat sources in conservative form. We defined C_{eq} and λ_{eq} with equations we have provided about the volume fraction θ, density ρ, specific

heat capacity C_p, and thermal conductivity λ that varies with temperature. The equations used to define C_{eq} and λ_{eq} are:

$$C_{eq} = \left(\sum \theta_{Li}\rho_{Li}C_p Li + \sum \theta_{Pi}\rho_{Pi}C_p Pi\right) \Big/ \left(\sum \theta_{Li} + \sum \theta_{Pi}\right) \quad \text{(II.26)}$$

$$\lambda_{eq} = \left(\sum \theta_{Li}K_{Li} + \sum \theta_{Pi}K_{Pi}\right) \Big/ \left(\sum \theta_{Li} + \sum \theta_{Pi}\right) \quad \text{(II.27)}$$

Here the subscripts L and P denote liquid and solid properties respectively.

2.3.2 Fluid Flow

The Navier-Stokes, Brinkman Richards and Darcy's law equations were done to describe free flows within a river; well, high and low-velocity flows in porous media.

2.3.2.1 Navier-Stokes equation

The Navier-Stokes equations characterize the flow of freely moving fluids. This suits assessments involving liquids and gases that migrate within rivers, pipes, fractures, and streams.

2.3.2.2 Richard's equation

The Richards' Equation analyzes flow in variably saturated porous media. With variably saturated flow, hydraulic properties change as fluids move through the medium, filling some pores and draining others.

2.3.2.3 Brinkman equation

The Brinkman equations describe fast moving fluids in porous media with the kinetic potential from fluid velocity, pressure, and gravity to drive the flow. These equations extend Darcy's law to describe the dissipation of the kinetic energy by viscous shear as with the Navier-Stokes equation. Consequently, this well suits transitions between slow flow in porous media governed by Darcy's law and fast flow in channels described by the Navier-Stokes equations.

2.3.2.4 Darcy's Law

The Darcy's law describes fluid movement through interstices in a porous medium. Fluid losing considerable energy to frictional resistance within pores, the velocities in porous media are very low. However, Darcy's law applies to describe water moving in an aquifer or stream bank, oil migrating to a well, and even magma rising through the earth to a chamber in a volcano.

Darcy's law was applied, when what derives fluid movement in the porous medium is the gradient in hydraulic potential. According to Darcy's law, the net flux across a face of porous surface is:

$$u = \frac{-K}{\mu}(\nabla P + \rho_f g \nabla z) \qquad \text{(II.28)}$$

Where u is the Darcy velocity, K is the permeability of the porous media, μ is the fluid's dynamic viscosity, ρ_f is the fluid's density and P is its pressure, g is the magnitude of gravitational acceleration, and z is the depth in m.

Continuity of generalized governing Darcy's Law is expressed by:

$$S.\partial P \Big/ \partial t + \nabla\left[\frac{-K}{\mu}(\nabla P + \rho_f g \nabla z)\right] = Q_s \qquad \text{(II.29)}$$

Where K is the permeability, S is the storage term and Q_s is the strength of a fluid source.

3. Model Setup

Prior to running any numerical model one requires initial and boundary conditions and governing equations. Although, numerical models of the hydrothermal circulations are based upon the same set of governing equations, described here in non-mathematical terms. Numerical methods differ in how the equations are solved; what approximations and assumptions are made and how one represents the physical processes in the physical parameters.

3.1 Model Construction

To construct a numerical model permits to investigate hypotheses concerning mineralization, and can be used in order to guide future mineral exploration, we selected parameters that affect in heat transfer and fluid flow to be varied based on incorporate of a wide range of experimental, natural, analogue, and theoretical data. These parameters are mentioned above followed by the second step is the simplification procedures.

3.1.1 Numerical Simplification

Most numerical studies simulate free convection in 2D only, because fluid patterns are more easily recognised with less complicated geometries, less computational time is required, or computer codes may be restricted to two dimensions. However, geometric complexity and stratigraphic heterogeneity around some ore deposits make it impossible to derive such an exact analytical solution for these systems. In numerical solutions, the simplicity of geometries which represent heterogeneous material properties is necessary for two raisons: 1) the complexity of geometries makes computation time sometimes too long, 2) that the complexity doesn't allow us to test different hypothesises by adding some new geometries to the geological setting; this simplicity doesn't mean ignoring the variabilities of physical parameters which created by the lithological heterogeneity. Based on this principle, we can

illustrate the interaction between fluid flow mechanisms and complex geometries and taking into account heterogeneous material properties.

Furthermore, pure water is appropriate for thermal fluid physical properties because meteoric and magmatic waters are composed mainly by pure water (XH_2O between 0.75 to 0.95 at P-T conditions between 1000-4000 bar and 720-930°C) based on data from experimental constraints on volatile abundances in arc felsic magma (Scaillet and Pichavant, 2003). They showed that the fluid compositions of different natural examples of granitic magma were mainly composed by water. Therefore, we have chosen pure water parameters (thermal conductivity, heat capacity, density and viscosity) to represent the physical parameter for fluid in our numerical models.

Finally, initial fluid pore pressure conditions are defined to be hydrostatic using Eq.(19). The porosity in the entire model is set to be constant regardless of the rock type or varying permeabilities. This simplification was done, because a lecture survey of different systems showed that the influence of changing porosity on the flow field is negligible (Kühn et al., 2006).

3.1.2 Parameters and numerical procedures

The initial permeability in the model has been adopted from the studies of Ingebritsen and Manning, (2003). Permeability varies with depth using Eq.(18) in the host rock. In contrast, it has homogeneous and isotropic distributions within the permeable zone (such as faults and fractured aureole).

Flow and heat transport are coupled in the way that the fluid parameters are functions of temperature (Eqs, 1, 2, 3, 7, 8, 10, 15 and 17), while pressure and permeability are varied with depth (Eqs. 18 and 19), all of them updated in the following time step. Therefore, the strength of coupling depends, in principle, on the time step size. As a consequence, sufficiently small time steps are required, and the numerical code adapts the time steps until a convergence criterion is validated. Thermal effects may induce buoyancy driven free convection.

Our coupling is done by incorporation between two parts; the first one is heat transfer and the second one is fluid flow. Our thermal models and coupled models incorporate simple temperature-dependent fluid viscosity, heat capacity, conductivity and density relationships (figure II.9).

Furthermore, in the fluid flow part, we vary the permeability and fluid pressure with depth and adding the viscosity and density which already vary with temperature in the thermal part (heat transfer). This allows the models to recalculate temperature, viscosity, density, heat capacity, thermal conductivity, fluid pressure and permeability at every time-step in solver

parameters. Based on these variable data every time-step we obtain a new output which becomes input for the next time-step.

The models were made in 2D except the model of Tighza pluton (the main natural example) which has been made in 3D. However, simpler models (i.e. thermal) have been tested extensively in the past and are routinely compared to results from field measurements.

3.1.3 Models Classification

One hundred ninety two models were carried out to examine three objectives mentioned above. Models of first scenario are divided into three types according to the objectives.

1. Numerous of models were made to verify the heat transfer and fluid flow coupling.
2. The first type (seventy seven models) includes simple geometry for intruded magma (square, tabular, rectangular and vertical magma bodies) within a host rock, and different hypotheses such as emplacing of different intrusions at the same or different depth at the same or different times. The physical properties of magma are represented in our simulations as granitic magma body, while host rock represents here a general metamorphic rock (mica-schist) by using the physical parameters of metamorphic rocks. These models were done to examine the first goal and to be as a data base and reference when we compare them with other models (Figure II.10).
3. The second type is to distinguish the role of apexes on the same system and the distribution of ore deposits around intrusion body. Thirty three models were created with different number and size of apexes; we keep the depth and the time of emplacement constant as they were tested in the first type.
4. In the third type, we attempted to simulate nineteen models to study the role of permeable zone (such as faults and fracture systems) which are derived from natural examples
   a- Ten models were made, to test the effect of permeable zone as a large fault nearby the magma chamber; we varied here the values of permeability for the permeable zone; the values of permeability were 10^{-14}, 10^{-15} and $10^{-16}m^2$.
   b- Nine models were to test the effect of fracture systems on the distribution of heat and fluid circulation around intruded magma and inside permeable zone. The same values of permeability for the large fault were kept as in the pervious class (the difference between fractured zone around pluton and large faults is that faults were active with permeability $10^{-15}m^2$ the whole computational time, while the fractured zone was activated only between 9.5 to 12Myr)

Other secondary models were added to validate our models (seven models) and study the different natural examples (thirty four models), which are divided into two major parts.

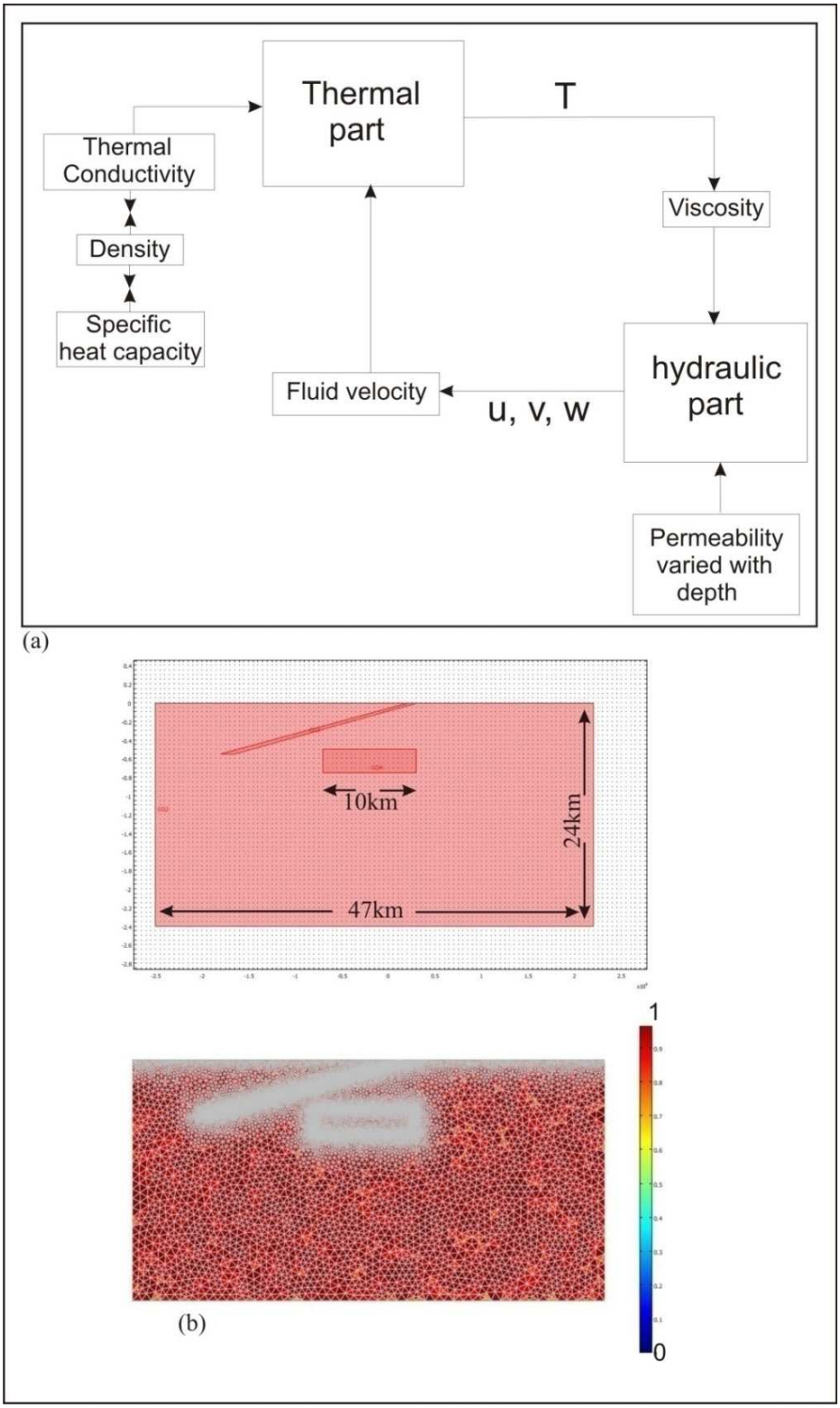

Figure (II.9) (a) Schematic digram of our hydrothermal numerical coupling, (b) an example of our models shows the quality of mesh elements (the minimum value is 0.7/1), the grey zone around the fault and intrusion represents refine mesh elements ($5*10^{-8}$ m) for the accuracy (in zones where parameters vary faster than in other zones), convergence and speed of the solution.

3.1.3.1 The first part (Theoretical and natural cases)

The models of this scenario were made to discuss the effects of depth of emplacement, emplacement of one or more pluton at the same or different time, geometry of pluton, large permeable faults and fracture systems and the role of apexes. Three domains were created, (1) A host rock with a permeability varied with depth by using Eq.(18), the geometry of host rock is fixed for all our models, with 47 km width and 24 km depth, the porosity is constant here (5%) as its influence on the flow field in negligible (Kühn et al., 2006).

Physical properties (such as thermal conductivity, heat capacity, density and viscosity) are varied by using equations (II.1, II.2, II.4, II.7, II.8, II.10, II.15 and II.17) based on data representing physical properties of metamorphic and igneous rocks, (2) intruded hot body in these models type is also fixed dimensionally (10 km width and 2.5 km length).

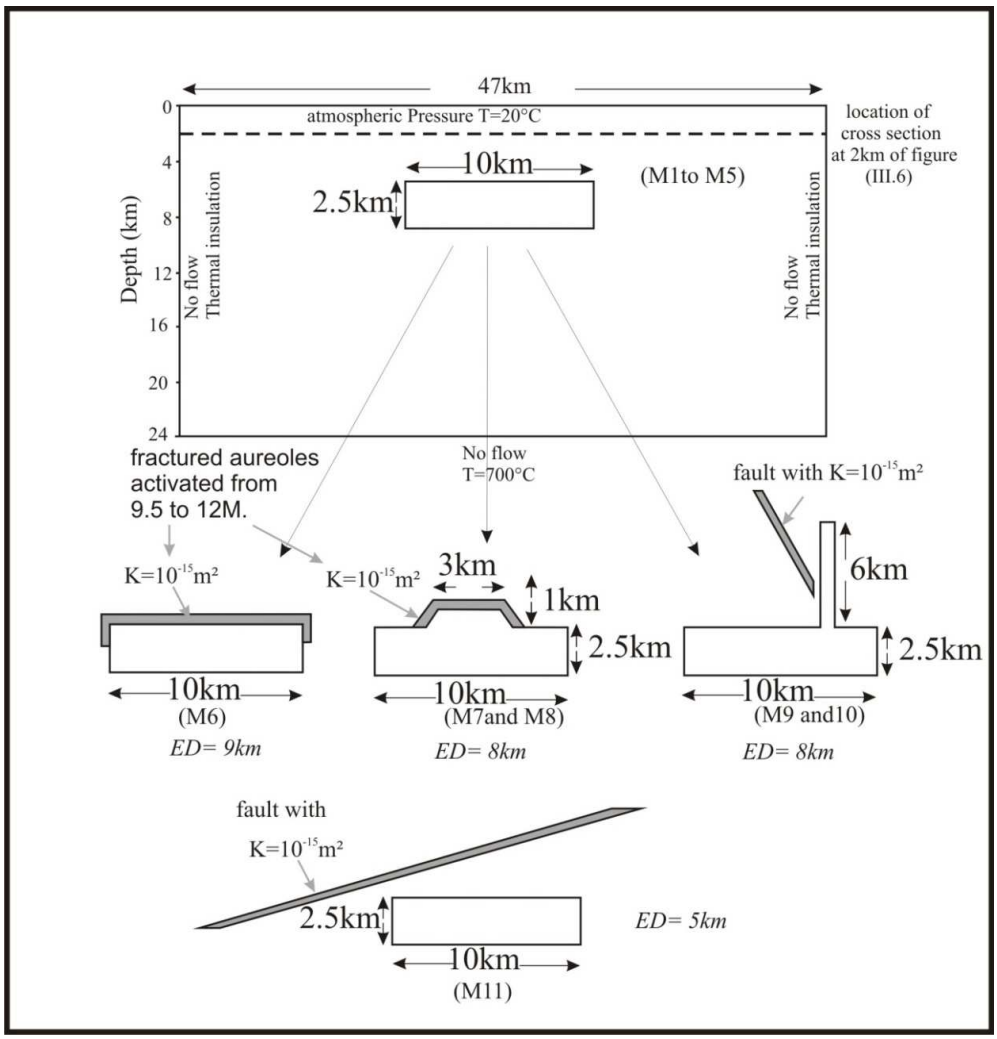

Figure (II.10): Boundary and initial conditions of our numerical models, with different forms of intruded magma. M1 to M11 correspond theoretical and natural examples mentioned in chapter (III), ED is emplacement depth.

The hot intruded body emplaced during 3 Myrs. and produces radiogenic heat 9.3 10^{-10} W/kg. We consider our pluton as a compacted crystalline granitic body by using granite physical parameters with constant porosity (5%), (3) in some cases, we added permeable systems such as fault and/or fracture, the permeability of these zones were varied between 10^{-14}, 10^{-15} and 10^{-16}m². Other hypothesis were made by changing the form of pluton by adding dykes or apexes with or without permeable fault (see below for details).

3.1.3.2 The second part (Tighza example)

In this part, we introduce a 3D geometry of pluton, and create a numerical model with real geometry. This example comes from Hercynian natural case (Tighza Pluton, central Morocco), where the mineralization related pluton is presented.

The 3D geometry of this pluton was constrained by gravity measurements, and made by using a software presented in chapter (IV) where we will discuss in detail the natural example and the processing to obtain the geometry of pluton.

3.2 Validation and applications

In order to make sure the computational results of a particular numerical model is reliable and consistent with the flow physics under investigation, capabilities of this numerical model for predicting realistic physical processes and phenomena have to be confirmed before the model is accepted and applied to simulating real world problems. A numerical model is a complex system of equations wrapped with boundary conditions, it is not guaranteed to have these capabilities even it has been proven to be mathematically correct, unless they have been validated with physical model data or with a model that was already published.

In addition, a numerical model for general flow simulation should have many validation tests using different physical models (natural examples and/or published numerical models) should be carried out to evaluate each one of them.

The test cases selected in this research are divided into two types, natural and published types. The natural models selected are four natural examples; they will be described in detail in next chapter, while the selected published numerical models are represented by two models done by (Rabinowicz et al., 1998 ; Gerdes et al., 1998).

3.2.1 The first validation test (Rabinowicz model)

This example explains the hydrothermal convection within a sedimentary layer in the Middle Valley which is a sedimented rift valley in the northern Juan de Fuca Ridge. Rabinowicz et al; (1998) have constructed their model by using the following initial conditions: (a) the equations are solved in a rectangular domain of (3 to 5.5 km). (b) No flow passes through the bottom of the box, and the dimensionless temperature along this interface is kept constant and

equal to 400°C. (c) Along the top of the box, the dimensionless temperature is equal to 0, and the fluid is free to enter and leave the simulation domain. (d) Pressure is constant along the top interface. (e) They also varied viscosity, density and pressure with temperature and depth respectively by inserting physical laws, while heat capacity and thermal conductivity were inserted to the model as constant values. (f) The governing equations were Darcy's law and heat transfer equations.

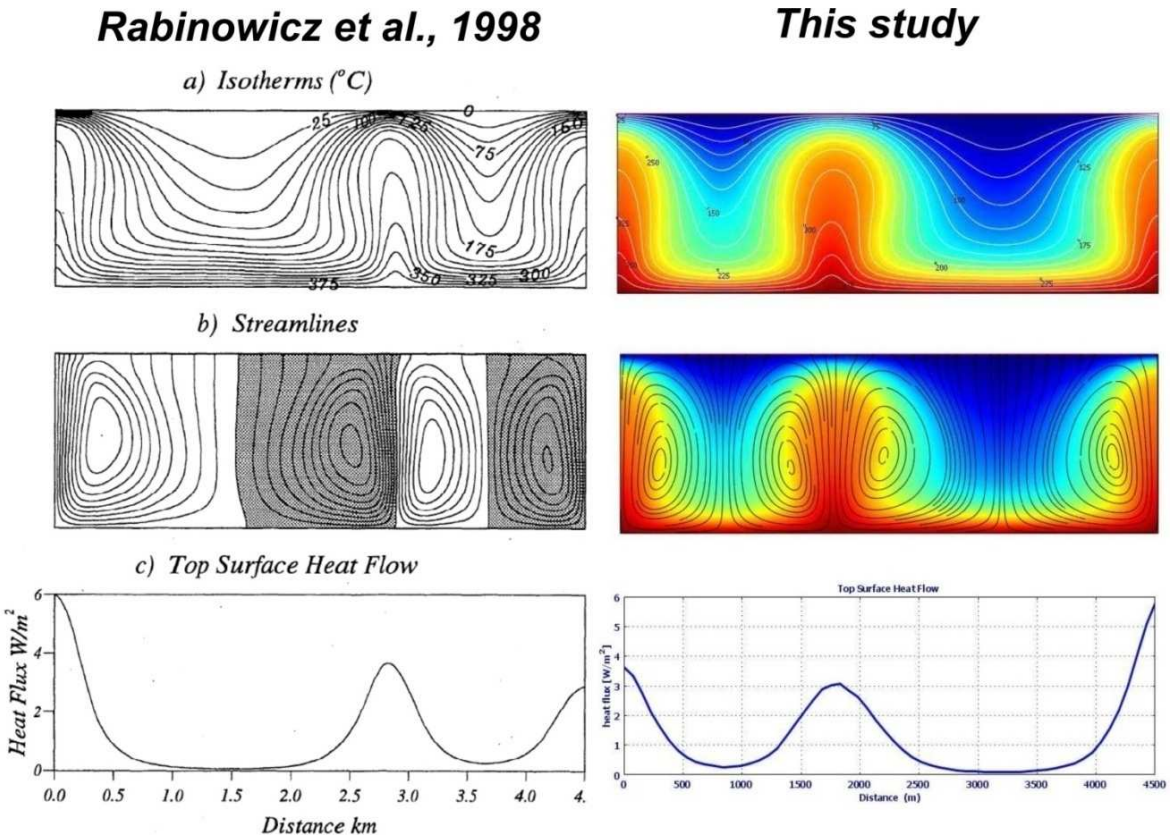

Fig.(II.11) Rabinowicz model (in the left side) and the equivalent test made by our numerical coupling (in the right side).

Figure (II.11) shows their model and the equivalent model made by us based on their available initial conditions. May you have noted the slight difference between the two models in heat flux, we referred this to their boundary condition at the base which was not well detailed. Therefore, we increased the temperature at the bottom to reach 400°C. During time, convective pattern adapts and gets a similar unsteady behavior as the one described by Rabinowicz et al. (1998).

3.2.2 The second validation test (Gerdes Model)

Gerdes et al. (1998) have used stochastic representations of permeability in a series of transient numerical simulations to assess how much small-scale rock heterogeneities influence kilometer-scale fluid convection around a shallow crustal pluton. They consider different permeability values by varying statistical characteristics of the permeability distribution.

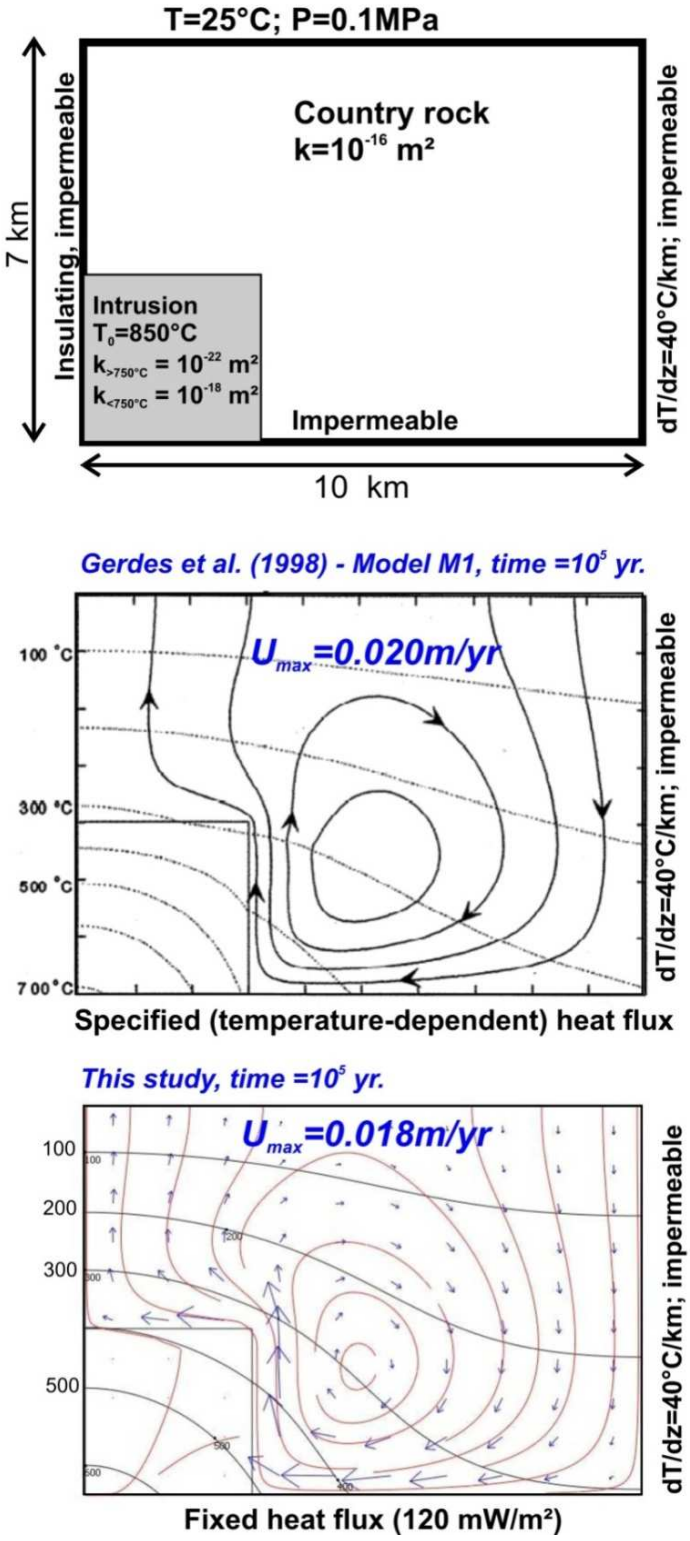

Figure (II.12) An identical model of (Gerdes et al (1998) at the middle) reproduced by our numerical coupling (at the bottom).

They have used the mass conservation equation and Darcy's law as governing equations for fluid flow, while the conservation of energy equation includes both conductive and advective heat transport. Figure (II.12) shows our simulation of their simplest model, where

permeability is constant in the host rock. A negligible difference in measured fluid velocity was noted ($0.002 m*yr^{-1}$), and convective patterns are almost identical, we referred the slight difference in streamlines to their boundary condition at the bottom which were not clear.The next chapter represents our work on different natural example and our discussion of different essential questions.

Chapter (III) Numerical investigation of transient hydrothermal processes around intrusions: heat transfer and fluid circulations leading to mineralization patterns.

Khalifa Eldursi[1], Yannick Branquet[1*], Laurent Guillou-Frottier[2], Eric Marcoux[1]

1. Université d'Orléans et Université François Rabelais de Tours / CNRS / INSU, ISTO - UMR 6113, Campus CNRS, 1A rue de la Férollerie, 45071 Orléans Cedex, France.

2: Bureau de Recherches Géologiques et Minières, 3 avenue Claude Guillemin, BP36009, Orléans, F45060, Cedex2, France.

*Corresponding author: Yannick.Branquet@univ-orleans.fr

Manuscript to be submitted to Earth & Planetary Science Letters, april 2009.

Résumé et conclusion français du chapitre (III)

1. Résumé

Les circulations de fluides autour des intrusions magmatiques ont été évaluées par modélisation numérique couplant circulation de fluide et transfert de chaleur. Ce travail rend compte de modèles physiques simples qui ne simulent pas i) les fluides polyphasés ; ii) la diffusion chimique, iii) la topographie, iv) l'entrée dans le système d'eaux météoriques ou magmatiques. Néanmoins, l'originalité de notre modélisation par rapport aux travaux préexistants repose sur les points suivants : i) la perméabilité varie de façon continue avec la profondeur (loi puissance) ; ii) les modèles ont été élaborés en tenant en compte de la période de mise en place de l'intrusion ; iii) un nouvel index de probabilité de précipitation minérale a été établi et cartographié sur les modèles (R^2AI) ; iv) de nombreuses de situations géologiques naturelles ont été testées. Elles présentent des différentes profondeurs d'emplacement, des zones de perméabilité élevée (auréoles thermiques fracturées, failles), ainsi que des géométries de pluton complexes avec des apex ; v) la zone en dessous de pluton a été explorée.

Nos résultats principaux sont :

1. L'hydrodynamique ainsi que la zone favorable de minéralisation autour du pluton sont fortement dépendants de la profondeur de mise en place du pluton. Les plutons mis en place en profondeur (dessous 10km) et non liés aux zones de perméabilité élevée (i.e. failles) n'induisent pas d'advection efficace pour former des zones minéralisées. Au-dessus de 4.5 km de profondeur, le seuil de perméabilité de 10^{-16} m² est atteint et les cellules convectives du second ordre peuvent créer des zones additionnelles de décharge focalisée de fluide où des minéralisations sont potentiellement présentes.
2. Pour toutes les profondeurs d'emplacement, la zone en dessous du pluton ne présente pas de potentiel de minéralisation.
3. Les apex plutoniques modifient fortement l'hydrodynamique autour de l'intrusion en focalisant et relocalisant des zones advectives de décharge probablement minéralisantes autour d'eux. Cette relocalisation a tendance à enlever ou restreindre les zones favorables autour du pluton principal.
4. La phase de refroidissement n'est pas nécessairement la phase convective principale lors de la mise en place d'un pluton de grande dimension. En effet, la zone advective principale la plus large et efficace pour dissiper la chaleur peut également se produire avant et pendant la phase la plus chaude de l'emplacement (i.e. avant que le magma ne

cristallise complètement). Ce résultat doit être pris en compte pour interpréter les datations absolues dans de tels systèmes (âge de mise en place de l'intrusion, du refroidissement, de la minéralisation).

5. En contexte extensif, les détachements sont à même de délocaliser et fortement modifier l'hydrodynamique induite par la mise en place d'un pluton syn-tectonique. Il paraît donc surprenant, que dans ces systèmes extensifs où aucune surpression fluide n'est nécessaire pour créer des sites dilatants, si peu de gisements soient reportés dans la littérature internationale.
6. Les conditions physiques favorables pour la minéralisation sont atteintes autour de plutons mis en place dans la croûte moyenne, pendant une durée courte centrée sur la phase la plus chaude de l'intrusion. Nous proposons que, même si les arguments chimiques sont absents pour démontrer un rôle génétique de l'intrusion, la circulation de fluides induite par la seule mise en place de magma, joue un rôle fondamental dans la genèse des gisements d'or associés aux intrusions. En ce sens, le lien génétique entre intrusion et minéralisation est fort. Par ailleurs, la formation de ce type de gisements aurifère est grandement favorisée par l'occurrence d'une auréole thermique fracturée autour de l'intrusion.

Abstract

Fluid circulations around magmatic intrusion have been re-estimated through coupled hydro-thermal numerical modeling. New insights were obtained based on: i) a continuous variation of permeability with depth; ii) transient models taking into account the emplacement period of intrusion, iii) testing the physical likelyhood of ore deposition using a restricted rock alteration index, iv) comparing our results with well-constrained natural cases where different emplacement depths, high permeability zones (cracked thermal aureoles), faults and plutonic apexes are accounted for, v) the pluton floor has been explored.

We show that the emplacement depth is a key physical parameter controlling the extent and geometries of advective heat dissipation zones. The apexes strongly modified the fluid flow pattern by focusing convective fluids and mineralization zones around them. The cooling phase is not the main phase of convection which is often associated with long-lived magma emplacement. Major advective heat dissipation and mineral deposition zone may also occur before and during the hottest phase of emplacement (before magma crystallization). Comparison with natural cases shows that we reproduced successfully in space and time the physical conditions required for mineral deposition. In particular, extensional detachments are able to delocalize and strongly modify classical fluid flow pattern induced by coeval intrusion. Finally, we conclude that, even if chemical arguments are absent, convections induced by granite emplacement play an important role in the genesis of granite-related Au deposits. Moreover, formation of this type of deposit is promoted and controlled by the occurrence of a fractured thermal aureole around the intrusion.

Keywords: Hydrothermal processes, Numerical modeling, magmatic intrusion, permeability-depth curve, mineralization, rock alteration index.

1. Introduction

Fluid flow around plutons has been extensively studied, traced and modeled within contact aureoles. Hydrodynamics around intrusions has also been assessed through 2D heuristic and finite element modeling, where heat transfer, mass transport and chemical alteration are dominant processes. Spatial distribution of ore deposits around plutonic rocks reveal particular interactions between heat transfer and fluid flow near and within contact aureoles (e.g. Gow et al., 2002). However, circulation of hot and variably pressurized fluid in the first upper kilometers of the crust is not easily predictable since rock and fluid properties may show large and time- or depth-dependent variations within such geological systems. For instance, ongoing deformation reduces effective stress and mineral reactions which are susceptible to change the host rock permeability during metamorphism (Cui et al., 2001). Thus, transient phenomena have to be considered when fluid flow around plutons is investigated.

The host rock permeability presents a threshold from which heat dissipation during cooling of the system is achieved by fluid advection rather than by conduction. Values of this threshold for homogenous country rocks span a 10^{-16}-10^{-18} m^2 interval (Norton and Knapp, 1977; Norton and Knight, 1977; Gerdes et al., 1998; Cui et al., 2001) , which is easily reached at a few kilometers depth (e.g. Ingebritsen and Manning, 1999). Moreover, hot plutons create density gradients and induce long-lived (>10^5 years after rapid magma emplacement) large-scale regional flows in the country rocks (Cathles, 1977; Norton and Knight, 1977; Cook et al.,1997). As a consequence, it was suggested that these heated fluids are responsible for development of large convective cells around the intrusion. Norton and Knight (1977) quantified a very large amount of fluid involved in convective cells far from the pluton. Expulsion of magmatic brines from intrusion increases fluid salinities and thus enhances buoyancy forces. However, production of magmatic and metamorphic fluids constitutes a pressure-driven force that interacts with buoyancy forces. Taking into account the fluid production, models of Hanson (1992), Hanson (1995) and Manning and Ingebritsen (1999) show that below a critical permeability threshold of 10^{-16} m^2, fluid production forces trigger supra-hydrostatic fluid pressures and dominate density-driven forces.

Sophisticated numerical models integrating fluid production, layered and transient permeabilities during chemical reaction emphasize the complexity and the partitioning of the flow pattern (Cui et al., 2001). This complex pattern of flow is confirmed by works on metamorphic mineral reactions and stable light isotopes distribution around natural aureoles (Ferry and Dipple, 1992; Nabelek and Labotka, 1993; Dipple and Ferry, 1996; Ferry et al.,

1998; Ferry et al., 2002; Rossetti et al., 2007). Controversial 1D models derived from some of these studies have a difficulty to trace peri-plutonic transient flow patterns in detail.

Regional metamorphic fluid flow and large scale structures (i.e. folds, faults, regional cleavage, etc) are considered to be first order controls on a bulk flow pattern, plutons acting only as second-order perturbations (e.g. Stern et al. 1992; Wing and Ferry, 2002). Nevertheless, second-order perturbations (i.e. anomalies) of fluid flow patterns are precisely assumed to be important factors during ore deposits genesis. Indeed, since pioneering works of De Launay (1913) to recent studies and syntheses, the role of magmatic intrusions as active agent during ore and raw materials depositing processes has been demonstrated (e.g.Sillitoe, 1991; Thompson and Newberry, 2000; Lang and Baker, 2001; Cerny et al., 2005). However, the contribution of intrusion on ore deposition is very different according to the types of deposits. We distinguish for instance: i) a strong contribution characterized by a genetic link between chemistry and mineralogy of intrusion and ore (e.g. Ni-Cu sulphide deposits within mafic-ultramafic magmas, Arndt et al., 2005); ii) a medium contribution, where it is well-established that a part of mineralizing fluids derived from the magmas (e.g. Au-Cu-Mo porphyries, Seedorf et al., 2005); iii) a limited and/or indirect contribution in which chemistry arguments for a magmatic connection are lacking or are equivocally established. For example, non-porphyry intrusion-related Au-Sn deposits present very subtle links with magmatic fluids (Thompson et al., 1999). However, even if a chemical genetic link between magma and ore is not obvious for this last class of deposits, absolute dating, spatial distribution and structural controls argue for a strong physical and/or rheological control of the intrusion on ore forming processes. Particularly, the thermo-mechanical anomaly generated by the intrusion emplacement appears to be a key factor triggering required fluid flows and mixing from different sources (magmatic, metamorphic, basinal, and meteoric). For example, genetic links between ash-flow calderas (related to a deeper magmatic source) and associated epithermal ore deposits were often debated. Guillou-Frottier et al. (2000) have however suggested that heat flow anomalies and increased fracture density at caldera margins - where epithermal ore deposits are clustered can be explained by particular thermo-mechanical processes occurring before, during and after caldera formation. Thus, heat transfer and fluid flows around magmatic intrusions appear to be of major importance in studying intrusion-related ore deposits (e.g. Cathles, 1981; Gow et al., 2002; Driesner and Geiger, 2007).

In the present study, we re-examine fluid flow pattern around intrusions in order to delineate the most favorable zones for ore deposition, as defined by a dynamic criterion. Our numerical

simulations (where transient heat and fluid flow equations are coupled) deal only with fluid

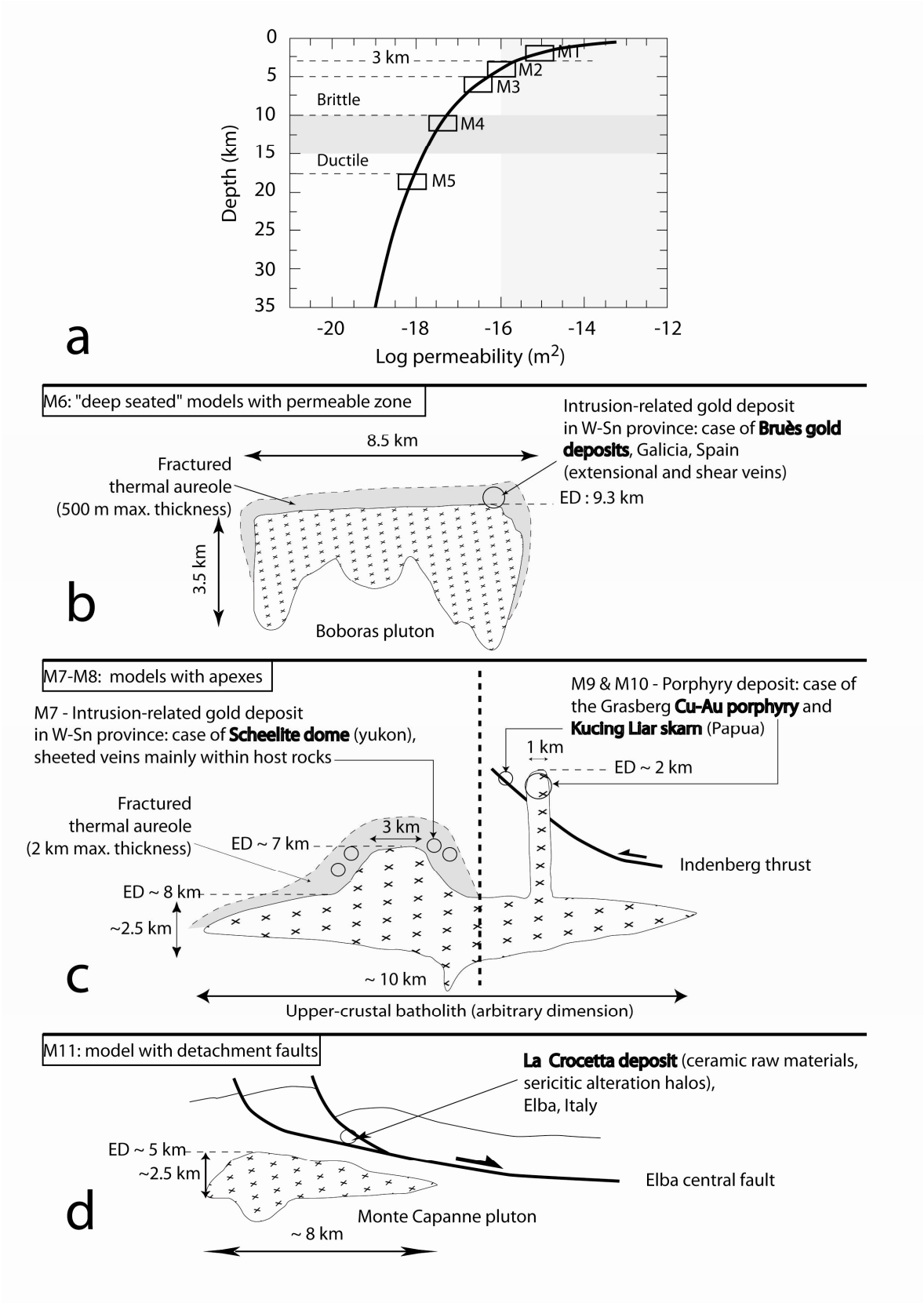

Figure (III.1): Compilation of the geometries, emplacement depth (ED) and geological context for different tested studies (see the text for more details). A: Emplacement depth of models M1-5 along the depth-permeability

curve used in this study (modified from Manning and Ingebritsen, 1999). All intrusions are 10 km width and 2.5 km-thick (see Figure III.2). Permeability threshold of free convection (10^{-16} m^2) established from literature B: Synthetic sketch of the Boboras pluton the associated Bruès gold deposit, Hercynian belt, Galicia, Spain (model M6). C: Natural examples of intrusion-related ore deposits associated with plutonic apexes. ED and dimensions (10 km x 2.5 km) of the main plutonic body (i.e. the upper crustal batholith) are realistic approximations. Models M7-8 is based on the Scheelite dome gold deposit. ED of the stock roof and mineralization (i.e. 7 km) is shallower than M6. M8 present a fractured aureole, absent in M7. Models M9 and M10 represent typical case of a porphyry-type mineralization; the selected example is the famous Grasberg Cu-Au porphyry in the Irian-Jaya fold and thrust belt. Different hypothesis will be tested: M9 without fault, M10 with fault. D: M11, models of fluid flow around plutons emplaced during low-angle extensional faulting. Geometries and structures of the Monte Capanne pluton and La Crocetta raw material deposit along the Elba central detachment.

convection triggered by heat source emplacement (i.e. plutons). Thus, excluding fluid production and solute transport, our models are designed to highlight and test some important points and hypotheses neglected in previous works:

First, fluid flow pattern has been explored below the intrusion, around the floor zone. Within a thermally equilibrated crust, the floor zone is obviously not symmetric to the roof zone through horizontal mirror operation. It is noteworthy that we address magma ascent through the dyke propagation mechanism (Clemens and Mawer, 1992). Hence, thermal structure of crust below the pluton is supposed to be less disturbed than during diapiric ascent mechanism. second, as our models are scaled to simulate large plutons within a 24 km-thick continental crust, the permeability-depth curve of Ingebritsen and Manning (1999) or Manning and Ingebritsen (1999) (figure III.1a) has been applied rather than uniform, layered or stochastic permeability models (Norton and Knight, 1977; Gerdes et al., 1998). Introduction of a depth-dependent permeability model may have important impact on fluid flow patterns. Third, an attempt has been made to evaluate the ore deposition potential. We used an improved version of the concept of Rock Alteration Index (RAI), as defined by Phillips (1991) and used by others (Zhao et al., 1998; Harcouët, 2005), and compared our results to natural well-constrained intrusion-related metal deposits. Gow et al. (2002) also undertook a numerical approach but used uniform permeabilities and investigated steady-state mineralization patterns; fourth, in previous fluid flow models (see references above), the cooling phase only was modeled, without taking into account the emplacement phase (heating phase). Even if this assumption is valid for small shallow intrusions (emplacement less than 100 000 years (Petford et al., 2000), melt production and pluton emplacement may take place over several million years in collision settings with no mantle contribution (Annen et al., 2006).

Moreover, accounting for magma emplacement duration implies that the maximum advective regime is expected to occur during the hottest phase of intrusion, before the cooling phase. Thus, in this study, sequential emplacement and subsequent cooling have been modeled in order to depict fluid flow patterns from incipient pluton inflation stage to the thermal re-equilibration into the crust. Possible effects of the intrusion shape, the emplacement depth and the role of stocks and permeable zones (such as fractures and/or faults) have been evaluated and related to hydrodynamics, duration of hydrothermal system and mineralization potential.

2. Intrusion-related ore deposits: tested natural examples

Several well-constrained natural cases of intrusion-related ore and raw material deposits have been selected in order to depict influence of various factors on the hydrodynamics of such systems. Principal characteristics of these deposits are summarized thereafter and are located in figure (III.1). Boboras pluton (318 ± 5 Myr) and its associated Bruès gold deposit (figure III.1B (M6)) have been selected to test the role of fractured thermal aureole associated with deep seated intrusion (data from Gloaguen et al., 2003; Gloaguen, 2006). It is located within the internal zone of the Spanish Hercynian belt of Galicia. Age of gold mineralization is uncertain (potential regional thermal resetting), but structural controls and fluid inclusions strongly argue for a coeval genetic link between granite emplacement and mineralizing event. Hosting micaschists are strongly veined (partially mineralized) within the thermal aureole.

Fluid expulsion from pluton might have caused hydraulic fracturing within the thermal aureole, which then appears as a high permeability zone. Note that the Bruès gold deposit is located at the roof zone around the northern edge upon a root zone. This gold deposit is characteristic of a deep seated intrusion-related gold deposit in Sn-W Province as defined by Lang and Baker (2001) and Thompson et al. (1999).

Natural examples of intrusion-related ore deposits associated with plutonic apexes have been also tested to depict the potential role of apexes. The Scheelite dome gold deposit (case M7-8, figure III.1c) is a well-established case of intrusion-related gold deposit in a Sn-W Province, around an apical granitic stock and co-genetic with it (Baker and Lang, 2001; Mair et al., 2006; Stephens et al., 2004). As in Boboras pluton, thermal aureole of the apex is intensively fractured and veined. Emplacement age of intrusion and mineralization occurred between 94 and 92 Myr. For a typical case of Porphyry-type mineralization (case M9-10, figure III.1c), we selected the famous Grasberg Cu-Au porphyry in the Irian-Jaya fold and thrust belt (see synthesis in Pollard et al., 2005). Ages span a 3.4–3.0 Myr interval from the first intrusive phase to the last mineralizing event. Along the Indenberg thrust, Kucing Liar Cu-Au skarn (3.4 Myr) is coeval with incipient intrusive phase of the Grasberg complex. For both Scheelite

Dome and Grasberg deposits, realistic size (i.e. 10*2.5km) for the main underlying plutonic body (i.e. the upper crustal "batholith") have been applied.

As a high permeability zone, detachment fault might have played an important role in channeling mineralizing fluid during extensional regime. Thus, we are interested in exploring fluid flow pattern around plutons emplaced during low-angle extensional faulting. Geometries and structures of the Monte Capanne pluton and La Crocetta deposit along the Elba central detachment is a well-constrained example of such system (case M11, figure III.1D, data compiled from Bouillin et al., 1993; Maineri et al., 2003; Rossetti et al., 2007). La Crocetta is an important economic concentration of ceramic raw materials, resulting from a strong hydrothermal alteration linked to the Monte Capanne magmatic activity. Pluton emplacement and sericitization at La Crocetta occurred between 7 and 6.8 Myr. It is noteworthy that hydrothermalism and mineralization of all tested deposits occurred within a maximum of 2Myr of magma emplacement.

3. Hydrothermal modeling: governing equations and parameters

For a fluid-saturated porous media (rock matrix), the mass conservation equation for variable density fluid without internal fluid source is:

$$\frac{\partial(\phi * \rho)}{\partial t} = -\nabla.(\rho.\vec{u}) \qquad \text{(III.1)}$$

where ϕ is the porosity; ρ is the density of fluid, t is time and $\vec{u}$ the fluid velocity vector (see Table 1 for units). Fluid is assumed to be incompressible with a constant chemical composition, and its density is temperature-dependent. The Darcy's law was used to describe the fluid velocity field:

$$u = \frac{-K}{\mu}(\nabla P + \rho_f g \nabla z) \qquad \text{(III.2)}$$

Where K is the intrinsic permeability; μ the dynamic fluid viscosity; P the fluid pressure, $\vec{g}$ the gravitational acceleration vector. The permeability has been varied with depth, using the equation of Manning and Ingebritsen (1999):

$$\log(K) = -14 - 3.2\log(z) \qquad \text{(III.3)}$$

where Z is depth expressed in km.

The fluid density was considered as a function of temperature only, one gets:

$$\rho = \rho_0(1 - \alpha_V(T - T_0)) \qquad \text{(III.4)}$$

Where ρ_0 is the fluid density at room temperature T_0 and α_v the volumetric coefficient of thermal expansion of the fluid.

Based on analytical approximation for the relationship of viscosity with temperature T (Kestin et al., 1978), fluid dynamic viscosity is given by:

$$\mu = 2.414 * 10^{-5} * 10^{\left(\frac{247.8}{T-140}\right)} \quad \text{(III.5)}$$

where T is in K and μ in Pa.s. Heat transport is achieved by both conduction and advection in porous media for an incompressible single fluid, and is described by the partial differential equation:

$$Q = C_{eq}\left(\frac{\partial T}{\partial t}\right) + \nabla\left[-\lambda_{eq}\nabla T + C_L \vec{u}\nabla T\right] \quad \text{(III.6)}$$

$\left[-\lambda_{eq}\nabla T + C_L \vec{u}\nabla T\right]$ represents the total heat flux and is composed of the conductive heat flux (first term) and the advective heat flux (second term). Q is the heat source provided by the pluton. C_L is the volumetric heat capaρ_f.Cp, and Cp is specific heat capacity. C_{eq} and λ_{eq} are weighted average volumetric (or "equivalent") heat capacity and thermal conductivity respectively, as defined in saturated porous media:

$$C_{eq} = \left(\frac{\left(\sum \phi_f \rho_f Cp_f + \sum \phi_S \rho_S Cp_s\right)}{\left(\sum \phi_f + \sum \phi_s\right)}\right) \quad \text{(III.7)}$$

where f and s subscripts for fluid and solids embeddings). The equivalent thermal conductivity writes:

$$\lambda_{eq} = \left(\frac{\left(\sum \phi_f \lambda_f + \sum \phi_s \lambda_s\right)}{\left(\sum \phi_f + \sum \phi_s\right)}\right) \quad \text{(III.8)}$$

Where λ_f and λ_s are thermal conductivities of the fluid and the country rock.

Fluid flow and heat transport are coupled through the density and viscosity of fluids (equations 4 and 5).

4. Defining a Restricted Rock Alteration Index

Coupling of heat and fluid flow equations has been computed numerically, with temperature-dependent properties (i.e. density, viscosity, heat capacity and thermal conductivity) and depth-dependent permeability. In order to gain some insight into how mineralization patterns can be deduced from thermal and velocity field, one may start from the initial work of Phillips (1991), who derived a mineralization rate which depends on diffusive and advective

processes. In short, fluids carrying dissolved chemical species move through a permeable matrix or fractures network. The resulting patterns of dissolution, precipitation, and fabric alteration depend on the reaction kinetics and on the influence of temperature, pressure and other constituents. However, in many geological situations, the controlling factor is the rate at which reactants in solution can be delivered to the reaction site by advection and diffusion in the flow. The dissolution/precipitation of an aqueous mineral is mainly dependent on advection term since diffusive processes are negligible when large-scale processes (fluid circulation over a large timescale) are considered.

As in buoyancy driven convective flows, the fluid pressure gradient is small, the sign of the mineral dissolution/precipitation rate depends on the scalar product of fluid velocity vector by temperature gradient (for more details see Phillips; 1991; Zhao et al. 1998; Raffensperger and Vlassopoulos, 1999; Zhao et al.,2001; 2003; Harcouët 2005). This scalar is called the Rock Alteration Index, or RAI, and is defined as:

$$RAI = \vec{u}.\vec{\nabla}T \qquad \text{(III.9)}$$

With an additional hypothesis on the sign of the partial derivative of solute concentration with taking into account the temperature, Phillips (1991) deduced that if RAI is positive, then mineral dissolution occurs, whereas for a negative value of RAI, mineral precipitation is promoted. Since RAI unit is expressed as $K.s^{-1}$, one may interpret negative RAI values as local cooling rates of the fluid, while positive values would correspond to local heating rates.

During regional metamorphism, pluton acts as second order intense fluid flow perturbation within slower regional fluid flow (Stern et al, 1992). For active regional metamorphism, a Darcy velocity of 10^{-11} $m.s^{-1}$ is considered to be an average value (Ingebritsen and Manning 1999). For contact metamorphism, Darcy velocities, from time integrated flux based on mineral reactions and stable isotopes studies range from 10^{-9} $m.s^{-1}$ to 10^{-11} $m.s^{-1}$ (Ferry et al., 2002). Hydrothermal numerical models of contact or regional metamorphism, predict Darcy velocities ranging from 10^{-8} $m.s^{-1}$ to 10^{-11} $m.s^{-1}$ (Cook et al., 1997; Gerdes et al. 1998; Oliver et al. 2006). Thus, in order to decipher the pluton contribution to fluid flow, a restricted fluid velocity condition ($u > 10^{-10}$ $m.s^{-1}$) was added parallel to RAI. This restricted RAI (R^2AI) is defined by the logical expression:

$R^2AI=[RAI<0$ and $u > 10^{-10}$ $m.s^{-1}]=1$ If it is valid and 0 if not (III.10)

5. Model construction: geometry, timing, boundary conditions and rock properties

5.1 Geometry

We constructed our models based on theoretical and selected well-known natural cases (M1 to M11, figure III.2). Along the depth-permeability curve of Manning and Ingebritsen (1999),

the models (M1 to M5) were performed to study the effect of emplacement depth on hydrothermal circulations and being as references for natural cases (figures III.1, 2). The basic geometry chosen for theoretical models (M1 to M5) was a rectangle with 2.5 km thick and 10 km width with emplacement depth varying from 3 to 17.5km (figure III.1, 2).

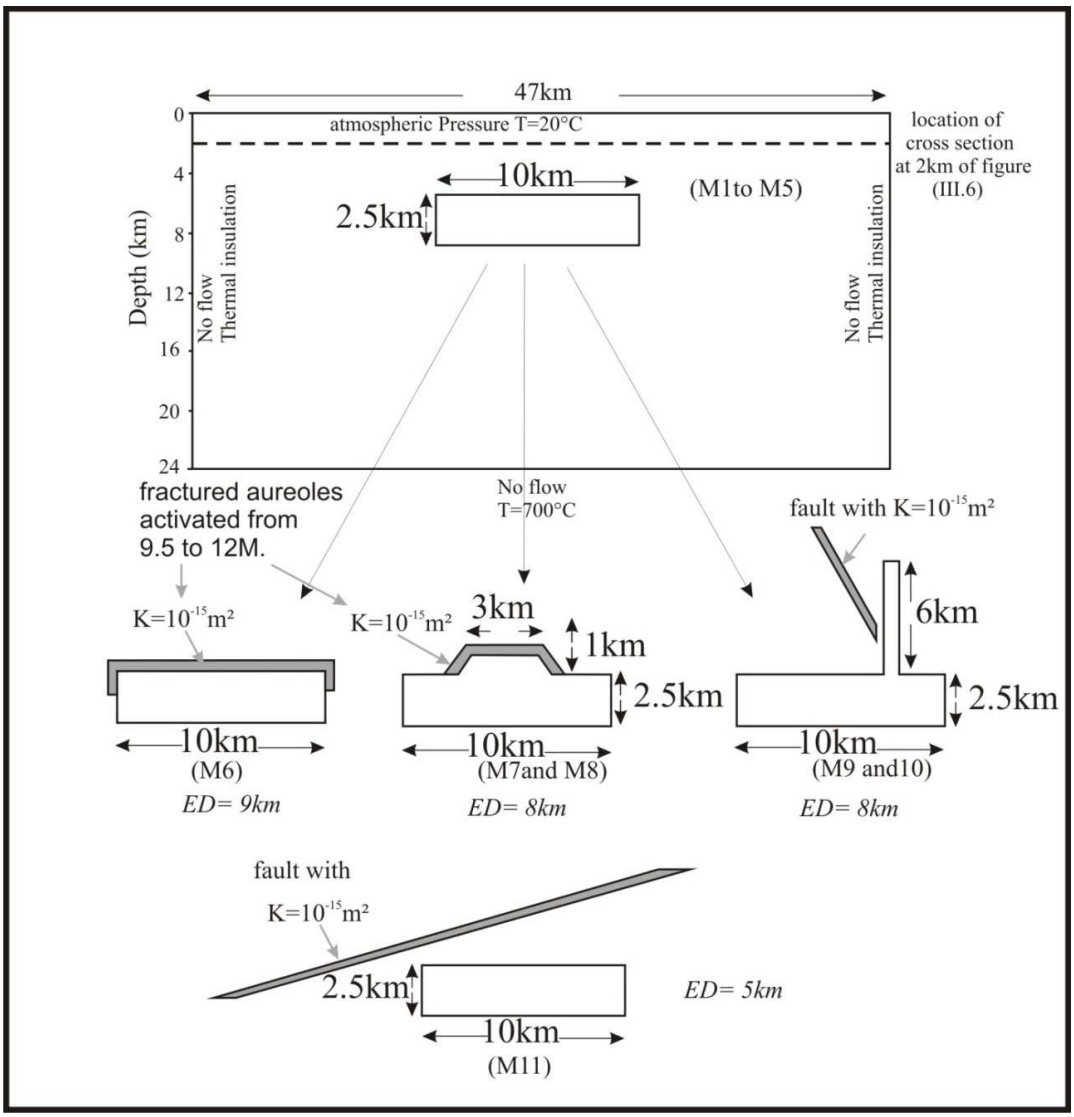

Figure (III.2): Simplified forms and boundary conditions for different models; M1 to M5 represent theoretical models with different emplacement depths while M6 to M11 represent models of tested natural cases, ED: emplacement depth of the intrusion roof. See text for more details.

In addition, models (M6 to M11 in figure III.2) were constructed to adapt the natural examples (figures III.1b, c, and d). The pluton area ranges from 25 to 31 km² and the roof of pluton covers depths ranges from 8 to 10 km. For the continental crust, we have used 2D model geometry of 47km in width and 24km in depth (figure III.2). Geometries of plutonic apexes, fractured aureoles and surrounding faults are described in figure (III.2).

5.2 Timing

Our transient models were designed to take into account the time of emplacement (cf. introduction). Total duration of numerical experiments is 20 Myr. From 0 to 7 Myr., the initial imposed (a priori) thermal state evolves by adjusting thermal field to the effective boundary conditions and material properties, until a steady-state is achieved. Duration of emplacement, represented by a time-varying heat source, lasts 3 Myr. (from 7 to 10 Myr).

The maximum temperature (the hottest phase) at the intrusion centre occurs therefore at 10 Myrs. The subsequent cooling phase occurs from 10 to 20 Myr, after which thermal equilibrium is reached again.

5.3 Boundary conditions and rock properties

The upper boundary represents the flat surface topography, which is permeable and maintained at 293K (T_0). The bottom is located at 24km depth with temperature fixed at 973K. The lateral boundaries are assumed to be impermeable and thermally insulated.

The initial thermal gradient inserted in the model is:

$$T = 293 + (0.024.(Z)) \qquad \text{(III.11)}$$

For simplification, the host rock was assumed to be a homogeneous saturated porous medium (constant porosity = 0.5%) with a depth-dependent permeability (Eq. III.3).

The intrusion has physical characteristics of granite and its centre reaches 973K (700°C) at the hottest phase. As magma above 400C° is considered as impermeable body, we fixed the permeability of intruded body at 10^{-24}m² during the emplacement from 7 to 10 Myr. This very low permeability implies no fluid production by the pluton. Before and after emplacement, the pluton permeability follows the depth-permeability curve (Eq. III.3).

High permeability zones such as faults (figures III.1, 2) have been modeled with constant permeability (K value of 10^{-15} m^2), whereas, fractured aureoles around pluton are transient permeable zones, which has been activated (K value of 10^{-15} m^2) from 9.5 to 12 Myr. Before and after this time span, the permeability of the aureole zone follows the depth-permeability curve (Eq. III.3). Our 2D models include one single homogenous fluid phase (pure water) which was chosen in order to compare with published models.

Finally, the coupled models have been performed using a commercial finite element code (Comsol Multiphysics™) which has been tested with various other configurations already published before (see benchmark in next section).

6. Fluid flow patterns: results and discussion

6.1 Benchmark

To validate our model, we simulated several cases explored by published models (Rabinowicz

et al., 1998; Gerdes et al., 1998). The example shown in figure 3 comes from Gerdes et al. (1998) where they solve transient hydrothermal circulation during pluton cooling. We reproduced their work after fitting the most probable bottom thermal boundary condition; the results of this model match those from the published study (figure III.3). We also reproduced results obtained by Rabinowicz et al. (1998), where higher permeabilities were involved. Identical unsteady convective patterns and steady-state ones were obtained within a rectangular box with permeability 10^{-15} m² and 5 10^{-15} m², respectively. In addition, for these two last cases, surface heat flow values and variations were recovered.

6.2 Spatial-temporal evolution of the fluid flow pattern and heat transfer

Even when streamlines described convective cell in different models before the emplacement (see below), heat transfer by advection may be neglected since fluid velocities are low (lower than 10^{-14} m.s^{-1}).

To estimate the efficiency of thermal advection, we used a local Peclet number *(Pe)* which denotes the ratio between advection and thermal diffusion. When the Peclet number is low (<1), the influence of heat advection is weak because of the slow fluid velocity. The critical Peclet number above which the influence of heat advection becomes significant is (>1).

During the cooling phase (after 10Myr), within the pluton roof area, fluid flow patterns obtained in this study correspond to those observed in previous studies (e.g. Norton and Knight 1977; Driesner and Geiger, 2007): fluids inside the host rock migrate toward the upper corners of pluton and create two convection cells above the pluton. The cell in the left side is anticlockwise, while the cell in the right side is clockwise. The pluton floor zone is characterized by a convergent fluid flow from both deep and shallow zones.

During cooling phase of shallow plutons, shallow fluids may migrate beneath the pluton. This constitutes a typical cooling fluid flow pattern. For shallow intrusions (such as model M1 (figure III.4), where the pluton is emplaced in a permeable zone of host rock), streamlines and isotherms are disturbed by a second order convective instability above the pluton roof (M1 and M2 in figures III.4 and III.5 respectively).

This is well expressed in figure (III.6), where the horizontal component of the fluid velocity is shifted from positive to negative value through four convective half cells. These second order convective cells depend on pluton length and emplacement depth, and may be important when considering mineralization potential.

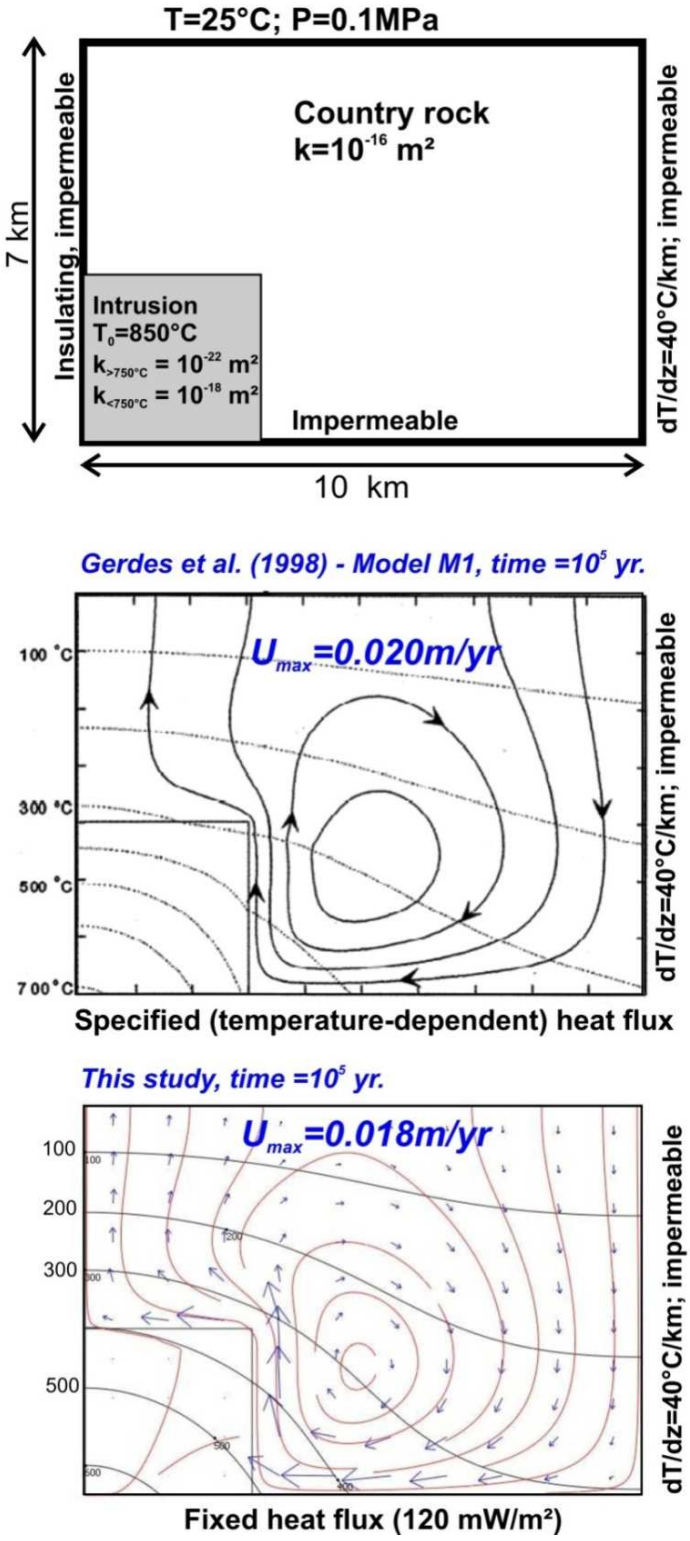

Figure (III.3): Benchmark test of our hydrothermal modeling. Model M1 of Gerdes et al., (1998) at 10^5 years is shown on the middle. Our model at the bottom reproduces at the same time the same thermal and fluid velocity patterns with a fixed heat flux condition at the base.

For shallow plutons, mapping of *Pe* number indicates that advective heat dissipation is still dominant 10^5 years after the hottest phase.

The main convective discharge zone appears to be the area above plutons and represents the most advective zone (M1 to M3, figures III.4, 5 and 7). As additional convective cells in M1 create two discharge zones (rather than one single for M2 and M3, figure III.4), the advective zone geometry presents two advective apexes for the chosen pluton length.

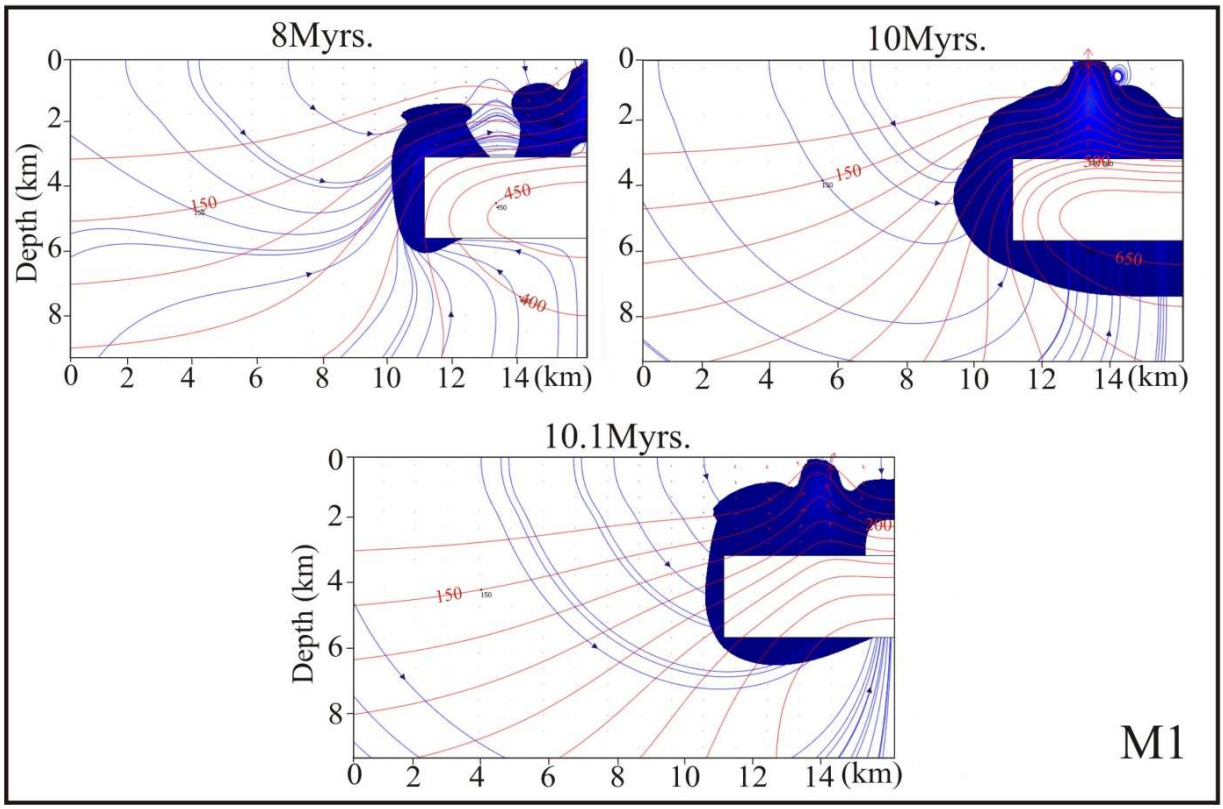

Figure (III.4) Snapshots of different time steps of M1, The blue area representss the advective zones (Pe >1) around pluton (Pe=1 in blue and increases in values to 6 (from blue to red for other models)). Streamlines are in blue and labeled isotherms in red. Red arrows represent fluid velocity vectors.

Moreover, as our models are designed to simulate long-lived magma injection, fluid flow and thermal transfer during magma emplacement can be investigated. Firstly, as expected, for all emplacement depth, extent of advective zones is the maximum at the hottest phase of melt injection (i.e. 10 Myr). This constitutes an important difference with models testing only cooling phase of plutons (e.g. Norton and Knight, 1977).

Secondly, shallow hydrothermal systems as M1 reach a cooling flow pattern (i.e. regular and concentric streamlines) before the hottest phase of emplacement. Before the establishment of this cooling flow pattern, divergent buoyant fluids that are expelled downward and laterally from the pluton roof zone are responsible for the deflection of streamlines beneath the pluton. This deflection of streamlines is characteristic of a warming flow pattern resulting in bell shape in M3 and M4 (figure III.7 & 8, time 10 Myr).

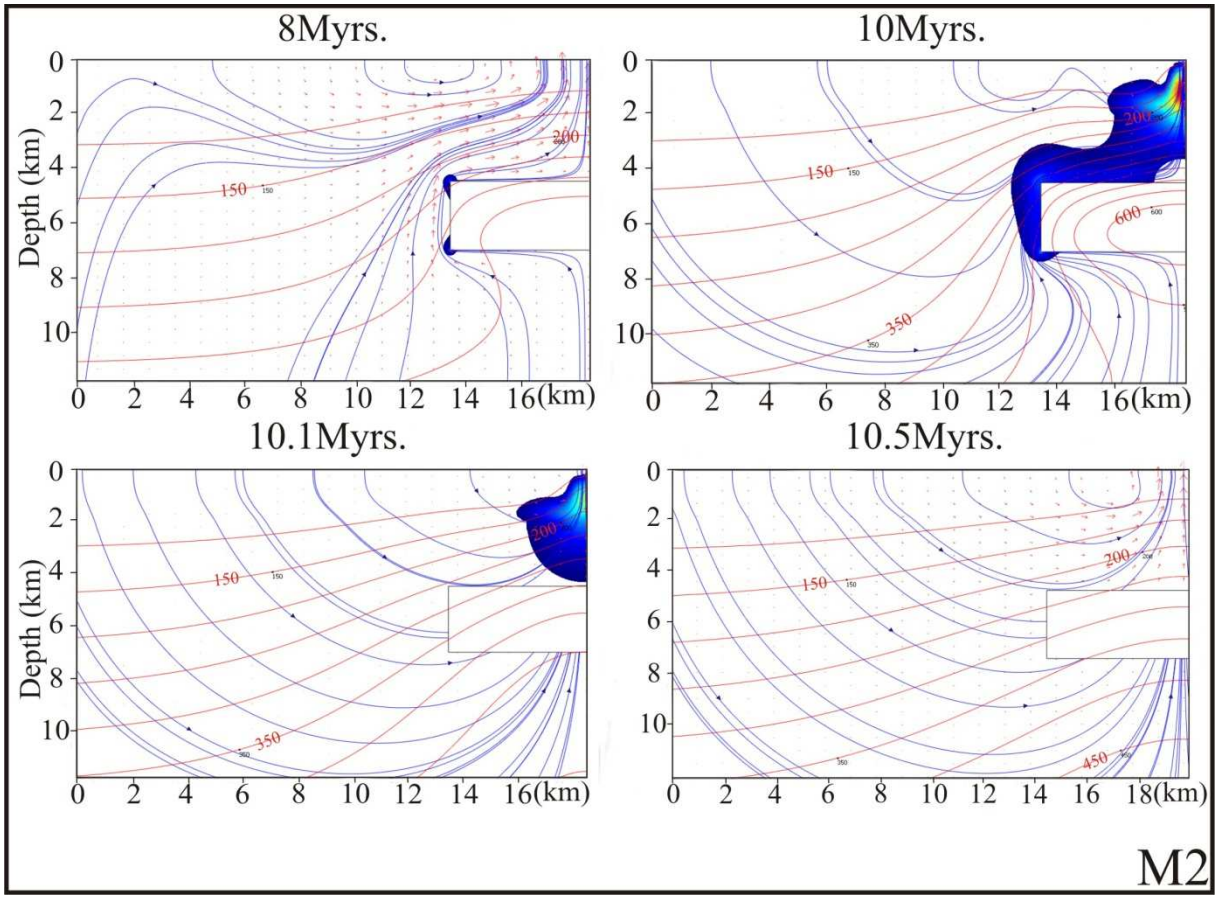

Figure (III.5) snapshots of different time steps of M2 model, velocity streamlines represented by blue line while thermal contours represented by red lines.

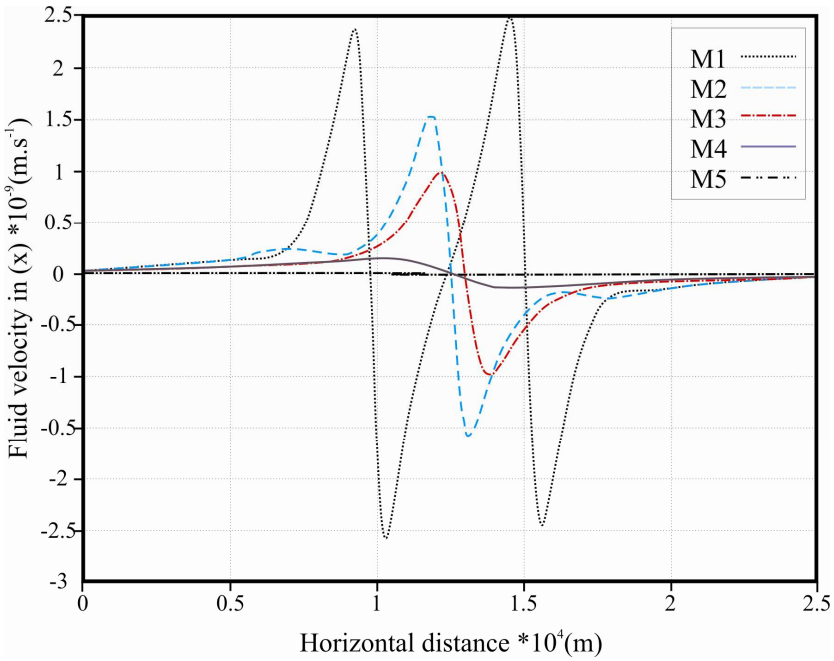

Figure (III.6): Horizontal component of the fluid velocity along horizontal cross-sections above the intrusion at the hottest phase of intrusion (i.e. 10 Myr, see cross-section location on figure 2). Each bulge and depression of

fluid velocities in x direction represents a convective cell. The shallowest pluton (M1) shows four convective cells while no significant variation was noted for the deepest pluton M5.

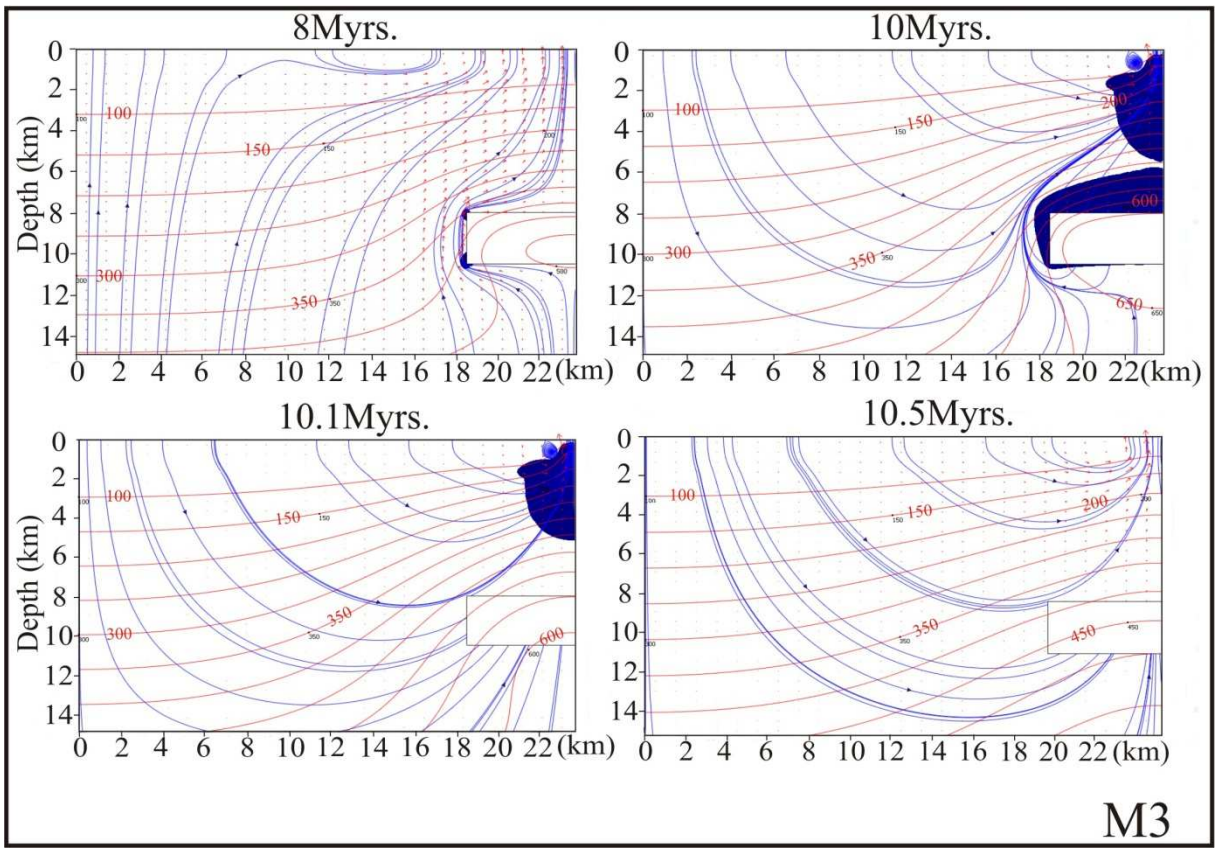

Figure (III.7) Hydrodynamics and illustration of local Peclet number values in different models at different time periods.

6.3 Influence of emplacement depth

For shallow intrusions (model M1, where the pluton is emplaced in permeable zone), four convective cells are distinguished, whereas with M5 (very deep emplacement) no convective cells are present (figure III.9). Significant differences in fluid velocity were identified: with shallow plutons (M1, M2), fluid velocity increased by two orders of magnitude during pluton emplacement (10^{-10} to 10^{-8} and 10^{-11} to 10^{-9}m.s^{-1} respectively), while with intermediate plutons, it increased by only one order of magnitude (10^{-}11 to 10-10m.s^{-1}). As we considered that fluid velocities lower than 10^{-10} m.s^{-1} were not induced by magma emplacement (cf. above), no significant variation in fluid velocity was noted with deep seated intrusion (M5) (10^{-13} to 10^{-12} m.s^{-1}). Peclet number distribution (figure III.4) shows that advective heat transfer decreases with emplacement depth. That is coherent with the removal of convective cells and low fluid velocities with increasing emplacement depth.

All these features are clearly related to the variation of permeability of host rock which is depth-dependent in our models (cf. Equation 3). It is noteworthy that as emplacement depth increases (M1 to M4 in figure III.4) advective heat transfer is restricted around the pluton. From 4.5 to 10 km of emplacement depth (M2 to M4 in figure III.4), at the hottest phase of pluton emplacement, the advective zone at the pluton floor zone thickens. Indeed, at that time, shallow plutons (emplaced in cool embeddings) already present a cooling fluid flow pattern (M1 in figure III.4), whereas deep seated intrusions still present a warming fluid flow pattern (bell shape of M3 and M4 in figure III.4). As a result, for magma emplacement deeper than 10 km depth, pluton buoyant fluids are divergent, and especially downward at the pluton roof zone, may constitute a narrow advective aureole around the pluton. Nevertheless; permeability being low, fluid velocity at the pluton floor zone remains moderate, and cooling is almost achieved by conduction.

6.4 Effects of apexes

To study the effects of added plutonic apexes, models M3, M7 and M9 with the same emplacement depth (8 km) were compared during the intrusion emplacement (figure III.7). In M7 where the apex is located in the deep zone of host rock (where the permeability of host rock is lower than $10^{-16}m^2$), no significant role of apex was observed (figure III.10). In contrast, the appearance of apex into the shallow zone (where the permeability is high, M9) disturbs the movement of fluid around main intrusive body by relocating convective cells and discharge zones along the apex rather than around the main intruded body (figure III.11). In the single case (with no apex, M3), fluids circulate upward from the pluton centre. Adding an apex to that geometry makes fluids circulate upward bordering the pluton roof and along the apex. Mapping of local Peclet number values (figure III.11) demonstrates that apexes are able to focus the advective zone around them, whereas the advective zone is located mainly around the intrusion in case of single intrusion M3.

As we have considered the magma itself as an impermeable zone, fluids rise and accumulate at the highest point of magma body (which is often stock); we related that to the variation of permeability that is higher in shallow zones (nearby the highest point of magma morphology). As apexes reach to shallow zones, effective advection initiates along them during the magma emplacement and before the hottest phase (e.g. M9 at 8 Myr in figure III.11).

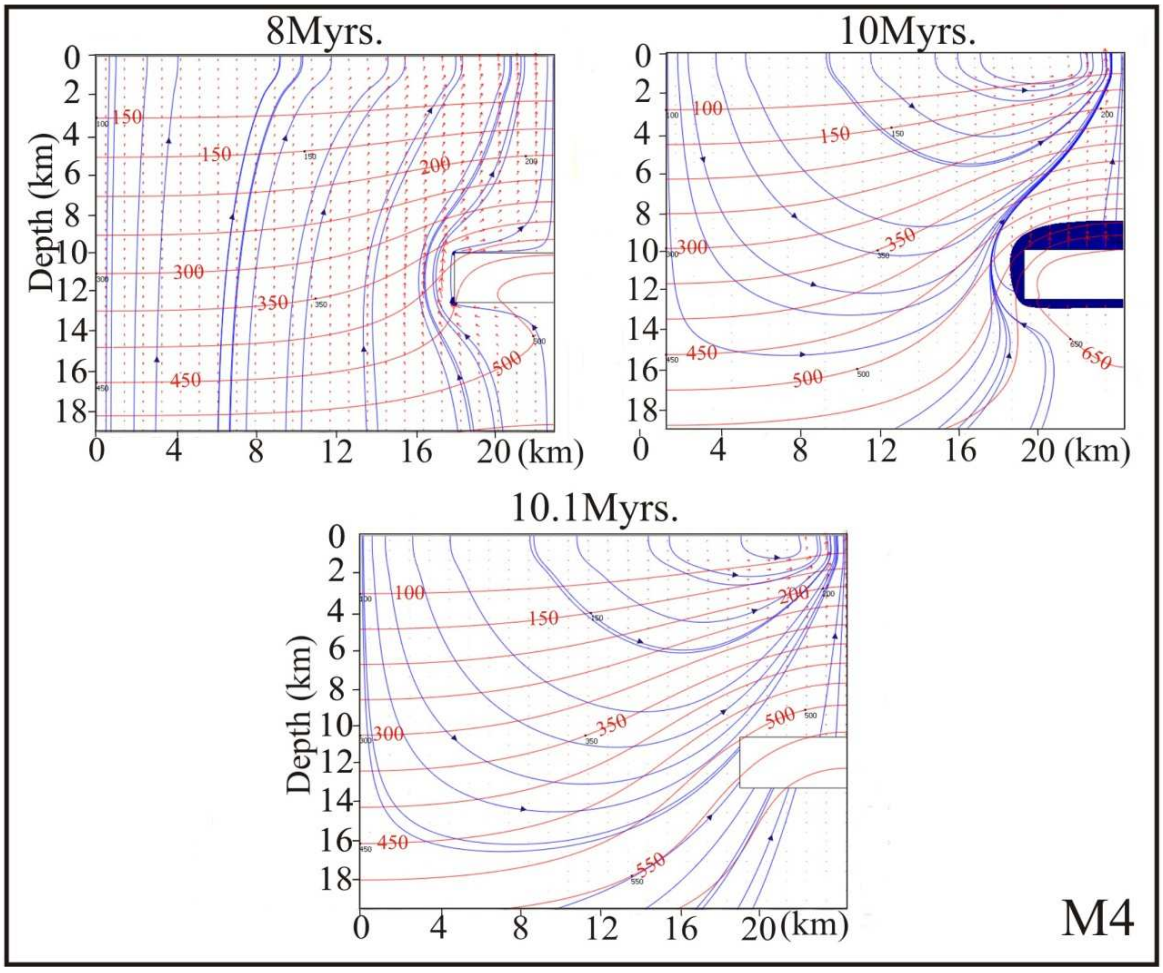

Figure (III.8) snapshots of different time steps for M4.

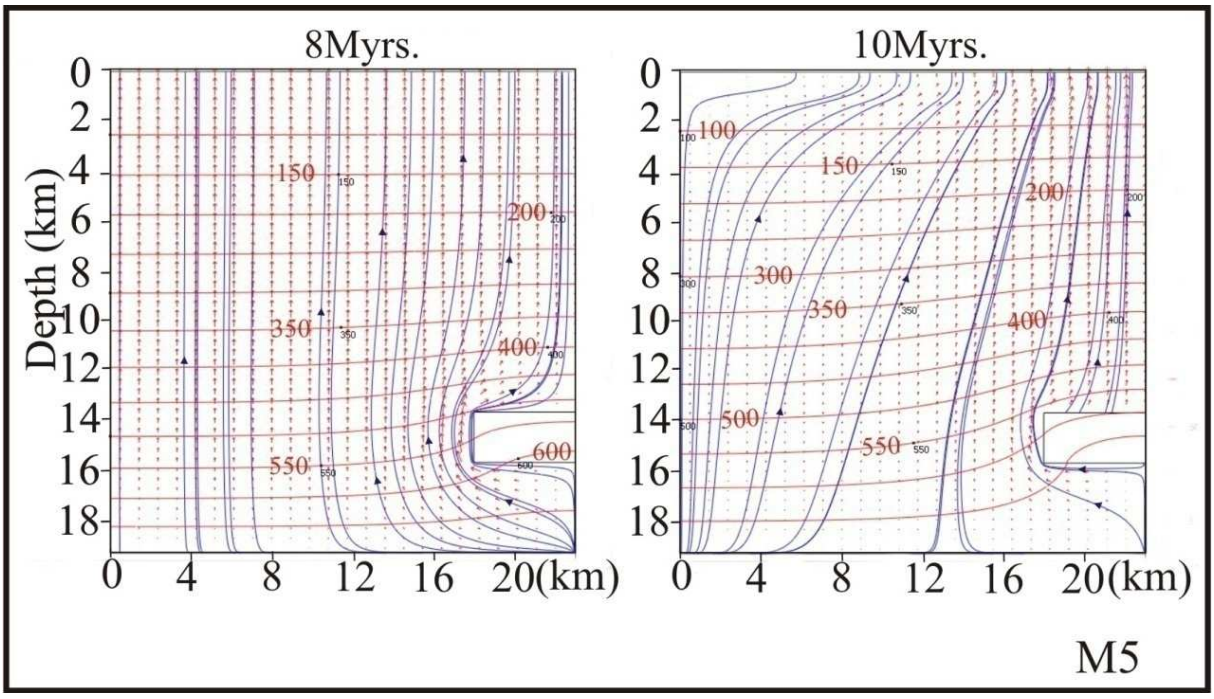

Figure (III.9) snapshots of different time steps for M5.

7. Probable mineralization patterns

The application of R^2AI (Eq. 10) shows probable zones of mineralization for the studied cases of well-known ore deposits (M6, M8, M10, M11). For each case, we depict the evolution of the mineralization potential from the incipient magma emplacement to the cooling phase (figures 7 and 8). To study the effects of fractured aureole and faults, R^2AI in model outputs (M1 to M4 and M7) at the hottest phase of magma emplacement is shown in figure III.12.

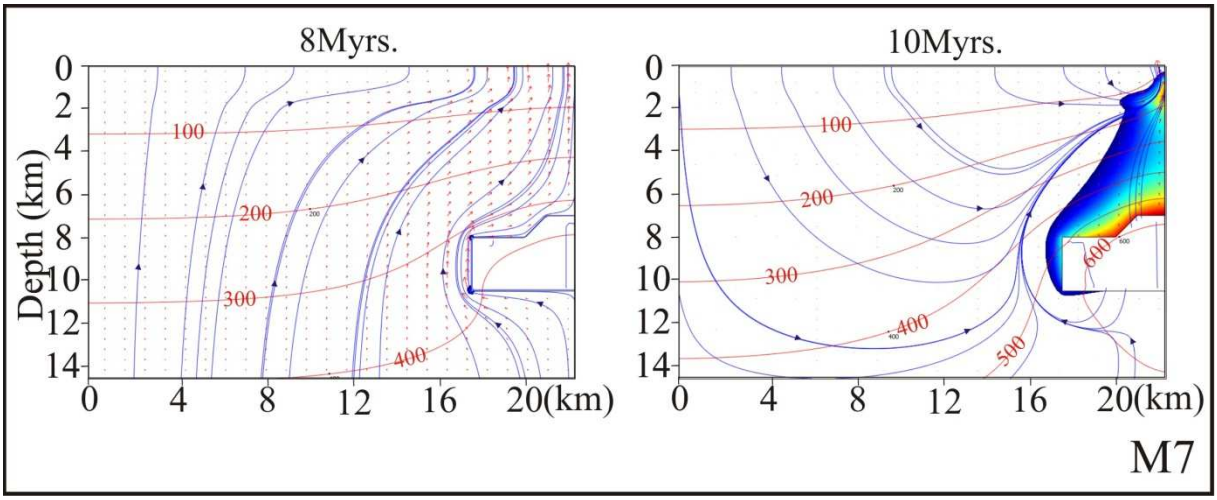

Figure (III.10) snapshots to study the effects of an apex. With deep intrusion, no significant role of apex was noted.

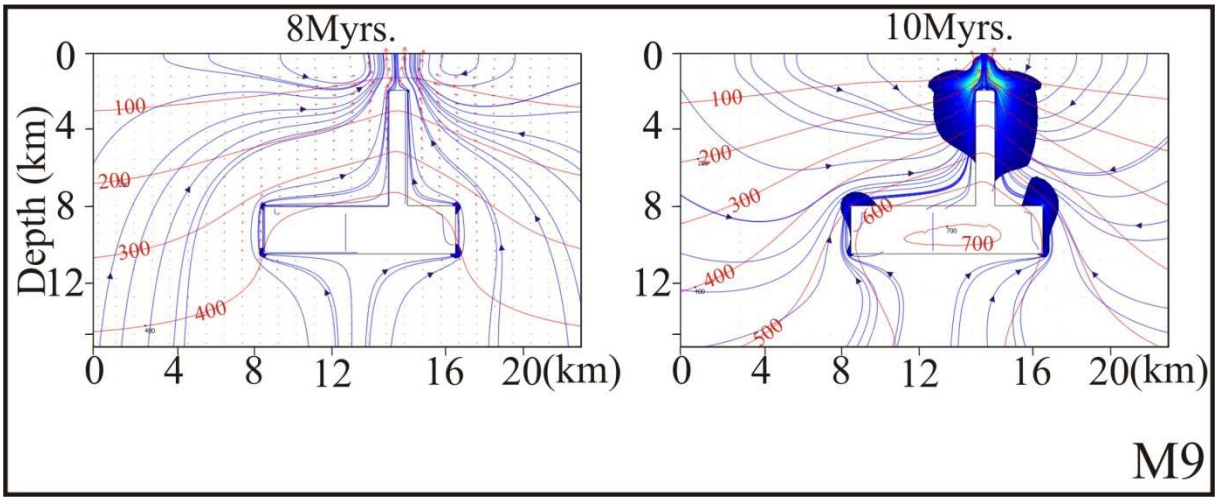

Figure (III.11) snapshots show the effects of an apex. In shallow intrusions, the significant role of apex was noted by shifting the advected zone to be located around apex.

7.1 Potential mineralization zones for models outputs

Comparing with Peclet number and streamlines distributions (figures III.4, 5 &7), favorable R^2AI was found around and above the pluton during the hottest phase (figure III.12) for all studied cases.

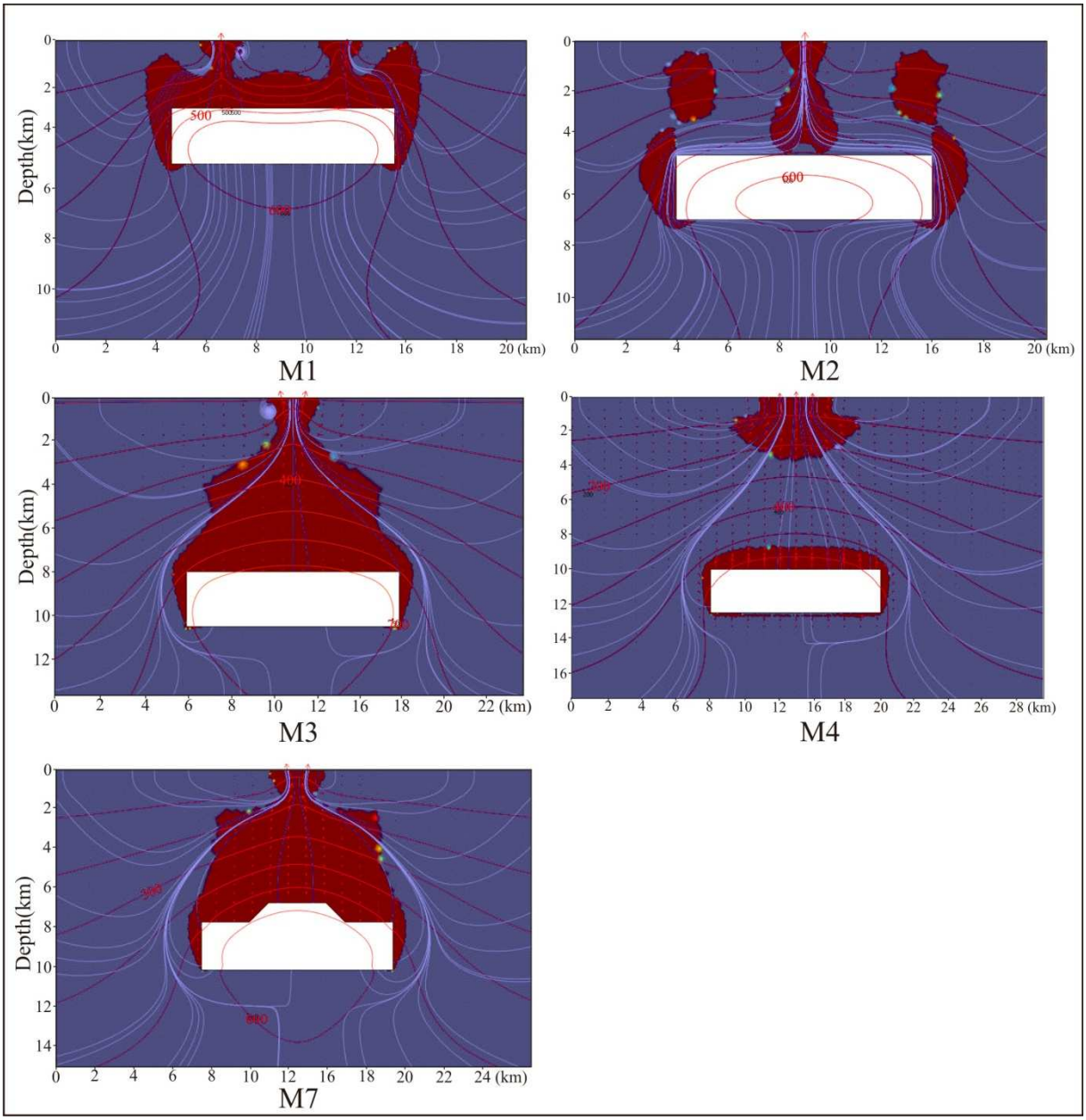

Figure (III.12): R²AI application around each pluton at the hottest phase (i.e. 10 Myr). Red areas represent physical favorable zone of mineral deposition corresponding to $R^2AI=1$. Streamline in light blue lines and isotherms contours represented here in red lines.

For all tested emplacement depths, no significant favorable mineral deposition area is observed below the pluton floor. Run M1 and M2 presents high potential mineralization zones which are localized along narrow discharge zones near the topographic surface.

They result from second order convection cells that developed above shallow plutons (cf. above). In figures III.4 &5, these advective narrow zones produce thermal bulges where fluids reach the surface at temperatures ranging from 150 to 100°C. We suggest that these shallow, focused mineralizing zones may correspond to low temperature hydrothermal systems.They may be responsible for either F-Ba (± Pb, Zn) mineralization characteristic of late orogenic granite emplacement, or strong alteration leading to kaolinite deposits. The R^2AI distributions are different between M3-M7 and M4, because the permeability of the host rocks overlying the pluton roof in M4 prevents fluids to circulate faster than $10^{-10}m.s^{-1}$. Consequently, the continuous potential zone from pluton roof to the topographic surface in M3 becomes restricted to two separate zones (near topographic surface and around pluton) in M4. For those deep seated pluton, the shallow and the large potential deposition zones in M3 appear unrealistic at first glance. This point will be discussed later.

7.2 Effects of permeable fractured aureoles

The model M6, based on the Bruès intrusion-related gold deposit, is emplaced at 9.3 km, i.e intermediate between M3 and M4. The model M8 is based on the Scheelite dome intrusion-related gold deposit and has to be compared to M7. The most important difference between M6 & M8 and theoretical models is the occurrence of fractured thermal aureole that acts as a high permeability zone. These high permeable zones (10-15m^2) have been activated late during magma emplacement, at 9.5 Myr, i.e. 5. 10^5 years before the hottest phase. The models show that highly permeable fractured aureoles play a key role in the mineralization pattern. Indeed, they are able to pump and focus the fluid flow and therefore to restrain and decrease the extent of favourable zones (figure III.13). In M6 model, upper corners of pluton become the most probable mineralization sites, particularly at 10^5 years of cooling phase. This is in agreement with the location of the Bruès gold deposit at the upper north corner of the Boboras pluton (figure III.1b). Focus and pumping of fluid into permeable zone is also responsible for the good agreement between the Scheelite dome gold deposit and the model M8 (figures III.1c and 13). As suggested before with emplacement depth (8 km), the stock does not play an important role for the R^2AI distribution because the permeability of host rock is still lower than the $10^{-16}m^2$ threshold (M3 vs. M7 on figure III.12).

However, development of a cracked thermal aureole around the stock induced formation of restricted and narrow probable mineralization zone along the stock flanks (M8 figure III.13).

7.3 Effects of apexes

A long apex reaching to shallow zone where permeability is greater than $10^{-16}m^2$ creates a dramatic change in R^2AI distribution (M10, figure III.14). The apex re-localizes the positive R^2AI around it (compare M3 figure III.12 and M10 figure III.14). As expected, the top of the apex acts as small shallow intrusion and plays a role in localizing a probable zone of mineralization, before the hottest phase of the magmatic system.One important implication is that the mineralization potential of main upper-crustal batholith is reduced when the apex is absent (M3, figure III.12). Comparison with natural porphyries (e.g. Grasberg Cu-Au porphyry, figure III.1c) is quite delicate because ore is hosted within the magmatic apex.However, the well-established concentric zoning of alterations halos (i.e. potassic, phyllitic and propylitic, Lowell and Guilbert, 1970) within Cu-porphyry host rocks might correspond to positive R^2AI distribution shown in M10 (figure III.14).

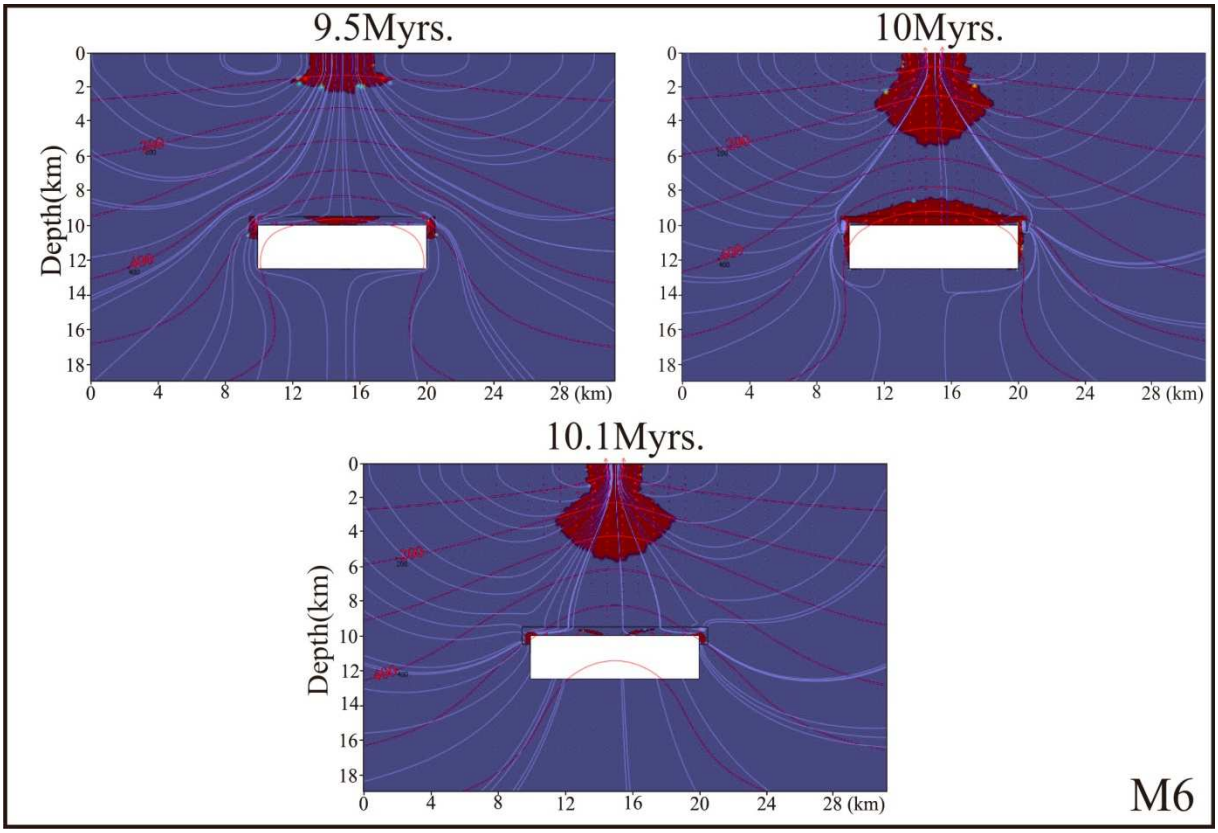

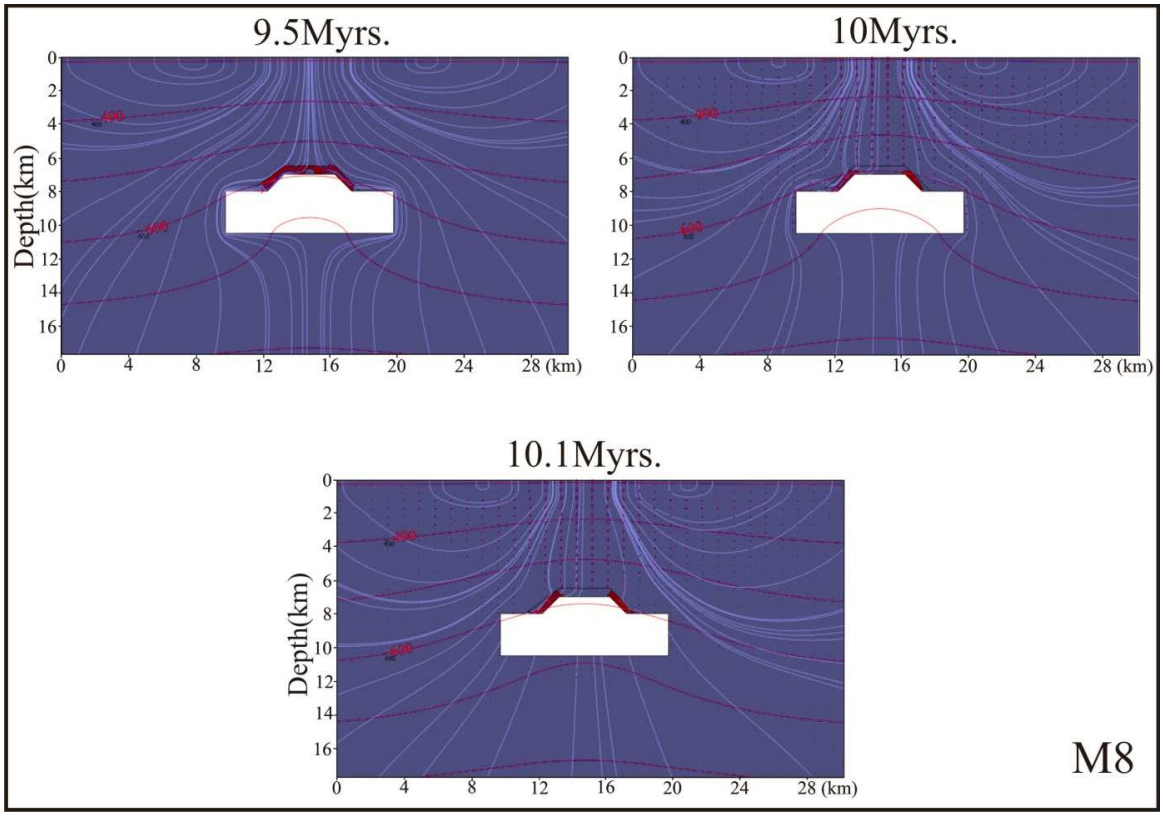

Figure (III.13): Focused snapshots during the warming and the cooling phase of pluton (hottest phase at 10 Myr) associated with fractured thermal aureole and apex. M6 and M8 are simplified numerical models of the Bruès and Scheelite Dome granite-related gold deposits respectively (see figure 1 for geologic context). Red areas are the favorable zones of mineral deposition corresponding to $R^2AI=1$. Streamline represented in light blue lines and isotherms contours in red lines.

7.4 Effects of faults

In our models, faults are activated ($k = 10^{-15}$ m^2) during the entire duration of the experiment (i.e. 20 Myr). As a result, it is expected that the deepest parts of faults accelerate fluid flow. In the Model M10 (figure III.14), the fault is mineralized from 8 to 10.1 Myr, but does not change drastically the R^2AI distribution around the apex which appears to be the major control. In the model M11, the probable zone emerges after 1 Myr of emplacement within the fault closer to pluton where the hot fluid migrates far from the pluton. After 2.5Myr of emplacement, this zone grows downward within the deeper part of the fault, where the permeability of fault is higher than the permeability of host rock (figure III.14). At the hottest phase, another zone appears at the surface near the fault where the permeability of host rock becomes higher than the fault. This zone disappears immediately at cooling period, while the zone inside fault vanishes after $8*10^5$ years of cooling. The M11 pluton roof is emplaced at 5 km, i.e. between M2 and M3. Comparison between these models at the hottest phase (figure

6) shows that the flat lying fault has a major effect on the fluid flow pattern and the resulting R^2AI distribution. Indeed, the fault cancels the development of potential zone around the pluton. A very good agreement was found with the Crocetta deposit in Elba (figure 1D). The Elba central detachment fault is a very efficient advective drain. Indeed, due to its low dip, it is able to pump and accelerate the fluids at depth and make them circulate along the horizontal branch of the pluton-induced convection cells. This constitutes an important difference with high angle dip fault (as in M10). Detachments are then able to delocalize and strongly modifies classical fluid flow pattern induced by coeval intrusion.

7.5 Validity of modeled mineralization pattern

The essential point to discuss is the significance and reality of the near surface favourable zone developed above the pluton at the hottest phase. This is particularly relevant for deep seated plutons (e.g. M2, M3, figure III.12). There are two main limitations; first, we approximated a homogeneous crust with a power-law variation of permeability with depth (Eq. 3). This approximation does not take into account the potential permeability barriers encountered in many orogenic hydrothermal systems (e.g. Sibson et al., 1988). Secondly, the R^2AI is a physical parameter that does not take into account the solute transport and chemical reaction. For those obvious reasons, interpretations have to be very carefully proposed. However, we think that the near surface potential zone observed in models is not totally unreasonable. In fact, rather than ore deposits, it may correspond to geothermal systems with hot springs associated with deep heat sources, and more generally to alteration zones where large amount of hot fluids are efficiently cooled down (Hall et al., 1974).

7.6 Model time evolution vs. age of mineralization and genetic link

Because R^2AI is a pure physical parameter, the evolution of mineralization potential through time is not described over short time intervals; a more detailed time stepping would be required. Therefore our modeling is not able to reproduce the very short radiometric time span measured in ore deposits. This assumption is particularly valid for the Kucing Liar skarn (along the Indenberg fault) and the Grasberg Cu-Au porphyry (figure III.1C) which formed during 4.10^5 years time span. As analogue, the model M10 at 8 Myr (figure III.14) points out that both the Indenberg fault and the porphyry are potential favorable zones at the same time before the hottest phase. However, our simulations show that, without taking into account chemical processes, a pure physical parameter such as R^2AI applied to models of granite-related gold deposits (M6 and M8, figure III.13) reproduces correctly in time and space the ore deposition pattern relative to the pluton.

Indeed, the convection of fluids induced by the intrusion appears to be a key physical control to explain the spatial distribution of ore around the magmatic body.

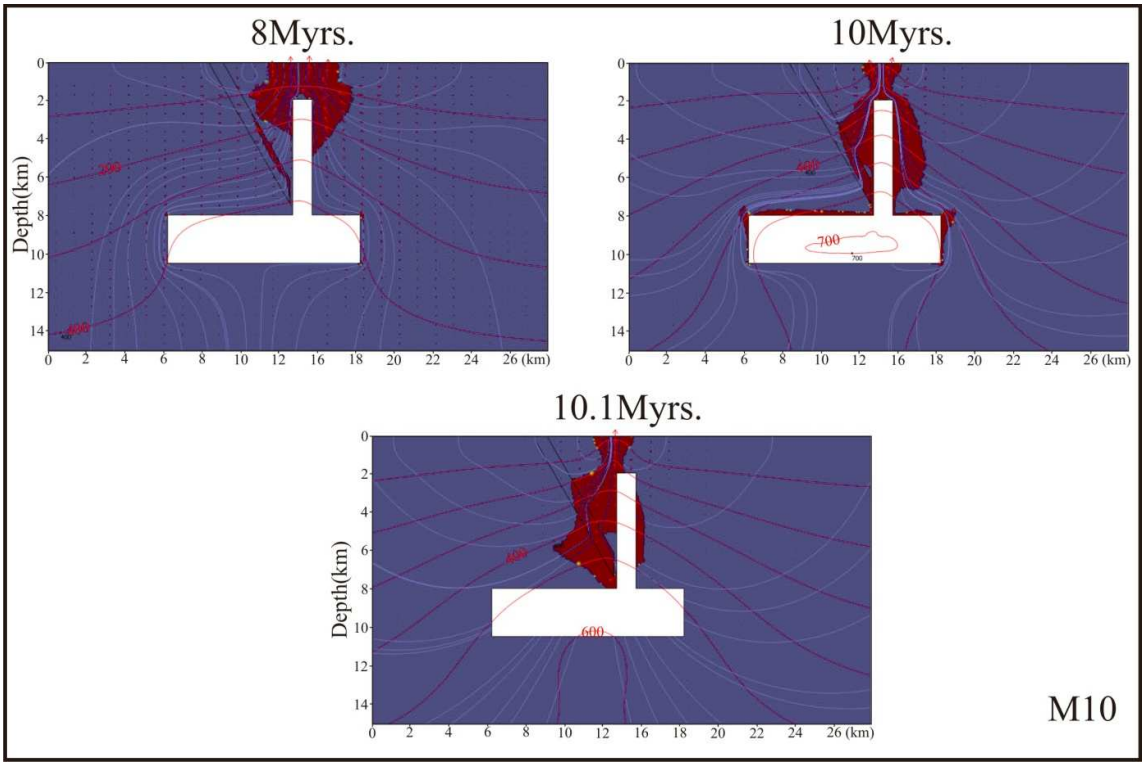

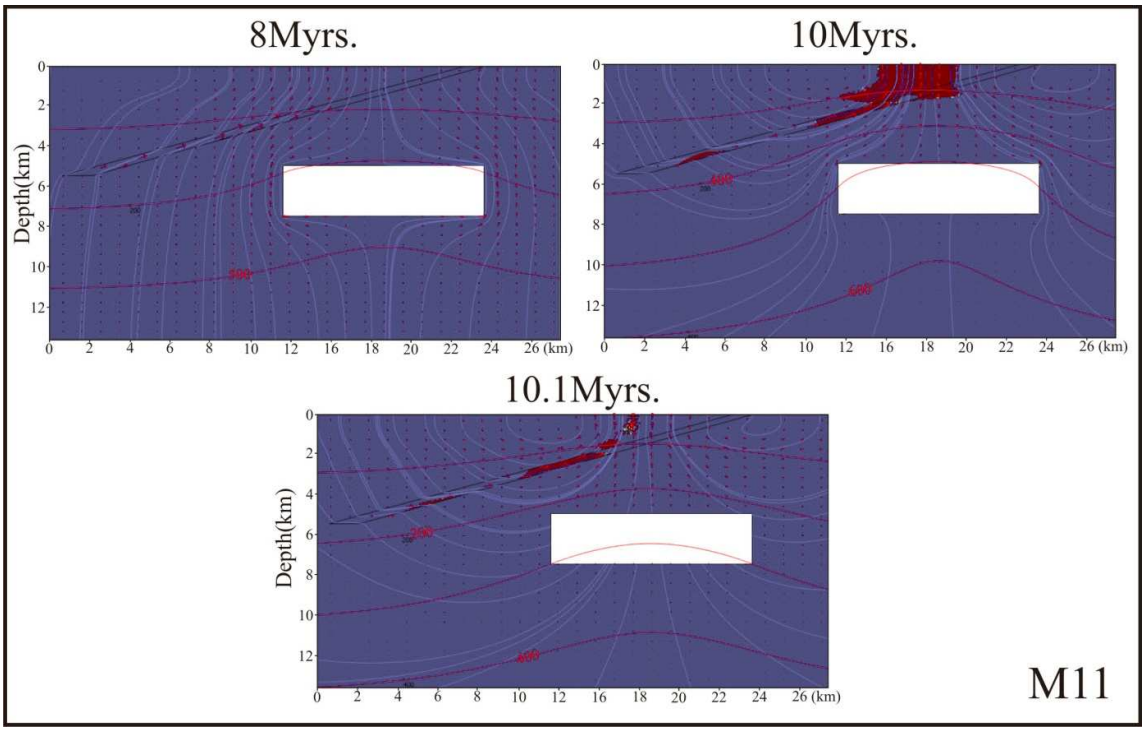

Figure (III.14): Same as Figure (III.13), M10 and M11 are simplified numerical models of the Grasberg porphyry and the Crocetta raw material deposits above the Elba detachment fault, respectively (see Figure 1 for geologic contexts).

This is valid because cracked thermal aureoles developed around the intrusion and focused the advective fluid flux (figure III.13). For M6 and M8, favourable zone developed from 9.5 Myr to 10.1 Myr (i.e. 6.10^5 years around the hottest phase figure III.13). This time span is shorter than the 2 Myr spanning granite emplacement and the mineralization events at Scheelite dome (cf. above). As it is emphasized in the introduction, fluid inclusion studies do not provide strong chemical arguments for a genetic link between granite and mineralization. Based on this lack of chemical evidences (e.g. no brines in fluid inclusions), granite is often only interpreted as a rheological and structural trap with no direct genetic relationships with ore deposition; even if radiometric time span between granite crystallization and mineralization is lower than 2 Myr. Our models show that from a physical point of view, hydrothermal convection created by magma emplacement is able to develop probable mineralized zone. The role of intrusion is then clearly genetic for this kind of the deep-seated granite-related Au deposits; and mineralization deposition might be nearly coeval with the hottest phase of intrusion.

8. Concluding remarks

Our models are simple physical models that do not simulate i) multiphase fluids; ii) chemical diffusion, iii) topography, iv) input of meteoric waters. Nevertheless, the originality of our modelling relatively to pre-existing works is: i) we varied continuously the crust permeability with depth; ii) models are transient and account for the emplacement period of intrusion, iii) we tested the physical favorability of ore deposition, iv) we compared with well-constrained natural examples at different emplacement depth with contribution of high permeability zones as cracked thermal aureoles and faults, v) the pluton floor zone has been explored.

Our main results are:

1. Fluid circulation and mineralization patterns are strongly dependent of the emplacement depth of the pluton. Deep seated plutons emplaced below 10 km and not connected to high permeability zones do not induce advective heat dissipation. Above 4.5 km of emplacement depth, the permeability threshold of 10^{-16} m^2 is reached and second order convection cells may create additional focused discharge zones where mineralization are expected.
2. For all emplacement depth, the pluton floor zone is not favorable for mineral deposition.
3. The apexes strongly modify the fluid flow pattern by focusing convective fluids and mineralization zones around them and depleting the main pluton of these fluids.

4. The cooling phase is not the main phase of convection for large pluton associated with long-lived magma emplacement. Major advective heat dissipation and mineral deposition zone may also occur sometime before and during the hottest phase of emplacement, before magma crystallizes. This is an important clue to interpret dating (emplacement, cooling age) of thermal aureole and intrusion-related ore deposits.
5. Detachment faults are able to delocalize and strongly modify classical fluid flow pattern induced by coeval intrusion. Extensional systems do not require lithostatic fluid overpressure to develop dilatant sites susceptible to drain and/or to trap mineralizations. This result implies that it is surprising that very few ore deposits are recognized in context of the detachments associated with metamorphic core.
6. Favorable physical conditions for mineral deposition are encountered around mid-crust pluton, during a short time span bracketing the hottest phase of intrusion. We conclude that even if chemical processes are absent from our models, fluid circulation induced by granite emplacement plays a key role in the genesis of granite-related Au deposits. Moreover, formation of this type of deposit is promoted and controlled by the occurrence of a fractured thermal aureole around the intrusion.

9. References

Annen, C., Scaillet, B., Sparks, S.J., 2006. Thermal constraints on the emplacement rate of a large intrusive complex: the Manaslu Leucogranite, Nepal Himalaya. Journal of Petrology. 47, 71-95.

Arndt, N.T., Lesher, C.M., Czamanske, G.K., 2005. Mantle-derived magmas and magmatic Ni–Cu– (PGE) deposits. Economic Geology. 100th Anniversary Volume, 5–24.

Baker, T., Lang, J.R., 2001. Fluid inclusion characteristics of intrusion-related gold mineralization, Tombstone-Tungsten magmatic belt, Yukon territory, Canada. Mineralium Deposita. 36, 563-582.

Bouillin, J.P., Bouchez, J.L., Lespinasse, P. Pêcher, A., 1993. Granite emplacement in an extensional setting: an AMS study of the magmatic structures of Monte Capanne (Elba, Italy). Earth and Planetary Science Letters. 118, 263-279.

Cathles, L.M., 1977. An analysis of cooling of intrusives by ground-water convection which includes boiling. Economic Geology. 72, 804-826.

Cathles, L.M., 1981, Fluid flow and genesis of hydrothermal ore deposits. Economic Geology. 75, 424-457.

Cerny, P., Blevin, P.L., Cuney, M., London, D., 2005. Granite-related ore deposits In: Hedenquist JW, Thompson JFH, Goldfarb RJ, Richards JP (eds) One hundredth Anniversory Volume 1905-2005. Society of Economic Geologists. 100th Anniversary, 337-370.

Clemens, J.D., Mawer, C.K. 1992. Granitic magma transport by fracture propagation. Tectonophysics. 204, 339-360.

Cook, S.J., Bowman, J.R., Forster, G.B., 1997. Contact metamorphism surrounding the Alta stock: finite element model simulation of heat- and $^{18}O/^{16}O$ mass-transport during prograde metamorphism. American Journal of Science. 297, 1-55.

Cui, X., Nabelek, P.I., Liu, M., 2001. Controls of layered and transient permeability on fluid flow and thermal structure in contact metamorphic aureoles, with application to the Notch Peak aureole, Utah. Journal of Geophysical Research. 106, 6477-6491.

De Launay, L., 1913. Traité de Minéralogie. Gîtes minéraux et métallifères. Beranger, Paris.

Dipple, G.M., Ferry, J.M., 1996. The effect of thermal history on the development of mineral assemblages during infiltration-driven contact metamorphism. Contributions to Mineralogy and Petrology. 124: 334.

Driesner, T., Geiger, S., 2007. Numerical simulation of Multiphase Fluid Flow in Hydrothermal Systems. Reviews in Mineralogy & Geochemistry. 65, 187-212.

Ferry, J.M., Dipple, G.M., 1992. Models for coupled fluid flow, mineral reaction, and isotopic alteration during contact metamorphism: The Nitch Peak aureole, Utah. American Mineralogist. 77, 577-591.

Ferry, J.M., Sorensen, S.S., Rumble, D., 1998. Structurally controlled fluid flow during contact metamorphism in the Ritter Range pendant. California, USA. Contributions to Mineralogy and Petrology. 130, 358.

Ferry, J.M., Wing, B., Penniston-Dorland, S., Rumble, D., 2002. The direction of fluid flow during contact metamorphism of siliceous carbonate rocks: new data for the Monzoni and Predazzo aureoles, northern Italy, and a global review. Contributions to Mineralogy and Petrology. 142, 679.

Gerdes, M.L., Baumgartner, L.P., Person, M. 1998. Convective fluid flow through heterogeneous country rocks during contact metamorphism. Journal of Geophysical Research 103(B10), 23,983-24,003.

Gloaguen, E., Chauvet, A., Branquet, Y., Gerbeaud, O., Ramboz, C., Bouchot, V., Lerouge, C., Monié, P., Cathelineau, M., Boiron M.C., Marignac, C., Pourraz, N., Fourcade, S., Ruffet, G., Iglesias Ponce de León, M., 2003. Relations between Au / Sn-W mineralizations and late Hercynian granite: Preliminary results from the Schistose Domain of Galicia-Trás-os-Montes Zone, Spain 7th biennal SGA meeting - Mineral Exploration and Sustainable Development. Athens, Greece, 271-274.

Gloaguen, E., 2006. Apports d'une étude intégrée sur les relations entre granites et minéralisations filoniennes (Au et Sn-W) en contexte tardi-orogénique (Chaîne Hercynienne, Galice Cnetrale, Espagne) unpublished PhD Thesis, Orléans University, France,http://tel.archivesouvertes.fr/index.php?halsid=cu41odhccmgnb1qt3rek9l1j61 &view_this_doc=tel-00107391&version=1, pp 571.

Gow, P.A., Upton, P., Zhao, C., Hill, K.C., 2002. Copper-gold mineralisation in New Guinea: numerical modelling of collision, fluid flow and intrusion-related hydrothermal systems. Australian Journal of Earth Sciences. 49, 753-771.

Guillou-Frottier, L., Burov, E.B., Milesi, J.-P., 2000. Genetic links between ash-flow calderas and associated ore deposits as revealed by large-scale thermo-mechanical modelling, Journal of Volcanology and Geothermal Research, 102, 339-361.

Hall W.E., Friedman I. & Nash J.T. 1974 Fluid inclusion and light stable isotope study of Climx molybdenum deposits, Colorado. Econo. Geol. 69. 884-901.

Hanson, R.B., 1995. The hydrodynamics of contact metamorphism. Geological Society of America Bulletin. 107, 595-611.

Hanson, R.B., 1992. Effects of fluid production on fluid flow during regional and contact metamorphism. Journal of Metamorphic Geology. 10, 87-97.

Harcouët, V., 2005. Modélisations thermiques de gisements orogéniques mésothermaux: application au Ghana, PhD Thesis, Institut de Physique du Globe de Paris, 266 pp.

Ingebritsen, S.E., Manning, C.E., 1999. Geological implication of a permeability-deph curve for the continental crust. Geology. 27, 1107-1110.

Lang, J.R., Baker, T., 2001. Intrusion-related gold systems: the present level of understanding. Mineralium Deposita. 36, 477-489.

Lowell, J.D., Guilbert, J.M., 1970. Lateral and vertical alteration – mineralization zoning in porphyry ore deposits. Economic Geology. 65, 373-408.

Maineri, C., Benvenuti, M., Costagliola, P., Dini, A., Lattanzi, P., Ruggieri, G., Villa, I.M., 2003. Sericitic alteration at the La Crocetta deposit (Elba Island, Italy): interplay between magmatism, tectonics and hydrothermal activity. Mineralium Deposita. 38, 67-86.

Mair, J.L., Goldfarb, R.J., Johnson, C.A., Hart, C.J.R., Marsh, E.E., 2006. Geochemical Constraints on the Genesis of the Scheelite Dome Intrusion-Related Gold Deposit, Tombstone Gold Belt, Yukon, Canada. Economic Geology. 101, 523-553.

Manning, C.E., Ingebritsen, S.E. 1999. Permeability of the continental crust: implications of geothermal data and metamorphic systems. Reviews of Geophysics. 37, 127-150.

Nabelek, P.I., Labotka, T.C., 1993. Implications of geochemical fronts in the Notch Peak contact-metamorphic aureole, Utah, USA. Earth and Planetary Science Letters. 119, 539.

Norton, D., Knapp, R., 1977. Transport phenomena in hydrothermal systems: the nature of porosity. American Journal of Science. 277.

Norton, D., Knight. J., 1977. Transport phenomena in hydrothermal systems: cooling plutons. American Journal of Science. 277, 937-981.

Oliver, N.H.S., McLellan, J.G., Hobbs, B.E., Cleverley, J.S., Ord, A., Feltrin, L. 2006. Numerical models of extensional deformation, heat transfer, and fluid flow across Basement-Cover interfaces during Basin-related Mineralization. Economic Geology. 101, 1-31.

Petford, N., Cruden, A.R., McCaffrey, K.J.W., Vigneresse, J-L. 2000. Granitic magma formation, transport and emplacement in the Earth's crust. Nature. 408, 669-673.

Phillips, O.M., 1991. Flow and reactions in permeable rocks. Cambridge University Press, Cambridge. 285pp.

Pollard, P.J., Taylor, R.G., Peters, L., 2005. Ages of Intrusion, Alteration, and Mineralization at the Grasberg Cu-Au Deposit, Papua, Indonesia. Economic Geology. 100, 1005-1020.

Rabinowicz M. Boulègue J. & Genthon P. 1998 Two and three-dimensional modeling of hydrothermal convection in the sedimented Middle Valley segment, Juan de Fuca Ridge. J. Geophys. Res., 103, No. B10. 24045-24065.

Raffensperger, J.P., Vlassopoloulos, D., 1999. The potential for free and mixed convection in sedimentary basins, Hydrogeology Journal, 7, 505-520.

Rossetti, F., Tecce, F., Billi, A., Brilli, M., 2007. Patterns of fluid flow in the contact aureole of the Late Miocene Monte Capanne pluton (Elba Island, Italy): the role of structures and rheology. Contributions to Mineralogy and Petrology, 153, 743.

Seedorf, E., Dilles, J.H., Proffett, J.M.J., Einaudi, M.R., Zurcher, L., Stavast, W.J.A., Johnson, D.A., Barton, M.D., 2005. Porphyry copper deposits: Characteristics and origin of hypogene features. Economic Geology, 100th Anniversary Volume, 251-298.

Sibson, R.H., Robert, F., Poulsen, H.H.A.F., 1988.High angle faults, fluid pressure cycling, and mesothermal gold-quartz deposits. Geology 16, 551-555.

Sillitoe, R.H., 1991. Intrusion-related gold deposits In: Foster RP (ed) Gold metallogeny and exploration. Blackie, Glasgow, 165-209.

Stephens, J.R., Mair, J.L., Oliver, N.H.S., Hart, C.J.R., Baker, T., 2004. Structural and mechanical controls on intrusion-related deposits of the Tombstone Gold Belt, Yukon, Canada, with comparisons to other vein-hosted ore-deposit types. Journal of Structural Geology. 26, 1025-1041.

Stern, L.A., Chamberlain, C.P., Barnett, D.E., Ferry, J.M., 1992. Stable isotope evidence for regional-scale fluid migration in a Barrovian metamorphic terrane, Vermont, USA. Contributions to Mineralogy and Petrology, 112: 475.

Thompson, J.F.H., Sillitoe, R.H., Baker, T., Lang, J.R., Mortensen, J.K., 1999. Intrusion-related gold deposits associated with tungsten-tin provinces. Mineralium Deposita. 34, 323-334.

Thompson, J.F.H., Newberry, R.J., 2000, Gold deposits related to reduce granitic intrusions In: Hagemann SG, Brown PE (eds) Gold in 2000. Reviews in Economic Geology. Society of Economic Geologists, Littleton, CO, USA, pp 377-400.

Wing, B.A., Ferry, J.M., 2002. Three-dimensional geometry of metamorphic fluid flow during Barrovian regional metamorphism from an inversion of combined petrologic and stable isotopic data. Geology. 30, 639-642.

Zhao, C., Hobbs, B.E., Mühlhaus, H.B., 1998. Finite element modelling of temperature gradient driven rock alteration and mineralization in porous rock masses. Computer Methods in Applied Mechanics and Engineering. 165, 175-187.

Zhao, C., Hobbs, B.E., Walshe, J.L., Mühlhaus, H.B., Ord, A., 2001b. Finite element modeling of fluid-rock interaction problems in pore-fluid saturated

hydrothermal/sedimentary basins, Computer Methods in Applied Mechanics and Engineering 190, 2277-2293.

Zhao, C., Ge Lin, Hobbs, Ord, A., Yuejun Wang, B.E., Mühlhaus, H. B. 2003. Effects of hot intrusions on pore fluid flow and heat transfer in fluid-saturated rocks, Computer Methods in Applied Mechanics and Engineering.192, 2007-2030.

Table (III.1): Units and symbols of parameters and variables used in this study.

Parameter	***Unit***	***symbol***
Fluid velocity	$m.s^{-1}$	u
Permeability	m^2	K
Dynamic viscosity	$Pa.s$	μ
Fluid density	$Kg.m^{-3}$	ρ_f
Fluid pressure	Pa	P
Gravitational acceleration	$m.s^{-2}$	g
Depth	m	z
	km	Z
Volumetric coefficient of thermal expansion	K^{-1}	α_v
Weighted average volumetric heat capacity	$J.m^{-3}.K^{-1}$	C_{eq}
Specific heat capacity	$J.kg^{-1}.K^{-1}$	C_p
Thermal conductivity	$W.m^{-1}.K^{-1}$	λ

Equivalent thermal conductivity	$W.m^{-1}.K^{-1}$	λ_{eq}
General heat source	$W.m^{-3}$	Q
Volumetric heat capacity of moving fluid	$J.m^{-3}.K^{-1}$	C_L
Temperature	$K, °C$	T
Porosity, (5% in pluton and host rocks)	–	ϕ

10. Supplementary results

The results presented here focus on the effects of pluton geometry on distribution and magnitudes of temperature and fluid velocity in the host rock, (as they are for us the main factors controlling the probable zone of mineralization R^2AI). We display the results for few relatively simple plan view geometries (horizontal rectangular, circular, square and tabular forms). The initial and boundary conditions were the same as those for the previous models.

The figure (III.15) illustrates the intrusion and the entire model domain. Black streamlines represent fluid velocities. Temperatures are shown with contour lines, which are roughly elliptical for all cases. A time progresses and distance from intrusion increases these contours become more flat. In all cases, two convective cells were located above the pluton corners near the topographic surface; the distance between them was controlled by the width of pluton.

To examine the effect of pluton shape on temperature and fluid velocities, we have drawn all pluton tops at constant depth (5km) with a constant surface area and we have made a cross section 1km above the pluton tops. Figure (III.16) shows temperature and fluid velocity curves evolution along the cross section. Thermal contours show that the tabular-like shape can heat a horizontal area larger than those heated by other shapes. As a result, the tabular shape can add 300C° to the area located 1km above the pluton. In contrast, the circular shape intruded the smallest horizontal plan in the host rock; therefore, the temperature does not rise significantly before and during emplacement.

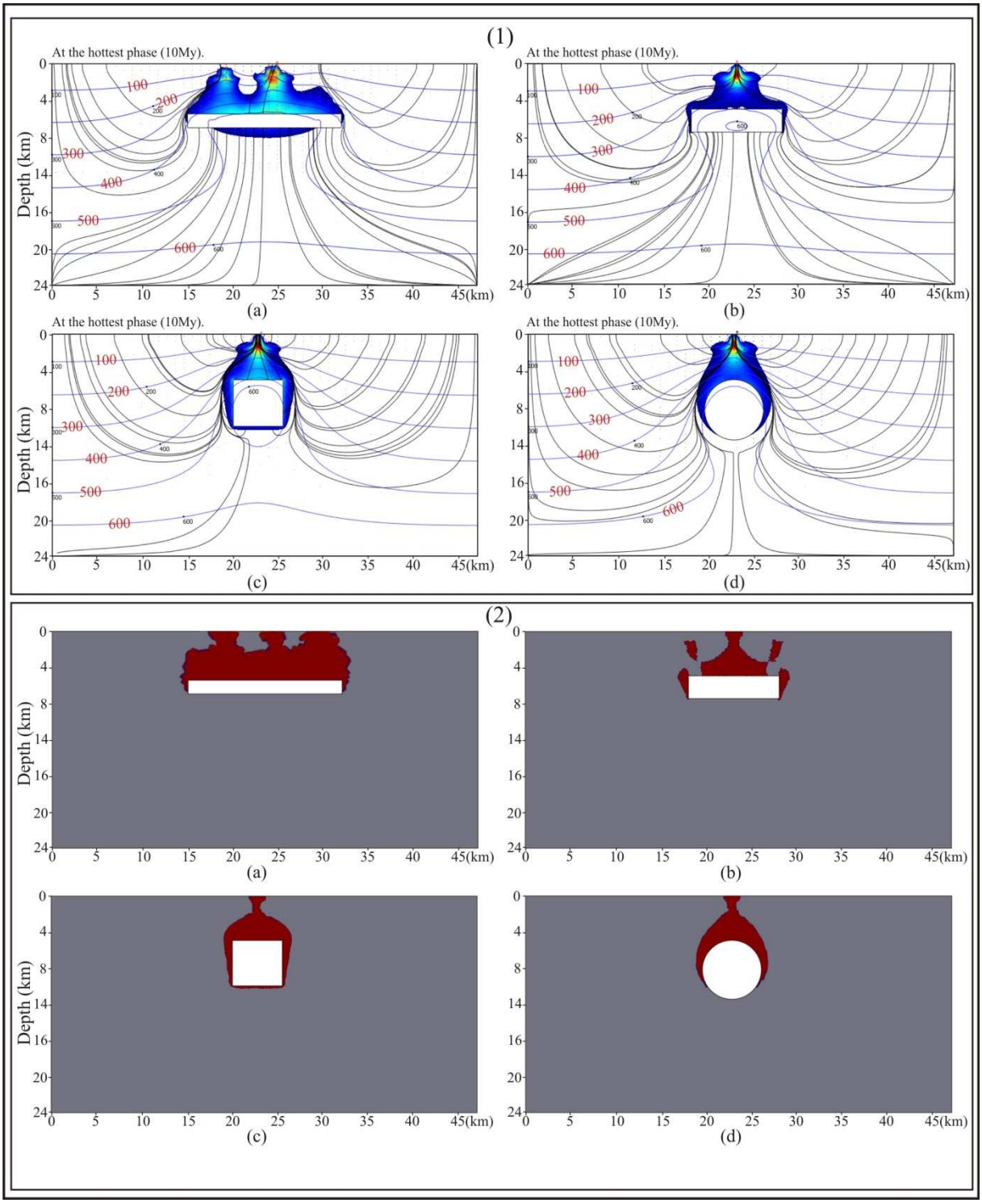

Figure (III.15): Four different shapes of pluton emplaced at the same depth, (1) the application of Peclet Number shows that the tabular-like form creates an advective zone (white zone represents the conductive zone

where P. Number is less than 1, while the coloured zone represents the advective zone where P. Number is equal or more than 1) larger than the other forms (blue lines represent the iso-thermal contours, and black lines represent the streamlines of fluid flow). (2) The application of RA^2I shows again that the tabular-like form produces a probable zone for mineralization wider than other geometries.

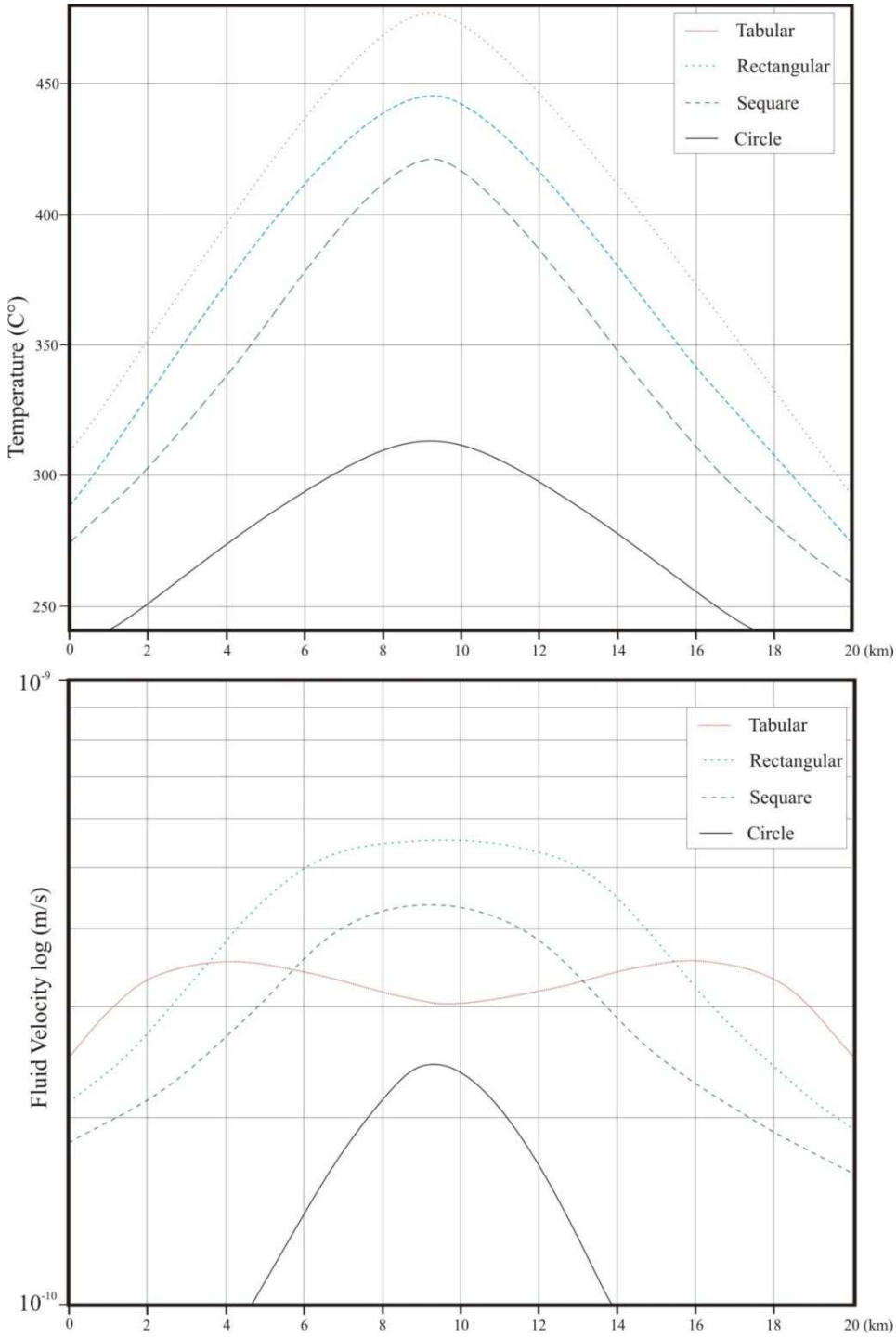

Figure (III.16): Temperature and fluid velocity curves at constant depth (1km above plutons), the results come from the models presented in figure 9. The curve which represents the fluid velocity above the tabular form shows two convective cells by two bulges and a depress of fluid velocities in x direction.

Here we do not discuss the effect of permeable zones (such as fractures and faults) which have a capacity to modify the permeability of host rock around intrusion. Therefore no significant effect of the shape was noticed in fluid velocity; we relate that to a constant permeability at each depth as we varied it vertically and not horizontally. In other words, the advected fluids could not circulate fast due to the vertical variation of permeability. This keeps hot fluids circulating slowly in deep zones be cause of the weak permeability. Multiple fractures around pluton could allow fluid to circulate faster and generate a more marked difference in fluid velocity (see previous results). The fluid velocity magnitudes also depend significantly on pluton geometry, but that is not observed here due to two reasons: a constant horizontal permeability and the emplacement depth of pluton (5km) which is considered as intermediate. These results show that, a great variety of additional factors, such as fracture system, spatial or temporal variations of material properties, varied horizontal permeability, shallow emplacement depth, more sophisticated geometry, can affect fluid velocities.

Moreover, the use of R^2AI on these model outputs shows that the tabular shape is able to generate more favourable physical conditions for mineralization than other shapes, as it occupies more horizontal space. This conclusion is well supported by natural examples where mineralization is found near tabular pluton (e.g. Galicia, Span, Gloaguen et al., 2006).

Chapter IV
The W-Au granite related mineralization of Tighza (Jbel Aouam, Morocco): 3D modeling of pluton shape and hydrothermal fluid flow

Résumé français du chapitre (IV)

Le pluton de Tighza offre un vrai défi pour améliorer la compréhension du rapport entre l'intrusion et la minéralisation aurifère. Précédemment, des études détaillées ont été faites au sujet de la minéralisation de Tighza (Cheilletz, 1984 ; Nerci, 2006). Cheilletz (1984) a proposé un âge pour le granite de la mine (286 Ma) et pour la minéralisation aurifère (285 Ma). Par contre, Nerci (2006) a proposé un âge de 291 Ma pour la minéralisation aurifère dans le filon W1 nord et 286 Ma pour le granite de la mine, les skarns et filons à W-Mo associés.

Nous présentons une nouvelle méthode pour interpréter le rapport spatial et le lien génétique (donc temporel) entre l'activité magmatique et la minéralisation aurifère, ainsi que, l'âge problématique obtenu pour la minéralisation aurifère du filon W1.

A partir de mesures de gravité, la forme 3D de l'intrusion de Tighza a été établie. Les architectures simplifiées 3D du pluton, et du filon W1, interprété comme une zone perméable, ont été alors injectées dans la modélisation couplée numérique 3D définie au chapitres précédents. Cette approche nous permet de comparer, explorer et discuter : i) la distribution de la minéralisation aurifère à Tighza; ii) la relation thermo-chronologique, et par conséquent, le lien génétique entre l'intrusion et la minéralisation aurifère.

Du fait de l'intégration d'une géométrie 3D complexe, le modèle de Tighza obtenu devient plus réaliste même s'il est simplifié en comparant au contexte géologique réel. Bien que beaucoup de paramètres n'ont pas été pris en compte, telle que la réaction chimique, la production des fluides magmatiques, ce modèle donne un nouvel éclairage sur les concepts des intrusions à enveloppes de minéralisation.

L'apparition d'une zone probable de minéralisation au début de la mise en place prouve que les conditions physiques favorables sont disponibles avant la phase la plus chaude ou avant son refroidissement pour former des gisements. En effet, le filon W1 représente la zone la plus probable pour la minéralisation, là où la perméabilité est relativement élevée; c'est donc une zone favorable pour que les fluides circulent plus rapidement depuis la proximité du corps

magmatique jusqu'aux zones froides où ils perdent leur température et leur vitesse, favorisant ainsi la précipitation de minéraux. Pour cette raison, W1 devient la zone la plus probable pour la minéralisation au début de la mise en place. Cette zone se prolonge pour couvrir la totalité de la zone autour du granite à la phase la plus chaude de la mise en place. La perturbation thermique diminue immédiatement pendant la cristallisation du corps magmatique après 0.6 Ma. L'application des contraintes thermiques liée à la température de fermeture isotopique avec le R²AI montre la possibilité de créer des conditions physiques favorables pour le dépôt d'une minéralisation plus jeune que l'âge de refroidissement du granite parent. Cependant, les expériences numériques montrent que, pour un même minéral, les âges de refroidissement (i.e fermeture isotopique) de la minéralisation et du granite ne peuvent être séparés de plus de quelques centaines de milliers d'années. Par conséquent, la datation obtenue pour la minéralisation dans le filon W1 nord (291Ma) correspond à un évènement hydrothermal antérieur, sans connexion avec l'hydrothermalisme induit par le granite de Tighza (286Ma).

Ainsi, ces résultats numériques sont cohérents avec les âges obtenus par Cheilletz (1984) et Nerci (2006) pour la minéralisation W-Au (285Ma), c'est-à-dire très proches de celui du granite (286 Ma). Ces résultats sont compatibles aux évaluations de Cathles (1981b) qui estime la vie maximum d'un système hydrothermal « efficace » (au sens minéralisant) dû à une intrusion à 800.000 ans, en conditions optimales.

1. Introduction

As mentioned in the first chapter, the morphology of pluton has a complicated effect in forming ore deposits. White et al. (1981), Wallace, (1991) Carten et al., (1988) and Seedorff (1988) have shown from different studies that the general orebody morphology depends on the morphology or the shape of related intrusions (I.5 & I.6). This is obviously valid for the porphyry type deposits genetically linked to intrusions. For example, Henderson deposits have revealed the existence of 12 stocks related to three intrusive bodies. High temperature, hydrothermal alteration assemblages were developed in numerous cycles, each corresponding to the emplacement of an ore shell around the stock. For non porphyry intrusion-related ore deposits where genetic link is not clarified, we can expect that the 3D shape of the intrusion has a strong influence in thermal exchanges that occur during emplacement and cooling magma, this is illustrated in chapter (III), (Bergbauer et al., 1998).

Knapp and Norton (1981) evaluated numerically thermal transfers around a pluton with a rectangular cross section. Gerla (1988) presented an analytical model for calculating stresses associated in cooling cylindrical pluton. Based on our knowledge, no thermal or hydrothermal evaluation around a complex geometry of pluton was studied in 3D modelling.

Hereunder, we try to progress our scientific research by going deeper with our models and introducing our 3D model for a natural example. We have chosen a natural example where the mineralization is supposed to be linked genetically and/or spatially somehow to a pluton (Tighza pluton, Central Morocco).

2. Geology and metallogeny of Tighza area

The Tighza deposit in the Jbel Aouam district is the second largest Pb producer in Morocco; it has been exploited continually since the eleventh century. The total production and reserves of the deposit are 1 Mt Pb, 0.3 Mt Zn, and 1,000 t Ag (Cheilletz and Isnard, 1985; Wadjinny, 1998). Tighza district is a polymetallic area constituted of: i) a major Pb-Zn-Ag in thick veins, ii) W-Au (±Mo-Cu) granite–related mineralization, iii) Ba mineralization and iv) low grade-Sb mineralization. In this research, we will focus on W-Au granite-related mineralization which has been studied by Cheilletz (1984) and Nerci (2006).

2.1 Location and morphology

The Tighza region (or Jbel Aouam region) belongs to the Paleozoic Moroccan Meseta, also known as central Morocco. The study area is located in the eastern part of central Morocco,

near the border of Middle Atlas, more or less thirty kilometers north-west of Khenifra town and 7 km from the Mrirt city (figure IV.1).

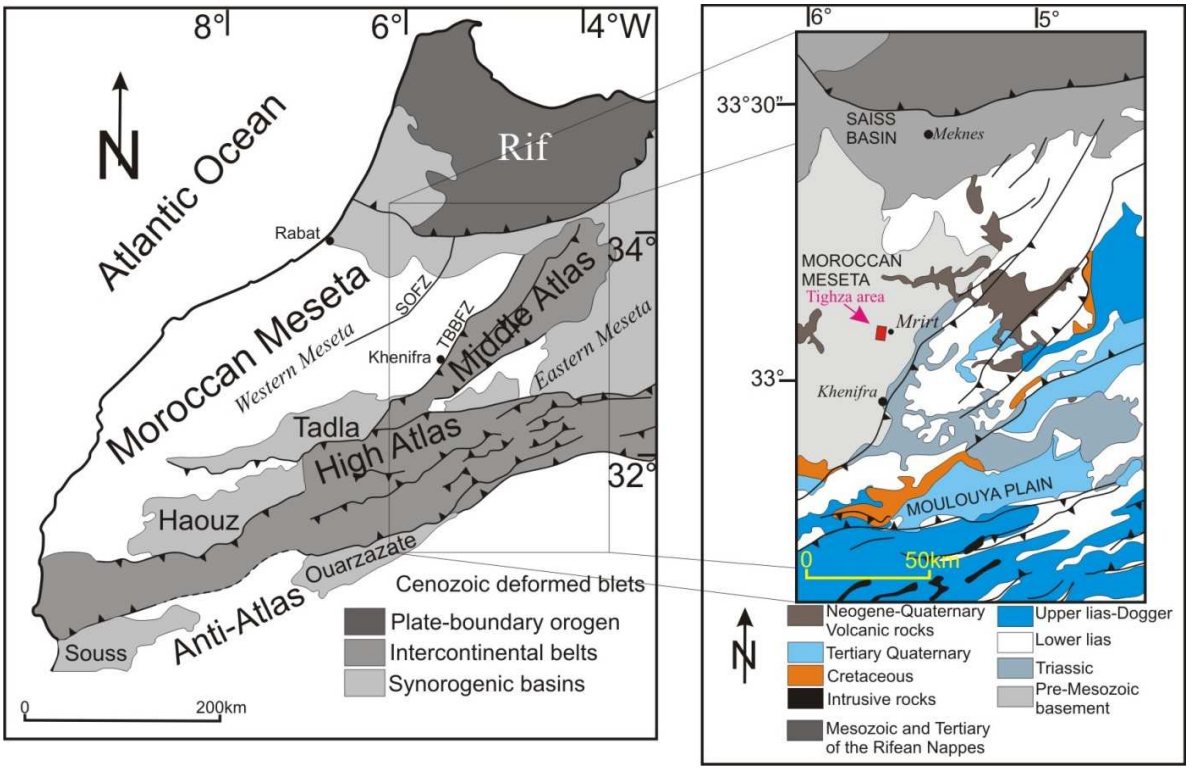

Figure (IV.1): The main geological features of Morocco (modified after Arboleya et al, 2004).

From the morphological view, the sector is an area of high to moderate reliefs (1220 m altitude), in the centre of which emerges the Jbel Aouam (1496 m).

The ridges are oriented roughly NE-SW following the Hercynian direction. This area is crossed by Wadi Tighza which runs through the area in its northern part following east-west direction.

2.2 Geology of Tighza

The Paleozoic basement of Tighza belongs to the band composite anticlines of Ziar-Azrou with huge overthrust in the eastern zone, Termier, (1936) and Ribeyrolles, (1972) (figure IV.2). The Paleozoic series more or less complete, ranges from Ordovician to Carboniferous (Upper Visean); but gaps and important disconformities exist in large series sediment, (Piqué, 1994).

2.2.1 Ordovician

The Ordovician sediments cover a large part of the study area. They form the mass of Jbel Aouam, Anajdam and Iguer oujana representing allochthoneous part of Mrirt nappe (Ribeyrolles, 1972).

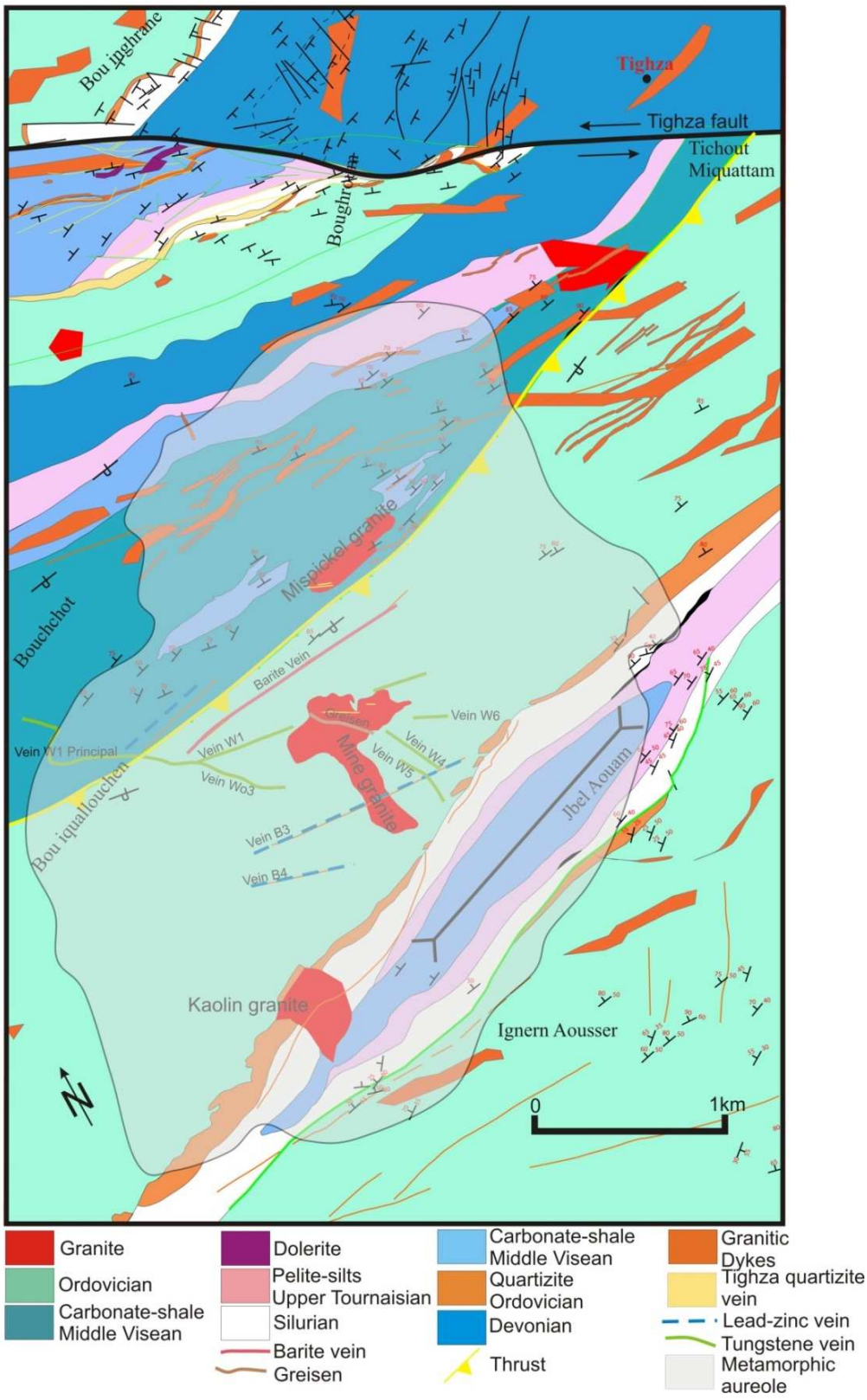

Figure (IV.2): the main geological features of Tighza district.

The upper Ordovician outcrops are limited in NW sector by visean formation (Bou-Iquellouchen), Arrad and Assaffah dykes, forming district of Jabal Aouam. In the South they are limited by the ridges of Iguer Oujana and Annajdam forming the Mrirt plain (Faïk, 1988). The upper Ordovician autochthonous is very thin and limited to a few scattered outcrops. It is found at Tichout Mihammamen, NE of the eroded anticline of Bouchchot at the end of the SW sector and also at Jbel Tanwalt (Faïk, 1988). The Ordovician in Mrirt area is represented by clay or sandy-claystone. The upper part shows the characteristic facies of upper Ordovician sandy-pelite and micro-conglomerate overlying by quartzitic layers. The upper Ordovician type section rises to 600 m in south of Tighza village. Its top is marked by the presence of quartzite, which is overlying by Silurian black mudstone (south of Jbel Aouam).

The fossil record (brachiopods and crinoids) has helped to date the Ordovician formation. But Bennasser (1996) takes into account the work of other authors which distinguished different ages for two different lithological units:

- The middle and lower members composed by an alternation of greywacke and pelites associated to mudstone can be attributed to the upper Caradoc.
- The upper member consists of the quartzitic layers with micro-conglomerate associated to bioturbated greywackes can be attributed to the Ashgill.

2.2.2 Silurian

Silurian outcrops appear in the north (Boughroun peak) and the middle east of the study area (Jbel Aouam). The Silurian succession consist mainly of schist with graptolites indicate Llandovery age. Agard et al. (1958) called this schist Mokattam schist. It is hard, from 1 to 2 cm thick silty mudstone dark red to black, reflecting the abundance of organic matter. The series continues with dark schist with graptolites of upper Wenlock (with sandy carbonate nodules), and ends with dark schist.

Silurian type section appears at the middle of the syncline, and is surrounded by the quartzitic bars of the Ordovician represented by a micro-conglomerate facies and laminated black schist. This schist is highly fossiliferous (graptolites) and characterizes by calcareous nodules.

2.2.3 Devonian

The Devonian is less represented in the study area than the Ordovician or Carboniferous, it appears in the northern section (north of the wadi Tighza). The Devonian is composed by shelly limestones, intercalated with white sandstone benches. This limestone is overlain by greenish argillaceous micaschist and underlying by Ordovician quartzites. In Tichout

Mihamam, (south of Tighza fault), Devonian consists of greenish schist with lenses of greywacke, and traces of bivalves and overlying by fossiliferous limestone. The lower Devonian deposits consist of mudstone indicating calm sedimentation environment, which is rich in chert nodules and limestone. (Bennasser, 1996).

2.2.4 Carboniferous

The lower part of Tournaisian is composed of conglomerates, quartzite, greywacke and silty mudstone described by Ribeyrolles (1972) and Desteucq (1974). The lower contact of this formation is marked by an unconformity with Devonian or Silurian deposits. In contrast, its upper contact is marked by the appearance of the limestone of Middle Visean (Faïk, 1988).

The Visean was first described by Termier (1936), and later by Agard et al., (1955) who defined that Jbel Aouam is composed by a clastic base overlied by a series of fossiliferous limestone. Faïk (1988) and Bouabdelli et al. (1989) have shown that deposits at the base have Tournaisian age, and overlied by limestone which represents the Middle Visean; the upper part of the series is attributed to the upper Visean.

The Visean deposits south of Jbel Aouam are represented by a carbonate facies overlying the upper Tournaisian. The top of the series is composed by black fossiliferous mudstone (foraminifera and brachiopods) Faïk (1988). In Bou-Iquellouchen area, visean deposits are steeply dipping to the NW. The basis of this series is mainly calcareous, consisting of calcareous sandy with gastropods, crinoids and bioclastic limestone rich in brachiopods and foraminiferas with marly intercalations. The series ends with black mudstone beds and conglomeratic lenses (Bennasser, 1996), and gray bioclastic limestone with intercalations of micaceous greywacke. This limestone has been studied by Desteucq (1974) and Cheilletz (1984) as equivalent to limestone formation described at the basis of synclinal structure. In the paleogeographic map, Bou Iquellouchen Basin is located in the central part of Khenifra-Azrou Visean basin, where sedimentation is due to visean transgression from NE (Bouabdelli, 1989).

2.3 Magma activity

In Tighza area, post-orogenic magmatism is represented by veins and stocks (figure IV.2). The veins are stricking NE-SW and extend from Bou-Iskra N to Lalla Tayefait. Stocks of Jbel Aouam overlap and metamorphose Ordovician to visean formations. They are spatially related to major polymetallic mineralization (Pb, Zn, Ag, W, Agard et al., 1958; Cheilletz, 1984).

Three isolated granite stocks, aligned in north-south direction, are exposed in the Paleozoic basement rocks. They are called from north to south Mispickel granite, Mine granite, and

Kaolin granite respectively, (Agard et al., 1958; figure IV.2). The granitic stocks are emplaced in the area during a brittle deformation, characterized by EW extension synchronous with a large EW shear zone represented by Tighza fault in the north (Cheilletz, 1984). Because of their small size and their separation at the surface, these stocks could be the apexes of an underlying pluton (Agard, 1958).

Granite of mispickel is located at the middle of the study area (300m length and 60m width) with NE-SW direction, in the Upper Visean formation (Agard et al., 1958; Faïk, 1988). Petrological analysis reveals a granodiorite with porphyritic texture (the crystal size is variable up to 7 mm), consisting of quartz, plagioclase, potassium feldspar, biotite and apatite.

The Mine granite is located to the south of Mispickel granite, in the schist of the Upper Ordovician. The massif is crossed by network of stockwork of quartz from 1 to 4 cm thick, with N100° to N120° direction. It is intersected by veins of aplite 15 to 20 cm thick stricking E-W. Mine granite has the same mineralogy of Mispickel granite, with a slightly high content of potassium feldspar and quartz, which allows us to call it a monzogranite (Nerci, 2006).

The Kaolin granite has a cylindrical shape; it is located in the southern part of the study area. It is intersected by Pb-Zn-Ag veins producing a significant quantity of kaolin. They are hosted in the north by Silurian schist and Visean limestone in the south. The three small granitic bodies of Tighza have a cylindrical pipe-like shape and there is no spatial relationship at the surface between them. They have an equigranular to porphyritic texture with a mineralogical composition includes: biotite, plagioclase, potassium feldspar and quartz (Cheilletz, 1984).

Based on different geochemical studies (Cheilletz, 1984 ; N'tarmouchant, 1991), the three granites of Tighza show a homogeneous magmatic calc-alkaline facies characterized by abundant feldspath (mine and kaolin granites) and less developed facies rich in elements such as (CaO, TiO, MgO, Fe_2O_3 and Sr), (Ishihara, 1977).

Several dating methods (K/Ar and Ar/Ar) have been applied to both the granites and mineralization (Cheilletz, 1984 ; Nerci, 2006). Biotite age of mine and mispickel granites are respectively: 287.9 ± 10.2 Myr and 293.0 ± 6.0 Myr (Cheilletz and Zimmermann, 1982). The ages were refined by (Cheilletz 1984) (Table IV.1). Lately, age dating (Ar/Ar) were carried out by (Watanabe, 2001) and (Nerci, 2006). Watanabe has given an age of 280.6 ± 5.5 Myr for "igneous biotite" of Kaolin granite, but they neither show the nature nor the precise location of sampling. Ar/Ar dating produced by Nerci (2006) for mine granite gave an age of

286.0 ± 0.4 Myr, confirming and clarifying the earlier data. These new dates strengthen and clarify the existence of a magmatic event around 286 Myr.

2.4 Aureole of metamorphism

An aureole of metamorphism surrounds the three granitic stocks figure (IV.2), occupying an area of 2 to 3km in diameter (Cheilletz, 1984). It is composed by the superposition of two distinct phenomena: a metamorphism occurred mainly by thermal contact and a another occurred due to a hydrothermal circulation with metasomatism.

Table (IV.1) results of Cheilletz (1984) and Nerci (2006) based on K/Ar and Ar/Ar respectively.

samples	Mineral/rock analysis	Cheilletz (1984)	Nerci (2006)
Mine granite	Biotite/total rock	287.9 ± 5.1 Myr	286 ± 0.4 Myr
Vein W1	Biotite	285 ± 3.8 Myr	291.8 ± 0.3 Myr
Tungsten	Biotite/Mascovite	285.3 ± 3 Myr	285.3 ± 0.5 Myr
Skarnoid	Muscovite		285,3 ± 0,5 Myr
Molybdenite vein	Muscovite		285,6 ± 0,5 Myr

Locally, these metamorphic facies have been retromorphosed by the effects of the hydrothermal fluids that lead a second biotite paragenesis (Fe/Mg = 0.4, Si_{IV}=5.6) developed through a network of veins and micro-veins (Cheilletz, 1984). These retromorphosed facies are also reflected by the emergence of new paragenesis in schist-sandstone series (except Devonian limestones which lie outside the aureole of thermal metamorphism). The non-foliated cordierite-schists is metamorphosed into chlorite and sericite. In contrast, the upper Visean limestone is metamorphosed into pyroxenites, grenatites, amphibolites and marble near the Mispikel and Kaolin granites (Nerci, 2006).

There are many small quartz veinlets in the sedimentary rocks and granite in the metamorphic halo, which locally contain scheelite and wolframite. Skarn including grossular, diopside, and vesuvianite formed where the pluton intruded in calcareous rocks (Agard et al., 1958; Cheilletz, 1983).

2.5 Tectonic history

Structurally, the District of Tighza is located in an area of strike-slip fault and nappe at the center of Azrou Khenifra Visean basin (Bouabdelli, 1989). Previous structural studies have revealed the nature of the polyphase Hercynian orogen and distinguished three major phases of deformation:

- Post-Devonian phase of an intense deformation and folding.
- A major post-folding of Visean phase responsible for the current architecture.
- A phase divided into several stages led by a succession of compression and extension tectonic regimes, lead to a shear zone EW and a dense fractures network of NE-SW and EW direction, through which Hydrothermal fluids have been channeled.

The district is divided into two units: the South-Eastern allochthonous and the north-western autochthonous. The allochthonous unit is composed mainly by the Upper Ordovician series with few Silurian-Devonian outcrops forming the front of the Mrirt nappe. The second is limited in SW part by Bou Waghaz fault oriented WNW-ESE. While, the autochthonous unit consists of Upper Ordovician, Silurian, Lower and Middle Devonian and Visean deposits. This unit forms an elongated band NE-SW direction.

The large structures of the region are resulted from the major Upper Visean post-folding. The folds are characterized by:

- The syncline of Jbel Aouam covering 2.5 km long and 300 m wide; its centre is occupied by Visean limestone
- Bouchot anticline has a 7 km long and 500 m to 1 km wide, with a NE-SW direction and with a dip of 50° to SW (Ribeyrolles, 1972), (Deusteuq, 1974), (Faïk, 1988) (Bouabdelli, 1989). It is composed by Lower Devonian and Silurian underlying angular unconformity with Upper Tournaisian conglomerate. (Bennasser, 1996).

In addition, there are three different orientations for fractures in Tighza area:

- N90° to N120°, which corresponds to faults perpendicular to the direction of Hercynian orogen.
- NS, N160 ° and N120 ° develop especially in Jbel Aouam area and the SW sector of the study area (Bouaghaz fault and Bouchchot area).
- N70°and N40° representing the extension of the Aguelmous-Mrirt fault. This fault is bordered by micro-granodiorite veins SW and leucogranites NE.

2.6 Tighza District (Pb/Ag, Sb and Au-W veins)

The Tighza district contains three types of deposits, economically significant and widely distributed: Pb-Zn-Ag veins, Sb-Ba veins, and W-Au occur in the central part of the district.

- Several large (average 2m wide) Pb-Zn-Ag veins (Signal, Ighem Ousser, Sidi Ahmed) are striking N50°E to N80°E and dipping N to NW collectively contain more than 11 Mt ore, with 1 Mt Pb and more than 1,000 t Ag (Wadjinny, 1998), with significant zinc production. These veins are hosted by the Paleozoic sediment and cut the granitic stocks (kaolin granite and mine granite) as well as tungsten veinlets. They are associated with conjugate strike-slip faults (NE-SW compression) and clearly post-date emplacement of the felsic stocks. Strontium isotopic data from siderite suggest a connection between these veins and the granitic intrusions, Castorina and Masi, (2000). There are five major veins in the Tighza deposit. These veins are 1 to 2 km long and have a vertical extent of more than 600m. The sulfide mineral assemblage is simple and fairly similar in the different veins with galena, sphalerite, chalcopyrite, pyrite, arsenopyrite, and marcasite, siderite, ankerite, calcite, barite, and quartz. The Signal vein has a different sulfide mineral content such that the vein partly includes tennantite-tetrahedrite, stannite, cassiterite, bismuthinite, and native bismuth.
- Sb- and Ba-bearing, they form small veins hosted by Paleozoic sediments out of district. Therefore, they are not considered in this reseach.
- Tungsten-bearing mineral occurrences have been described by Cheilletz (1984) and Cheilletz and Isnard (1985) within the metamorphic aureole of the mine granite.

The tungsten veins have been previously studied (Cheilletz, 1984; Cheilletz et Isnard, 1985, Nerci, 2006) in particularly W veins.

2.7 vein W1:

The vein W had already been noted for its economic contents of gold. However, the veins "W" are organized into sometimes anastomosing network, near Mine granite. Figure (IV.2) adopting a per-granitic relationship quite clear. These veins include several surface and sub-surface veins, started by the vein W1, clearly visible in outcrop, W1 north, WO3, W4 and W5, figure (IV.2 &3).

These veins cut-out areas of Visean Paleozoic and a part of the Ordovician and the front of the thrust to the west of the mine. They show a series of tectonic events realized by a series of sinistral and dextral strike-slip faults and joints to very small displacement faults. All these veins are composed of quartz. W1, W1 north WO3 have embedded muscovite in quartz, the others (W4 and W5) include phlogopite-biotite. The main branch of the W1 vein in east is W1 north, which continues almost 1200 m to Mine granite. Within the granite, the main branch consists of veins of quartz, muscovite (greisen) with quartz nodules and sulphides and continues to the south-east of Mine Granite by W4 and W5 structures (figure IV. 2).

The mineralogical and geochemical studies show that W1, W1 north and the greisens have the same mineralogical contents, which allow us to say that from a structural view, W1 north, greisens, W4 and W5 belong to W1 and this set of veins could be interpreted as horsetail structure.

The formation of skarn and tungsten mine is almost synchronous with the magmatic event of 286 Myr. The scheelite-molybdenite vein observed in the mine is also synchronous to this event. In contrast, a sample of the vein W1 north gives an age of 291.8 Myr, Nerci (2006). This age is older than the Mine and Mispickel granites. Table (IV.1) shows different results of age dating of Tighza granites and mineralization.

Cheillez (1984) has used K/Ar method to measure the absolute age of Mine granite and mineralization. Accuracy and average of error of this method are lower and higher respectively. Different advantages of Ar/Ar method were maintained by Saito (1994); the most important advantage is that K/Ar method requires separate fractions for the K and Ar analyses. This means that inhomogeniety of K in a sample could cause a significant error in age determination. The Ar^{40}-Ar^{39} method, on the contrary, requires a single analysis of Ar isotopes for an age determination. Hence, this method is free from sample inhomogeniety, so, its results are more accurate. This allows us to look at the results of Nerci (2006) as more precise results and therefore more useful in our study.

3. Gravity anomalies of Tighza pluton, processing, interpretation and 3D modelling

The 3D geologic and geophysical model allows to simultaneously integrats the data from different sources such as petrophysical measurements, structural orientations of different lithologies, 2D conjoint gravity and cross sections. The coherent integration of information from various sources allows proceeding from an intuitive and qualitative geological

understanding to a quantitative description of the geology. On the basis of these integrated results, an emplacement model in relation with its host rocks can be proposed.

In this section a detailed investigation of gravity anomalies of Tighza granite complex in conjunction with field observation is thus made to delineate its subsurface batholithic proportion and find a geological model to which the present-day local mineralisation of the region can be related. We present results from potential field modeling, which allow assessment of the pluton geometry at depth.

We thereby construct results presented in this part based essentially on the observations at the surface and gravity measurements. In order to constrain this modeling, petrophysical parameter (density) was determined by laboratory measurements for granite.

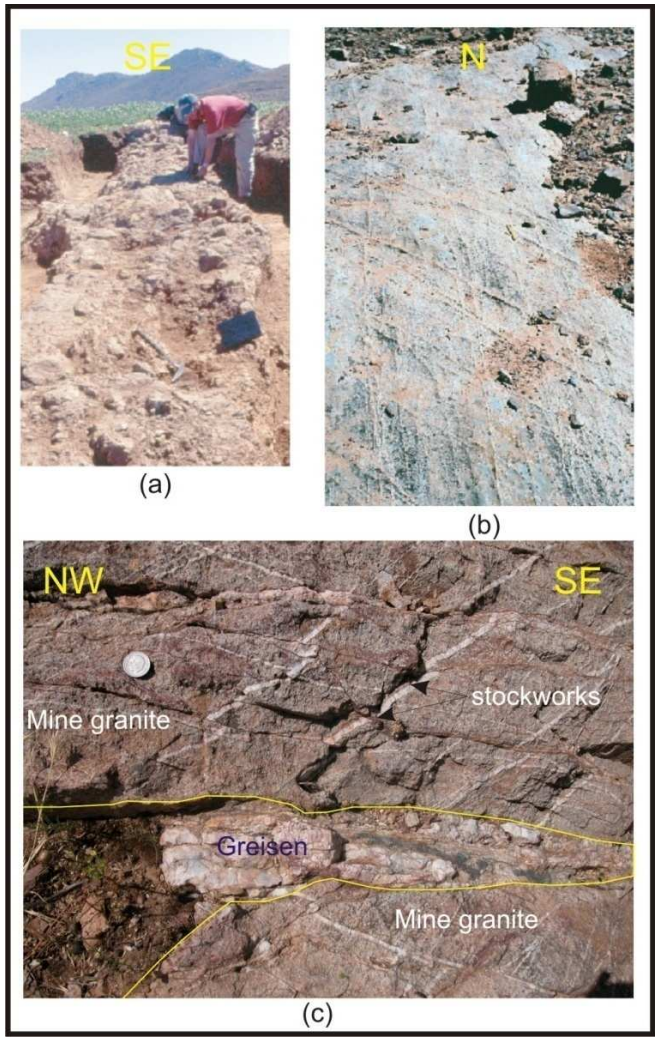

Figure (IV.3): (a) W1 extends about 1200m WE, (b) stockworks in Mine granite and (c) Greisen the (extended part of W1 and W1 north), the photo shows that Mine granite is crossed by the greisen and small faults.

Furthermore, several cross sections strengthen the geometrical and topological consistency of the interpretative geological model. Despite the lack of other geophysical data such as seismic reflection or magnetism surveys which could help decipher the shape of pluton, we are integrating here multidisciplinary information into a realistic geological 3D model. Although non-unique, the obtained model is consistent with available geophysical data and integrates the present-day geological knowledge. In this work, regional modeling has been performed by gravity investigations in order to image the 3D geometry of the pluton. Gravity measurements were carried out throughout the study area using a SCINTREX CG3-M Micro-gravimeter.

3.1 Processing of Gravity Data

Processing of gravity data (measured from a gravity meter) includes different procedures to obtain the final gravity differences between the base and the stations referred to it. The final calculated values, which are the values of gravity at particular zones, constitute the value that subtracted from a modified theoretical value to give the so-called Bouguer anomaly. The Bouguer anomaly is named after a French scientist (Pierre de Bouguer. In simple terms, the Bouguer anomaly is the difference between what gravity is at a particular zone, and what it should be at that same zone.

The measured value is affected by different factors: 1) elevation of the location (often sea level), 2) mass between the location and the arbitrary reference point, 3) terrain around the location, 4) latitudinal position, and 5) the curvature of the Earth. Any lateral deviation could affect on gravity values. In particularly, the lateral deviations in density are the most important goal of a gravity survey, but their effects are less important than the previously-cited factors of (mass, elevation, terrain, latitude, and curvature). Therefore, the density-change portion of the gravity value must be separated from the rest of the gravity measurement by making some corrections; to obtain the Bouguer anomaly.

Three steps are followed in calculating the Bouguer anomaly:

1. Calculate the theoretical value for a station, based on its latitudinal position.
2. Then modify the theoretical value, as if it had been obtained with the same elevation.
3. Subtract the modified theoretical value from the observed absolute value.

3.1.1 The theoretical value

The theoretical value of gravity at any position can be calculated by a mathematical formula:

$$g = 978.031846(1 + 0.005278895(\sin^2\varphi) + 0.000023462(\sin^4 \varphi) \quad \text{(IV.1)}$$

where (φ) is the latitude angle at each station. This produces a gravity value in Gals. The theoretical value needs to be calculated for the base station and for each station in the survey (the base represents here a reference point in the field).

3.1.2 How to modify the theoretical value

Different steps are required to calculate the final value (Bouguer anomaly):

1. Free air correction
2. Bouguer correction
3. Terrain correction
4. Curvature correction

The terrain modification required a manual work for each station using a template and topographic map. Whereas, curvature corrections can be ignored since the differential effect between the two most extremely-positioned stations is negligible.

3.1.2.1 Free air correction

The gravity changes with vertical distance, decreases with increased elevation above Earth's surface. The rate of change (free-air correction) is 0.3086 mGals/m of elevation. The value of the modification is found by multiplying the rate of change times the number of meters above (or below) the reference value. The form of the Free-Air gravity anomaly, ***gfa***, is given by:

$$gfa = gobs - (gn - 0.3086\ h)\ (mgal) \qquad \text{(IV.2)}$$

where *h* is the elevation at which the gravity station is above the elevation datum chosen for the survey (this is usually sea level).

3.1.2.2 Bouguer correction *(simple Bouguer)*

The amount of gravity of increase is proportional not only to the distance (elevation), but also to the density of rocks. The mass factor per foot of elevation is 0.01277*(ρ) in milligals, where ρ is the density expressed in $g.cm^{-3}$ (a value of 2.60 $g.cm^{-3}$ is usually used, since it is an average value for the density crustal rocks).

The Bouguer correction is a first-order correction to account for the excess mass underlying observation points located at elevations higher than the elevation datum. Conversely, it accounts for a mass at observations points located below the elevation datum. The form of the Bouguer gravity anomaly, ***GB***, is given by:

$$GB = gobs - (gn - 0.3086\ h + 0.04193\ \rho\ h)\ (mgal) \qquad \text{(IV.3)}$$

where ρ is the average density of the rocks underlying in survey area. When the modified theoretical gravity value is now subtracted from the observed absolute gravity value, a simple bouguer anomaly value is obtained.

The more usual practice is to also apply a terrain modification to the theoretical value too.

3.1.2.3 Terrain Correction

To compute the gravitational attraction produced by the topography, we need to estimate the mass of the surrounding terrain and the distance of this mass from the observation point. The specifics of this computation will vary for each observation point in the survey because the distances to the various topographic features vary for each gravity station.

Estimating the distribution of topography surrounding each gravity station is not a trivial task. It is realised by plotting the location of each gravity station on a topographic map, estimating the variation in topographic relief about the station location at various distances, computing the gravitational acceleration due to the topography at these various distances, and applying the resulting correction to the observed gravitational acceleration.

The terrain correction is positive regardless of whether the local topography consists of a mountain or a valley. The form of the terrain corrected, Bouguer gravity anomaly, ***gt***, is given by:

$$gt = gobs – (gn - 0.3086\ h + 0.04193\ \rho\ h – TC)\ (mgal) \qquad (IV.4)$$

where *TC* is the value of the computed terrain correction (for more details see e.g. Dubois & Diament, 2001).

Assuming these corrections have accurately accounted for the variations in gravitational acceleration they were intended to account for, any remaining variations in the gravitational acceleration associated with the Terrain Corrected Bouguer Gravity, ***gt***, can now be assumed to be caused by geologic structure.

3.2 Interpretation

3.2.1 Gravity Data

Over the past decade, there has been extensive work documenting the emplacement of plutons in a variety of structural settings. Pluton emplacements were described in extensional tectonic environments such as pull-apart structures (e.g., McCaffre, 1992; Tikoff and Teyssier, 1992), tensional cracks (Hutton, 1982; Castro, 1986; McNulty et al., 2000), shear zone terminations (Hutton, 1988; Neves and Vauchez, 1995; Tikoff and de Saint Blanquat, 1997), flower structures (Pe-Piper et al., 1998) and the shoulders of shear zones (Weinberg et al., 2004). In recent years, application of gravity techniques has contributed to important advances in the

understanding of pluton emplacement mechanisms, and in the use of syntectonic granitoids as markers of regional kinematics and strain fields (Cruden and Launeau, 1994; Leblanc et al., 1994, 1996; Bouchez and Gleizes, 1995; Tobisch and Cruden, 1995; Benn et al., 1997, 1998; Gleizes et al., 1997).

Therefore Gravity Technique is a useful tool to describe the shape of the pluton at depth, its thickness variations and the location of possible root zones (e.g. Vigneresse, 1990; Lyons et al., 1996). Thus, prior to 3D modeling, indirect analyses applied to the gravity data have been performed, in order to extract quantitative estimates of densities, vertical extents and shapes of the different units involved in the model (Martelet et al., 1999). The approach used here is mainly based on inversion techniques in which the geometry of any geological body is defined by an aggregate of bodies of simple geometry.

This methodology is based on approaching the geometry of the anomalous density body by a series of vertical prisms. Iterative forward modelling is preformed, in which the prisms are modified until a reasonable fit of the observed and theoretical gravity anomalies is obtained.

About 320 principal gravity measurements were made in the study area for the exclusive purpose of this investigation, with a Scintrex (Model-CG3-M) gravimeter of sensitivity 0.01 mGal. We did not remove any regional component from the gravity signal and modeled directly the Bouguer anomaly.

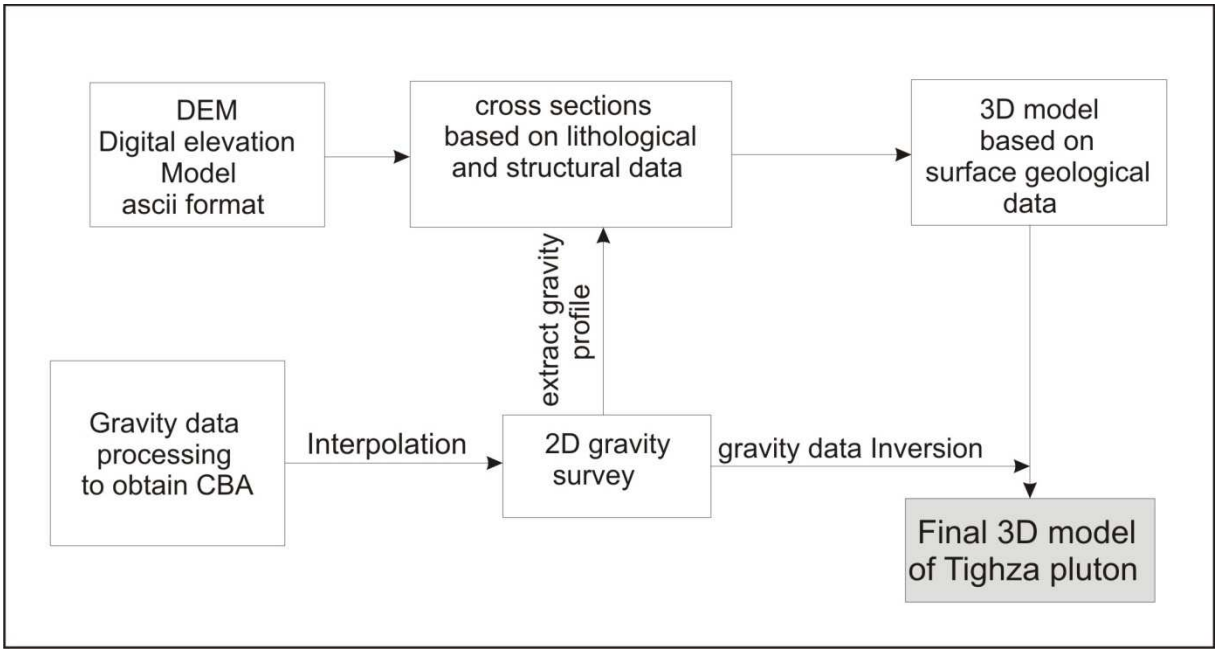

Figure (IV.4): Processing procedures to extract the final 3D geometry of Tighza pluton.

The majority of the stations were located at places where we can create a grid covers all the study area, the distance between each two stations was approximately 250m, the elevations were measured by a GPS and controlled by a very precise topographic map made by (CMT: Compagnie Minière de Touisit), expected error on elevation does not exceed 4 m. Figure (IV.4) shows the procedures we need to follow to construct our 3D geometry of Tighza pluton. The first step of the proposed methodology concerns the creation of a geological database, which includes all the information needed for 3D modelling.

The Bouguer anomaly map reflects the heterogeneous distribution of masses at depth, figure (IV.5). Positive anomalies, corresponding to high densities, are normally associated with the host rock (mica schists), whereas granite has lower densities, are prominently displayed as negative anomalies. This imports a trend which indicates a decrease in gravitational acceleration from the centre to edges of the map with a prominent concentration related to three main granitic outcrops, and scattered anomalies associated to granitic dykes and thicker zones of pluton. This step has been realized in a GIS environment, exploiting the available tools and techniques to store and manage the following layers:

1. Topographic data, including detailed 2D elevation contour lines (10m contour interval) and single points with elevation values. Vector to Raster conversions and linear interpolations are needed to obtain Digital Elevation Models (DEM), (figure IV.6).
2. 2D linear features representing stratigraphic boundaries, faults, fold axial traces, etc. These polylines have been obtained by generalising the surveyed geological maps.
3. 2D polygonal features and related attributes representing the spatial distribution of outcropping units (figure IV.5).
4. Mesoscopic field structural measurements (bedding, faults, fold axes, etc.) represented as points with properties (strike, dip-direction, dip, etc.).
5. Bouguer anomaly map reflecting the gravity anomalies calculated from field measurements.

Hence, we can define two different areas (figure IV.5): a) the central region of the study area characterized by the presence of strong anomalies and b) marginal zone in which the anomalies decreases. The gravity lows of the central region probably delineate the presence of a large buried intruded body with discrete spots of dense anomalies overlapping granitic and dykes outcrops.

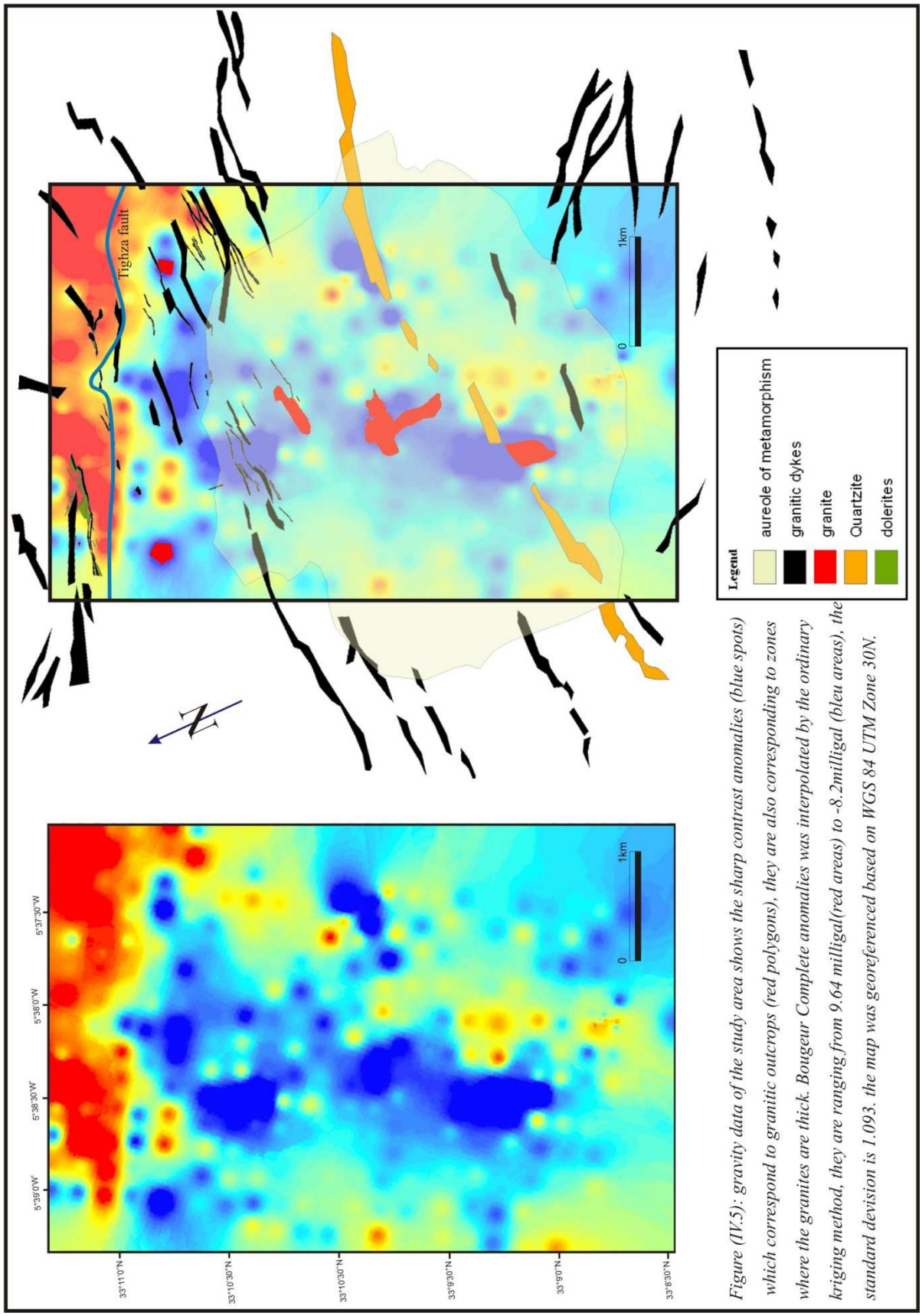

Figure (IV.5): gravity data of the study area shows the sharp contrast anomalies (blue spots) which correspond to granitic outcrops (red polygons), they are also corresponding to zones where the granites are thick. Bougeur Complete anomalies was interpolated by the ordinary kriging method, they are ranging from 9.64 milligal(red areas) to -8.2milligal (bleu areas), the standard devision is 1.093. the map was georeferenced based on WGS 84 UTM Zone 30N.

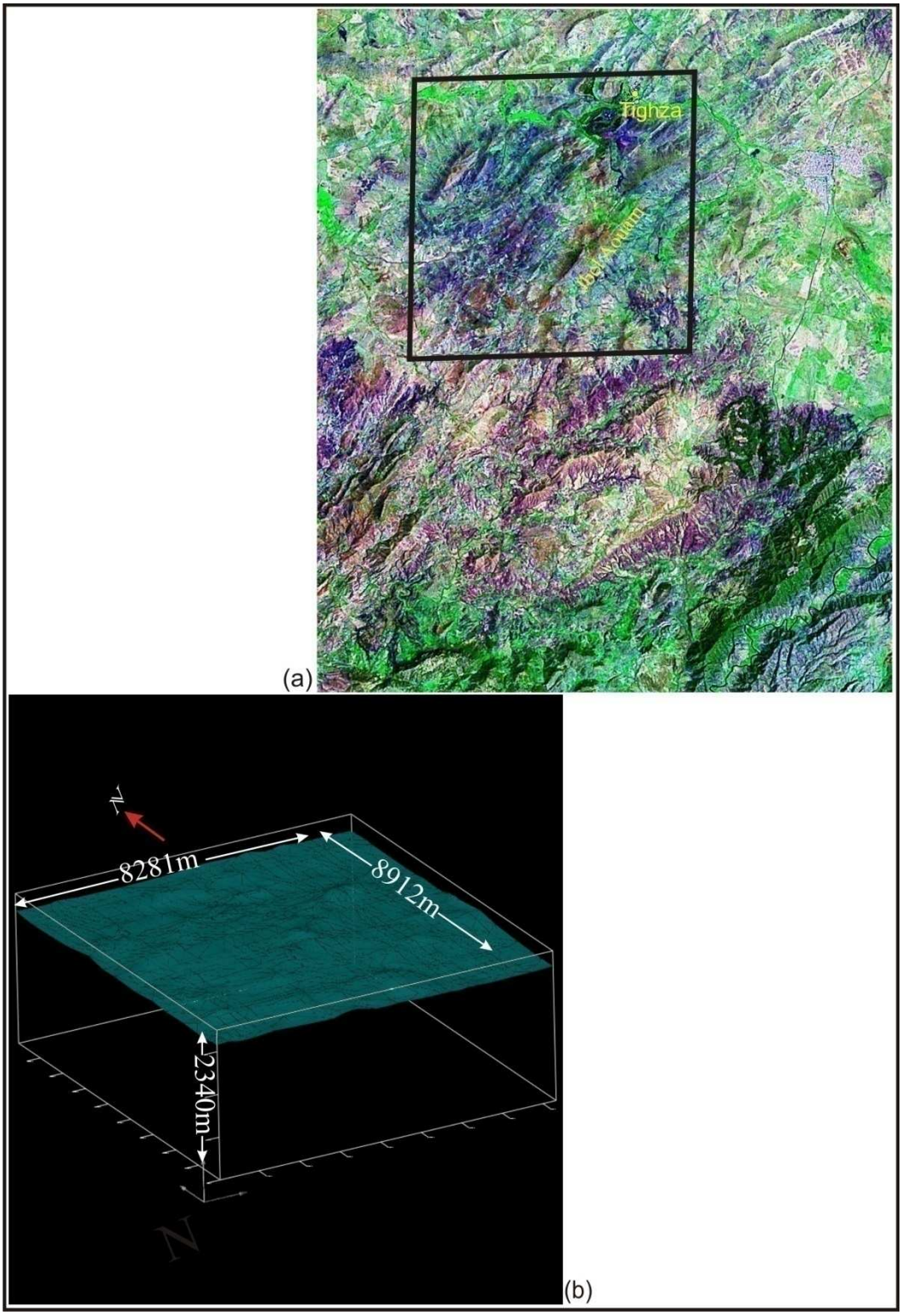

Figure (IV.6) Extracting DEM from SRTM (Shuttle Radar Topography Mission) in Geotiff format (a), this type of files allows us to extract (x,y,z) coordinates of each point in the selected area (b). Black square shows the location of Tighza area.

In addition, the main fault is well defined on the Bouguer anomaly map; it is outlined by a sharp gravity gradient corresponding to the contact between the low-density pluton to the middle and the high-density metamorphic series to the north. The negative anomaly along the fault suggests thickening of the pluton in relation with the fault. The sharp Bouguer anomalies contrast is indicative of a fault that coincides with the valley in W-E trend in the northern part of the study area. Furthermore, there is no hint of a negative Bouguer anomaly over the Northern zone of the fault, in addition, gravitational structures sharply end against the fault; we began the reconstruction of the intruded body from the gravitational structures by a sharp contact with the main fault (E-W) figure (IV.5).

This lets us assume that the fault might have controlled the emplacement of Tigzha pluton, and it is possible that a feeder zone is located nearby the fault and extend to the south with decreasing in thickness of the granite towards the centre. In addition, plotting Bouguer anomalies demonstrates other roots; this was easily marked by strong anomalies in the north western and southern parts of study area. We suggest that this zone could represent the location of other feeder zones. In contrast, the western, eastern and the southern regions are associated with a positive gravity anomaly. This suggests that the western and eastern extensions of Tighza pluton are thin and therefore the pluton probably spreads southward from the main fault as a laccolith. Geochemical analyses suggest that the granitic outcrops of Tighza, (Granite à Mispickel, Granite de la Mine and Granite du Kaolin from the north to the south respectively) have evolved from a single source, with chemical differences attributable to the source-rock in homogeneity and the degree of fractionation (Nerci, 2006). At this point, we suggest that the three out crops of Tighza granites are connected to each other somewhere at depth. Though, the map with the observed Bouguer anomaly does not reveal clearly the proposed batholitic boundary, it does not negate it as well. Despite of that, we assume that we have only one buried body as the low gravity anomalies with southward extension and the size of aureole of metamorphism around the three granitic out crops (mentioned above) suppose a large body concealed beneath them.

Notice that as the batholith is intruded more deeply or have flat thin form, the gravity anomaly decreases in amplitude and spreads out in width. In other words, the more deeply or thin intruded body produces a gravity anomaly of smaller amplitude that is spread over more of the length of the profile. Thus, the more shallow intruded body (in case is a thick body) produces a large negative anomaly. That means sharp anomalies are usually associated with the

shallower and thick sources, while smooth and small anomalies are associated to deep or thin intruded bodies. Apply this theory in our case gives that the high gravitational anomaly reflects a thick intruded body which is indicated by the strong anomalies over Kaolin granite and next to Mispickel granite, while the remained zones of the study area show low gravitational anomalies (covered almost the central and southern parts of the map) and reflects a thin intruded body. In this case, even when the three granites are emplaced as branches of discrete granitic bodies at the surface, we suppose that they are connected in the subsurface as the amplitude of gravity anomaly around them is less than the amplitude over a host rock, this allows to propose a flat layer lies between them.

The surface data alone does not provide an accurate constraint on the thickness of the granite. In the absence of any more convincing indications to the contrary, our favorite interpretation of the gravity data must be the simplest one. Based on this geological knowledge 2D forward gravity modeling has been performed using the Geosoft-GM-SYS software along cross sections. A cross section was drawn perpendicularly to the pluton to image the relationships between the three granites and host rocks based on gravity data. We attempted to find the same curve of Bouguer anomalies by proposed theoretical densities for different formations and modifying the form of three granites in the subsurface to have identical curves between theoretical and measured gravity anomalies (figure IV.7). The curve north-south shows that the three granites outcrops should be connected in the subsurface, figure (IV.7). Because there is no other possibility or other shape can give the same curve correspond to the measured gravity curve, there was a certainty in modeling that the three granites compose a single body (figure IV.7) with a thickness in the range 0.3-1 km.

In other words, to have a better comparison and comprehension between the geological map and the Bouguer anomaly map, we supposed that, three thick plutons were a part (apexes) of a thin batholith lying beneath them; this was confirmed by 1) a large aureole metamorphism (with ≥3km in radius, Cheilletz & Isnard, 1985) which shows that the zone was affected by a large intrusive body, since this aureole illustrates gradational metamorphic loops (consist of cordierite, andalousite, biotite and chlorite schist) including the three granitic outcrops at the centre. As well as, 2) the high restricted anomalies around granitic outcrops and low and wide anomalies overlap the aureole of metamorphism.

Our modeling philosophy has been done to introduce a simple model improved by the fit between calculated and observed data; it is inherently less likely to approximate the true

geological structure in the subsurface. Nevertheless, we admit that it would be possible to obtain equally good fits by respecting the surface data to construct the model of the intrusion. A high-theoretical density contrast was proposed for the host rock based on the reference density of granite measured in the lab (table IV.3), this mathematic processing was obligatory to respect the surface observations and gravity anomalies. 2D modeling cannot eliminate such possibilities, so it is quite possible that the magmatic body is disconnected or connected in such zones. The negative anomaly extends over the metamorphic terrains, suggesting that the pluton gently plunges below the mica schists. The granite appears as a thin sheet with a much broader extension.

The negative gravity anomalies along the fault support the interpretation that this syntectonic pluton is rooted (as a feeder zone for the magma) at the fault and spreads toward the south with a laccolite-like shape. Indeed, if the fault existed at the time of pluton emplacement, as mentioned above, we could say that the geometry of the pluton may have been approximately cylindrical form, large in the northern region and thinner in the south.

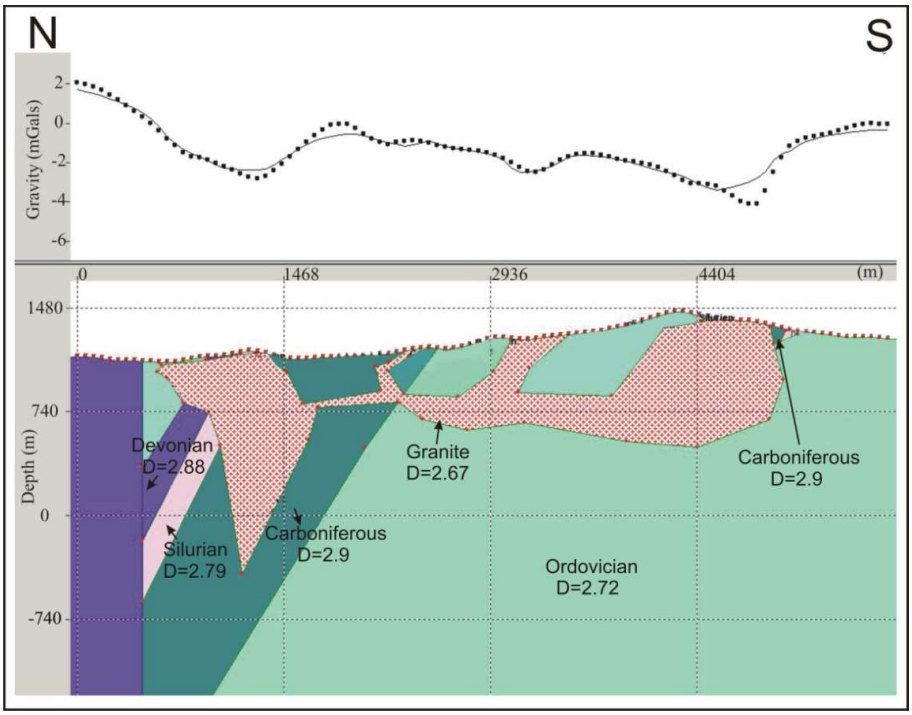

Figure (IV.7): The form of Tighza pluton in 2D made by Geo-soft, theoretical density values and the form of pluton were modified until we obtain the same Bouguer anomalies curves.

During emplacement, we suggest that the hotter, less viscous magma moved upwards to form a batholith in the form of oblate in northern half and spheroid southern part. Assuming that this hemi-spheroid achieved a diameter of 0.5-1 km, equal to the average diameter of the

present Northern division, and its height remained at (the first 0.7 km) depth. However, the limited depth extent of Tighza Granite determined by gravity modeling is 1km in recent day. Given that the Granite is a shallow body, thus the limited depth of Tighza pluton below the ground surface as interpreted from the gravity data is strongly confirmed figures (IV.7).To realize the compatibility between cross sections and the whole gravity data; 3D modeling has been taken as an approach to determine the most realistic geometry of pluton.

3.2.2 3D modeling of granite shape

We used the *3D GeoModeller*, a software which allowed us to integrate available information such as geophysical cross sections and geological knowledge into a 3D geometrical model. The data used to constrain the model were 1) the 10 geological modeled cross sections, 2) the geological map including lithological boundaries and structural data and 4) petrophysical measurement (density).

This software developed at the BRGM (French geological survey; Lajaunie et al., 1997, Calcagno et al., 2002), is especially devoted to geological modeling. In the 3D Geomodeller, interpolation of the available information to the whole 3D space is achieved using implicit surfaces (Lajaunie et al., 1997). The 3D geological space is described through a potential field, in which geological boundaries are iso-potential surfaces, and structural dips correspond to the gradients of the potential.

This formulation further allows a pseudo-geological description of the relationships between geological bodies through a (geological pile) geometric relationships, such as normal sedimentation, unconformity, erosion or intrusion, can be modeled and allow the reproduction of complex geological systems as realistically as possible.

In this software, lithological units are described by a pseudostratigraphic pile, intended to image the geology and structural relationships as best as possible. Compared with the other existing 3D solid modeling approaches (e.g. Boissonnat, 1988; Bertrand et al., 1992), a major original feature of this modeler is that the 3D description of the geological space is achieved through a potential field formulation in which geological boundaries are iso-potential surfaces, and their dips are represented by gradients of the potential.

The advantages follow these methodologies are:

1. Giving the opportunity to construct and image preliminary geometrical models starting from surface geological data including general structural setting of the area, which is established by field mapping and stratigraphic/structural data.

2. A 3D visualisation of geometrical proposal helps one to understand the extension at depth of geological objects and avoid unrealistic interpretations.
3. The definition of the volume of the reconstructed bodies provides a more complete and quantitative evaluation of the geological setting of the area.

From the input data (geological maps and cross sections, structural dips, 2D geological information), a geostatistical interpolation produces a 3D model divided into geometrical bodies representing different lithologies. Structural measurements have been transformed into down-dip plunging lines to be used in the construction of cross-sections. Cross-sections automatically interpolated in 3D GeoModeller contain the topographic profile, its intersection with geological boundaries and structural measurement corrected with apparent dip. These cross-sections have been completed manually taking into account geometrical constraints and using 2D balancing techniques.

In order to compute the 3D gravity contribution of the model, physical parameters (density) can be attributed to each representative lithology. An interactive comparison between modeled and measured potential fields provides a best-fit adjustment of the model geometry. In the next step, integration in 3D produces consistency between all cross-sections and the geological map.

Table (IV.3): measured densities of granite and host rocks.

Geological formations	***Density (kg.m^{-3})***	***Remarks***
Ordovician	*2.72*	*Theoretical value*
Silurian	*2.79*	*Theoretical value*
Devonian	*2.88*	*Theoretical value*
Carboniferous	*2.88*	*Theoretical value*
Granite	*2.67*	*Measured density*

Based on a specific geostatistical interpolation procedure (Lajaunie et al., 1997), the Geological Editor interpolates the local input data to the whole 3D space.Finally, using the densities reported in table (IV.3), the gravity contribution of the resulting 3D model is computed and compared with the Bouguer anomaly.When discrepancies between computed

and observed gravity fields are identified, the geology is locally reinterpreted, the model being interactively adjusted in 3D.

3.3 Model Construction:

A few crustal-scale geological sections have first been drawn. 8.281*8912*2340m^3 3D model of the regional geology of Tighza area was thus interpolated.

The model is built in a geo-referenced system, it takes into account (i) a digital elevation model (DEM), (ii) a simplified geological map (lithological contact information), (iii) dips measured within different units, and (iv) geological cross-sections. As a starting point, we have assumed that the base of pluton is located at 1km as a maximum depth, with a thin flat form. As the high contrast in gravity anomalies is located at the major fault (E-W), figure (IV.5), we supposed that may be explained as a feeder zone and lateral extension of magma in the south direction. As well as, we assume that the intruded body is thick at apexes (Mispikel, Mine and Kaolin granites) and at different positions where the gravity anomaly is high. The initial model was calculated with considering the observed gravity anomalies at surface and cross sections. Based on this consideration, the initial model was subsequently modified until a good fit was obtained. Unfortunately, we didn't have a subsurface data supported or discouraged our initial model.

For that reason, we processed the 3D model of Tighza to propose simple subsurface contacts between formations based on restricted structural field observations (dips of strata, sharp contacts) with a maximum depth 1km. Therefore, the interfaces between metamorphic units were primarily modeled according to the geological map and keeping these interfaces as smooth as possible at depth. Then we have created the body of intruded magma by following the gravity map, figure (IV.5).

Afterward, the geological model is discretised into a 3D matrix of cells or (voxels: are used to characterize a volume element; they are a generalization of the notion of *pixel* that stands for a picture element) in order to produce an initial 'lithology' 3D model. The gravity inversion holds the lithology of voxels at surface fixed throughout the inversion. While, the lithology associated with subsurface voxels is free to vary. The inversion helps to discover variations in the initial model which reproduces a theoritical gravity (gravity tensor) data based on analytical expressions (density contrast between geological units falls off by a square root of distance rule; Plouff, 1976; Okabe, 1979; Holstein, 2003) to compare the gravity field and the corresponding tensor effect of these voxels, (Calcagno et al, 2008).

The geological model will be investigated as an assembly of homogeneous voxels with adjustable density contrast. Direct and inverse modeling can thus generate a very large number of models that will satisfy the observed gravity feild using an iterative procedure. The adopted strategy is to randomly walk around the space of possible models for a given set of a priori information.

Therefore, for a selected voxel that is separated from the boundary of that unit, may be modified. Alternatively, the lithology of a voxel that lies on the interface between two or more units may be modified, and a new physical property may be assigned to that voxel according to a selection from the probability density function (pdf) of the relevant physical property. The voxels to which the latter operation can be applied is restricted by the constraint that the topology of the model not be altered. The change in the misfit between the observed gravity field and tensor components data and the responses calculated for the modified model is determined.

The initial model thus being modified until a good fit between obsereved gravity feild and gravity tensor is obtained. Figure (IV.8) shows the misfit between the measured Bouguer anomaly and the modified priori model of Tighza area. This ensures that 1) all complex 3D effects of the geological bodies are correctly taken into account and 2) the 3D interpolation has not introduced spurious deformations. Our model is valid in the case where the gravity inversion is compatible with the primary model which reproduces the same observed Bougeur anomalies figure (IV8a & b). Although certainly non-unique, the 3D model we propose here has an internal geometrical consistency, and it is compatible with available geophysical data (gravity), and integrates the present-day geological knowledge at a regional scale figure (IV.9).

3.4 Numerical modeling of hydrothermal fluid flow and thermo-chronological constraints around Tighza pluton

3.4.1 Model setup

3D Tighza model has been realized in Comsol Multiphysics based on the geometry obtained by gravity processing (Geomodeller Editor). Firstly, we are going to summarize the numerical procedures to obtain the final model. As mentioned above, all numerical studies simulate the geometry of pluton in 2D only, with simple rectangular or square form, because this allows fluids and thermal streamlines to be more easily recognised with less computational time.

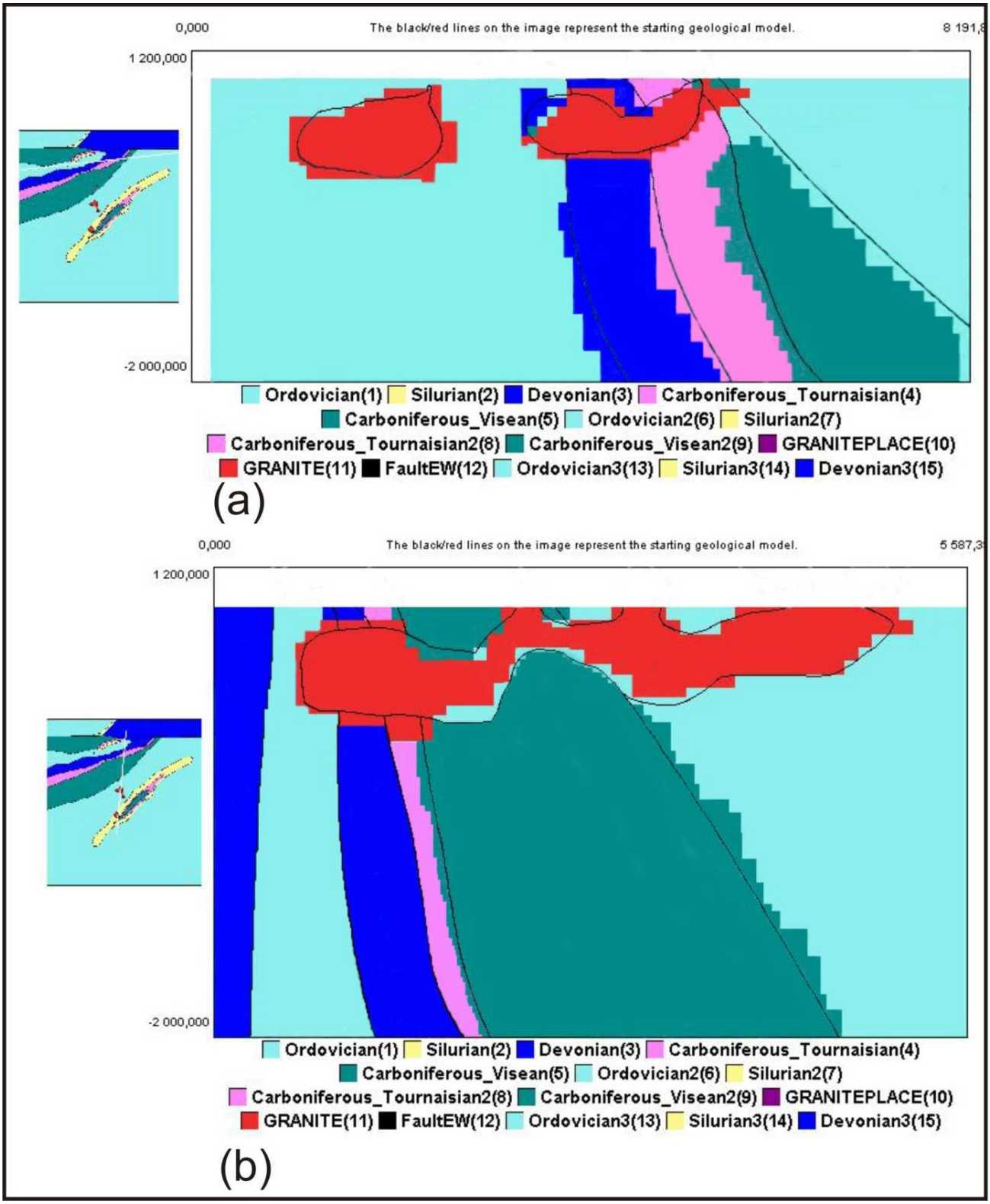

Figure (IV.8): N-S (a) and NE-SW (b) cross sections show the most probable model based on gravity inversion; dark lines represent the starting geological model, note that the primary model is now well-matched with the gravity data measured in the field.

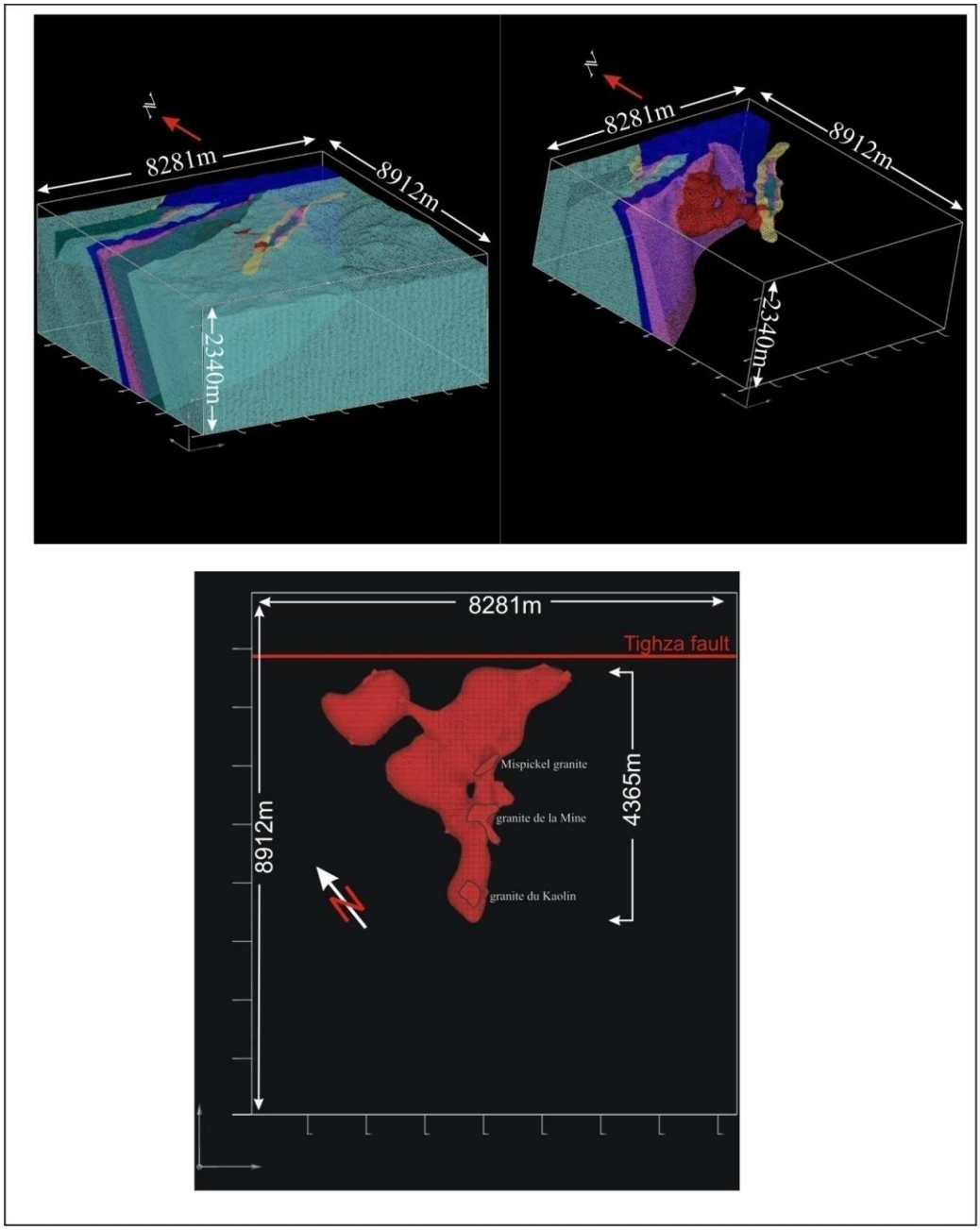

Figure (IV.9): Map view of the final 3D model which represents the most probable model based on available data.

In numerical solutions, the simplicity of geometries which represent heterogeneous materials is necessary for two raisons: 1) the complexity of geometries makes computation time sometimes too long or out of memory capacity. 2) Taking into account the real geometries and stratigraphic heterogeneities around some ore deposits make running a 3D model impossible

in the recent days. Because of these technical problems, the geometry of Tighza pluton was simplified to a box-like shape with dimensions of (4000*1200*500m^3).

The three apexes were presented with unique dimensions (500*500*1000m). No method was available to distinguish the length of eroded part of apexes, therefore an arbitrary length was proposed. The pluton of Tighza was emplaced at 5500m depth based on fluid inclusions analysis done by Nerci, (2006).

Until 7Myr of numerical time, the model deals with granitic shape as a part of host rock, between 7 to 10Myr. The model deals with that part as an intruded felsic magma by changing the physical parameters such as (thermal conductivity, heat capacity and density which are varied continually with temperature). To simulate the complicated fracture system, we have chosen only W1 (cause of its economic importance) as a permeable fracture with a vertical rectangular located next to the middle apex which represents Mine granite. W1 has 200m width, 1000m length and $10^{-16}m^2$ of permeability, we manage W1 to be permeable during all the computational time, figure (IV.10). The variations of physical properties (thermal conductivities, heat capacities, densities and viscosities) of granite and host rock, as well aspermeability and pressure were done based on equations mentioned in chapter 2; intruded magma was simulated to take a place during 3Myr to simulate the emplacement of Tighza pluton. Finally R^2AI was applied to distinguish the probable zone of mineralization during and after emplacement.

3.4.2 Results

Figure (IV.11) shows the history of probable zone of mineralization by applying R^2AI factor during emplacement and cooling phases. 1) The first appearance of probable zone was during the first 0.2Myr. of emplacement, this probable zone located at the bottom of W1, figure (IV.11a). 2) After 0.3Myr of emplacement, the probable zone extend laterally along the board of magmatic body and upward within the permeable zone (W1) figure (IV.11b). 3) The probable zone continues to cover all the board of magmatic body and rises up inside the permeable zone during 1.2 Myr.

4) As the temperature increases, the probable zone extends and covers the top of the middle apex which represents here Mine granite after 1.5Myr.5) At the hottest phase of emplacement, the probable zone covers almost the intruded body and fills up the permeable zone, figure (IV.11e, f and g).

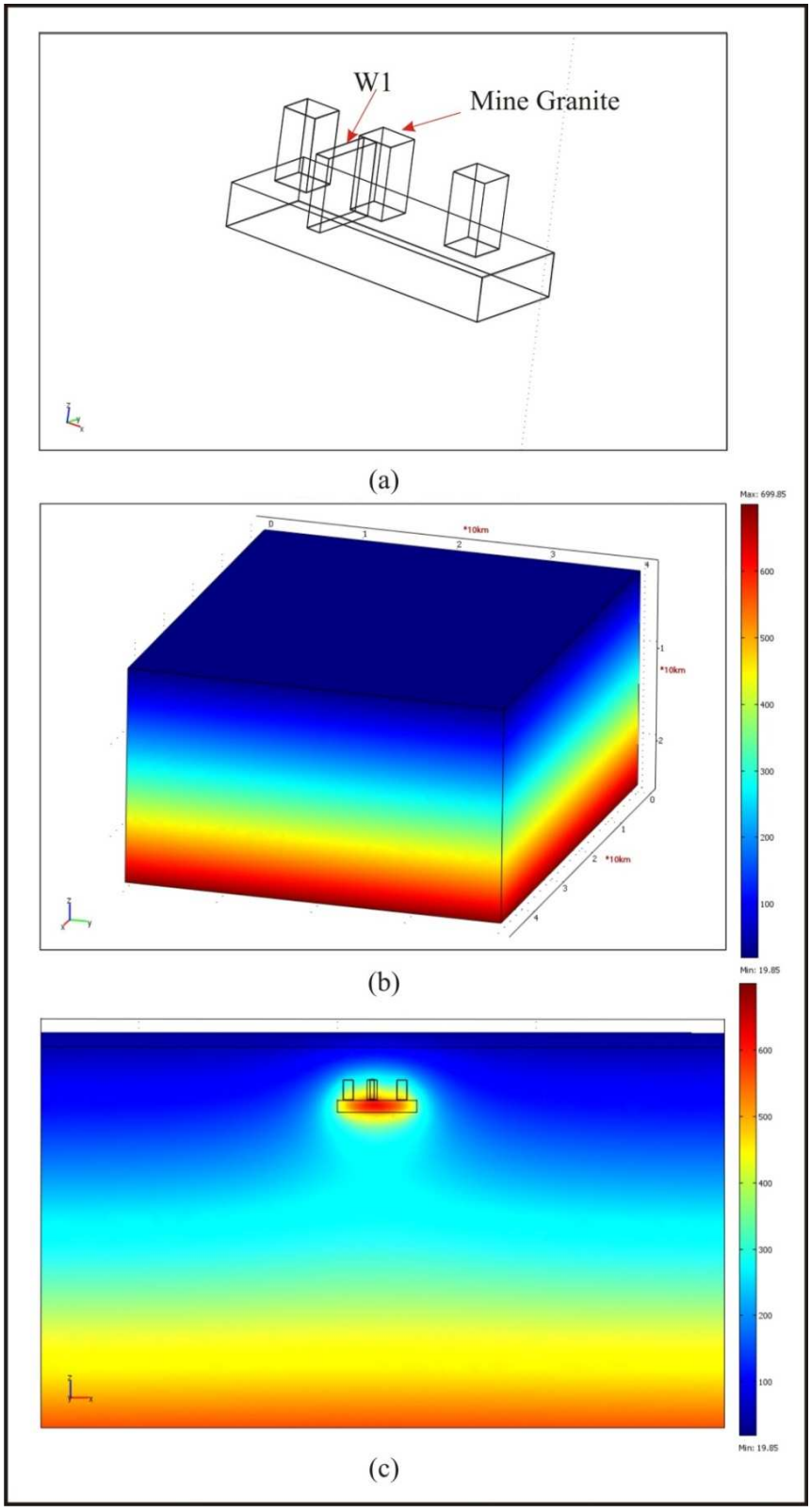

Figure (IV.10): Model setup of Tighza example; a) simplified 3D geometry of Tighza pluton, b) thermal gradient of the whole area as a result of 20Myr of numerical time. c) Slice snapshot of the hottest phase of emplacement (thermal isosurfaces are in (C°)).

6) During the cooling phase, as the temperature decreases within this period, the probable zone is restricted around the apexes and the permeable zone within 0.02Myr, and restricted only in the permeable zone (W1) after 0.06Myr of cooling, figure (IV.11h and i). Pre-main type mineralization appears 3Myr before the hottest phase of emplacement where the pluton produces the maximum heat energy, pre-main mineralization or the favorable physical conditions for mineralization increase with time to cover the entire zone around pluton at the hottest phase. The main type of mineralization appears after the hottest phase but it does not continue for long time (the probable zone disappears after 0.6Myr of cooling. When the pluton is completely cold, the thermal equilibrium returns again as before the emplacement and no favorable physical conditions were noticed within this period. Moreover, we generate a map in which we attempt to produce the recent mineralogical field observation. To obtain the current patterns of Au mineralization, we created a slice parallel to the horizontal plane and take into account the eroded part of Tighza area. Figure (IV.12) shows that the closer numerical map for Au distribution patterns to field observations can be made after 0.03Myr of cooling. It confirms that Au mineralization in W1 was probably formed in the cooling phase as (main type of mineralization).

3.5 Discussion and Conclusion

3.5.1 Time-Lag

The main problem faces us in Tighza area is the *Time-Lag* between pluton and mineralization, where mineralization in W1 and pluton have 291.8 Myr and 286 Myr respectively, with 0.3-0.4 Myr of error average. These absolute ages are based on Ar/Ar dating method on mica samples (Nerci, 2006). Whereas, Cheilletz (1984) has proposed 287.9 Myr for Mine granite, based on K/Ar measurements done by total rock and biotite samples, with 5.1 of error average and 285 Myr with 3.8 Myr as an average error for Au mineralization in W1, with the same dating method applied in mica samples. This uncertainty in ages makes us doubt if Au mineralization is older than Mine granite. In other words, we speculate if the measured ages bring true values for mineralization and granite ages. We are persuaded that the certainty about granite age is higher than those for Au mineralization, since results of Cheilletz (1984) and (Nerci, 2006) for the age of Mine granite are ranging between 287±5.1 and 286±0.4 Myr, thus a magmatic activity has taken a place at that age. As a result, the principal question could be asked here: Is Au mineralization older than Mine granite with an age of 291.8±0.3 Myr or younger with an age of 285±3.8Myr? Based on the numerical results, shallow plutons (less

than 8km depth) are able to create physical conditions to precipitate mineralization during emplacement period (pre-main mineralization).

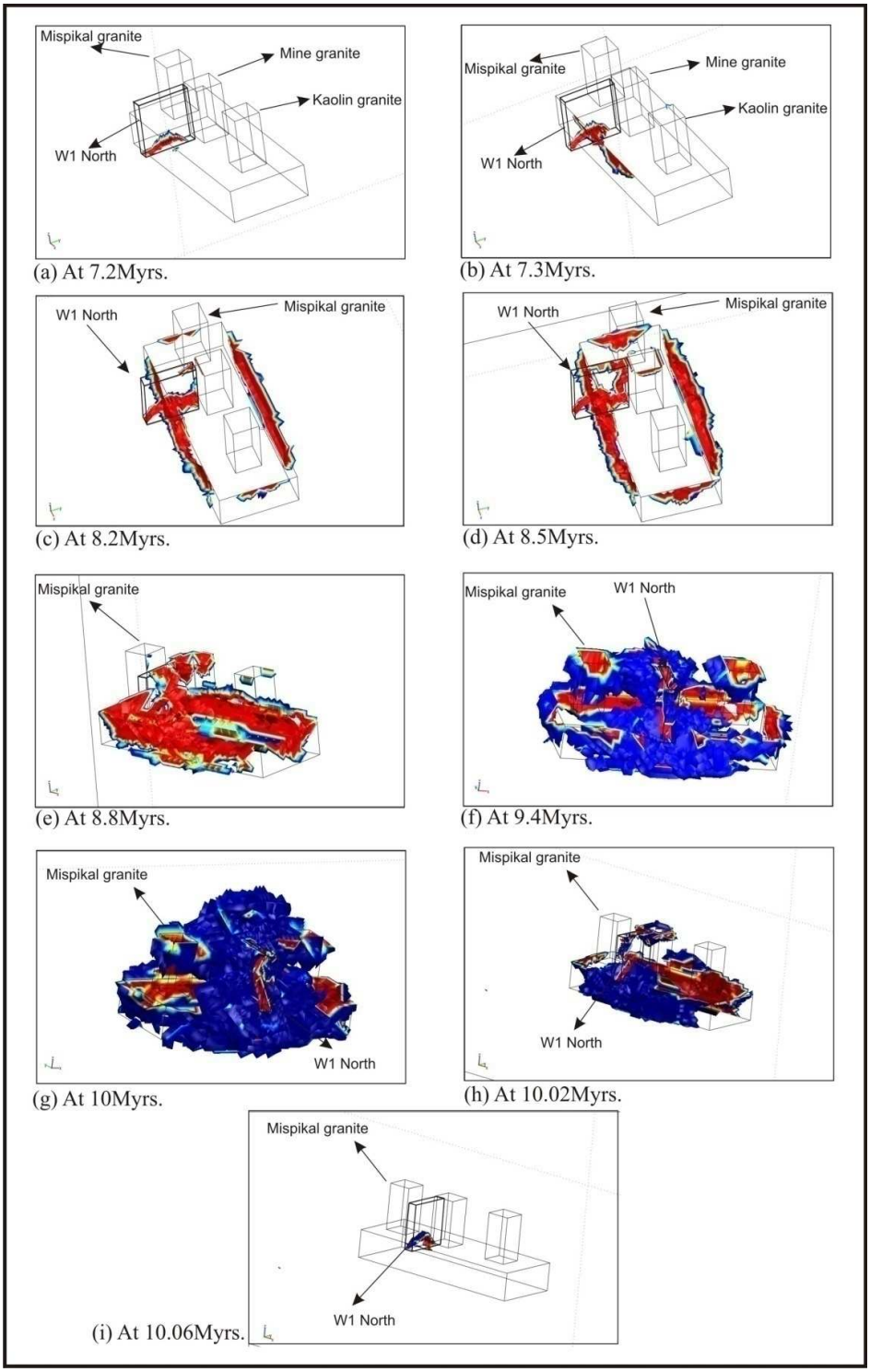

Figure (IV.11): The history of R^2AI during emplacement and cooling phases, the colored range shows the most probable zone close to 1 (red area) and less probable zone (blue area) close to 0, while the white zone reflects 0 value. (see the text for more details).

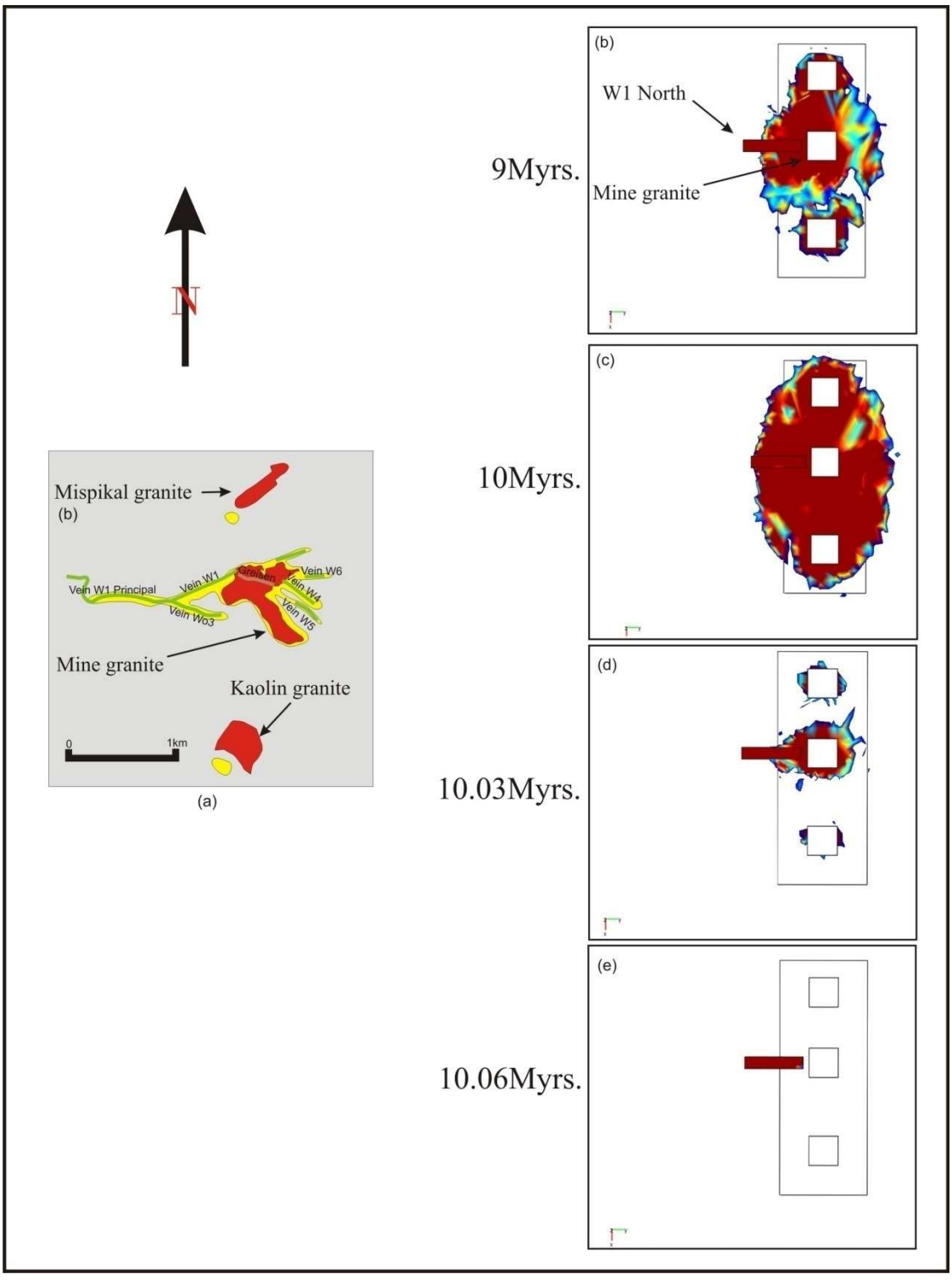

Figure (IV.12): The correlation between numerical map of probable mineralization patterns and the recent field observations: (a) map view of Au mineralization in Tighza area, the red and yellow zones represent the three granitic apexes and Au mineralization patterns respectively, (b) the numerical distribution of probable zone of mineralization during emplacement (1M.y. before the hottest phase), (c) at the hottest phase, (d&e) after 0.03and 0.06Myr of cooling respectively.

These physical conditions could have an age older than the hottest phase of pluton with 3Myrs. During the cooling period of shallow plutons, the lag time between the hottest phase and the complete crystallization of magma appears to be quite small (0.6Myr).

In addition, with the simplified numerical model of Tighza, the probable zone of mineralization could be younger with 0.6 Myr or older with 3 Myr than pluton. To make the physical conditions more specific and useful to explain the chronological problem of Tighza, thermal constraints of absolute age method were added to the model.

One of the most important terms in age dating is the closure temperature. In a cooling system, there is the transition zone from open system (radiogenic isotope diffuses away) to closed system (radiogenic isotope accumulates); this called the closure temperature of a mineral which is the temperature of the system at its apparent age.

3.5.2 Definition of Closure Temperature

When the age of a rock or mineral is calculated from its accumulated products of radioactive decay, whether those products are crystal structural changes caused by fission fragments or radiogenic isotopes such as Ar or Sr, the result ideally represents a point in time at which a completely mobile daughter product became completely immobile. Mobility here means either rapid diffusion from the lattice site at which a radiogenic isotope is formed, or very fast annealing of a disturbed crystal lattice. At one time, it was believed that the change in mobility of a radiogenic isotope could always be identified with either the crystallization of an igneous rock from a melt, or recrystallisation during metamorphism. In recent years, however, it has become increasingly clear that for some methods of age determination, notably the dating of separated minerals by methods such as K/Ar or Ar/Ar, such a simple interpretation is inadequate; radiogenic argon evidently is mobile in some minerals at temperatures well below that of crystallization.

Figure (IV.13) shows how calculated ages related to the true age could be shifted cause of different reasons, at high temperatures the daughter product escapes as fast as it is formed, and so cannot accumulate. At low temperatures its rate of escape is negligible, so that it can accumulate peacefully. There is a continuous transition from one extreme to the other. As well as, the following reasons could shift the calculated age: 1) losing radiogenic argon by a volume diffusion in a thermal perturbation, 2) mixing of two mineralizing phases, 3) increasing the argon quantity by a foreign argon or 4) displacement of argon in the crystal with a partial loss on the edge of the grains (up to 0.2μm). This is very important for small

grains and very fine and low of surface and volume, for more details see (Turner, 1968; Dodson, 1973; Wijbrans & McDougall, 1986; Ruffet et al., 1991; Ganguly & Tirone 1999; McDougall & Harrison 1999; Alexandrov et al., 2002).

As Tighza pluton and mineralization ages were estimated by Ar/Ar method, argon can diffuse and escape from the mineral structure such as muscovite and biotite as mentioned above. Argon diffusion is a function of many parameters; the most important parameter is the temperature.

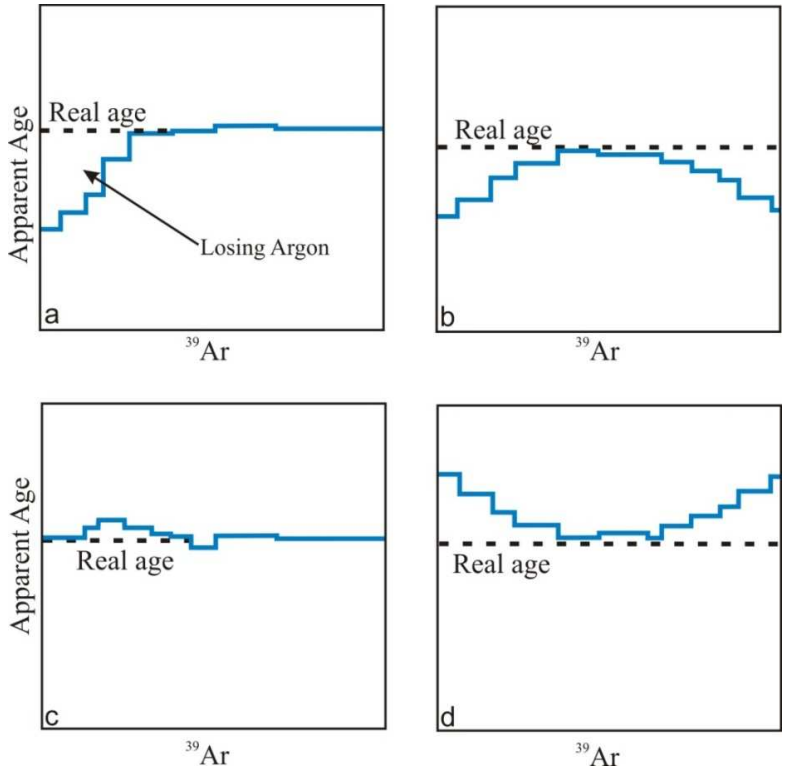

Figure (IV.13): Different theoretical forms of age perturbations; a) losing radiogenic argon cause of thermal diffusion, b) mixing of two mineral phases, c) increasing argon quantity by foreign argon, and d) displacement of argon in the crystal with a partial loss on the edge of the grains (modified after Wijbrans & McDougall, 1986).

Its diffusion also depends on the chemical composition of minerals and the form and size of the crystals. In the case of a granite intrusion or mineralization, there is a gap in time after the crystallization of micas during which the argon is not accumulated yet in crystal structure because the temperature of medium is high. The accumulation of argon in crystal phase will begin less than certain temperature, when diffusion becomes negligible. This phenomenon corresponds to the concept of isotopic closure temperature proposed by Jäger et al. (1967) and Dodson (1973). This concept proposes that during the cooling of a rock there is a time t_1 and

temperature T_1, at which the amount of argon diffusion is high, and a time t_2 and temperature T_2, at which the diffusion becomes small and negligible.

When the crystallization of micas occurs at time t_0 and temperature T_0, then cooling temperatures reached T_1 and T_2 successively and the time exceeded t_1 and t_2, the retention of argon will be partial and also the registration of the age. It appears obviously that if granite is hosted in a cold host rock, the cooling rate will be rapid and the age obtained will be very close to t_0 and the error average will be too small. Conversely, if the host rock is hot, cooling rate could be slow and therefore the obtained age could be substantially younger than t_0. (Dunlap, 1997). Muscovites and biotite form over a range of 600 to 200°C (Hames & Bowring, 1994; McDougall & Harrison, 1999).

However as mentioned above, the closure temperature of muscovites and biotite depends on several parameters and are estimated to be between 450 ±50°C (Villa, 1998) and 350 ±50°C for biotite (Spear, 1993). As we accept the concept of Isotopic Closure Temperature, the ages obtained between granite and mineralizations are less clear than we suppose. Cause of two reasons:

1. The obtained ages at the internal parts of the granite are usually younger than those found on the edges, or external parts.
2. The obtained ages by biotites are generally younger than those obtained by muscovites and show a quite significant gap.

Regardless of the nature of the host rock, magma or hydrothermal system, many cases show age perturbations in intrusion-related ore deposits by the existence of at least two separated ages (Gloaguen, 2006). These disturbance and age anomalies together by the existence of granite with (older or young) mineralization in Tighza area can be explained by two assumptions:

1. Granite has been hosted in a country rock relatively warm inducing a slow cooling from the external to internal parts. We suppose that mineralization (in W1veins) was formed in the external part around granite where the temperature is relatively lower than the temperature in the internal part. Figure (IV.14) shows that the range of closure temperature of muscovite and biotite 350-450°C crosses the permeable zone at the hottest phase of emplacement while the temperature of granitic core is still higher than this average. This average crossed the granite after 0.04Myr, that means the closure

temperature of muscovite and biotite in granite formed after 0.04Myr. Therefore, granite becomes younger than the mineralization.

On one side, the numerical results are consistent with measured age of Tighza pluton and W1 by showing the possibility to form ore deposits at the hottest phase of emplacement where W1 zone is relatively cold comparing to the granite. On the other side, the time-lag calculated in numerical model between the appearance of mineralization in the permeable zone and the solidification of granite is nearly 0.04Myrs. which is not convenient with field results which show a time-lag of 5Myrs . That leads us to the second assumption.

2. As the greisen and W4 represent the extended parts of W1 to form horsetail-like structure (figureIV.3), no one of the authors (Nerci, 2006 ; Cheilletz, 1984) who have measured the age dating of mineralization has measured the age of Au mineralization in the greisen.

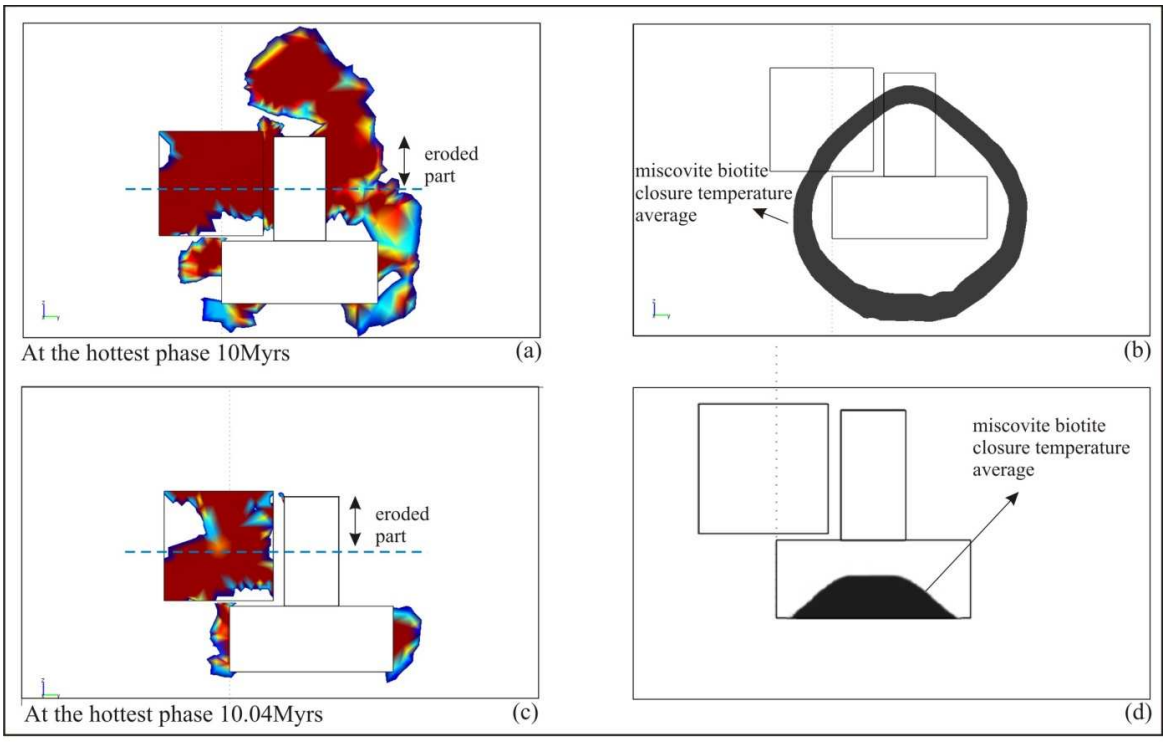

Figure (IV.14): A correlation between the probable zone of mineralization (R^2AI) and biotite-muscovite closure temperatures. The internal zone of the gray circle in (b) is hotter than the average closure temperature of muscovite and biotite.

Nerci (2006) has made mica sampling to determine the age of Au mineralization in (W1 north) far from the granite, while no sampling was done in the greisen or W4.

The sampling method done by Cheilletz (1984) is not detailed enough and we do not know whether the sampling was done within W1 or in greisen.

Thus, we suppose that the age of mineralization in W1 north (291Myrs) is well measured but it is related to a previous magmatic event.

Based on figure (IV.14), the first hypothesis is plausible; if the mineralization is older than granite by as much as hundreds of thousands of year, we suggest that the difference in lag time between natural example and numerical modeling to the numerical simplification where we did not take into account the production of magmatic fluids, the real fracture network of the area and finally the real geometry of pluton. Nevertheless, there is no numerical evidence confirming that the lag time between older mineralization and young granites could be over a 0.1Myrs in case we take into our account the concept of isotopic temperature.

If we suppose that the mica samples which reflect the age 291Myr for Au mineralization measured by Nerci (2006) are related to another magmatic event than Mine granite, the age proposed by Cheillez (1984) for Au deposits (285Myr) which show that the mineralization was formed after Mine granite with more or less 0.5Myr of difference is more likely acceptable and convenient with the numerical results. This conclusion is supported by the following points:

1. The extended part of W1 (Gresien) is cutting Mine granite to confirm that this fracture is younger than the granite and consequently Au deposits must also be younger than granite (figure IV.3).
2. Except the age of Au deposits in W1 north which shows an age of 291Myr, all other measured ages for Au mineralization are around 285Myrs. which make the Au deposits younger than granite.
3. The numerical evidence confirms that the probable zone of mineralization could be created earlier than the hottest phase of parent intrusion with time lag of several millions of years if we take the isotopic closure temperature conditions into account. The maximum time-lag measured between the probable zone at the hottest phase and crystallization of magma is represented here by several thousand of years.
4. The numerical map corresponds to the field observation of Au deposits suggests that Au deposits was formed in the cooling phase of granite with 0.04Myr after the hottest phase, see figure (IV.12).

Finally, with a simple 3D model of Tighza pluton we are allowed to conclude that the argument of different ages between young pluton and surrounded old mineralization to prove that there is no genetic link between them is now disputable.

Moreover, the numerical model offers us a possibility to confirm that a mineralization-linked genetically to granite could take a place before the crystallization of granite parent, but this does not sustain the long time-lag of millions of years between intrusion and mineralization. In contrast, numerical modeling shows that the time-lag between old mineralization and young granite could take place with several thousands of years only.

The most probable hypothesis for Mine granite and related ore deposits in W1 north is that:

W1 is a multi-phased fault, active before the emplacement of Mine granite, therefore, Au mineralization related to 291 Myr in age is related to another magmatic event older than Mine granite. During the emplacement of Mine granite, the granite was crossed by the gresien as it represents the extended part of W1. Consequently, Au mineralization located close to Mine granite reflects an age of 285 Myr and becomes younger than Mine granite.

Chapter (V) General Conclusion

Résumé français du chapitre (V)

Cette étude est consacrée à l'effet physique des intrusions magmatiques en tant que générateur de chaleur capable d'induire la mise en place de larges cellules de convection. Deux principales questions ont été évaluées : l'intrusion est elle à elle seule capable de créer des conditions advectives favorables à la formation d'une minéralisation ? Si, oui, quelles sont les contraintes temporelles depuis l'emplacement du magma jusqu'à la précipitation des minéraux utiles ?

Ci-dessous sont résumés, les principaux résultats basés sur une approche numérique ainsi que sur l'étude d'un cas naturel spécifique :

1. Modélisation numérique couplée hydro-thermale et probabilité de minéralisation : nouveaux apports.

De nouveaux modèles numériques de circulations de fluides autour de plutons ont été réalisés dans cette étude. Cette modélisation par éléments finis couple les équations de transfert de la chaleur à la loi de Darcy par un jeu de grandeurs et paramètres physiques entièrement interdépendants. Cependant, afin de bien résoudre les questions liées à l'hydrodynamisme de tels systèmes, ces modèles restent simples et axés sur la seule physique des écoulements : les fluides multiphasés, la diffusion chimique, la topographie et la production de fluides par les magmas ne sont pas simulés.

Les innovations principales sont les suivantes : i) la perméabilité varie de façon continue avec la profondeur suivant une loi puissance. Aucune discrétisation n'a donc été nécessaire ; ii) les modèles sont transitoires et permettent un pas de temps précis ainsi que l'étude du flux de fluide pendant la mise en place de l'intrusion, et pas seulement pendant la phase de refroidissement ; iii) les simulations mettent un jeu de grands plutons mis en place dans une section de croûte continentale atteignant la profondeur de 24 km. Ceci permet d'explorer des plutons asymétriques ainsi que la zone sous l'intrusion ; iv) A notre connaissance, pour la première fois dans ce type de modélisation péri-plutonique, des modèles 3D ont été calculés avec succès aboutissant à des résultats importants ; v) un nouvel indice de probabilité de minéralisation a été défini (R^2AI) ; il apparaît extrêmement fiable lorsque des comparaisons sont faites avec des gisements naturels.

2. Le rôle de la profondeur d'emplacement du pluton.

La perméabilité des roches encaissantes est liée dans les modèles étudiés à la profondeur. La profondeur d'emplacement du pluton joue donc un rôle fondamental en modifiant fortement l'hydrodynamique classique à deux cellules de convection connues pour les plutons supra-crustaux depuis les études pionnières sur ce sujet.

Les plutons mis en place à une profondeur supérieure à 10 km n'induisent pas d'advection significative, le transfert de chaleur est exclusivement conductif. Ceci est cohérent avec le peu d'altération hydrothermale observée autour de plutons mis en place à la limite ductile fragile de la croûte continentale.

Pour des profondeurs d'emplacement inférieures à 4.5 km, le seuil de perméabilité de 10^{-16} m^2 est atteint et des cellules de convection de second ordre induisent des zones de décharge supplémentaires propices au dépôt de phases minérales. Autour de ces plutons peu profonds, d'importantes augmentations des vitesses sont reconnues (deux ordres de grandeur).

Il apparaît également que la zone sous jacente au pluton est peu favorable, ce qui est cohérent avec le peu de gisements de ce type localisés en base d'intrusion.

3. Les effets de la géométrie du pluton et des apex.

Pour des volumes équivalents de magma, les formes de pluton tabulaires (laccolithe) engendrent des zones de forte probabilité de minéralisation bien plus étendues que celles induites par d'autres géométries de pluton. Cette zone favorable occupe une large surface dans les roches encaissantes au-dessus du laccolithe. Les apex de faible hauteur de pluton mis en place profondément jusqu'à 8 km n'engendrent aucun effet sur l'hydrodynamique autour du corps magmatique.

Par contre, des apex très longs, qui atteignent des zones au dessus du seuil de perméabilité, provoquent des changements importants dans la circulation des fluides. Ces grands apex, similaires aux intrusions de type porphyres, re-localisent et focalisent les cellules de convections autour d'eux plutôt qu'autour du pluton parent principal. Ce point doit avoir des conséquences importantes dans la genèse des porphyres cuprifères.

4. Le rôle des zones de haute perméabilité : les auréoles fracturées et les failles.

A l'inverse des apex courts, les auréoles thermiques fracturées jouent un rôle important sur la distribution des zones favorables de minéralisation autour des plutons intermédiaires à profonds.

Ces auréoles fracturées restreignent et localisent fortement le flux des fluides et les zones favorables aux bordures et surtout aux coins des intrusions. Il est remarquable que pour les cas naturels de gisements d'or associés à des granites, ces « coins » de pluton sont effectivement riches en minéralisation. Les détachements extensifs synchrones de la mise en place d'un pluton (cas classique dans les « metamorphic core complexes » pendant l'extension post orogénique) sont capables de changer drastiquement la distribution des fluides autour du pluton. Ces failles plates sont très « efficaces » pour pomper les fluides mis en mouvement par convection thermique et localiser des zones probables de minéralisation. C'est une différence importante avec les failles à fort pendage.

5. La thermo-chronologie et le lien génétique de l'intrusif dans le processus de minéralisation.

Tout d'abord, pour de grands pluton souvent mis en place par injections successives depuis les zones d'alimentation, la phase de refroidissement n'est pas la phase de convection maximale des fluides de l'encaissant. L'advection de chaleur et les zones les plus probables de minéralisation peuvent se mettre en place légèrement avant ou pendant la phase de température maximum dans le pluton (i.e. avant que le magma ne cristallise complètement).

De plus, pour des intrusions de la croûte supérieure, les conditions physiques favorables pour une précipitation minérale se réalisent pendant un court laps de temps encadrant la phase de température maximale du pluton. C'est pourquoi nous pensons que, malgré le manque d'arguments chimiques (e.g. haute salinité dans les inclusions fluides), les gisements aurifères associés à des granites peuvent s'expliquer d'un point de vue hydrodynamique par les seules convections hydrothermales induites lors de la mise en place du magma granitique. Dans ce cas le granite a bien un rôle génétique, sa chimie (granite de type réduit souvent) pouvant éventuellement contribuer à fournir les éléments utiles. Cependant, le volume d'encaissant lessivé par les fluides convectifs est tel que (importante altération hydrothermale, métasomatose…) pour certaines concentrations minérales peri-granitiques (e.g. Pb, Zn), la contribution de l'intrusif pourrait se réduire uniquement à son rôle thermique (déclenchement des cellules hydrothermales).

6. Un cas naturel spécifique : le système W-Au associé au granite de Tighza (Maroc central)

Le pluton de Tighza offre un vrai défi pour améliorer la compréhension du rapport entre l'intrusion et la minéralisation aurifère. Précédemment, des études détaillées ont été faites au

sujet de la minéralisation de Tighza pour obtenir le grade de docteur (Cheilletz, 1984; Nerci, 2006). Cheilletz (1984) a proposé un âge pour le granite de la mine (286 Ma) et pour la minéralisation aurifère (285 Ma). Par contre, Nerci (2006) a proposé un âge de 291 Ma pour la minéralisation aurifère dans le filon W1 nord et 286 Ma pour le granite de la mine.

Nous présentons une nouvelle méthode pour interpréter le rapport spatial et le lien génétique (donc temporel) entre l'activité magmatique et la minéralisation aurifère, ainsi que, l'âge problématique obtenu pour la minéralisation aurifère du filon W1.

A partir de mesures de gravité, la forme 3D de l'intrusion de Tighza a été établie. Les architectures simplifiées 3D du pluton, et du filon W1, interprété comme une zone perméable, ont été alors injectées dans la modélisation couplée numérique 3D définie au chapitres précédents. Cette approche nous permet de comparer, explorer et discuter : i) la distribution de la minéralisation aurifère à Tighza; ii) la relation thermo-chronologique, et par conséquent, le lien génétique entre l'intrusion et la minéralisation aurifère.

Du fait de l'intégration d'une géométrie 3D complexe, le modèle de Tighza obtenu devient plus réaliste même s'il est simplifié en comparant au contexte géologique réel. Bien que beaucoup de paramètres n'ont pas été pris en compte, telle que la réaction chimique, la production des fluides magmatiques, ce modèle donne un nouvel éclairage sur les concepts des intrusions à enveloppes de minéralisation.

L'apparition d'une zone probable de minéralisation au début de la mise en place prouve que les conditions physiques favorables sont disponibles avant la phase la plus chaude ou avant son refroidissement pour former des gisements. En effet, le filon W1 représente la zone la plus probable pour la minéralisation, là où la perméabilité est relativement élevée; c'est donc une zone favorable pour que les fluides circulent plus rapidement depuis la proximité du corps magmatique jusqu'aux zones froides où ils perdent leur température et leur vitesse, favorisant ainsi la précipitation de minéraux. Pour cette raison, W1 devient la zone la plus probable pour la minéralisation au début de la mise en place. Cette zone s'étend pour couvrir la totalité de la zone autour du granite à la phase la plus chaude de la mise en place.

La perturbation thermique diminue immédiatement pendant la cristallisation du corps magmatique après 0.6 Ma. L'application des contraintes thermiques liée à la température de fermeture isotopique avec le R^2AI montre la possibilité de créer des conditions physiques favorables pour le dépôt d'une minéralisation plus jeune que l'âge de refroidissement du granite parent. Cependant, les expériences numériques montrent que, pour un même minéral,

les âges de refroidissement (i.e fermeture isotopique) de la minéralisation et du granite ne peuvent être séparés de plus de quelques centaines de milliers d'années. Par conséquent, la datation obtenue pour la minéralisation dans le filon W1 nord (291Ma) correspond à un évènement hydrothermal antérieur, sans connexion avec l'hydrothermalisme induit par le granite de Tighza (286Ma).

Ainsi, ces résultats numériques sont cohérents avec les âges obtenus par Cheilletz (1984) et Nerci (2006) pour la minéralisation W-Au (285 Ma), c'est-à-dire très proches de celui du granite (286 Ma). Ces résultats sont compatibles aux évaluations de Cathles (1981b) qui estime la vie maximum d'un système hydrothermal « efficace » (au sens minéralisant) dû à une intrusion à 800.000 ans, en conditions optimales.

The hydrothermal mineralization is a subject to debate in numerous cases where mineral deposits are spatially related to magmatic intrusions. In most of cases, the question is about the role of intrusion: what is the exact contribution of the intrusion on ore deposition? Rheological, structural, Thermal, and/or Chemical? Coupled with dating consideration, the balance between these contributions defines the degree of genetic link of the intrusion within the ore forming process. As mentioned in Chapter I, intrusion-related ore deposits constitutes our main source of Cu, Mo, Sn, W, and Bi, and a significant source of Au, Ag, Fe, Pb, and Zn. Styles of mineralization vary from vein, skarn, and greisen to porphyry type. Deciphering between physical and chemical contributions of the intrusion is then interesting for exploration strategy. Models of the genesis of these types of deposits have evolved significantly over time, from early days when the intrusions were regarded as the source of all components of the ore deposits (i.e. strong genetic link), to a time when most researchers regarded the intrusions only as heat sources (i.e. subtle genetic link), driving large convection cells of metamorphic and/or meteoric waters which leached metals out of the surrounding country rocks.

Finally, in some case, the intrusion is only spatially associated with ore deposits, the magmatic body being reduced to play the role of a structural or rheological trap (i.e. no genetic link). In contrast, in Cu-Mo porphyries and polymetallic skarns, fluid inclusions, mineralogy and/or stable isotope studies provide very strong chemical arguments for a genetic link between the intrusion and ore deposits. Indeed, high salinities measured within mineralizing fluid suggest an important contribution of magmatic waters expelled from the parent intrusion. On the contrary, granite related gold deposits present a very subtle link with no clear evidence of a magmatic contribution in the ore forming process. This thesis focused on the question of physical effects of intrusion in ore genesis as a heat source driving convection cells. Two main questions were evaluated:

Is the intrusion able to create alone, favorable physical conditions for ore formation? If yes, what are the chronological constraints between intrusion emplacement and ore formation?

To answer the questions, the results of numerical modeling supported by natural cases have been summarized.

1. Hydro-thermal numerical modeling and ore deposition probability (new insights)

A new fully coupled hydro-thermal modeling has been developed during this study. The modeling procedures have been benchmarked by published models. Our models are simple

physical models which do not simulate i) multiphased fluid productions; ii) chemical diffusion, iii) topography, iv) input of meteoric and magmatic waters. Nevertheless, the main innovations are: i) the permeability of host rocks has been varied continuously with depth with no need of discretization; ii) the models are transient for a precise time stepping, taking into account the warming phase (i.e. emplacement of magma) as well as the cooling phase; iii) models represent large plutons intrud within a thick section of the continental crust (24 km depth). This allows exploring asymmetric plutons with apexes and/or associated faults. Hence, fluid flow patterns beneath the pluton are also explored; iv) 3D hydro-thermal modeling of complex pluton architecture associated with fault has been successfully realized and has led to important results; v) a Restricted Rock Alteration Index (R^2AI) has been defined to evaluate the physical probability of mineral precipitation. This index appears to be powerful indicator when a comparison with well-constrained natural cases is made.

2. The role of emplacement depth of pluton

As previously shown for upper crustal plutons in pioneering works, the emplacement of magma creates a thermal perturbation within the surrounding rocks triggering an effective zone of advection. Two convective cells are created above simple intrusion geometry; the cell in the left side is anticlockwise, while the cell in the right side is clockwise. However, fluid circulation and mineralization patterns are strongly dependent of the emplacement depth of pluton (as depth and permeability are related by a power law). Deep seated plutons emplaced below 10 km and not connected to high permeability zones do not induce advective heat dissipation. This was confirmed by Peclet number distribution which is coherent with absence of convective cells and decrease in fluid velocities. This is also coherent with the weak hydrothermal alteration observed around the deep seated plutons (e.g. Annen et al, 2006). Above 4.5 km, the permeability threshold of 10^{-16} m^2 is reached and second order convection cells may create additional convection cells which triggers supplementary focused discharge zones where mineralization are expected. Around shallow plutons significant increase in fluid velocity were also identified (from 10^{-10} to$10^{-8}$$m.s^{-1}$). Another important result is that, for all emplacement depth, the pluton floor zone seems to be not favorable for mineral deposition. Based on our knowledge, intrusion related ore deposits flanking the floor zone of the co-genetic intrusion are not reported.

3. Effects of pluton geometry and apexes

For equivalent magma volume, the tabular-like form (i.e. laccolith) is a convenient shape to produce a favorable mineralized zone larger than those produced by other forms (figure III.15), because it covers a wide horizontal area in the host rock above the pluton.

No significant role was remarked for small apexes of deep or intermediate intrusions where the permeability of host rock is too low. However, a long apex that reaches shallow zones where permeability is greater than $10^{-16}m^2$ creates a dramatic change in distribution of probable zone of mineralization. In that case, the apexes strongly modified the fluid flow pattern by focusing convective fluids and mineralization zones around them. Apexes are then able to relocate the convective cells and discharge zones along them rather than around the main magma body. This result suggests that, although porphyry deposits record important magmatic waters inputs, the relocation of convective fluids along the apical intrusion (i.e. the porphyry), may play an important role (see example of the Cu-Au Grasberg, figure III.14a). This is particularly valid to explain fluid mixing observed in some cases or at some stage of the paragenetic succession.

4. The role of high permeability zones: fractured thermal aureoles and faults

Due to volume forces and fluid overpressure (expelled from crystallizing magma), thermal aureoles around intrusions are often fractured, acting as high permeability zones. In contrast with apexes, fractured aureoles play significant role in distribution of favorable zone of mineralization around deep and intermediate intrusions. They are able to restrict and localized fluid flow, discharge zones and favorable mineralized zones, very close to the pluton border and edges. This is in agreement with the location of deep intrusion related gold deposits with or without apex [e.g. the Bruès gold deposit at the upper north corner of Boborás pluton figure (III.13a), Galicia, Spain; the Scheelite dome gold deposit figure (III.13b), Yukon, Canada].

Extensional detachments faults are able to delocalize and strongly modify classical fluid flow patterns induced by coeval intrusion. Indeed, the probability of potential zone of mineralization around intrusion was removed from the zone around pluton and restricted within the fault. A very good agreement was found with the Crocetta deposit in Elba, Italy (figure (III.14b). Elba central detachment fault is a very efficient advective drain. It is able to pump fluids from deep zones and makes them circulate along the horizontal branch of the pluton-induced convection cells. Extensional systems do not required lithostatic fluid overpressure to develop dilatant sites susceptible to drain and/or to trap mineralization. In that

sense, it is surprising that very few ore deposits are recognized in context of detachment faults associated to metamorphic core. This constitutes an important difference with high angle dip fault.

5. Time evolution and the genetic link of intrusion in the ore deposition

The cooling phase is not the main phase of convection for large pluton often associated with long-lived magma emplacement. Major advective heat dissipation and mineral deposition zone may also occur sometime before and during the hottest phase of emplacement (before magma crystallizes). This is an important clue to interpret dating (emplacement and cooling age) of thermal aureole and intrusion-related ore deposits.

We conclude that, even if chemical arguments are absent, fluid circulation induced by granite emplacement plays a key role in the genesis of granite-related Au deposits. Then, the role of intrusion appears to be clearly genetic for this kind of ore deposits, and mineralization might be nearly coeval with the hottest phase of intrusion.

Finally, the pure physical indicator (R^2AI) reproduces accurately in time and space the location of intrusion related deposits of natural resources, for different natural examples. That means that convection of metamorphic and/or meteoric fluids induced by the intrusion appears to be a major physical key to explain the spatial distribution of ore around a magmatic body. Input of magmatic fluids within such localized convective systems might only contribute to the chemistry of the ore forming process.

6. The natural case: granite-related W-Au deposits (Tighza-Morocco)

This example has been specifically studied during this work. In the Tighza area, the thermal perturbation, which triggered an important hydrothermal alteration and ore deposit, comes from a hot intruded body (286 Myr). The thermal aureole is well-developed, absolute dating and metallogeny data are well-constrained, and the complex morphology of the pluton is attested by the occurrence of three main apexes spatially associated to W-Au mineralization. In the first step, based on a detailed gravimetric study in the field, density measurements, cartography and structural analysis, the complex 3D shape of the intrusion has been characterized with a good approximation. The 3D model has been realized following the inversion procedure of the Bouguer anomaly constrained by geological cross-sections. The resulting architecture corresponds to a flat lying intrusion with three main apexes and at least two roots (i.e. feeder zones). The pluton was limited to the north by the main Tighza fault. In the second time, the coupled hydro-thermal modeling procedure, defined above, has been

applied to a simplified 3D model of the Tighza area (including pluton geometry and mineralized fracture "W1"). The emplacement depth of the intrusion has been evaluated by fluid inclusion data from previous studies. The experiments show that, during the incipient emplacement of magma, the fracture W1 represents the most probable zone for mineralization. This zone extends to cover the entire zone around granite at the hottest phase of emplacement. The thermal perturbation decreases rapidly during crystallization of intruded body after 0.6Myr. Tentative correlation between the model and absolute dating available for Tighza deposit has been realized, accounting for closure temperature of isotopic systems. The convergence between isotopic closure temperature and R^2AI is confirmed by the appearance of favorable physical conditions and the average of isotopic closure temperature in W1 around the hottest phase, and before magma crystallizes (figure IV.14). However, after the hottest phase, the time-lag to close the isotopic system within the granite couldn't be longer than 0.1Myr. Therefore, the age of (291Myr) measured in W1 north (Nerci, 2006) does not date the hydrothermal event coeval to the Tighza pluton. It might be linked to a previous hydrothermal event. Related to the age of the intrusion (286 Myrs), these numerical results are in agreement with other ages measured by Cheilletz (1984) and Nerci (2006) for the W-Au mineralization (285 Myr).

7. Future work

Although, the results presented in this thesis provide significant new insights into magma emplacement and related hydrothermal circulations. In particular, the effects of magma emplacement and the variation of different thermal and physical parameters in hydrothermal circulation and consequently ore formation.

The potential exists for further works: 1) the geochemistry has to be incorporated in the coupled modeling through the chemical diffusion equation. 2) the magmatic fluid production at the end of magma crystallization, the chemical reaction at the rock wall between host rock and magmatic elements could bring new insights for this type of geo-systems. 3) Creating a realistic mechanical system able to form inhomogeneous and deformed temporal permeability is also important for more realistic model. Based on these parameters with a realistic geometry of pluton, we can be more specific and simulate more complicated examples for more deep exploration method.

References

A

Agard J., Balcon J.M. & Morin P. 1958 Etude géologique et métallogénique de la région minéralisée du Jbel Aouam (Maroc central) : Notes et Mém. Serv. Géol. Maroc, 126-132.

Agard J., Morin P. & Termier H. 1955 Esquisse d'une histoire géologique de la région de Mrirt (Maroc central) Notes et Mém. Serv. Géol. Maroc, T. 12, p. 15-28.

Alderton D.H.M. 1978 Fluid inclusion data for lead-zinc ores from south-west England. Trans. Instn. Min. Metall. (sec. B: Appl. Earth Sci.), 87, B132-5.

Alduncin, G. 1993. Primal and mixed upwind finite element approximations of control advection-diffusion problems, Computational Mechanics. 11, 93-106.

Aleva G.J.J. & Dijkstra S. 1986 Host rock lithology as principal criterion for an ITC-adopted classification of mineral deposits. ITC J. 3, 243-47.

Alexandrov P. Ruffet G. & Cheilletz A. 2002 Muscovite recrystallization and saddle-shaped 40Ar/39Ar age spectra: example from the Blond granite (Massif Central, France), Geoch. et Cosmoch. 66. 1793-1807.

Annels A.E. & Roberts D.E. 1989 Turbidite-hosted gold mineralization at the Dolaucothi Gold Mines, Dyfed, Wales, United Kingdom. Econo. Geol., 85, 293-314

Annen, C., Scaillet, B., Sparks, S.J., 2006. Thermal constraints on the emplacement rate of a large intrusive complex: the Manaslu Leucogranite, Nepal Himalaya. Journal of Petrology. 47, 71-95.

Arboleya M.L., Teixell A., Charroud M. & Julivert M. 2004 Astructural transect through the High and Middle Atlas of Morocco J. Afr. Earth Sci. 39, 319-327.

Arndt, N.T., Lesher, C.M., Czamanske, G.K., 2005. Mantle-derived magmas and magmatic Ni–Cu– (PGE) deposits. Economic Geology. 100th Anniversary Volume, 5–24.

B

Baker, T., Lang, J.R., 2001. Fluid inclusion characteristics of intrusion-related gold mineralization, Tombstone-Tungsten magmatic belt, Yukon territory, Canada. Mineralium Deposita. 36, 563-582.

Barrie C.T., Cathles L.M., Erendi A., Schwaiger H. & Murray C. 1999 Heat and fluid flow in volcanic-associated massive sulphide forming hydrothermal systems. Econo. Geol. 8, 201–220.

Beaudoin G., Therrien R. & Savard C. 2006 3D numerical modelling of fluid flow in the Val-d'Or orogenic gold district: major crustal shear zones drain fluids from overpressured vein fields. Mineralium Deposita 41. 82-98.

Benn K., Horne R. J., Kontak D. J., Pignotta G. & Evans N. G. 1997 Syn-Acadian emplacement model for the South Mountain Batholith, Meguma Terrane, Nova Scotia: Magnetic fabric and structural analyses, Geol. Soc. Am. Bull., 109, 1279– 1293.

Benn, K., N. M. Ham, G. S. Pignotta, and W. Bleeker 1998 Emplacement and deformation of granites during transpression: Magnetic fabrics of the Archean Sparrow pluton, Slave Province, Canada, J. Struct. Geol. 20, 1247–1259.

Bennasser M. 1996 Lithostratigraphie, tectonique Hercynienne, paléochamps de contraintes tardi-hercyniennes et relation fracturation-minéralisation de la région de l'Aouam (Maroc central oriental). Thèse de 3ème cycle, Univ. Mohamed V Fac. Sc. Rabat 300p.

Berger B.R. & Henley R.W. 1989 Recent advances in the understanding of epithermal gold-silver deposits-with special reference to the western United States. Econo. Geol. Monoger. 6, 405-23.

Berger B.R. & Bagby W.C. 1991 The geology and origin of Carlin-type gold deposits. In Foster R.P. (ed.), Gold Metallogeny and Exploration, 210-48. Blackie, Glasgow.

Bertrand P., Dufour J.F., Françon J. & Lienhardt P. 1992 Modélisation volumique à base topologique. Hermès, Paris. 1. 59–74.

Bergbauer S., Martel S. & Hieronymus C. 1998 Thermal stress evolution in cooling pluton environments of different geometries. Geophys. Res. Let. 25, No. 5. 707-710.

Best M.G. 2001 Igneous Petrology. Blackwell Science Inc., Malden. 458.

Boissonnat J.D., 1988 Shape reconstruction from planar crosssections. CVGIP. Graphical Models and Image Processing 44. 1–29.

Bouabdelli M. 1989 Tectonique et sédimentation dans un bassin orogénique : Le sillon viséen d'Azrou-Khénifra (Est du massif hercynien central du Maroc). Thèse 3ème cycle, Univ. Strasbourg, Fac. Sci., 262p.

Bouchez, J. L. & G. Gleizes 1995 Two-stage deformation of the Mont-Louis –Andorra granite pluton (Variscan Pyrenees) inferred from magnetic susceptibility anisotropy, J. Geol. Soc. London, 152, 669 – 679.

Bouillin, J.P., Bouchez, J.L., Lespinasse, P. Pêcher, A., 1993. Granite emplacement in an extensional setting: an AMS study of the magmatic structures of Monte Capanne (Elba, Italy). Earth and Planetary Science Letters. 118, 263-279.

Bowman J.R., Parry W.T., Kropp W.P. & Kruer S.A. 1987 Chemical and isotopic evolution of hydrothermal solutions at Bingham, Utah. Econo. Geol. 82. 395-428.

Brimhall G.H. 1979 Lithologic determination of mass transfer mechanisms of multiple-stage porphyry copper mineralization at Butte, Montana: vein formation by hypogene leaching and enrichment of potassium-silicate protore. Econo. Geol., 74, 235-321.

Brimhall G.H. & Crerar D.A. 1987 Ore fluids: magmatic to supergene. Rev. Mineral, 17, 235-321.

C

Calcagno P., Martelet G. & Gumiaux, C., 2002. Apport de la modélisation géométrique 3D à l'interprétation géologique du complexe de Champtoceaux (massif armoricain). 19ème RST, Nantes. 79.

Calcagno P., Chilès J.P., Courrioux G. & Guillen A. 2008 Geological modeling from field data and geological knowledge Part I. Modelling method coupling 3D potential-field interpolation and geological rules. Physics of the Earth and Planetary Interiors. 171. 147-157.

Cameron E.M. & Hattori K. 1987 Archean gold mineralization and oxidized hydrothermal fluids. Econo. Geol., 82. 77-91.

Candela P.A. & Holland H.D. 1986 A mass transfer model for copper and molybdenum in magmatic hydrothermal systems: the origin of porphyry-type ore deposits. Econo. Geol. 81. No.1, 1-19.

Carten R.B. 1986 Sodium-calcium metasomatism: chemical, temporal and spatial relationships at the Yerington, Nevada, porphyry copper deposit. Econo. Geol. 81. 1495-1519.

Carten R.B., Walker B.M., Geraghty E.P. & Gunow A.J. 1988 Comparison of field-based studies of the Henderson porphyry molybdenum deposits, Colorado, with experimental and theoretical models of porphyry systems. In Taylor R.P. & Strong D.F. (eds), Recent Advances in the geology of Granite-related Mineral Deposits, 351-66, Spec. Vol.39, Can. Inst. Min. Metall., Montréal.

Castorina F. & Masi U. 2000 Sr-isotopic composition of siderite for assessing the origin of mineralizing fluids: the case study from Jebel Awam deposit (Central Morocco). Ore Geology Reviews, 17:83-89.

Castro A. 1986 Structural pattern and ascent model in the Central Extremadura Batholith, Hercynian Belt, Spain, J. Struc. Geol. 8. 633– 645.

Cathelineau M. 1982 Signification de la fluorine dans les gisements d'uranium de la chaine hercynienne. Bull. Bur. Rech. Geol. Mini. Sect. 2, 4, 407-13.

Cathles L.M. 1977 An analysis of the cooling of intrusives by Ground-Water convection which including boiling. Econo. Geol. 77. 804-826.

Cathles, L.M., 1981, Fluid flow and genesis of hydrothermal ore deposits. Economic Geology. 75, 424-457.

Cerny P., Blevin P., Cuney M. & London, D. 2005 Granite related ore deposits. Soc. Of Econ. Geol. 100th anniversary Vol, 337-370.

Cheilletz A., 1983, Le contrôle structural des minéralisations filoniennes en tungstène du Jbel Aouam, Maroc central; application au système filonien plomb-zinc-argent: Comptes Rendus de l'Académie des Sciences de Paris, v. 297, Série 2. 417–420.

Cheilletz A. 1984 Contribution à la géologie du district polymétallique (W-Mo-Cu-Pb-Zn-Ag) du Jbel Aouam, Maroc Central : Thèse d'état, I.N.P.L., C.R.P.G., E.N.S.G. Nancy, 250p.

Cheilletz A. & Isnard P. (1985) : Contribution à la prospection des gisements hydrothermaux de tungstène sur l'exemple du district polymétallique W-Pb-Zn-Ag du jbel Aouam (Maroc central). Mineralium deposita 20, p. 220-230 (Extended abstract).

Cheilletz A. & Zimmermann J.L. 1982 Datations par la méthode K-Ar du complexe intrusif et des minéralisations en tungstène du jbel Aouam (Maroc central). C.R. Acad. Sc. Paris, t. 295 série II, p. 255-258

Christie A.B. & Braithwaite R.L. 1986 Epithermal gold-silver and porphyry copper deposits of the Hauraki Goldfield-a review. In Henley R.W., Hedenquist J.W. & Roberts P.J. (eds), Guide to the Epithermal (Geothermal) Systems and Precious Metal Deposits of New Zealand, 129-45. S.G.A. Monoger. Ser. 26, Gebrüder Borntraeger, Berlin.

Clauser C., 1988 Opacity-the concept of radiative thermal conductivity. In: Haenel, R., Rybach, L., Stegena, L. (eds.), Handbook of Terrestrial Heat-Flow Density Determination. Kluwer Academic Publishers, Dordrecht.

Clauser C. & Huenges E. 1995 Thermal conductivity of rocks and minerals. In: AGU Reference Shelf 3 rock Physics Relations. A Handbook of Physical Constants. 105-125.

Clemens, J.D., Mawer, C.K. 1992. Granitic magma transport by fracture propagation. Tectonophysics. 204, 339-360.

Collin F., Li X.L., Radu J.P. & Charlier R. 2002 Thermo-hydro-mechanical coupling in clay barriers. Eng. Geol. 64.179-193.

Cook S.J., Bowman J.R. & Forstar C.B., 1997 Contact metamorphism surrounding the alta stock : finite element model simulation of heat-and $^{18}O/^{16}O$ Mass-Transport during prograde metamorphism. Amer. J. Sci. 297. 1-55.

Cruden A. R. & P. Launeau 1994 Structure, magnetic fabric and emplacement of the Archean Lebel Stock, SW Abitibi Greenstone Belt, J. Struct. Geol., 16. 677–691.

Cui X., Nabelek P.I. & Liu M., 2001 Heat and fluid flow in contact metamorphic aureoles with layered and transient permeability, with application to the Notch Peak aureole, Utah. J. of Geophys. Res, 106 No. B4, 6477-6491.

D

Dawson B.V. Johnson P.D., Goldberg S.J. & Ulreich. J.B. 1990 Cardiac teratogenesis of trichloroethylene and dichloro-ethylene in a mammalian model. J. Am. Col Cardiol.16(5).1304–1309.

De Launay, L., 1913. Traité de Minéralogie. Gîtes minéraux et métallifères. Beranger, Paris.

Desteucq C. 1974 Le système filonien du Jbel Aouam (Maroc Central) ; essai d'interprétation structurale. Thèse de 3ème cycle Univ. Paul Sabatier Toulouse.

Dines H.G. 1956 The metalliferous mining region of south-west England. Mem. Geol. Surv. G.B., 1.

Dipple, G.M., Ferry, J.M., 1996. The effect of thermal history on the development of mineral assemblages during infiltration-driven contact metamorphism. Contributions to Mineralogy and Petrology. 124: 334.

Dobson P.F., Salah S., Spycher N. & Sonnenthal, E. L. 2004 Simulation of water–rock interaction in the Yellowstone geothermal system using. Geothermics. 33. 493-502.

Dodson, M. H. 1973 Closure temperature in cooling geochronological and petrological systems – Contrib. Mineral Petrol., 40, pp.259-274.

Domenico P.A. & Schwartz F.W. 1998 Physical and Chemical Hydrogeology. John Wiley & Sons, Inc., New York, NY, p 506.

Driesner, T., Geiger, S., 2007 Numerical simulation of Multiphase Fluid Flow in Hydrothermal Systems. Reviews in Mineralogy & Geochemistry. 65, 187-212.

Dubois J. & Diament M. 2001 Géophysique cours et exercises corrigés. 2ème édition. Paris. P 211.

Dubois M. Weisbrod A. & Shtuka A. 1994 Experimental determination of the two-phase (liquid and vapour) region in water-alkali chloride binary systems at 500° and 600°C

using synthetic fluid inclusions Chemi. Geol., Volume 115, Issues 3-4, 1 August, Pages 227-238.

Dunlap W. J. 1997 Neocrystallization or cooling? $^{40}Ar/^{39}Ar$ ages of white micas from low grade mylonites – Chemi. Geol. 143, 181-203.

E

Etheridge M.A., Wall V.J., Cox S.F. & Vernon R.H. 1984 High fluid pressures during regional metamorphism and deformation: Implications for mass transport and deformation mechanisms, J. Geophys. Res. 89, 4344-4358.

Evans A.M. 1998. Ore Geology and Industrial Minerals An Introduction, 3ed Edition, Blackwell Science Inc., Oxford and Northampton; 389p.

F

Faïk F. 1988 Le paléozoïque de la région de Mrirt (Est du Maroc Central) ; évolution stratigraphique et structurale. Thèse de 3ème Cycle Fac. Sci. Univ. Paul Sabatier Toulouse. p 233.

Famin V., Philippot P., Jolivet L. & Agard P. 2004 Evolution of hydrothermal regime along a crustal shear zone, Tinos Island, Greece. TECTONICS, Vol. 23, TC5004, doi: 10.1029/2003TC001509.

Ferry, J.M., Dipple, G.M., 1992. Models for coupled fluid flow, mineral reaction, and isotopic alteration during contact metamorphism: The Nitch Peak aureole, Utah. American Mineralogist. 77, 577-591.

Ferry, J.M., Sorensen, S.S., Rumble, D., 1998. Structurally controlled fluid flow during contact metamorphism in the Ritter Range pendant. California, USA. Contributions to Mineralogy and Petrology. 130, 358.

Ferry, J.M., Wing, B., Penniston-Dorland, S., Rumble, D., 2002. The direction of fluid flow during contact metamorphism of siliceous carbonate rocks: new data for the Monzoni and Predazzo aureoles, northern Italy, and a global review. Contributions to Mineralogy and Petrology. 142, 679.

Fischer G.J. & Paterson M.S. 1985 Dilatancy and permeability in rock during deformation at high temperature and pressure. Eos. Trans. Am. Geophys. Union, 46, 10-65.

Forster C. & Smith L., 1989 The influence of groundwater flow on thermal regimes in mountainous terrain. A model study. J. Geophys. Res. 94, 9439-9451.

Fournier R.O. 1973 An empirical Na---K---Ca geothermometer for natural waters. Geoch. et Cosmo. Acta, 37. 5. 1255-1275.

Fournier R.O. 1977 Chemical geothermometers and mixing models for geothermal systems. Geothermics, Volume 5, Issues 1-4, Pages 41-50.

Fowler S.J. 2001 Application of the energetically-constrained replenishment assimilation-fractional crystallization (EC-RAFC) model to the evolution of magmas within the north Atlantic igneous province, unpublished MS. Thesis, Central Washington Univ.

Francis P.W., Halls C. & Baker M.C.W. 1983 Relationships between mineralization and silicic volcanism in the central Andes. Geothermics. J. Volc. Res., 18, 165-90.

Friedhelm V.B. & Igel H. 1999 Lateral mixing and advection of reactive isotope tracers in ocean basins: observations and mechanisms. Earth & Plan. Sci. Let. 169. 113-128.

Fyfe W.S. & Henley R.W. 1973 Some thoughts on chemical transport processes, with particular reference to gold. Mineral. Sci. Eng., 5, 295-303.

G

Ganguly J. & Tirone M. 1999 Diffusion closure temperature and age of a mineral with arbitrary extent of diffusion: theoretical formulation and applications, Earth & Plan. Sci. Let. 170, 131-140.

Garavito A.M., Kooi H & Neuzil C.E. 2006 Numerical modeling of a long-term in situ chemical osmosis experiment in the Pierre Shale, South Dakota. Adv. Water Resource. 29.481-492.

Garven G., Raffensperger J.P., Dumoulin J. A., Bradley D. A., Young L.E., Kelley K. D. & Leach, D. L. 2003 Coupled heat and fluid flow modeling of the Carboniferous Kuna Basin, Alaska: implications for the genesis of the Red Dog Pb-Zn-Ag-Ba ore district. . J. Geoch. Expl. 78-79.215-219.

Gerdes M.L. & Baumgartner L.P., 1998 Convective fluid flow through heterogeneous country rocks during contact metamorphism. J. Geophys. Res. 103 No. B10. 23,983-24,003.

Gerdes, M.L., Baumgartner, L.P., Person, M. 1998. Convective fluid flow through heterogeneous country rocks during contact metamorphism. Journal of Geophysical Research 103(B10), 23,983-24,003.

Gerla J.P. 1988 Stress and fracture evolution in a cooling pluton: An example from the Diamond Joe stock, western Arizona, USA, J. Volcano. Geotherm. Res. 34. 267-282.

Gerya, T.V. & Burg J. 2007 Intrusion of ultramafic magmatic bodies into the continental crust: Numerical simulation. Physc. Earth & Plant. Interi. 160. 124-142.

Gessner K., Jones P., Andy R. Wilde D., Kühn M. 2006 Significance of strain localization and fracturing in relation to hydrothermal mineralization at Mount Isa, Australia, J. Geoch. Expl. 89. 129–132.

Gleizes G., D. Leblanc & J. L. Bouchez 1997 Variscan granites of the Pyrenees revisited: Their role as syntectonic markers of the orogen, Terra Nova, 9. 38–41.

Gloaguen, E., Chauvet, A., Branquet, Y., Gerbeaud, O., Ramboz, C., Bouchot, V., Lerouge, C., Monié, P., Cathelineau, M., Boiron M.C., Marignac, C., Pourraz, N., Fourcade, S., Ruffet, G., Iglesias Ponce de León, M., 2003. Relations between Au / Sn-W mineralizations and late Hercynian granite: Preliminary results from the Schistose Domain of Galicia-Trás-os-Montes Zone, Spain 7th biennal SGA meeting - Mineral Exploration and Sustainable Development. Athens, Greece, 271-274.

Gloaguen, E., 2006. Apports d'une étude intégrée sur les relations entre granites et minéralisations filoniennes (Au et Sn-W) en contexte tardi-orogénique (Chaîne Hercynienne, Galice Cnetrale, Espagne) unpublished PhD Thesis, Orléans University, France.
http://tel.archivesouvertes.fr/index.php?halsid=cu41odhccmgnb1qt3rek9l1j61&view_this_doc=tel-00107391&version=1, pp 571.

Gow P.A., Upton P., Zhao C. & Hill K.C. 2002 Copper-gold mineralization in New Guinea: numerical modeling of collision, fluid flow and intrusion-related hydrothermal systems. Aust. J. of Earth Sci. 49. 753-771.

Guillou-Frottier L., Burov E.B. & Milési, J.P. 2000 Genetic links between ash-flow calderas and associated ore deposits as revealed by large-scale thermo-mechanical modelling. J.of Volcano. & Geothermics. Res. 102. 339-361.

H

Hall A. 1990 Geochemistry of the Cornbian tin province. Miner. Deposita, 25. 1-6.

Hall W.E., Friedman I. & Nash J.T. 1974 Fluid inclusion and light stable isotope study of Climx molybdenum deposits, Colorado. Econo. Geol. 69. 884-901.

Hames W.E. & Bowring S.A. 1994 - An empirical evaluation of the argon diffusion geometry in muscovite - Earth & Plan. Sci. Let. 124.161-167.

Hammer S. 1939. Terrain corrections for gravimeter stations. Geophys. 4. 184-194.

Hanson, R.B., 1995. The hydrodynamics of contact metamorphism. Geological Society of America Bulletin. 107, 595-611.

Hanson, R.B., 1992. Effects of fluid production on fluid flow during regional and contact metamorphism. Journal of Metamorphic Geology. 10, 87-97.

Harcouët, V., 2005. Modélisations thermiques de gisements orogéniques mésothermaux: application au Ghana, PhD Thesis, Institut de Physique du Globe de Paris, 266 pp.

Harcouët, V., Guillou-Frottier, L., Bonneville, A., Bouchot, V., Milesi, J. 2007. Geological and thermal conditions before the major Palaeoproterozoic gold-mineralization event at Ashanti, Ghana, as inferred from improved thermal modelling. Precambrian Research. 154, 71-87.

Harmathy T.Z. 1970 Thermal properties of concrete at elevated temperatures. J. Mater. 5(1). 47–74.

Harmathy T.Z. & Allen L.W. 1973 Thermal properties of selected masonry unit concretes. J. of Amer. Conc. Inst. 70, No 2. 132-142.

Harris M. 1980; Hydrothermal alteration at Salave gold prospect, northwest Spain. Trans. Inst. Mining Metall., Appl. Earth Sci. 89. 5-15.

Hayba D.O., Bethke P.M., Heald P. & Foley N.K. 1986 Geologic, mineralogic and geochemical characteristics of volcanic-hosted epithermal precious metal deposits. In Berger B.R. & Bethke P.M. (eds.), Geology and Geochemistry of Epithermal Systems, 129-67. Soc. of Econo. Geol. El Paso.

Heald P., Foley N.K. & Hayba D.O. 1987 Comparative anatomy of volcanic-hosted epithermal deposits: acid-sulfate and adularia-sericite types. Econo. Geol. 82. 1-26.

Henley R.W. 1991 Epithermal gold deposits in volcanic terranes. In Foster R.P. (eds.), Gold Metal. & Expl. 133-64. Blacjie, Glasgow.

Henley R.W. & Ellis A.J. 1983 Geothermal systems ancient and modern: a geochemical review. Earth Sci. Rev. 19. 1-50.

Holstein, H., 2003. Gravimagnetic anomaly formulas for polyhedra of spatially linear media. Geophysics 68, 157–167.

Holzbecher E. 2005 Free and forced convection in porous media open at the top, Heat Mass Transfer, 41. 606-614.

Hutton D. H. W. 1988 Granite emplacement mechanisms and tectonic controls: Inferences from deformation studies, Trans. R. Soc. Edinburgh Earth Sci., 79. 452–455.

Hutton D. H.W. 1982 A tectonic model for the emplacement of the Main Donegal granite, NW Ireland, J. Geol. Soc. London, 139. 615– 631.

I

Ingebritsen, S.E., Manning, C.E., 1999. Geological implication of a permeability-deph curve for the continental crust. Geology. 27, 1107-1110.

Ingebritsen S.E. & Manning C.E. 2003; Implications of crustal permeability for fluid movement between terrestrial fluid reservoirs. J. Geoch. Expl. 78-79:1-6.

Ishihara S. 1977 The magnetite-series and ilmenite-series granitic rocks. Mining Geol. 27. 293 – 305.

J

-Jäger E., Niggli, E. & Wenk, E. 1967 Altersbestimmungen an Glimmer der Zentralalpen-Beitr. Geol. Karte Schweiz, N.F.L., 134, pp.1-67 (abstract).

K

Kerrich R. & Fryer B.J. 1979 Archaean precious metal hydrothermal systems, Dome Mine, Abitibi Greenstone H Belt. II. REE and oxygen isotope relations. Can. J. Earth Sci. 16. 440-58.

Kestin J., H.E. Khalifa Y. Abe, C.E. Grimes, H. Sookkiazian & Wakeham, W.A., 1978, Effect of pressure on viscosity of aqueous NaCl solutions in the temperature range 20-150 oC: Journal of Chemical and Engineering Data, **23**, 328-336.

Khitarov N.I., Malinin S.P., Lebedev Ye.B. & Shibayeva N.P. 1982 The distribution of Zn, Cu, Pb and Mo between a fluid phase and a silicate melt of granitic composition at high temperatures and pressures. Geochem. Int. 19 (4), 123-36.

Knapp R.B. & Norton D.L., 1981 Preliminary numerical analysis of processes related to magma crystallization and stress evolution in cooling pluton environment. Am. J. Sci. 281. 35-68.

Kühn M., Dobert F. & Gessner K. 2006 Numerical investigation of the effect of heterogeneous permeability distributions on free convection in the hydrothermal system at Mount Isa, Australia. Earth & Plan. Sci. Let. 244:655-671.

L

Lajaunie C., Courrioux G. & L. Manuel 1997 Foliation fields and 3D cartography in geology: Principles of a method based on potential, interpolation, Math. Geol. 29. 571– 584.

Lang, J.R., Baker, T., 2001. Intrusion-related gold systems: the present level of understanding. Mineralium Deposita. 36, 477-489.

Large R.R., Bull S.W., McGoldrick P.J., Derrick G.M., Carr G.R. & Walters S. 2005 Stratiform and strata-bound Zn-Pb-Ag deposits of the Proterozoic sedimentary basins of northern Australia: Econo. Geol. 100th Anniv. Vol. 931–963.

Leach D.L., Sangster D.F., Kelley K.D., Large R.R., Garven G., Allan C.R., Gutzmer J. & Walters S.K. 2005 Sediment-hosted lead-zinc deposits: A global perspective: Econo. Geol. 100th Anniv. Vol. 561–607.

Leblanc D., G. Gleizes P. Lespinasse P. Olivier & J. L. Bouchez 1994 The Maladeta granite polydiapir, Spanish Pyrenees: A detailed magnetostructural study, J. Struct. Geol., 16, 223–235.

Leblanc D., G. Gleizes L. Roux & J. L. Bouchez 1996 Variscan dextral transpression in the French Pyrenees: New data from the Pic des Trois-Seigneurs granodiorite and its country rocks, Tectonophysics. 261. 331–345.

Lindgren W. 1913 (second edition, 1933). Mineral Deposits. McGrow-Hill, New York.

Lowell, J.D., Guilbert, J.M., 1970. Lateral and vertical alteration – mineralization zoning in porphyry ore deposits. Economic Geology. 65, 373-408.

Lyons J.B., Campbell J.G., Erikson J.P., 1996 Gravity signatures and geometric configurations of some Oliveran plutons: their relation to Acadian structures. Geol. Soc. of Amer. Bulletin 108. 872–882.

M

Ma F. Al-Aasm & Yang J. 2006 Numerical modeling of hydrothermal fluid flow coupled with mass transport: An example from the Devonian Wabamun Group, northeast British Columbia, Canada. J. Geoch. Expl. 89. 247-250.

Macfarlane A.W. & Petersen U. 1990 Pb isotopes of the Hualgayoc area, northern Peru: Implications for metal provenance and genesis of a cordilleran polymetallic mining district. Econo. Geol. 85. 1303-27.

Madu B.E., Nesbitt B.E. & Muehlenbachs K. 1990 A mesothermal gold-stibnite-quartz vein occurrence in the Canadian Cordillera. Econo. Geol., 85, 1260-8.

Maineri, C., Benvenuti, M., Costagliola, P., Dini, A., Lattanzi, P., Ruggieri, G., Villa, I.M., 2003. Sericitic alteration at the La Crocetta deposit (Elba Island, Italy): interplay between magmatism, tectonics and hydrothermal activity. Mineralium Deposita. 38, 67-86.

Mair, J.L., Goldfarb, R.J., Johnson, C.A., Hart, C.J.R., Marsh, E.E., 2006. Geochemical Constraints on the Genesis of the Scheelite Dome Intrusion-Related Gold Deposit, Tombstone Gold Belt, Yukon, Canada. Economic Geology. 101, 523-553.

Manning D.A.C. 1984 Volatile control of tungsten partitioning in granitic melt-vapour systems. Trans. Instn Min. Metall. Sect. B Appl. Earth Sci. 93. B185-94.

Manning, C.E., Ingebritsen, S.E. 1999. Permeability of the continental crust: implications of geothermal data and metamorphic systems. Reviews of Geophysics. 37, 127-150.

Marcoux E. 1982 Etude géologique et métallogénique du district plombozincifère de Pontivy (Massif armoricain, France). Bull. Bur. Rech. Geol. Minères (2). Sect. II. (1). 1-24.

Martelet G., Diament M. & Truffert C. 1999 Un lever gravimétrique détaillé dans les Cévennes: apport à l'imagerie crustale (programme GéoFrance 3D-Massif central). Comptes Rendus de l'Académie des Sciences de Paris 328. 727–732.

McCaffre K. J. W. 1992 Igneous emplacement in a transpressive shear zone: Ox Mountains igneous complex, J. Geol. Soc. London, 149. 221–235.

Mcdougall I. & Harrison T. M. 1999 Geochronology and Thermochronology by the $^{40}Ar/^{39}Ar$ Method. Oxford University Press, New York, 282.

McKenna J.R. & Blackwell D.D. 2004 Numerical modeling of transient Basin and Range extensional geothermal systems. Geothermics. 33. 457-476.

McLaren S.N., Sandiford M. & Hand M. 1999 High radiogenic heat-producing granites and metamorphism-an example from the Mount Isa Inlier, Australia. Geology, 27. 679-682.

McNulty B. A., Tobisch O. T., Cruden A. R. & Gilder S. 2000 Multistage emplacement of the Mount Givens pluton, central Sierra Nevada Batholith, California, Geol. Soc. Am. Bull., 112, 119 – 135.

Moore J.M. 1982 Mineral zonation near the granite batholiths of south-west and northern England and some geothermal analogues. In Evans A.M. (eds.), Metallization Associated with Acid Magmatism, 229-41. Wiley, Chichester.

Moore D.E., Lockner D. & Byerlee J.D. 1994 Reduction of permeability in granite at elevated temperatures. Science. 256. 1588-1561.

Murase A. & McBirney B. 1973 Properties of some common igneous rocks and their melts at high Temperatures. Bull. Geol. Soc. Amer, 84. 3563-3592.

N

Nabelek, P.I., Labotka, T.C., 1993. Implications of geochemical fronts in the Notch Peak contact-metamorphic aureole, Utah, USA. Earth and Planetary Science Letters. 119, 539.

Nerci K. 2006 Les minéralisations aurifères du district polymétallique de Tighza (Maroc central) : un exemple de mise en place périgranitique tardi-hercynienne. Thèse de 3ème cycle, Univ. D'Orléans Fac. Sci. Fes 210p.

Nesbitt B.E., Muehlenbachs K. & Murowchick J.B. (1989) Genetic implications of stable isotope characteristics of mesothermal Au deposits and related Sb and Hg deposits in the Canadian Cordillera. Econ. Geol., 84, 1489-506.

Nesbitt B.E. (1991) Phanerozoic gold deposits in tectonically active continental margins. In foster R.P. (ed.), Gold Metal. & Expl. 104-32. Blackie, Glasgow.

Neuzil C.E. 1995 Abnormal pressures as hydrodynamic phenomena, Am. J. Sci. 295. 742-786.

Neves, S., and A. Vauchez (1995), Magmas emplacement and shear zone nucleation and development in northeast Brazil (Fazenda Nova and Pernambuco shear zones; state of Pernambuco), J. S. Am. Earth Sci., 8, 289– 298.

Newberry R.J., Burns L.E., Swanson S.E. & Smith T.E. 1990 Comparative petrologic evolution of the Sn and W granites of the Fairbanks-Circle Area, interior Alaska. In Stein H.J. & Hannah J.L. Ore-bearing Granite Systems; Petrogenesis and mineralizing Processes, 121-42 Geol. Soc. Am. Spec. paper 246, Boulder, Colorado.

Norton D. 1979 Quantitative simulation of the hydrothermal systems of crystallizing magmas on the basis of transport theory and oxygen istope data: an analysis of the Skaergaard intrusion. J. Petrol. 20. Part 3. 421-486.

Norton D.L. & Hulen J.B. 2001 Preliminary numerical analysis of the magma-hydrothermal history of the Geysers geothermal system, California, USA. Geothermics. 30. 211-234.

Norton, D., Knapp, R., 1977. Transport phenomena in hydrothermal systems: the nature of porosity. American Journal of Science. 277.

Norton, D., Knight. J., 1977. Transport phenomena in hydrothermal systems: cooling plutons. American Journal of Science. 277, 937-981.

N'tarmouchant A. 1991 Le magmatisme hercynien de la région de Mrirt. Thèse de 3ème cycle, Univ. Sidi Mohamed Ben Abdellah Fac. Sci. Fes p169.

O

Ochs F. A. & Lange R. A. 1997 The partial molar volume, thermal expansivity, and compressibility of H_2O in $NaAlSi_3O_8$ liquid: new measurements and an internally consistent model. Contrib. to Miner. Petrol. 129. 155–165.

Okabe M., 1979. Analytical expressions for gravity anomalies due to homogeneous polyhedral bodies and translations intomagnetic anomalies. Geophysics 44 (4), 730–741.

Oliver N.H.S & MaLellan J.G. 2006 Numerical models of extentional deformation, heat Transfer, and fluid flow across Basement-Cover Interfaces during Basin-related Mineralization. Econo. Geol. Especial Paper, 100th Anniv. 101, 1-31.

Oliver, N.H.S., McLellan, J.G., Hobbs, B.E., Cleverley, J.S., Ord, A., Feltrin, L. 2006. Numerical models of extensional deformation, heat transfer, and fluid flow across Basement-Cover interfaces during Basin-related Mineralization. Economic Geology. 101, 1-31.

Ondrak R. & Möller P. 1999 Modeling coupled heat and mass transport applied to the hydrothermal system of the Upper Harz Mountains (Germany). Chemic. Geol. 155.171-185.

P

Papale P. 1999 Numerical simulations of magma ascent along volcanic conduits. Phys. Chem. Earth.24. No. 11-12. 957-961.

Pe-Piper G., Koukouvelas I. & Piper D. J. W. 1998 Synkinematic granite emplacement in a shear zone: The Pleasant Hills pluton, Canadian Appalachians, Geol. Soc. Am. Bull., 110, 523–536.

Peratta A & Popov V. 2006 A new scheme for numerical modelling of flow and transport processes in 3D fractured porous media. Adv. Water Resources. 29. 42-61.

Petford, N., Cruden, A.R., McCaffrey, K.J.W., Vigneresse, J-L. 2000. Granitic magma formation, transport and emplacement in the Earth's crust. Nature. 408, 669-673.

Phillips W.J. 1972. Hydraulic fracturing and mineralization. J. Geol. Soc. London, 128, 337-59.

Phillips O. 1991 Flow and reactions in permeable rocks, p 285. Cambridge University Press.

Phillips G.N. Groves D.I. & Martyn J.E. 1984 An epigenetic origin for Archaean banded iron formation hosted gold deposits. Econo. Geol. 79. 162-71.

Plimer I.R., 1984 The mineralogical history of the Broken Hill lode, NSW. Aust. J. Earth Sci. 31. 379–402.

Plimer I.R. 1985 Broken Hill Pb-Zn-Ag deposits-a product of mantle metasomatism. Miner. Deposita, 20, 147-53.

Plouff D., 1976 Gravity and magnetic fields of polygonal prisms and application to magnetic terrain corrections. Geophysics 41, 727–741.

Piqué A., 1994 Géologie du Maroc. Les domaines régionaux et leur évolution structurale. Editons PUMAG, Marrakech, p 284.

Polyansky O.P. & Poort J. 2000 2D modelling of fluid flow and heat transport during the evolution of the Baikal rift. J. Geoch. Expl. 69.77-81.

Pollard, P.J., Taylor, R.G., Peters, L., 2005. Ages of Intrusion, Alteration, and Mineralization at the Grasberg Cu-Au Deposit, Papua, Indonesia. Economic Geology. 100, 1005-1020.

R

Rabinowicz M. Boulègue J. & Genthon P. 1998 Two and three-dimensional modeling of hydrothermal convection in the sedimented Middle Valley segment, Juan de Fuca Ridge. J. Geophys. Res., 103, No. B10. 24045-24065.

Raffensperger, J.P., Vlassopoloulos, D., 1999. The potential for free and mixed convection in sedimentary basins, Hydrogeology Journal, 7, 505-520.

Regenauer-Lieb K. & Yuen D. 2004 Positive feedback of interacting ductile faults from coupling of equation of state, rheology and thermal-mechanics. Phys. Earth & Plan. Interi. 142. 113-135.

Ribeyrolles M. 1972 Etude tectonique et microtectonique d'un segment de la chaîne hercynienne dans la partie Sud Orientale du Maroc Central. Thèse 3^{éme} cycle, Fac. Sci. Montpellier, p 163.

Rossetti, F., Tecce, F., Billi, A., Brilli, M., 2007. Patterns of fluid flow in the contact aureole of the Late Miocene Monte Capanne pluton (Elba Island, Italy): the role of structures and rheology. Contributions to Mineralogy and Petrology, 153, 743.

Ruffet G., Féraud G. & Amouric M. 1991 Comparison of 40Ar-39Ar conventional and laser dating of biotites from the North Tregor Batholith, Geoch. et Cosmoch. Acta, 55. 1675-1688.

S

Saager R., Meyer M. & Muff R. 1982 Gold distribution in supracrustal rocks from Archaean greenstone belts of southern Africa and from Paleozoic ultramafic complexes of the European Alps: metallogeneic and geochemical implications. Econo. Geol. 77. 1-24.

Saito K. 1994 Excess Ar in some Metamorphic and Plutonic Rocks and Reduction of Thermal Neutron induced Ar40 by Cd Shielding. Sci. Rep. RITU A40. 185-189.

Sawkins F.J. 1984 & 1990 Metal Deposits in relation to Plate Tectonics. Springer-Verlag, Berlin.

Scaillet B. & Pichavant M. 2003 Experimental constraints on volatile abundances in arc magmas and their implications for degassing processes. Volcanic degassing. Geo. Soc. Londan, Special Pub. 213. 23-52.

Schardt C., Yang J. & Large R. 2003 Formation of massive sulfide ore deposits on the seafloor constraints from numerical heat and fluid flow modelling. J. of Geoch. Expl. 78-79. 257-259.

Schardt C., Yang J., Large R., 2005 Numerical heat and fluid flow modelling of the Panorama volcanic-hosted massive sulphide district, western Australia. Econo. Geol. 100. 547–566.

Schärli U. & Rybach L. 2000. Determination of specific heat capacity on rock fragments. Geothermics. Volume 30, Issue 1, P. 93-110.

Scratch R.B., Watson G.P., Kerrich R. & Hutchinson R.W. 1984 Fracture-controlled antimony-quartz mineralization, Lake George deposit, New Brunswick: mineralogy, geochemistry, alteration and hydrothermal regimes. Econo. Geol., 79. 1159-86.

Seedorff E. 1988 Cyclic development of hydrothermal mineral assemblages related to multiple intrusions at the Henderson porphyry molybdenum deposit, Colorado; Geology. 35.64-79.

Seedorff, E., Dilles, J.H., Proffett, J.M.J., Einaudi, M.R., Zurcher, L., Stavast, W.J.A., Johnson, D.A., Barton, M.D., 2005. Porphyry copper deposits: Characteristics and origin of hypogene features. Economic Geology, 100th Anniversary Volume, 251-298.

Shepherd T.J. & Allen P.M. 1985 Metallogenesis in the Harlech Dome, North Wales: a fluid inclusion interpretation. Mineralium Deposita, 20, 159-68.

Sheppard S.M.F. 1977 Identification of the origin of ore-forming solutions by the use of stable isotopes. In Volcanic Processes in Ore Genesis, Spec. Publ. 7, Geol. Soc. London.

Sibson R.H. 2001 Seismogenic Framework for Hydrothermal Transport and Ore Deposition, Soc. of Econo. Geol. 14. 25-50.

Sillitoe R.H. 1973 The tops and bottoms of porphyry copper deposits. Econo. Geol. 68. 799-815.

Simms M. A. & Garven G. 2004 Thermal convection in faulted extensional sedimentary basins: theoretical results from finite-element modeling. Geofluids. 4. 109-130.

Skinner B.J. 1979 The many origins of hydrothermal mineral deposits. In Barnes H.L. (eds.), Geochemistry of Hydrothermal Ore Deposits, 2nd edn, 1-21. Wiley, New York.

Smirnov V.I. 1976 Geology of Mineral Deposits. MIR, Moscow.

Spear F. S. 1993 Metamorphic phase equilibria and pressure-temperature-time paths. Miner. Soc. of Amer. p 799.

Stanton R.L. 1972 Ore Petrology. McGraw-Hill, New York.

Stimac J. A., Goff F. & Wohletz K. 2001 Thermal modelling of the Clear Lake magmatic-hydrothermal system, California, USA. Geothermics. 30. 349-390.

Strong D.F. 1981 Ore deposit models: 5. A model for granophile mineral deposits. Geosci. Can. 8, 155-60.

Sibson, R.H., Robert, F., Poulsen, H.H.A.F., 1988.High angle faults, fluid pressure cycling, and mesothermal gold-quartz deposits. Geology 16, 551-555.

Sillitoe, R.H., 1991. Intrusion-related gold deposits In: Foster RP (ed) Gold metallogeny and exploration. Blackie, Glasgow, 165-209.

Stephens, J.R., Mair, J.L., Oliver, N.H.S., Hart, C.J.R., Baker, T., 2004. Structural and mechanical controls on intrusion-related deposits of the Tombstone Gold Belt, Yukon, Canada, with comparisons to other vein-hosted ore-deposit types. Journal of Structural Geology. 26, 1025-1041.

Stern, L.A., Chamberlain, C.P., Barnett, D.E., Ferry, J.M., 1992. Stable isotope evidence for regional-scale fluid migration in a Barrovian metamorphic terrane, Vermont, USA. Contributions to Mineralogy and Petrology, 112: 475.

T

Taylor R.P. 1981 Isotope geology of the Bakircay Porphyry Copper Prospect, northern Turkey. Mineralium Deposita, 16, 375-90.

Taylor R.P. & Fryer B.J. 1982 Rare earth element geochemistry as an aid to interpretating hydrothermal ore deposits. In Evans A.M. (ed.), Metallization Associated with Acid Magmatism, 357-65. Wiley, Chichester.

Taylor R.P. & Fryer B.J. 1983 Strontium isotope geochemistry of the Santa Rita Porphyry Copper Deposits, New Mexico. Econo. Geol., 78. 170-4.

Termier H. 1936 Etudes géologiques sur le Maroc central et le Moyen Atlas septentrional. Notes et Mémoires du Service des Mines et de la Carte géologique du Maroc n°33.

Thompson, J.F.H., Sillitoe, R.H., Baker, T., Lang, J.R., Mortensen, J.K., 1999. Intrusion-related gold deposits associated with tungsten-tin provinces. Mineralium Deposita. 34, 323-334.

Thompson, J.F.H., Newberry, R.J., 2000, Gold deposits related to reduce granitic intrusions In: Hagemann SG, Brown PE (eds) Gold in 2000. Reviews in Economic Geology. Society of Economic Geologists, Littleton, CO, USA, pp 377-400.

Tikoff B. & Teyssier C. 1992 Crustal-scale, en echelon‘‘P-shear’’ tensional bridges: A possible solution to the batholithic room problem, Geology. 20. 927–930.

Tikoff, B. & M. de Saint Blanquat 1997 Transpressional shearing and strike-slip partitioning in the Late Cretaceous Sierra Nevada magmatic arc, California, TECTONICS, 16(3), 442– 459.

Tobisch, O. T.& A. R. Cruden 1995 Fracture-controlled magma conduits in an obliquely convergent continental magmatic arc, Geology. 23. 941– 944.

Turcotte D. & Schubert G.L. 2002 Geodynamics, 2nd edition. Cambridge University Press, Cambridge, UK.

Turner, G. 1968 The distribution of potassium and argon in chondrite, in Ahrens, L. H., (ed.), in Origin and Distribution of the elements, Pergamon, 387-398.

V

Vigneresse J. L. 1990 Use and misuse of geophysical data to determine the shape at depth of granitic intrusions, Geology. J. 25, 249– 260.

Vigneresse J.L. 2007 The role of discontinuous magma inputs in felsic magma and ore generation. Ore Geol. Rev. 30. 181–216.

Villa I. 1998 Isotopic closure - Terra Nova. 10. 42-47.

Vosteen H.D. & Schellschmidt, R. 2003 Influence of temperature on thermal conductivity, thermal capacity and thermal diffusivity for different types of rock. Physics and Chemistry of the Earth, Parts A/B/C, 28, Issues 9; 11.499-509.

W

Wadjinny A. 1998 Le plomb au Maroc: cas des districts de Touissit et de Jbel Aouam. Chronique de la Recherche Minière 531-532, 9-28.

Wallace S.R. 1991 Model development: porphyry molybdenum deposits. Econo. Geol. Monoger. 8. 207-24.

Watanabe Y. 2001 Timing of volcano-sedimentary massive sulfide and vein-type Pb-Zn mineralization in the western meseta of Morocco: ^{40}Ar- ^{39}Ar geochronology. Exploration Technology and interpreting methods Part IV, JICA-B.R.P.M. project (1998- 2002).

Webb S. L. & Dingwell D. B. 1990 Relaxation in silicate melts. European Journal of Mineralogy 2.427–449.

Weinberg R. F., Hodkiewicz P. F. & Groves D. I. 2004 What controls gold distribution in Archean terranes?, Geology. 32. 545–548.

White D.E. 1974 Diverse origins of hydrothermal ore fluids. Econo. Geol. 69. 954-73.

White D.E. 1981 Active geothermal systems and hydrothermal ore deposits. In Skinner B.J. (eds.), Econo. Geol. 75th Anniv. Vol. 392-423.

Wijbrans J.R. & McDougall I. 1986 40Ar/39Ar dating of white micas from an Alpine high-pressure metamorphic belt on Naxos (Greece): the resetting of the argon isotopic system. Contr. Mineral Petrol. 93. 187-194.

Williams P.J. 1990 Evidance for a late metamorphic origin of disseminated gold mineralization in Grenville gneisses at Calumet, Quebec. Econo. Geol. 85. 556-84.

Wing, B.A., Ferry, J.M., 2002. Three-dimensional geometry of metamorphic fluid flow during Barrovian regional metamorphism from an inversion of combined petrologic and stable isotopic data. Geology. 30, 639-642.

Wisian K. W. & Blackwell D.D. 2004 Numerical modeling of Basin and Range geothermal systems. Geothermics. 33. 713-741.

Wu Y., Zhang K., Ding C., Pruess K., Elmroth E. & Bodvarsson G.S. 2002 An efficient parallel-computing method for modeling nonisothermal multiphase flow and multicomponent transport in porous and fractured media. Adv. Water Resources. 25. 243-261

Y

Yang J. 2006 Full 3-D numerical simulation of hydrothermal fluid flow in faulted sedimentary basins: Example of the McArthur Basin, Northern Australia. J. of Geoch. Expl. 89. 440-444.

Yardley B.W.D. 1983 Quartz veins and devolatilization during metamorphism. J. Geol. Soc. London, 140. 657-63.

Yasukawa K., Mogi T., Widarto D. & Ehara S. 2003 Numerical modeling of a hydrothermal system around Waita volcano, Kyushu, Japan, based on resistivity and self-potential survey results. Geothermics. 32. 21-46.

Yin S., Dusseault M,B. & Rothenburg L. 2007 Analytical and numerical analysis of pressure drawdown in a poroelastic reservoir with complete overburden effect considered. Adv. Water Resources. 30.1160-1167.

Z

Zhao C., Hobbs B.E. & Mühlhaus H.B. 1998 Finite element modelling of temperature gradient driven rock alteration and mineralization in porous rock masses. Comp. Methods Appl. Mech. Eng. 165. 175-187.

Zhao C., Hobbs B.E., Mühlhaus H. B., Ord A. & Ge Lin 2003 Convective instability of 3D fluid-saturated geological fault zones heated from below. Geophys. J. Int. 155. 213-220.

Zhu K. & Yang J. 2006 Numerical investigation of the influence of volcanic facies architecture on hydrothermal fluid migration: Example of the Mount Read Volcanics, western Tasmania, Australia. J. Geoch. Expl. 89. 474-479.

Zhao, C., Hobbs, B.E., Mühlhaus, H.B., 1998. Finite element modelling of temperature gradient driven rock alteration and mineralization in porous rock masses. Computer Methods in Applied Mechanics and Engineering. 165, 175-187.

Zhao, C., Hobbs, B.E., Walshe, J.L., Mühlhaus, H.B., Ord, A., 2001b. Finite element modeling of fluid-rock interaction problems in pore-fluid saturated hydrothermal/sedimentary basins, Computer Methods in Applied Mechanics and Engineering 190, 2277-2293.

Zhao, C., Ge Lin, Hobbs, Ord, A., Yuejun Wang, B.E., Mühlhaus, H. B. 2003. Effects of hot intrusions on pore fluid flow and heat transfer in fluid-saturated rocks, Computer Methods in Applied Mechanics and Engineering.192, 2007-2030.

Appendix

1. Numerical construction of M4 as an example to explain the numerical procedures followed in this research.

The model was made to test the effect of emplacement depth on heat transfer and describes subsurface flow in porous media driven by density variations that result from temperature changes. This model of fluid flow and heat transfer uses Darcy's Law and the Convection and Conduction equation. The development of convection cells was noticed over the pluton. Figure (A.1) reveals the convection cells with the help of velocity streamlines at 10Myrs. At early times (at the beginning of emplacement) small convection cells develop over the pluton corners. At late times (at hottest phase) two single convection cells cover the upper zone of the model.

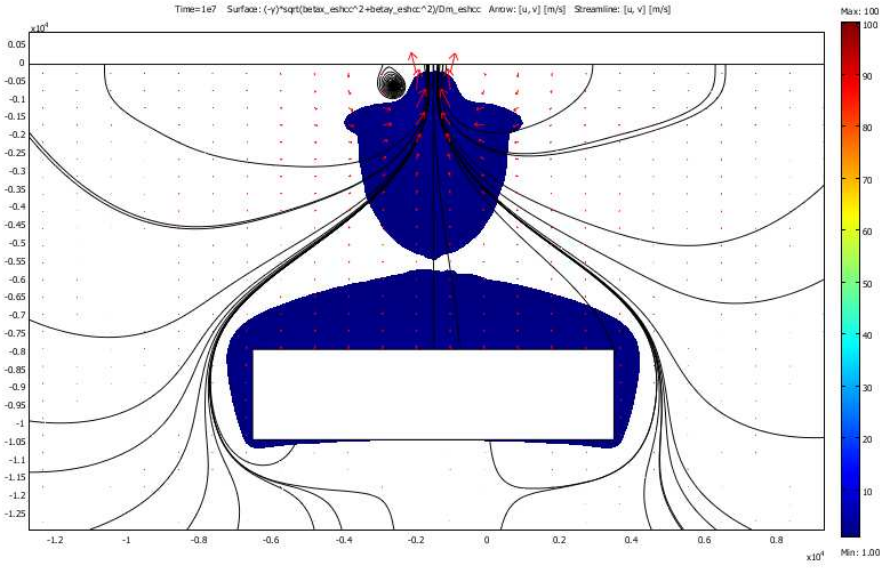

Figure (A.1): Application of Peclet number in M4 subjected to temperature gradients and subsequent free advection around intrusion.

The following procedures show the way we constructed our model:

1.1 Geometry

The model was composed by two rectangulars, the first represents a country rock, with 47km width (x axis) and 25km length (y axis). Whereas, the second rectangular represents an intruded body with 10km width and 2.5km length, and, figure (A.2).

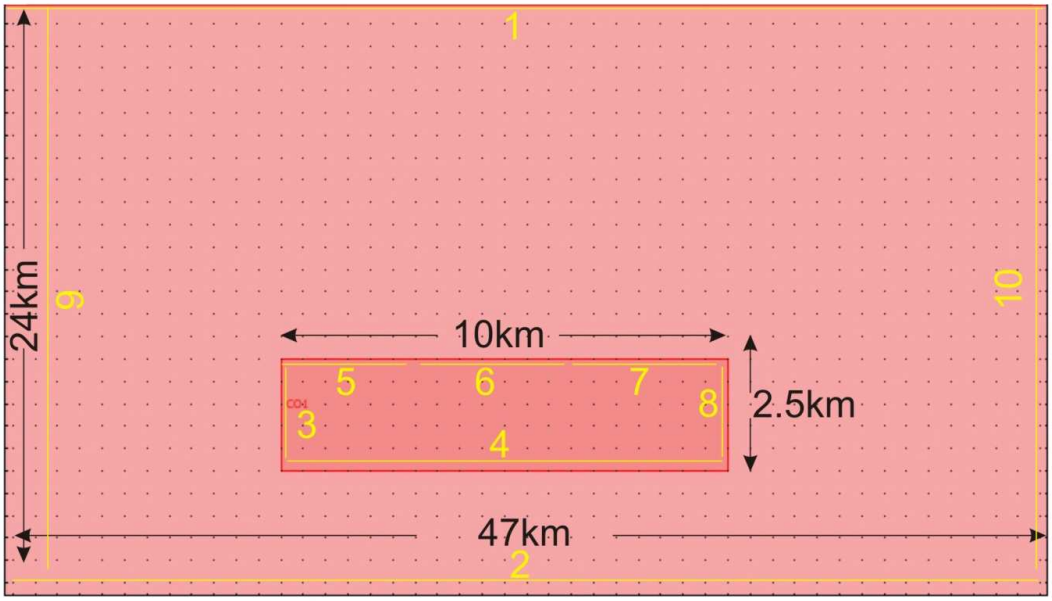

Figure (A.2): Two rectangles simulate the country rock and the intruded body. The boundaries in yellow correspond to the boundaries conditions mentioned in table (A.2).

The variation of physical parameters was injected by mathematical expressions adapted by Comsol and related to equations mentioned in chapter (II). In addition, we expressed mathematically the initial and boundary conditions to respect time limits of different physical parameters. For example, we created a mathematical expression to simulate physically the intruded body as a part of the country rock during the first 7Myrs and modified the physical parameters of this part to be a magma and crystalline granite between 7-10Myrs and 10-20Myrs respectively. These modified parameters include density, thermal conductivity, heat capacity, permeability and time of emplacement. During the time of emplacement, the intruded body was expressed mathematically to be a source of heat for 3Myrs (table A.1). So that a temperature of 700°C is maintained during 3Myr.

1.2 The Meshing

Two types of mesh were considered for this model: homogeneous and inhomogeneous mesh cases. Inhomogeneous meshing (refining mesh) was applied where fine mesh is needed to provide improved accuracy around the point where the solution is supposed to be changed frequently and strongly. Figure (A.3) shows the two cases of meshing.

Table (A.1) shows the mathematical expressions used for different parameters.

Name	Comsol expression	
Density of fluid (rho)	1000*(1-(0.00021*(T-293)))	

The fluid velocity in x component	-kaps_esdl/eta_esdl*px		
y-velocity (v)	-kaps_esdl/eta_esdl*(py+rho*g_esdl)		
domains	**Unite**	**Country rock**	**Intruded body**
Time-scaling coefficient	s	0.0000000317	0.0000000317 (represents 1/year)
General heat source (QH) (Period of emplacement)	W/m^3	0	(t>0.7e7)*(t<1e7)*(T<973)*flc2hs(t-1.3e8,1.3e8)*0.5 flc2hs is a smoothing function to prevent a sharp transition in boundary conditions.
Demain type	kg/m^3	porous	porous
x-velocity (u)	m/s	u	u
y-velocity (v)	m/s	v	v
Volume fraction (pore space)	1	0.05	0.05
Density (rho)	kg/m^3	1000*(t<0.7E7)+(t>=0.7E7)*rho	1000*(t<0.7E7)+(t>=0.7E7)*rho1
Specific heat capacity (CpLiquid)	J/(kg·K)	16.782*(T)-2013.2	16.782*(T)-2013.2
Volume fraction (solid space)	1	{0.95}	{0.95}
Density (rhoP)	kg/m^3	{ 2800*(1-(0.000024*(T-293))) }	{'(t<0.7E7)* 2800*(1-(0.000024*(T-293))) +(t>=0.7E7)* 2800*(1-(0.000024*(T-293))) }
Specific heat capacity (CpSolid)	J/(kg·K)	{ 0.5915*(T)+636.14}	{ (t<0.7e7)*(2800*(1-(0.000024*(T-293))))+(t>=1e7)*(0.6169*(T)+626.32) }

Thermal conductivity (KP)	W/(m·K)	{ (3.1138-0.0023*(T))}	{(t<0.7E7)* (3.1138-0.0023*(T)) +(t>=0.7E7)* (2.6842-0.0016*(T))}
Saturated permeability (kaps)	m^2	(0.00004*(-y)^-3.2)	(t<0.7E7)*(0.00004*(-y)^-3.2) + (t>=0.7E7*t<1E7)*1e-24+(t>=1E7)*0.00004*(-y)^-3.2
Density-liquid (rhof)	kg/m^3	rho	rho
Viscosity-liquid (eta)	Pa·s	0.00002*exp(2.302*(247/(T-140)))	0.00002*exp(2.302*(247/(T-140)))

1.3 Boundary and initial conditions

Boundary and initial conditions were made based on the following table:

Table (A.2) shows the boundary and initial conditions of heat transfer and fluid flow.

Boundary N°	1, 9	2	3-8
Type	Thermal insulation	Temperature	Continuity
Inward heat flux	0	0.03 W/m^2	
Subdomain initial value		Country rock	Intruded body
Temperature (T) The initial condition of thermal gradient (24°C/km).	K	293+(0.024*(-y))	293+(0.024*(-y))
Pressure (p)	Pa	1E5+(1000*9.81*(-y))	1E5+(1000*9.81*(-y))
(g) Gravity	m/s^2	9.82	
(z) Elevation/vertical axis	m	y	
Boundary		2-10	1
Type		Zero flux/Symmetry	Pressure
Pressure (p_0)	Pa	0	101125

Meshing is related to the number of degree of freedom (DOFs), it is evident that the inhomogeneous mesh case gives more accurate and more stable results already for high

number of DOFs. However, for low number of DOFs the solution time is longer, the solution might not converge at all or errors might be large. Moreover, if the mesh element size becomes large, the mesh elements eventually have a very bad quality or even become inverted. For this reason, the quality of mesh elements and the number of DOF are important to ensure that there is only one constant solution. Therefore, the minimum element quality and DOF for a convergent and accurate solution are 0.6/1 and 30000 respectively in such model. The table (A.3) resumes the characteristic features of mesh elements of this model. In Tighza model, DOF were 90786 with minimum quality elements 0.65/1.

Table (A.3) Mesh Statistics of M4.

Number of degrees of freedom	43820
Number of elements	11355
Number of boundary elements	472
Minimum element quality	0.70

Hereunder, the physical parameters and their comsol expressions to construct model M4.

The abbreviations mentioned here correspond the equations and parameters used in comsol, for example, eshcc corresponds to earth science heat convection and conduction, esdl corresponds to earth science darcy law and dtfluxx is a diffusive heat flux in x direction and so on

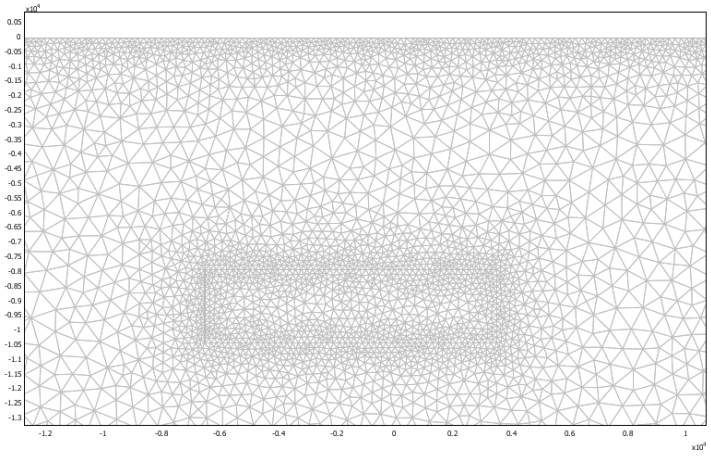

.

Figure (A.3): An inhomogeneous mesh for M4 model, the element size is refined around the intruded body because fluid velocities and temperature have significant changes while the element size is relatively large far from the intruded body.

Name	Description	Expression
ndtflux_eshcc	Normal diffusive heat flux	nx_eshcc * dtfluxx_eshcc+ny_eshcc * dtfluxy_eshcc
ncflux_eshcc	Normal convective heat flux	nx_eshcc * cfluxx_eshcc+ny_eshcc * cfluxy_eshcc
ntflux_eshcc	Normal total heat flux	nx_eshcc * tfluxx_eshcc+ny_eshcc * tfluxy_eshcc
nU_esdl	Normal velocity	u_esdl * nx_esdl+v_esdl * ny_esdl
flux_esdl	Outward flux	u_esdl * nx_esdl+v_esdl * ny_esdl
thetaP_eshcc	Volume fraction (solids)	0.95
CL_eshcc	Volume heat capacity (mobile fluid)	rho_eshcc * CpL_eshcc
Ceq_eshcc	Equivalent volume heat capacity	(CL_eshcc * thetaL_eshcc+CP_eshcc * thetaP_eshcc)/(thetaL_eshcc+thetaP_eshcc)
Keq_eshcc	Equivalent thermal conductivity	(KL_eshcc * thetaL_eshcc+KP_eshcc * thetaP_eshcc)/(thetaL_eshcc+thetaP_eshcc)
rhogeo_eshcc	Geothermal density	(rho)/(thetaP_eshcc+thetaL_eshcc)
QG_eshcc	Geothermal heating per volume	rhogeo_eshcc * qgeo_eshcc
U_eshcc	Velocity field	sqrt(u_eshcc^2+v_eshcc^2)
dtfluxx_eshcc	Diffusive heat flux, x component	-Keqxx_eshcc * Tx-Keqxy_eshcc * Ty
cfluxx_eshcc	Convective heat flux, x component	CL_eshcc * u_eshcc * T
tfluxx_eshcc	Total heat flux, x component	CL_eshcc * u_eshcc * T-Keqxx_eshcc * Tx-Keqxy_eshcc * Ty
dtfluxy_eshcc	Diffusive heat flux, y component	-Keqyx_eshcc * Tx-Keqyy_eshcc * Ty
cfluxy_eshcc	Convective heat flux, y component	CL_eshcc * v_eshcc * T
tfluxy_eshcc	Total heat flux, y component	CL_eshcc * v_eshcc * T-Keqyx_eshcc * Tx-Keqyy_eshcc * Ty
gradT_eshcc	Temperature gradient	sqrt(Tx^2+Ty^2)
dtflux_eshcc	Diffusive heat flux	sqrt(dtfluxx_eshcc^2+dtfluxy_eshcc^2)
cflux_eshcc	Convective heat flux	sqrt(cfluxx_eshcc^2+cfluxy_eshcc^2)
tflux_eshcc	Total heat flux	sqrt(tfluxx_eshcc^2+tfluxy_eshcc^2)
cellPe_eshcc	Cell Peclet number	y* sqrt(betax_eshcc^2+betay_eshcc^2)/Dm_eshcc
betax_eshcc	Convective field, x component	CL_eshcc * u_eshcc
betay_eshcc	Convective field, y component	CL_eshcc * v_eshcc
da_eshcc	Total time scale factor	Dts_eshcc * Ceq_eshcc
ressc_eshcc	Shock capturing residual	Tx * CL_eshcc * u_eshcc+Ty * CL_eshcc * v_eshcc-QG_eshcc-QH_eshcc
S_esdl	Storage term	eps * CSs_esdl
kapxx_esdl	Permeability tensor	kap_esdl
gradP_esdl	Pressure gradient	sqrt(px^2+py^2)

Table (A.4) the mathematical expression of different parameters used in heat transfer and fluid flow domains

Name	**Description**	**Expression**
thetaP_eshcc	Volume fraction (solids)	0.95
CP_eshcc	Volume heat capacity (solids)	(t<0.7e7)*(2800*(1-(0.000024*(T 293))))+(t>=1e7)*(0.6169*(T)+626.32)
CL_eshcc	Volume heat capacity (mobile fluid)	rhoL_eshcc * CpL_eshcc
Ceq_eshcc	Equivalent volume heat capacity	(CL_eshcc * thetaL_eshcc+CP_eshcc * thetaP_eshcc)/(thetaL_eshcc+thetaP_eshcc)
KP_eshcc	Thermal conductivity (solids)	(t<0.7E7)* (3.1138-0.0023*(T)) +(t>=0.7E7)* (2.6842-0.0016*(T))
Keq_eshcc	Equivalent thermal conductivity	(KL_eshcc * thetaL_eshcc+KP_eshcc * thetaP_eshcc)/(thetaL_eshcc+thetaP_eshcc)
rhogeo_eshcc	Geothermal density	rho
QG_eshcc	Geothermal heating per volume	rhogeo_eshcc * qgeo_eshcc
U_eshcc	Velocity field	sqrt(u+v)
dtfluxx_eshcc	Diffusive heat flux, x component	-Keqxx_eshcc * Tx-Keqxy_eshcc * Ty
cfluxx_eshcc	Convective heat flux, x component	CL_eshcc * u_eshcc * T
tfluxx_eshcc	Total heat flux, x component	CL_eshcc * u_eshcc * T-Keqxx_eshcc * Tx-Keqxy_eshcc * Ty
dtfluxy_eshcc	Diffusive heat flux, y component	-Keqyx_eshcc * Tx-Keqyy_eshcc * Ty
cfluxy_eshcc	Convective heat flux, y component	CL_eshcc * v_eshcc * T
tfluxy_eshcc	Total heat flux, y component	CL_eshcc * v_eshcc * T-Keqyx_eshcc * Tx-Keqyy_eshcc * Ty
gradT_eshcc	Temperature gradient	sqrt(Tx^2+Ty^2)
dtflux_eshcc	Diffusive heat flux	sqrt(dtfluxx_eshcc^2+dtfluxy_eshcc^2)
cflux_eshcc	Convective heat flux	sqrt(cfluxx_eshcc^2+cfluxy_eshcc^2)
tflux_eshcc	Total heat flux	sqrt(tfluxx_eshcc^2+tfluxy_eshcc^2)
cellPe_eshcc	Cell Peclet number	h * sqrt(betax_eshcc^2+betay_eshcc^2)/Dm_eshcc
betax_eshcc	Convective field, x component	CL_eshcc * u_eshcc
betay_eshcc	Convective field, y component	CL_eshcc * v_eshcc
da_eshcc	Total time scale factor	Dts_eshcc * Ceq_eshcc
equ_eshcc	Equation residual	-Keqxx_eshcc * Txx-Keqxy_eshcc * Txy+Tx * CL_eshcc * u_eshcc-Keqyx_eshcc * Tyx-Keqyy_eshcc * Tyy+Ty * CL_eshcc * v_eshcc-QG_eshcc-QH_eshcc
ressc_eshcc	Shock capturing residual	Tx * CL_eshcc * u_eshcc+Ty * CL_eshcc * v_eshcc-QG_eshcc-QH_eshcc

Dm_eshcc	Mean diffusion coefficient	(Keqxx_eshcc * CL_eshcc^2 * u_eshcc^2+Keqxy_eshcc * u_eshcc * CL_eshcc^2 * v_eshcc+Keqyx_eshcc * v_eshcc * CL_eshcc^2 * u_eshcc+Keqyy_eshcc * CL_eshcc^2 * v_eshcc^2)/((CL_eshcc * u_eshcc)^2+(CL_eshcc * v_eshcc)^2+eps)
S_esdl	Storage term	

2. Gravity Data :

ALT_GPS	ALT_MAP	LABEL	GRAVITY_VALUE	TEMPS	DATE (2006)
1103	1103	GRAVBASE	5719.8650	14:17	11-Apr
1117	1108	GRAV	5718.3410	14:35	11-Apr
1100	1098	GRAV	5720.8460	14:56	11-Apr
1105	1097	GRAV	5720.4700	15:26	11-Apr
1130	1110	GRAV	5716.7020	15:58	11-Apr
1147	1135	GRAV	5712.5710	16:25	11-Apr
1116	1103	GRAV	5719.5090	17:18	11-Apr
1138	1147	GRAV	5714.9830	17:58	11-Apr
1156	1138	GRAV	5711.3530	18:22	11-Apr
1108	1103	GRAVBASE	5719.7990	19:24	11-Apr
1112	1103	GRAVBASE	5719.8990	8:40	12-Apr
1103	1092	GRAV	5722.3030	8:54	12-Apr
1102	1088	GRAV	5722.5100	14:23	12-Apr
1116	1115	GRAV	5718.3460	14:40	12-Apr
1106	1093	GRAV	5721.4470	15:02	12-Apr
1102	1087	GRAV	5721.9630	15:15	12-Apr
1102	1090	GRAV	5721.3350	15:30	12-Apr
1110	1100	GRAV	5719.6990	15:40	12-Apr
1139	1127	GRAV	5713.1330	15:56	12-Apr
1101	1088	GRAV	5720.8230	16:18	12-Apr
1098	1088	GRAV	5721.6860	16:31	12-Apr
1095	1085	GRAV	5721.7860	16:41	12-Apr
1099	1073	GRAV	5721.7700	17:12	12-Apr
1098	1092	GRAV	5721.9600	17:31	12-Apr
1131	1124	GRAV	5715.4410	17:45	12-Apr
1107	1103	GRAV	5719.5980	18:07	12-Apr
1090	1085	GRAV	5723.9100	18:20	12-Apr
1097	1085	GRAV	5724.3960	18:39	12-Apr
1113	1103	GRAVBASE	5720.0050	19:33	12-Apr
1116	1103	GRAVBASE	5720.0050	7:35	13-Apr
1167	1152	GRAV	5708.0190	8:21	13-Apr
1130	1104	GRAV	5716.5830	8:36	13-Apr
1110	1093	GRAV	5719.1620	8:53	13-Apr
1151	1129	GRAV	5710.3980	9:16	13-Apr
1094	1075	GRAV	5722.0430	9:40	13-Apr
1096	1078	GRAV	5723.0860	9:57	13-Apr
1092	1070	GRAV	5722.7020	10:13	13-Apr
1140	1115	GRAV	5713.1160	10:34	13-Apr

1095	1077	GRAV	5722.4460	10:59	13-Apr
1090	1077	GRAV	5722.4160	11:24	13-Apr
1141	1136	GRAV	5712.9920	11:46	13-Apr
1114	1109	GRAV	5717.8260	12:04	13-Apr
1094	1075	GRAV	5721.2120	12:20	13-Apr
1142	1119	GRAV	5711.9430	12:48	13-Apr
1200	1177	GRAV	5699.5580	13:09	13-Apr
1185	1175	GRAV	5702.1130	13:27	13-Apr
1136	1103	GRAVBASE	5720.2450	14:53	13-Apr
1225	1202	GRAV	5694.9280	15:43	13-Apr
1197	1175	GRAV	5702.4010	16:22	13-Apr
1185	1167	GRAV	5704.8050	16:41	13-Apr
1202	1165	GRAV	5702.3930	17:03	13-Apr
1131	1107	GRAV	5715.0770	17:40	13-Apr
1172	1163	GRAV	5706.2260	17:58	13-Apr
1156	1159	GRAV	5709.1290	18:21	13-Apr
1157	1146	GRAV	5708.1540	18:38	13-Apr
1115	1118	GRAV	5717.0850	18:52	13-Apr
1110	1109	GRAV	5717.9770	19:03	13-Apr
1109	1103	GRAVBASE	5720.2560	19:26	13-Apr
1113	1103	GRAVBASE	5720.4970	7:58	14-Apr
1245	1224	GRAV	5689.1200	8:39	14-Apr
1242	1223	GRAV	5690.1360	8:58	14-Apr
1243	1227	GRAV	5689.2810	9:12	14-Apr
1257	1236	GRAV	5686.8920	9:30	14-Apr
1259	1246	GRAV	5686.1170	9:43	14-Apr
1256	1235	GRAV	5687.3380	9:55	14-Apr
1261	1242	GRAV	5686.2020	10:07	14-Apr
1256	1244	GRAV	5686.8080	10:23	14-Apr
1264	1254	GRAV	5685.4830	10:59	14-Apr
1283	1265	GRAV	5680.9300	11:17	14-Apr
1296	1282	GRAV	5677.9710	11:33	14-Apr
1279	1270	GRAV	5681.8610	11:45	14-Apr
1264	1250	GRAV	5684.9220	11:57	14-Apr
1248	1237	GRAV	5687.5290	12:18	14-Apr
1106	1103	GRAVBASE	5720.5790	12:48	14-Apr
1234	1222	GRAV	5691.0390	14:45	14-Apr
1259	1248	GRAV	5686.3880	14:57	14-Apr
1286	1265	GRAV	5681.3530	15:10	14-Apr
1281	1267	GRAV	5682.0420	15:30	14-Apr
1312	1295	GRAV	5675.7450	15:43	14-Apr
1323	1314	GRAV	5672.5450	15:58	14-Apr
1382	1365	GRAV	5660.2740	16:26	14-Apr
1324	1319	GRAV	5672.5120	16:40	14-Apr
1294	1280	GRAV	5679.6390	16:54	14-Apr
1273	1256	GRAV	5683.9410	17:07	14-Apr
1258	1239	GRAV	5687.5930	17:18	14-Apr
1244	1233	GRAV	5688.8110	17:30	14-Apr
1235	1218	GRAV	5691.8240	17:52	14-Apr
1245	1235	GRAV	5689.6790	18:04	14-Apr
1257	1246	GRAV	5686.7370	18:16	14-Apr

1286	1275	GRAV	5681.1020	18:28	14-Apr
1313	1300	GRAV	5675.3590	18:39	14-Apr
1272	1259	GRAV	5683.9310	18:48	14-Apr
1245	1229	GRAV	5689.7260	18:56	14-Apr
1224	1210	GRAV	5693.9550	19:04	14-Apr
1110	1103	GRAVBASE	5720.6450	19:27	14-Apr
1111	1103	GRAVBASE	5720.8850	8:03	15-Apr
1350	1326	GRAV	5668.2660	8:40	15-Apr
1377	1356	GRAV	5661.5870	9:00	15-Apr
1378	1353	GRAV	5661.9640	9:20	15-Apr
1408	1404	GRAV	5654.2930	9:45	15-Apr
1400	1387	GRAV	5656.5680	10:10	15-Apr
1345	1332	GRAV	5668.0460	10:38	15-Apr
1300	1285	GRAV	5677.9260	10:52	15-Apr
1334	1315	GRAV	5670.4630	11:02	15-Apr
1399	1357	GRAV	5657.4360	11:16	15-Apr
1405	1384	GRAV	5655.0570	11:29	15-Apr
1447	1426	GRAV	5645.0760	11:41	15-Apr
1370	1358	GRAV	5661.3080	12:02	15-Apr
1312	1297	GRAV	5675.1020	12:16	15-Apr
1106	1103	GRAVBASE	5720.9380	12:42	15-Apr
1184	1165	GRAV	5702.4420	15:04	15-Apr
1218	1200	GRAV	5696.8720	15:24	15-Apr
1270	1250	GRAV	5685.2640	16:10	15-Apr
1168	1147	GRAV	5707.0170	16:30	15-Apr
1197	1180	GRAV	5702.5000	16:57	15-Apr
1139	1125	GRAV	5713.0470	17:21	15-Apr
1159	1147	GRAV	5706.8150	17:52	15-Apr
1213	1200	GRAV	5696.9240	18:09	15-Apr
1143	1130	GRAV	5710.5190	18:36	15-Apr
1170	1165	GRAV	5704.4270	18:53	15-Apr
1190	1177	GRAV	5701.6190	19:05	15-Apr
1113	1103	GRAVBASE	5720.9840	19:22	15-Apr
1106	1103	GRAVBASE	5721.1990	8:07	16-Apr
1255	1236	GRAV	5688.3780	8:48	16-Apr
1220	1210	GRAV	5695.4220	9:05	16-Apr
1202	1183	GRAV	5699.7880	9:23	16-Apr
1179	1169	GRAV	5705.0240	9:36	16-Apr
1153	1138	GRAV	5710.3570	9:56	16-Apr
1174	1162	GRAV	5706.1320	10:19	16-Apr
1203	1195	GRAV	5699.9770	10:31	16-Apr
1197	1190	GRAV	5701.4130	10:43	16-Apr
1254	1247	GRAV	5688.9700	10:59	16-Apr
1203	1194	GRAV	5699.3570	11:10	16-Apr
1186	1175	GRAV	5703.1950	11:25	16-Apr
1205	1192	GRAV	5698.8820	11:40	16-Apr
1232	1221	GRAV	5692.7950	11:55	16-Apr
1277	1260	GRAV	5683.5170	12:21	16-Apr
1365	1357	GRAV	5664.1360	12:50	16-Apr
1270	1271	GRAV	5684.5260	13:08	16-Apr
1109	1103	GRAVBASE	5721.2500	13:34	16-Apr

1216	1200	GRAV	5697.7370	15:53	16-Apr
1277	1263	GRAV	5684.6300	16:06	16-Apr
1222	1207	GRAV	5696.2460	16:50	16-Apr
1202	1191	GRAV	5700.8240	17:12	16-Apr
1180	1173	GRAV	5705.1380	17:31	16-Apr
1175	1160	GRAV	5706.2500	17:45	16-Apr
1179	1162	GRAV	5705.7930	17:57	16-Apr
1147	1134	GRAV	5711.3900	18:08	16-Apr
1107	1103	GRAVBASE	5721.3360	18:35	16-Apr
1107	1103	GRAVBASE	5721.5770	8:13	17-Apr
1116	1103	GRAV	5717.1470	8:47	17-Apr
1113	1104	GRAV	5717.4340	8:56	17-Apr
1134	1125	GRAV	5713.9660	9:16	17-Apr
1232	1207	GRAV	5693.9520	9:38	17-Apr
1184	1159	GRAV	5705.5800	9:54	17-Apr
1142	1124	GRAV	5714.6150	10:28	17-Apr
1151	1125	GRAV	5712.3060	10:40	17-Apr
1137	1115	GRAV	5715.2600	10:55	17-Apr
1222	1200	GRAV	5696.7360	11:11	17-Apr
1227	1213	GRAV	5695.8460	11:26	17-Apr
1149	1137	GRAV	5711.0060	11:45	17-Apr
1178	1155	GRAV	5705.9430	12:02	17-Apr
1211	1188	GRAV	5698.7640	12:34	17-Apr
1105	1103	GRAVBASE	5721.6780	14:53	17-Apr
1269	1250	GRAV	5687.2620	15:43	17-Apr
1261	1246	GRAV	5688.5450	15:56	17-Apr
1242	1235	GRAV	5692.6760	16:07	17-Apr
1205	1193	GRAV	5699.9840	16:33	17-Apr
1217	1204	GRAV	5697.7340	16:45	17-Apr
1236	1223	GRAV	5693.5690	16:58	17-Apr
1217	1210	GRAV	5696.3060	17:16	17-Apr
1200	1188	GRAV	5700.8910	17:26	17-Apr
1195	1180	GRAV	5701.9140	17:41	17-Apr
1202	1188	GRAV	5700.4480	17:56	17-Apr
1172	1162	GRAV	5706.3170	18:19	17-Apr
1203	1178	GRAV	5702.7270	18:34	17-Apr
1191	1170	GRAV	5704.2930	18:45	17-Apr
1163	1152	GRAV	5708.4970	18:59	17-Apr
1116	1103	GRAVBASE	5721.7930	19:18	17-Apr
1116	1103	GRAVBASE	5721.9970	8:17	18-Apr
1324	1308	GRAV	5675.5990	8:57	18-Apr
1284	1263	GRAV	5682.9900	9:09	18-Apr
1259	1240	GRAV	5687.6880	9:35	18-Apr
1282	1268	GRAV	5683.8710	9:50	18-Apr
1270	1252	GRAV	5687.3690	10:03	18-Apr
1288	1273	GRAV	5683.2940	10:18	18-Apr
1252	1239	GRAV	5690.0020	10:39	18-Apr
1251	1241	GRAV	5690.9480	10:57	18-Apr
1261	1244	GRAV	5688.7680	11:07	18-Apr
1216	1197	GRAV	5698.7830	11:18	18-Apr
1216	1207	GRAV	5697.8020	11:29	18-Apr

1211	1205	GRAV	5689.3140	11:40	18-Apr
1230	1213	GRAV	5694.8990	12:06	18-Apr
1110	1103	GRAVBASE	5722.0570	12:37	18-Apr
1329	1317	GRAV	5674.8250	14:31	18-Apr
1273	1260	GRAV	5685.4820	14:46	18-Apr
1297	1274	GRAV	5680.4400	15:00	18-Apr
1396	1368	GRAV	5657.7340	15:26	18-Apr
1351	1342	GRAV	5669.3270	15:46	18-Apr
1387	1355	GRAV	5661.6040	16:03	18-Apr
1324	1297	GRAV	5675.9240	16:23	18-Apr
1301	1290	GRAV	5680.4120	16:44	18-Apr
1304	1300	GRAV	5678.8850	16:56	18-Apr
1273	1254	GRAV	5686.7490	17:10	18-Apr
1276	1270	GRAV	5685.1390	17:31	18-Apr
1272	1254	GRAV	5686.1430	17:47	18-Apr
1236	1213	GRAV	5694.2860	18:00	18-Apr
1263	1245	GRAV	5687.1570	18:16	18-Apr
1111	1103	GRAVBASE	5722.1350	18:50	18-Apr
1104	1103	GRAVBASE	5722.3750	8:44	19-Apr
1287	1277	GRAV	5682.7190	9:13	19-Apr
1315	1295	GRAV	5677.5780	9:24	19-Apr
1358	1342	GRAV	5669.1820	9:40	19-Apr
1384	1365	GRAV	5662.8240	9:48	19-Apr
1382	1368	GRAV	5663.6250	10:00	19-Apr
1350	1332	GRAV	5670.2710	10:12	19-Apr
1368	1356	GRAV	5667.0480	10:28	19-Apr
1403	1397	GRAV	5657.6780	10:45	19-Apr
1457	1445	GRAV	5647.2610	10:57	19-Apr
1428	1422	GRAV	5652.1070	11:22	19-Apr
1353	1336	GRAV	5668.4930	11:34	19-Apr
1313	1302	GRAV	5676.3540	11:50	19-Apr
1296	1279	GRAV	5680.0590	12:02	19-Apr
1342	1333	GRAV	5671.4110	12:15	19-Apr
1311	1300	GRAV	5678.3100	12:30	19-Apr
1113	1103	GRAVBASE	5722.4620	13:07	19-Apr
1456	1434	GRAV	5646.4350	16:25	19-Apr
1425	1410	GRAV	5652.9950	16:40	19-Apr
1365	1350	GRAV	5666.7130	16:58	19-Apr
1320	1302	GRAV	5676.1740	17:45	19-Apr
1319	1301	GRAV	5675.7140	18:00	19-Apr
1298	1282	GRAV	5680.6270	18:17	19-Apr
1122	1103	GRAVBASE	5722.4870	18:53	19-Apr
1108	1103	GRAVBASE	5722.7320	8:07	20-Apr
1302	1287	GRAV	5679.7210	8:44	20-Apr
1262	1252	GRAV	5687.5610	8:54	20-Apr
1298	1282	GRAV	5681.2400	9:08	20-Apr
1289	1272	GRAV	5683.4250	9:27	20-Apr
1305	1288	GRAV	5679.8600	9:44	20-Apr
1274	1256	GRAV	5686.8800	9:51	20-Apr
1252	1239	GRAV	5690.9030	10:07	20-Apr
1240	1225	GRAV	5693.5630	10:17	20-Apr

1227	1213	GRAV	5696.6150	10:37	20-Apr
1239	1228	GRAV	5693.6460	10:51	20-Apr
1273	1260	GRAV	5687.0490	11:05	20-Apr
1285	1270	GRAV	5684.2190	11:26	20-Apr
1264	1250	GRAV	5688.0730	11:39	20-Apr
1272	1256	GRAV	5686.5070	11:54	20-Apr
1247	1230	GRAV	5692.8530	12:17	20-Apr
1245	1226	GRAV	5692.1370	12:28	20-Apr
1241	1223	GRAV	5692.3330	12:41	20-Apr
1268	1247	GRAV	5687.8890	12:55	20-Apr
1114	1103	GRAVBASE	5722.9270	14:01	20-Apr
1117	1103	GRAVBASE	5723.1740	7:51	21-Apr
1379	1360	GRAV	5663.0760	8:45	21-Apr
1429	1417	GRAV	5650.5560	9:02	21-Apr
1381	1365	GRAV	5662.3730	9:23	21-Apr
1369	1360	GRAV	5664.4770	9:46	21-Apr
1301	1287	GRAV	5680.0310	10:00	21-Apr
1246	1238	GRAV	5690.9330	10:13	21-Apr
1226	1220	GRAV	5695.4430	10:25	21-Apr
1263	1248	GRAV	5688.3380	10:47	21-Apr
1320	1308	GRAV	5675.0450	11:02	21-Apr
1295	1277	GRAV	5681.4190	11:13	21-Apr
1253	1239	GRAV	5690.8620	11:29	21-Apr
1225	1208	GRAV	5697.5280	11:44	21-Apr
1114	1103	GRAVBASE	5723.2070	13:46	21-Apr
1241	1218	GRAV	5694.7500	15:45	21-Apr
1235	1223	GRAV	5694.7310	16:19	21-Apr
1223	1225	GRAV	5694.4430	16:34	21-Apr
1215	1230	GRAV	5693.7610	16:49	21-Apr
1116	1103	GRAVBASE	5723.2370	18:08	21-Apr
1110	1103	GRAVBASE	5723.6010	9:08	22-Apr
1218	1195	GRAV	5700.0680	10:12	22-Apr
1246	1235	GRAV	5693.8020	10:31	22-Apr
1242	1230	GRAV	5694.7850	10:42	22-Apr
1187	1173	GRAV	5705.6180	10:53	22-Apr
1109	1103	GRAVBASE	5723.6300	12:44	22-Apr
1169	1135	GRAV	5710.9880	14:57	22-Apr
1087	1060	GRAV	5728.6550	15:09	22-Apr
1090	1085	GRAV	5727.6890	15:28	22-Apr
1120	1093	GRAV	5722.4270	15:47	22-Apr
1156	1127	GRAV	5715.6830	16:02	22-Apr
1171	1155	GRAV	5712.3590	16:12	22-Apr
1180	1140	GRAV	5713.0770	16:20	22-Apr
1144	1123	GRAV	5719.0140	16:29	22-Apr
1151	1185	GRAV	5716.4860	16:43	22-Apr
1142	1127	GRAV	5718.2230	16:50	22-Apr
1123	1104	GRAV	5723.0650	17:06	22-Apr
1191	1187	GRAV	5707.2970	17:23	22-Apr
1149	1138	GRAV	5716.3580	17:35	22-Apr
1162	1137	GRAV	5715.0460	17:54	22-Apr
1106	1100	GRAV	5725.1200	18:07	22-Apr

1098		1093	GRAV	5726.4010	18:16	22-Apr
1114		1107	GRAV	5723.8470	18:28	22-Apr
1120		1117	GRAV	5724.4570	18:36	22-Apr
1101		1093	GRAV	5726.2400	18:42	22-Apr
1110		1103	GRAVBASE	5723.7670	18:50	22-Apr
1110		1103	GRAVBASE	5723.6010	9:08	23-Apr
1244		1217	GRAV	5693.6220	9:21	23-Apr
1250		1233	GRAV	5691.9950	9:32	23-Apr
1260		1238	GRAV	5690.3400	9:39	23-Apr
1260		1243	GRAV	5690.1530	9:47	23-Apr
1267		1248	GRAV	5688.8670	10:06	23-Apr
1271		1252	GRAV	5688.1350	10:13	23-Apr
1264		1246	GRAV	5689.6210	10:32	23-Apr
1257		1238	GRAV	5690.9300	10:44	23-Apr
1253		1240	GRAV	5691.8000	10:55	23-Apr
1248		1236	GRAV	5692.3880	11:12	23-Apr
1246		1235	GRAV	5692.8670	11:30	23-Apr
1252		1238	GRAV	5691.5270	11:40	23-Apr
1256		1243	GRAV	5691.1140	11:48	23-Apr
1258		1247	GRAV	5690.3350	11:53	23-Apr
1255		1252	GRAV	5690.0770	11:58	23-Apr
1109		1103	GRAVBASE	5723.6300	12:44	22-Apr

HEURE	MINUTES	LE TEMPS EN SECONDES	DIFFERENCE DU TEMPS ENTRE DEUX STATIONS EN SECONDES	A	CORRECTION DE CHAQUE MESURE PENDANT UNE JOURNEE
14	17	51420	0	0	5719.865000
14	35	52500	1080	-3.58306E-06	5718.344870
14	56	53760	2340	-3.58306E-06	5720.854384
15	26	55560	4140	-3.58306E-06	5720.484834
15	58	57480	6060	-3.58306E-06	5716.723713
16	25	59100	7680	-3.58306E-06	5712.598518
17	18	62280	10860	-3.58306E-06	5719.547912
17	58	64680	13260	-3.58306E-06	5715.030511
18	22	66120	14700	-3.58306E-06	5711.405671
19	24	69840	18420	-3.58306E-06	5719.865000
8	40	31200	0	0	5719.899000
8	54	32040	840	2.70546E-06	5722.300727
14	23	51780	20580	2.70546E-06	5722.454322
14	40	52800	21600	2.70546E-06	5718.287562
15	2	54120	22920	2.70546E-06	5721.384991
15	15	54900	23700	2.70546E-06	5721.898881
15	30	55800	24600	2.70546E-06	5721.268446
15	40	56400	25200	2.70546E-06	5719.630822
15	56	57360	26160	2.70546E-06	5713.062225
16	18	58680	27480	2.70546E-06	5720.748654
16	31	59460	28260	2.70546E-06	5721.609544

16	41	60060	28860	2.70546E-06	5721.707920
17	12	61920	30720	2.70546E-06	5721.686888
17	31	63060	31860	2.70546E-06	5721.873804
17	45	63900	32700	2.70546E-06	5715.352531
18	7	65220	34020	2.70546E-06	5719.505960
18	20	66000	34800	2.70546E-06	5723.815850
18	39	67140	35940	2.70546E-06	5724.298766
19	33	70380	39180	2.70546E-06	5719.899000
7	35	27300	0	0	5720.005000
8	21	30060	2760	9.13242E-06	5707.993795
8	36	30960	3660	9.13242E-06	5716.549575
8	53	31980	4680	9.13242E-06	5719.119260
9	16	33360	6060	9.13242E-06	5710.342658
9	40	34800	7500	9.13242E-06	5721.974507
9	57	35820	8520	9.13242E-06	5723.008192
10	13	36780	9480	9.13242E-06	5722.615425
10	34	38040	10740	9.13242E-06	5713.017918
10	59	39540	12240	9.13242E-06	5722.334219
11	24	41040	13740	9.13242E-06	5722.290521
11	46	42360	15060	9.13242E-06	5712.854466
12	4	43440	16140	9.13242E-06	5717.678603
12	20	44400	17100	9.13242E-06	5721.055836
12	48	46080	18780	9.13242E-06	5711.771493
13	9	47340	20040	9.13242E-06	5699.374986
13	27	48420	21120	9.13242E-06	5701.920123
14	53	53580	26280	9.13242E-06	5720.005000
15	43	56580	29280	5.88373E-06	5694.755724
16	22	58920	31620	5.88373E-06	5702.214956
16	41	60060	32760	5.88373E-06	5704.612249
17	3	61380	34080	5.88373E-06	5702.192482
17	40	63600	36300	5.88373E-06	5714.863421
17	58	64680	37380	5.88373E-06	5706.006066
18	21	66060	38760	5.88373E-06	5708.900947
18	38	67080	39780	5.88373E-06	5707.919945
18	52	67920	40620	5.88373E-06	5716.846003
19	3	68580	41280	5.88373E-06	5717.734120
19	26	69960	42660	5.88373E-06	5720.005000
7	58	28680	0	0	5720.497000
8	39	31140	2460	4.71264E-06	5689.108407
8	58	32280	3600	4.71264E-06	5690.119034
9	12	33120	4440	4.71264E-06	5689.260076
9	30	34200	5520	4.71264E-06	5686.865986
9	43	34980	6300	4.71264E-06	5686.087310
9	55	35700	7020	4.71264E-06	5687.304917
10	7	36420	7740	4.71264E-06	5686.165524
10	23	37380	8700	4.71264E-06	5686.767000
10	59	39540	10860	4.71264E-06	5685.431821
11	17	40620	11940	4.71264E-06	5680.873731
11	33	41580	12900	4.71264E-06	5677.910207
11	45	42300	13620	4.71264E-06	5681.796814
11	57	43020	14340	4.71264E-06	5684.854421

12	18	44280	15600	4.71264E-06	5687.455483
12	48	46080	17400	4.71264E-06	5720.497000
14	45	53100	24420	3.58007E-06	5690.951575
14	57	53820	25140	3.58007E-06	5686.297997
15	10	54600	25920	3.58007E-06	5681.260205
15	30	55800	27120	3.58007E-06	5681.944909
15	43	56580	27900	3.58007E-06	5675.645116
15	58	57480	28800	3.58007E-06	5672.441894
16	26	59160	30480	3.58007E-06	5660.164880
16	40	60000	31320	3.58007E-06	5672.399872
16	54	60840	32160	3.58007E-06	5679.523865
17	7	61620	32940	3.58007E-06	5683.823073
17	18	62280	33600	3.58007E-06	5687.472710
17	30	63000	34320	3.58007E-06	5688.688132
17	52	64320	35640	3.58007E-06	5691.696406
18	4	65040	36360	3.58007E-06	5689.548829
18	16	65760	37080	3.58007E-06	5686.604251
18	28	66480	37800	3.58007E-06	5680.966673
18	39	67140	38460	3.58007E-06	5675.221311
18	48	67680	39000	3.58007E-06	5683.791377
18	56	68160	39480	3.58007E-06	5689.584659
19	4	68640	39960	3.58007E-06	5693.811940
19	27	70020	41340	3.58007E-06	5720.497000
8	3	28980	0	0	5720.885000
8	40	31200	2220	3.16607E-06	5668.258971
9	0	32400	3420	3.16607E-06	5661.576172
9	20	33600	4620	3.16607E-06	5661.949373
9	45	35100	6120	3.16607E-06	5654.273624
10	10	36600	7620	3.16607E-06	5656.543875
10	38	38280	9300	3.16607E-06	5668.016556
10	52	39120	10140	3.16607E-06	5677.893896
11	2	39720	10740	3.16607E-06	5670.428996
11	16	40560	11580	3.16607E-06	5657.399337
11	29	41340	12360	3.16607E-06	5655.017867
11	41	42060	13080	3.16607E-06	5645.034588
12	2	43320	14340	3.16607E-06	5661.262599
12	16	44160	15180	3.16607E-06	5675.053939
12	42	45720	16740	3.16607E-06	5720.885000
15	4	54240	25260	2.43004E-06	5702.380617
15	24	55440	26460	2.43004E-06	5696.807701
16	10	58200	29220	2.43004E-06	5685.192994
16	30	59400	30420	2.43004E-06	5706.943078
16	57	61020	32040	2.43004E-06	5702.422141
17	21	62460	33480	2.43004E-06	5712.965642
17	52	64320	35340	2.43004E-06	5706.729122
18	9	65340	36360	2.43004E-06	5696.835644
18	36	66960	37980	2.43004E-06	5710.426707
18	53	67980	39000	2.43004E-06	5704.332228
19	5	68700	39720	2.43004E-06	5701.522479
19	22	69720	40740	2.43004E-06	5720.885000
8	7	29220	0	0	5721.199000

8	48	31680	2460	2.59939E-06	5688.371606
9	5	32700	3480	2.59939E-06	5695.412954
9	23	33780	4560	2.59939E-06	5699.776147
9	36	34560	5340	2.59939E-06	5705.010119
9	56	35760	6540	2.59939E-06	5710.340000
10	19	37140	7920	2.59939E-06	5706.111413
10	31	37860	8640	2.59939E-06	5699.954541
10	43	38580	9360	2.59939E-06	5701.388670
10	59	39540	10320	2.59939E-06	5688.943174
11	10	40200	10980	2.59939E-06	5699.328459
11	25	41100	11880	2.59939E-06	5703.164119
11	40	42000	12780	2.59939E-06	5698.848780
11	55	42900	13680	2.59939E-06	5692.759440
12	21	44460	15240	2.59939E-06	5683.477385
12	50	46200	16980	2.59939E-06	5664.091862
13	8	47280	18060	2.59939E-06	5684.479055
13	34	48840	19620	2.59939E-06	5721.199000
15	53	57180	27960	3.63588E-06	5697.635341
16	6	57960	28740	3.63588E-06	5684.525505
16	50	60600	31380	3.63588E-06	5696.131906
17	12	61920	32700	3.63588E-06	5700.705107
17	31	63060	33840	3.63588E-06	5705.014962
17	45	63900	34680	3.63588E-06	5706.123908
17	57	64620	35400	3.63588E-06	5705.664290
18	8	65280	36060	3.63588E-06	5711.258890
18	35	66900	37680	3.63588E-06	5721.199000
8	13	29580	0	0	5721.577000
8	47	31620	2040	4.20833E-06	5717.138415
8	56	32160	2580	4.20833E-06	5717.423143
9	16	33360	3780	4.20833E-06	5713.950093
9	38	34680	5100	4.20833E-06	5693.930538
9	54	35640	6060	4.20833E-06	5705.554498
10	28	37680	8100	4.20833E-06	5714.580913
10	40	38400	8820	4.20833E-06	5712.268883
10	55	39300	9720	4.20833E-06	5715.219095
11	11	40260	10680	4.20833E-06	5696.691055
11	26	41160	11580	4.20833E-06	5695.797268
11	45	42300	12720	4.20833E-06	5710.952470
12	2	43320	13740	4.20833E-06	5705.885178
12	34	45240	15660	4.20833E-06	5698.698098
14	53	53580	24000	4.20833E-06	5721.577000
15	43	56580	27000	5.41353E-06	5687.115835
15	56	57360	27780	5.41353E-06	5688.394612
16	7	58020	28440	5.41353E-06	5692.522039
16	33	59580	30000	5.41353E-06	5699.821594
16	45	60300	30720	5.41353E-06	5697.567696
16	58	61080	31500	5.41353E-06	5693.398474
17	16	62160	32580	5.41353E-06	5696.129627
17	26	62760	33180	5.41353E-06	5700.711379
17	41	63660	34080	5.41353E-06	5701.729507
17	56	64560	34980	5.41353E-06	5700.258635

18	19	65940	36360	5.41353E-06	5706.120164
18	34	66840	37260	5.41353E-06	5702.525292
18	45	67500	37920	5.41353E-06	5704.087719
18	59	68340	38760	5.41353E-06	5708.287171
19	18	69480	39900	5.41353E-06	5721.577000
8	17	29820	0	0	5721.997000
8	57	32220	2400	3.84615E-06	5675.589769
9	9	32940	3120	3.84615E-06	5682.978000
9	35	34500	4680	3.84615E-06	5687.670000
9	50	35400	5580	3.84615E-06	5683.849538
10	3	36180	6360	3.84615E-06	5687.344538
10	18	37080	7260	3.84615E-06	5683.266077
10	39	38340	8520	3.84615E-06	5689.969231
10	57	39420	9600	3.84615E-06	5690.911077
11	7	40020	10200	3.84615E-06	5688.728769
11	18	40680	10860	3.84615E-06	5698.741231
11	29	41340	11520	3.84615E-06	5697.757692
11	40	42000	12180	3.84615E-06	5689.267154
12	6	43560	13740	3.84615E-06	5694.846154
12	37	45420	15600	3.84615E-06	5721.997000
14	31	52260	22440	3.63349E-06	5674.743464
14	46	53160	23340	3.63349E-06	5685.397194
15	0	54000	24180	3.63349E-06	5680.352142
15	26	55560	25740	3.63349E-06	5657.640474
15	46	56760	26940	3.63349E-06	5669.229114
16	3	57780	27960	3.63349E-06	5661.502408
16	23	58980	29160	3.63349E-06	5675.818047
16	44	60240	30420	3.63349E-06	5680.301469
16	56	60960	31140	3.63349E-06	5678.771853
17	10	61800	31980	3.63349E-06	5686.632801
17	31	63060	33240	3.63349E-06	5685.018223
17	47	64020	34200	3.63349E-06	5686.018735
18	0	64800	34980	3.63349E-06	5694.158900
18	16	65760	35940	3.63349E-06	5687.026412
18	50	67800	37980	3.63349E-06	5721.997000
8	44	31440	0	0	5722.375000
9	13	33180	1740	5.51331E-06	5682.709407
9	24	33840	2400	5.51331E-06	5677.564768
9	40	34800	3360	5.51331E-06	5669.163475
9	48	35280	3840	5.51331E-06	5662.802829
10	0	36000	4560	5.51331E-06	5663.599859
10	12	36720	5280	5.51331E-06	5670.241890
10	28	37680	6240	5.51331E-06	5667.013597
10	45	38700	7260	5.51331E-06	5657.637973
10	57	39420	7980	5.51331E-06	5647.217004
11	22	40920	9480	5.51331E-06	5652.054734
11	34	41640	10200	5.51331E-06	5668.436764
11	50	42600	11160	5.51331E-06	5676.292471
12	2	43320	11880	5.51331E-06	5679.993502
12	15	44100	12660	5.51331E-06	5671.341202
12	30	45000	13560	5.51331E-06	5678.235240

13	7	47220	15780	5.51331E-06	5722.375000
16	25	59100	27660	3.06513E-06	5646.350218
16	40	60000	28560	3.06513E-06	5652.907460
16	58	61080	29640	3.06513E-06	5666.622149
17	45	63900	32460	3.06513E-06	5676.074506
18	0	64800	33360	3.06513E-06	5675.611747
18	17	65820	34380	3.06513E-06	5680.521621
18	53	67980	36540	3.06513E-06	5722.375000
8	7	29220	0	0	5722.732000
8	44	31440	2220	9.18079E-06	5679.700619
8	54	32040	2820	9.18079E-06	5687.535110
9	8	32880	3660	9.18079E-06	5681.206398
9	27	34020	4800	9.18079E-06	5683.380932
9	44	35040	5820	9.18079E-06	5679.806568
9	51	35460	6240	9.18079E-06	5686.822712
10	7	36420	7200	9.18079E-06	5690.836898
10	17	37020	7800	9.18079E-06	5693.491390
10	37	38220	9000	9.18079E-06	5696.532373
10	51	39060	9840	9.18079E-06	5693.555661
11	5	39900	10680	9.18079E-06	5686.950949
11	26	41160	11940	9.18079E-06	5684.109381
11	39	41940	12720	9.18079E-06	5687.956220
11	54	42840	13620	9.18079E-06	5686.381958
12	17	44220	15000	9.18079E-06	5692.715288
12	28	44880	15660	9.18079E-06	5691.993229
12	41	45660	16440	9.18079E-06	5692.182068
12	55	46500	17280	9.18079E-06	5687.730356
14	1	50460	21240	9.18079E-06	5722.732000
7	51	28260	0	0	5723.174000
8	45	31500	3240	1.5493E-06	5663.070980
9	2	32520	4260	1.5493E-06	5650.549400
9	23	33780	5520	1.5493E-06	5662.364448
9	46	35160	6900	1.5493E-06	5664.466310
10	0	36000	7740	1.5493E-06	5680.019008
10	13	36780	8520	1.5493E-06	5690.919800
10	25	37500	9240	1.5493E-06	5695.428685
10	47	38820	10560	1.5493E-06	5688.321639
11	2	39720	11460	1.5493E-06	5675.027245
11	13	40380	12120	1.5493E-06	5681.400223
11	29	41340	13080	1.5493E-06	5690.841735
11	44	42240	13980	1.5493E-06	5697.506341
13	46	49560	21300	1.5493E-06	5723.174000
15	45	56700	28440	1.70178E-06	5694.701601
16	19	58740	30480	1.70178E-06	5694.679130
16	34	59640	31380	1.70178E-06	5694.389598
16	49	60540	32280	1.70178E-06	5693.706066
18	8	65280	37020	1.70178E-06	5723.174000
9	8	32880	0	0	5723.601000
10	12	36720	3840	2.23765E-06	5700.059407
10	31	37860	4980	2.23765E-06	5693.790856
10	42	38520	5640	2.23765E-06	5694.772380

10	53	39180	6300	2.23765E-06	5705.603903
12	44	45840	12960	2.23765E-06	5723.601000
14	57	53820	20940	4.75372E-06	5710.888457
15	9	54540	21660	4.75372E-06	5728.552034
15	28	55680	22800	4.75372E-06	5727.580615
15	47	56820	23940	4.75372E-06	5722.313196
16	2	57720	24840	4.75372E-06	5715.564918
16	12	58320	25440	4.75372E-06	5712.238065
16	20	58800	25920	4.75372E-06	5712.953784
16	29	59340	26460	4.75372E-06	5718.888216
16	43	60180	27300	4.75372E-06	5716.356223
16	50	60600	27720	4.75372E-06	5718.091227
17	6	61560	28680	4.75372E-06	5722.928663
17	23	62580	29700	4.75372E-06	5707.155814
17	35	63300	30420	4.75372E-06	5716.213392
17	54	64440	31560	4.75372E-06	5714.895973
18	7	65220	32340	4.75372E-06	5724.966265
18	16	65760	32880	4.75372E-06	5726.244698
18	28	66480	33600	4.75372E-06	5723.687275
18	36	66960	34080	4.75372E-06	5724.294993
18	42	67320	34440	4.75372E-06	5726.076282
18	50	67800	34920	4.75372E-06	5723.601000
9	8	32880	0	0	5723.601000
9	21	33660	780	2.23765E-06	5693.620255
9	32	34320	1440	2.23765E-06	5691.991778
9	39	34740	1860	2.23765E-06	5690.335838
9	47	35220	2340	2.23765E-06	5690.147764
10	6	36360	3480	2.23765E-06	5688.859213
10	13	36780	3900	2.23765E-06	5688.126273
10	32	37920	5040	2.23765E-06	5689.609722
10	44	38640	5760	2.23765E-06	5690.917111
10	55	39300	6420	2.23765E-06	5691.785634
11	12	40320	7440	2.23765E-06	5692.371352
11	30	41400	8520	2.23765E-06	5692.847935
11	40	42000	9120	2.23765E-06	5691.506593
11	48	42480	9600	2.23765E-06	5691.092519
11	53	42780	9900	2.23765E-06	5690.312847
11	58	43080	10200	2.23765E-06	5690.054176
12	44	45840	12960	2.23765E-06	5723.601000

LA CORRECTION DES MESURES PAR APPORT A UNE SUEL BASE	SD	ETC	SIN(φ)	SIN(2φ)	SIN²(φ)
5719.865000	0.017	0.032	0.5473434	0.9161523	0.2995848085
5718.344870	0.013	0.079	0.5473410	0.9161500	0.2995821436
5720.854384	0.018	0.004	0.5473407	0.9161497	0.2995818771
5720.484834	0.015	-0.017	0.5473407	0.9161497	0.2995818771
5716.723713	0.016	-0.038	0.5473400	0.9161490	0.2995810776
5712.598518	0.015	-0.052	0.5473398	0.9161488	0.2995808111
5719.547912	0.014	-0.072	0.5473419	0.9161509	0.2995832096

5715.030511	0.021	-0.077	0.5473412	0.9161502	0.2995824101
5711.405671	0.014	-0.074	0.5473410	0.9161500	0.2995821436
5719.865000	0.017	-0.054	0.5473458	0.9161546	0.2995874735
5719.865000	0.020	0.000	0.5473432	0.9161520	0.2995845420
5722.266727	0.065	0.012	0.5473429	0.9161518	0.2995842756
5722.420322	0.022	0.044	0.5473456	0.9161544	0.2995872070
5718.253562	0.031	0.030	0.5473432	0.9161520	0.2995845420
5721.350991	0.017	0.013	0.5473427	0.9161516	0.2995840091
5721.864881	0.045	0.003	0.5473120	0.9161222	0.2995504309
5721.234446	0.031	-0.009	0.5473110	0.9161213	0.2995493649
5719.596822	0.018	-0.017	0.5473113	0.9161215	0.2995496314
5713.028225	0.017	-0.029	0.5473108	0.9161210	0.2995490984
5720.714654	0.014	-0.044	0.5473113	0.9161215	0.2995496314
5721.575544	0.013	-0.052	0.5473093	0.9161196	0.2995474995
5721.673920	0.020	-0.057	0.5473084	0.9161187	0.2995464336
5721.652888	0.043	-0.072	0.5473023	0.9161129	0.2995397714
5721.839804	0.023	-0.078	0.5473045	0.9161150	0.2995421698
5715.318531	0.018	-0.081	0.5473030	0.9161136	0.2995405708
5719.471960	0.014	-0.083	0.5473049	0.9161154	0.2995427027
5723.781850	0.015	-0.083	0.5473086	0.9161189	0.2995467000
5724.264766	0.016	-0.081	0.5473091	0.9161194	0.2995472330
5719.865000	0.016	-0.065	0.5473437	0.9161525	0.2995850750
5719.865000	0.015	-0.031	0.5473432	0.9161520	0.2995845420
5707.853795	0.013	-0.010	0.5472760	0.9160877	0.2995109912
5716.409575	0.011	0.002	0.5472752	0.9160870	0.2995101918
5718.979260	0.021	0.017	0.5472743	0.9160860	0.2995091259
5710.202658	0.014	0.037	0.5472779	0.9160895	0.2995131231
5721.834507	0.036	0.057	0.5472677	0.9160797	0.2995019310
5722.868192	0.015	0.070	0.5472762	0.9160879	0.2995112577
5722.475425	0.018	0.082	0.5472769	0.9160886	0.2995120571
5712.877918	0.014	0.096	0.5472769	0.9160886	0.2995120571
5722.194219	0.015	0.110	0.5472750	0.9160867	0.2995099253
5722.150521	0.013	0.121	0.5472404	0.9160536	0.2994720860
5712.714466	0.017	0.127	0.5472412	0.9160543	0.2994728854
5717.538603	0.029	0.129	0.5472392	0.9160524	0.2994707537
5720.915836	0.025	0.129	0.5472395	0.9160527	0.2994710201
5711.631493	0.017	0.125	0.5472390	0.9160522	0.2994704872
5699.234986	0.015	0.119	0.5472390	0.9160522	0.2994704872
5701.780123	0.016	0.111	0.5472395	0.9160527	0.2994710201
5719.865000	0.018	0.053	0.5473437	0.9161525	0.2995850750
5694.615724	0.014	0.010	0.5472363	0.9160496	0.2994675560
5702.074956	0.015	-0.022	0.5472380	0.9160513	0.2994694213
5704.472249	0.013	-0.036	0.5472375	0.9160508	0.2994688884
5702.052482	0.015	-0.051	0.5472699	0.9160818	0.2995043293
5714.723421	0.014	-0.070	0.5472718	0.9160837	0.2995064611
5705.866066	0.016	-0.078	0.5472390	0.9160522	0.2994704872
5708.760947	0.014	-0.084	0.5472382	0.9160515	0.2994696878
5707.779945	0.015	-0.086	0.5472380	0.9160513	0.2994694213
5716.706003	0.016	-0.086	0.5472716	0.9160835	0.2995061946
5717.594120	0.016	-0.086	0.5472706	0.9160825	0.2995051287
5719.865000	0.018	-0.082	0.5473429	0.9161518	0.2995842756

5719.865000	0.014	-0.042	0.5473434	0.9161523	0.2995848085
5688.476407	0.017	-0.010	0.5466988	0.9155339	0.2988796265
5689.487034	0.018	0.006	0.5466996	0.9155346	0.2988804255
5688.628076	0.027	0.019	0.5466988	0.9155339	0.2988796265
5686.233986	0.019	0.035	0.5466988	0.9155339	0.2988796265
5685.455310	0.018	0.046	0.5467320	0.9155658	0.2989158464
5686.672917	0.015	0.057	0.5467317	0.9155655	0.2989155801
5685.533524	0.019	0.067	0.5467300	0.9155639	0.2989137158
5686.135000	0.016	0.080	0.5467288	0.9155627	0.2989123842
5684.799821	0.018	0.106	0.5467281	0.9155620	0.2989115852
5680.241731	0.015	0.117	0.5467310	0.9155648	0.2989147811
5677.278207	0.030	0.125	0.5467305	0.9155644	0.2989142485
5681.164814	0.016	0.130	0.5466979	0.9155330	0.2988785613
5684.222421	0.021	0.134	0.5467001	0.9155351	0.2988809581
5686.823483	0.013	0.139	0.5466998	0.9155349	0.2988806918
5719.865000	0.018	0.141	0.5473439	0.9161527	0.2995853415
5690.319575	0.019	0.092	0.5467649	0.9155973	0.2989518012
5685.665997	0.017	0.083	0.5467649	0.9155973	0.2989518012
5680.628205	0.018	0.072	0.5467641	0.9155966	0.2989510022
5681.312909	0.030	0.055	0.5467631	0.9155957	0.2989499369
5675.013116	0.030	0.044	0.5467658	0.9155983	0.2989528666
5671.809894	0.019	0.031	0.5467656	0.9155980	0.2989526002
5659.532880	0.021	0.007	0.5467965	0.9156277	0.2989864255
5671.767872	0.013	-0.005	0.5467958	0.9156270	0.2989856265
5678.891865	0.022	-0.016	0.5467951	0.9156263	0.2989848275
5683.191073	0.017	-0.027	0.5467946	0.9156259	0.2989842948
5686.840710	0.019	-0.035	0.5467948	0.9156261	0.2989845611
5688.056132	0.016	-0.043	0.5467953	0.9156266	0.2989850938
5691.064406	0.015	-0.056	0.5468262	0.9156563	0.2990189202
5688.916829	0.016	-0.062	0.5468250	0.9156551	0.2990175884
5685.972251	0.018	-0.068	0.5468257	0.9156558	0.2990183875
5680.334673	0.014	-0.073	0.5468265	0.9156565	0.2990191865
5674.589311	0.021	-0.077	0.5468589	0.9156876	0.2990546122
5683.159377	0.023	-0.079	0.5468581	0.9156869	0.2990538131
5688.952659	0.017	-0.081	0.5468576	0.9156864	0.2990532804
5693.179940	0.016	-0.083	0.5468581	0.9156869	0.2990538131
5719.865000	0.011	-0.084	0.5473437	0.9161525	0.2995850750
5719.865000	0.015	-0.053	0.5473432	0.9161520	0.2995845420
5667.238971	0.039	-0.027	0.5468839	0.9157117	0.2990820479
5660.556172	0.028	-0.011	0.5468506	0.9156797	0.2990455559
5660.929373	0.015	0.007	0.5468189	0.9156493	0.2990109296
5653.253624	0.021	0.023	0.5467856	0.9156172	0.2989744401
5655.523875	0.022	0.051	0.5467536	0.9155866	0.2989395498
5666.996556	0.027	0.075	0.5467210	0.9155552	0.2989038618
5676.873896	0.014	0.087	0.5467213	0.9155555	0.2989041281
5669.408996	0.017	0.094	0.5467544	0.9155873	0.2989403488
5656.379337	0.016	0.105	0.5467873	0.9156189	0.2989763045
5653.997867	0.018	0.113	0.5468184	0.9156488	0.2990103969
5644.014588	0.033	0.121	0.5468423	0.9156717	0.2990364997
5660.242599	0.021	0.131	0.5468859	0.9157136	0.2990841788
5674.033939	0.018	0.137	0.5469178	0.9157442	0.2991190739

5719.865000	0.012	0.125	0.5473434	0.9161523	0.2995848085
5701.360617	0.018	0.108	0.5470612	0.9158818	0.2992759831
5695.787701	0.025	0.094	0.5470588	0.9158795	0.2992733189
5684.172994	0.024	0.057	0.5470904	0.9159098	0.2993079539
5705.923078	0.030	0.036	0.5471219	0.9159399	0.2993423236
5701.402141	0.021	0.016	0.5471552	0.9159719	0.2993788259
5711.945642	0.013	-0.004	0.5471579	0.9159745	0.2993817568
5705.709122	0.020	-0.027	0.5471574	0.9159740	0.2993812240
5695.815644	0.019	-0.037	0.5471231	0.9159411	0.2993436557
5709.406707	0.167	-0.053	0.5471221	0.9159402	0.2993425900
5703.312228	0.013	-0.061	0.5470921	0.9159115	0.2993098189
5700.502479	0.015	-0.066	0.5470929	0.9159122	0.2993106181
5719.865000	0.015	-0.072	0.5473429	0.9161518	0.2995842756
5719.865000	0.013	-0.063	0.5473432	0.9161520	0.2995845420
5687.037606	0.031	-0.039	0.5470603	0.9158809	0.2992749174
5694.078954	0.014	-0.027	0.5470593	0.9158799	0.2992738517
5698.442147	0.013	-0.012	0.5470917	0.9159110	0.2993092860
5703.676119	0.011	-0.002	0.5471238	0.9159418	0.2993444550
5709.006000	0.014	0.015	0.5471598	0.9159764	0.2993838884
5704.777413	0.035	0.035	0.5471594	0.9159759	0.2993833555
5698.620541	0.015	0.045	0.5471591	0.9159757	0.2993830891
5700.054670	0.016	0.056	0.5471620	0.9159785	0.2993862864
5687.609174	0.019	0.069	0.5471289	0.9159467	0.2993500502
5697.994459	0.015	0.078	0.5471292	0.9159470	0.2993503167
5701.830119	0.018	0.089	0.5471279	0.9159458	0.2993489845
5697.514780	0.013	0.100	0.5470951	0.9159143	0.2993130160
5691.425440	0.013	0.110	0.5470615	0.9158820	0.2992762495
5682.143385	0.014	0.125	0.5470291	0.9158510	0.2992408163
5662.757862	0.019	0.138	0.5470284	0.9158503	0.2992400171
5683.145055	0.016	0.143	0.5470617	0.9158823	0.2992765159
5719.865000	0.012	0.147	0.5473439	0.9161527	0.2995853415
5696.301341	0.011	0.100	0.5470987	0.9159178	0.2993170124
5683.191505	0.013	0.091	0.5470982	0.9159173	0.2993164796
5694.797906	0.014	0.058	0.5471630	0.9159794	0.2993873522
5699.371107	0.013	0.041	0.5471947	0.9160097	0.2994219910
5703.680962	0.015	0.026	0.5471949	0.9160100	0.2994222575
5704.789908	0.017	0.015	0.5472112	0.9160256	0.2994401102
5704.330290	0.019	0.006	0.5472141	0.9160284	0.2994433077
5709.924890	0.014	-0.001	0.5471968	0.9160118	0.2994243891
5719.865000	0.010	-0.020	0.5473432	0.9161520	0.2995845420
5719.865000	0.023	0.070	0.5473432	0.9161520	0.2995845420
5715.426415	0.019	-0.059	0.5471934	0.9160086	0.2994206587
5715.711143	0.030	-0.043	0.5471927	0.9160079	0.2994198593
5712.238093	0.020	-0.037	0.5471922	0.9160074	0.2994193264
5692.218538	0.023	-0.023	0.5471925	0.9160076	0.2994195929
5703.842498	0.021	-0.011	0.5471910	0.9160062	0.2994179942
5712.868913	0.014	0.015	0.5471908	0.9160060	0.2994177277
5710.556883	0.015	0.025	0.5471910	0.9160062	0.2994179942
5713.507095	0.016	0.037	0.5471905	0.9160058	0.2994174612
5694.979055	0.015	0.050	0.5471581	0.9159747	0.2993820233
5694.085268	0.014	0.061	0.5471576	0.9159743	0.2993814904

5709.240470	0.017	0.076	0.5471557	0.9159724	0.2993793588
5704.173178	0.023	0.088	0.5471579	0.9159745	0.2993817568
5696.986098	0.017	0.107	0.5471574	0.9159740	0.2993812240
5719.865000	0.015	0.139	0.5473437	0.9161525	0.2995850750
5685.403835	0.030	0.125	0.5469689	0.9157933	0.2991750151
5686.682612	0.030	0.119	0.5469677	0.9157921	0.2991736831
5690.810039	0.021	0.114	0.5469677	0.9157921	0.2991736831
5698.109594	0.025	0.100	0.5470008	0.9158239	0.2992099132
5695.855696	0.039	0.093	0.5470003	0.9158234	0.2992093804
5691.686474	0.017	0.085	0.5469994	0.9158225	0.2992083148
5694.417627	0.029	0.074	0.5470330	0.9158547	0.2992450789
5698.999379	0.018	0.066	0.5470303	0.9158521	0.2992421484
5700.017507	0.016	0.056	0.5470284	0.9158503	0.2992400171
5698.546635	0.021	0.046	0.5470622	0.9158827	0.2992770487
5704.408164	0.022	0.030	0.5470622	0.9158827	0.2992770487
5700.813292	0.018	0.019	0.5470651	0.9158855	0.2992802458
5702.375719	0.028	0.012	0.5470975	0.9159166	0.2993156803
5706.575171	0.021	0.004	0.5471236	0.9159416	0.2993441886
5719.865000	0.018	-0.008	0.5473427	0.9161516	0.2995840091
5719.865000	0.017	-0.071	0.5473429	0.9161518	0.2995842756
5673.457769	0.020	-0.059	0.5469877	0.9158113	0.2991955276
5680.846000	0.016	-0.054	0.5469884	0.9158120	0.2991963268
5685.538000	0.017	-0.042	0.5469874	0.9158110	0.2991952612
5681.717538	0.016	-0.034	0.5469874	0.9158110	0.2991952612
5685.212538	0.024	-0.027	0.5469865	0.9158101	0.2991941956
5681.134077	0.017	-0.017	0.5470181	0.9158405	0.2992288279
5687.837231	0.017	-0.004	0.5470174	0.9158398	0.2992280287
5688.779077	0.018	0.008	0.5470673	0.9158876	0.2992826436
5686.596769	0.016	0.015	0.5470680	0.9158883	0.2992834428
5696.609231	0.017	0.023	0.5470999	0.9159189	0.2993183446
5695.625692	0.018	0.300	0.5470999	0.9159189	0.2993183446
5687.135154	0.015	0.038	0.5471311	0.9159488	0.2993524482
5692.714154	0.015	0.056	0.5471311	0.9159488	0.2993524482
5719.865000	0.022	0.075	0.5473432	0.9161520	0.2995845420
5672.611464	0.030	0.125	0.5469809	0.9158047	0.2991880684
5683.265194	0.022	0.128	0.5469814	0.9158052	0.2991886012
5678.220142	0.016	0.129	0.5470133	0.9158358	0.2992234998
5655.508474	0.014	0.129	0.5470481	0.9158692	0.2992615965
5667.097114	0.018	0.127	0.5470473	0.9158685	0.2992607973
5659.370408	0.022	0.124	0.5470157	0.9158381	0.2992261639
5673.686047	0.019	0.120	0.5469865	0.9158101	0.2991941956
5678.169469	0.016	0.113	0.5469882	0.9158117	0.2991960604
5676.639853	0.012	0.108	0.5469877	0.9158113	0.2991955276
5684.500801	0.015	0.102	0.5470220	0.9158442	0.2992330905
5682.886223	0.017	0.092	0.5470203	0.9158426	0.2992312256
5683.886735	0.019	0.084	0.5470264	0.9158484	0.2992378858
5692.026900	0.021	0.077	0.5470184	0.9158407	0.2992290943
5684.894412	0.014	0.048	0.5469982	0.9158213	0.2992069828
5719.865000	0.021	0.049	0.5473437	0.9161525	0.2995850750
5719.865000	0.018	-0.061	0.5473432	0.9161520	0.2995845420
5680.199407	0.014	-0.056	0.5469168	0.9157433	0.2991180084

5675.054768	0.016	-0.053	0.5469512	0.9157762	0.2991555685
5666.653475	0.013	-0.048	0.5469470	0.9157722	0.2991510399
5660.292829	0.019	-0.046	0.5469205	0.9157468	0.2991220041
5661.089859	0.018	-0.042	0.5469151	0.9157416	0.2991161438
5667.731890	0.030	-0.037	0.5469137	0.9157402	0.2991145455
5664.503597	0.020	-0.030	0.5468820	0.9157098	0.2990799169
5655.127973	0.027	-0.023	0.5468457	0.9156750	0.2990402287
5644.707004	0.022	-0.018	0.5468404	0.9156698	0.2990343688
5649.544734	0.017	-0.005	0.5468749	0.9157030	0.2990721923
5665.926764	0.019	0.002	0.5469042	0.9157311	0.2991041568
5673.782471	0.020	0.011	0.5469263	0.9157524	0.2991283972
5677.483502	0.015	0.018	0.5469633	0.9157879	0.2991688880
5668.831202	0.016	0.025	0.5469631	0.9157877	0.2991686216
5675.725240	0.021	0.034	0.5469563	0.9157811	0.2991611627
5719.865000	0.017	0.054	0.5473437	0.9161525	0.2995850750
5643.840218	0.022	0.116	0.5468153	0.9156458	0.2990069343
5650.397460	0.059	0.115	0.5467892	0.9156207	0.2989784352
5664.112149	0.017	0.114	0.5467624	0.9155950	0.2989491379
5673.564506	0.023	0.106	0.5468150	0.9156455	0.2990066680
5673.101747	0.024	0.100	0.5468506	0.9156797	0.2990455559
5678.011621	0.022	0.095	0.5468908	0.9157182	0.2990895063
5719.865000	0.025	0.081	0.5473437	0.9161525	0.2995850750
5719.865000	0.016	-0.049	0.5473432	0.9161520	0.2995845420
5676.833619	0.020	-0.048	0.5469594	0.9157842	0.2991646258
5684.668110	0.015	-0.048	0.5469599	0.9157846	0.2991651586
5678.339398	0.019	-0.047	0.5469592	0.9157839	0.2991643594
5680.513932	0.049	-0.046	0.5469582	0.9157830	0.2991632938
5676.939568	0.013	-0.044	0.5469285	0.9157545	0.2991307947
5683.955712	0.017	-0.043	0.5469295	0.9157554	0.2991318602
5687.969898	0.019	-0.041	0.5469351	0.9157608	0.2991379870
5690.624390	0.019	-0.039	0.5469363	0.9157619	0.2991393190
5693.665373	0.019	-0.035	0.5469356	0.9157612	0.2991385198
5690.688661	0.016	-0.032	0.5468869	0.9157145	0.2990852443
5684.083949	0.016	-0.029	0.5468912	0.9157187	0.2990900390
5681.242381	0.017	-0.023	0.5468874	0.9157150	0.2990857771
5685.089220	0.018	-0.019	0.5468537	0.9156827	0.2990490186
5683.514958	0.015	-0.014	0.5468537	0.9156827	0.2990490186
5689.848288	0.015	-0.006	0.5468584	0.9156871	0.2990540794
5689.126229	0.016	-0.001	0.5468250	0.9156551	0.2990175884
5689.315068	0.015	0.004	0.5468248	0.9156549	0.2990173220
5684.863356	0.107	0.010	0.5468223	0.9156525	0.2990146585
5719.865000	0.014	0.039	0.5473437	0.9161525	0.2995850750
5719.865000	0.014	-0.026	0.5473429	0.9161518	0.2995842756
5659.761980	0.053	-0.024	0.5467782	0.9156102	0.2989664498
5647.240400	0.014	-0.024	0.5467459	0.9155791	0.2989310272
5659.055448	0.019	-0.025	0.5467113	0.9155459	0.2988932088
5661.157310	0.026	-0.025	0.5467062	0.9155410	0.2988876161
5676.710008	0.014	-0.026	0.5467066	0.9155414	0.2988881487
5687.610800	0.027	-0.026	0.5467103	0.9155449	0.2988921436
5692.119685	0.014	-0.026	0.5467461	0.9155793	0.2989312935
5685.012639	0.013	-0.027	0.5467497	0.9155828	0.2989352885

5671.718245	0.043	-0.027	0.5467500	0.9155831	0.2989355548
5678.091223	0.031	-0.027	0.5467860	0.9156177	0.2989749727
5687.532735	0.026	-0.027	0.5467909	0.9156224	0.2989802996
5694.197341	0.121	-0.026	0.5467826	0.9156144	0.2989712440
5719.865000	0.013	-0.006	0.5473437	0.9161525	0.2995850750
5691.392601	0.022	0.037	0.5469032	0.9157302	0.2991030913
5691.370130	0.020	0.052	0.5469356	0.9157612	0.2991385198
5691.080598	0.013	0.058	0.5469650	0.9157895	0.2991707528
5690.397066	0.021	0.065	0.5469967	0.9158199	0.2992053844
5719.865000	0.020	0.093	0.5473432	0.9161520	0.2995845420
5719.865000	0.019	0.008	0.5473429	0.9161518	0.2995842756
5696.323407	0.023	0.004	0.5471245	0.9159425	0.2993452544
5690.054856	0.027	0.001	0.5471226	0.9159406	0.2993431229
5691.036380	0.014	-0.001	0.5470939	0.9159131	0.2993116839
5701.867903	0.018	-0.003	0.5470929	0.9159122	0.2993106181
5719.865000	0.021	-0.026	0.5473437	0.9161525	0.2995850750
5707.152457	0.022	-0.025	0.5472395	0.9160527	0.2994710201
5724.816034	0.174	-0.022	0.5472752	0.9160870	0.2995101918
5723.844615	0.020	-0.017	0.5473088	0.9161192	0.2995469665
5718.577196	0.027	-0.010	0.5473419	0.9161509	0.2995832096
5711.828918	0.035	-0.004	0.5473753	0.9161828	0.2996197204
5708.502065	0.069	0.000	0.5473782	0.9161856	0.2996229184
5709.217784	0.022	0.004	0.5473797	0.9161870	0.2996245175
5715.152216	0.017	0.008	0.5473787	0.9161861	0.2996234515
5712.620223	0.031	0.014	0.5473794	0.9161868	0.2996242510
5714.355227	0.017	0.018	0.5473777	0.9161852	0.2996223854
5719.192663	0.025	0.026	0.5473787	0.9161861	0.2996234515
5703.419814	0.039	0.035	0.5473797	0.9161870	0.2996245175
5712.477392	0.017	0.041	0.5473797	0.9161870	0.2996245175
5711.159973	0.022	0.052	0.5473787	0.9161861	0.2996234515
5721.230265	0.016	0.059	0.5473797	0.9161870	0.2996245175
5722.508698	0.060	0.063	0.5473811	0.9161884	0.2996261165
5719.951275	0.054	0.069	0.5473807	0.9161880	0.2996255835
5720.558993	0.016	0.014	0.5473797	0.9161870	0.2996245175
5722.340282	0.023	0.075	0.5473495	0.9161581	0.2995914710
5719.865000	0.017	0.080	0.5473434	0.9161523	0.2995848085
5719.865000	0.019	0.008	0.5473429	0.9161518	0.2995842756
5689.884255	0.020	0.094	0.5466285	0.9154663	0.2988026635
5688.255778	0.030	0.101	0.5467064	0.9155412	0.2988878824
5686.599838	0.033	0.105	0.5467154	0.9155498	0.2988977363
5686.411764	0.024	0.108	0.5467220	0.9155562	0.2989049271
5685.123213	0.023	0.117	0.5467288	0.9155627	0.2989123842
5684.390273	0.024	0.119	0.5467322	0.9155660	0.2989161127
5685.873722	0.018	0.124	0.5467286	0.9155625	0.2989121178
5687.181111	0.022	0.126	0.5467203	0.9155545	0.2989030628
5688.049634	0.018	0.126	0.5467130	0.9155475	0.2988950731
5688.635352	0.015	0.124	0.5467057	0.9155405	0.2988870835
5689.111935	0.020	0.121	0.5466991	0.9155342	0.2988798929
5687.770593	0.022	0.118	0.5467064	0.9155412	0.2988878824
5687.356519	0.015	0.115	0.5467132	0.9155477	0.2988953394
5686.576847	0.064	0.113	0.5467193	0.9155536	0.2989019975

5686.318176	0.024	0.110	0.5467264	0.9155604	0.2989097209
5719.865000	0.021	-0.026	0.5473437	0.9161525	0.2995850750

SIN²(2φ)	Gth,	L'ANOMALIE DE L'AIR LIBRE	CORRECTION A L'AIR LIBRE	CORRECTION DE PLATEAU OU DE BOUGUER (Cp)	L'ANOMALIE DE BOUGUER SIMPLE
0.8393350041	979580.6527024180	-973520.4019	340.3858	-120.1608	-973640.5627
0.8393307313	979580.6389065900	-973520.3652	341.9288	-120.7055	-973641.0708
0.8393303040	979580.6375270090	-973520.9403	338.8428	-119.6161	-973640.5565
0.8393303040	979580.6375270090	-973521.6185	338.5342	-119.5072	-973641.1257
0.8393290221	979580.6333882690	-973521.3637	342.5460	-120.9234	-973642.2871
0.8393285949	979580.6320086900	-973517.7725	350.2610	-123.6469	-973641.4194
0.8393324404	979580.6444249170	-973520.7107	340.3858	-120.1608	-973640.8715
0.8393311586	979580.6402861720	-973511.6456	353.9642	-124.9542	-973636.5998
0.8393307313	979580.6389065900	-973518.0464	351.1868	-123.9737	-973642.0202
0.8393392769	979580.6664982810	-973520.4157	340.3858	-120.1608	-973640.5765
0.8393345769	979580.6513228340	-973520.4005	340.3858	-120.1608	-973640.5613
0.8393341496	979580.6499432500	-973521.392	336.9912	-118.9625	-973640.3545
0.8393388497	979580.6651186930	-973522.488	335.7568	-118.5267	-973641.0147
0.8393345769	979580.6513228340	-973518.3088	344.0890	-121.4681	-973639.7769
0.8393337223	979580.6485636660	-973521.9978	337.2998	-119.0714	-973641.0692
0.8392798810	979580.4747389590	-973523.1617	335.4482	-118.4178	-973641.5794
0.8392781716	979580.4692208070	-973522.8608	336.3740	-118.7446	-973641.6054
0.8392785989	979580.4706003440	-973521.4138	339.4600	-119.8340	-973641.2478
0.8392777442	979580.4678412700	-973519.6474	347.7922	-122.7754	-973642.4228
0.8392785989	979580.4706003440	-973523.9991	335.7568	-118.5267	-973642.5259
0.8392751802	979580.4595640530	-973523.1272	335.7568	-118.5267	-973641.6539
0.8392734708	979580.4540459170	-973523.9491	334.8310	-118.1999	-973642.1490
0.8392627870	979580.4195576900	-973527.6389	331.1278	-116.8926	-973644.5315
0.8392666332	979580.4319734260	-973521.601	336.9912	-118.9625	-973640.5634
0.8392640690	979580.4236962650	-973518.2388	346.8664	-122.4486	-973640.6873
0.8392674879	979580.4347324820	-973520.577	340.3858	-120.1608	-973640.7378
0.8392738981	979580.4554254500	-973521.8426	334.8310	-118.1999	-973640.0425
0.8392747528	979580.4581845190	-973521.3624	334.8310	-118.1999	-973639.5623
0.8393354314	979580.6540820030	-973520.4033	340.3858	-120.1608	-973640.5641
0.8393345769	979580.6513228340	-973520.4005	340.3858	-120.1608	-973640.5613
0.8392166295	979580.2705710950	-973516.9096	355.5072	-125.4989	-973642.4085
0.8392153472	979580.2664326370	-973523.1625	340.6944	-120.2698	-973643.4322
0.8392136376	979580.2609146990	-973523.9819	337.2998	-119.0714	-973643.0533
0.8392200487	979580.2816069970	-973521.6695	348.4094	-122.9933	-973644.6628
0.8392020973	979580.2236687630	-973526.6442	331.7450	-117.1105	-973643.7547
0.8392170569	979580.2719505810	-973524.733	332.6708	-117.4373	-973642.1703
0.8392183391	979580.2760890430	-973527.5987	330.2020	-116.5658	-973644.1645
0.8392183391	979580.2760890430	-973523.3092	344.0890	-121.4681	-973644.7773
0.8392149198	979580.2650531520	-973525.7086	332.3622	-117.3284	-973643.0370
0.8391542228	979580.0691698640	-973525.5564	332.3622	-117.3284	-973642.8848
0.8391555053	979580.0733081700	-973516.7892	350.5696	-123.7558	-973640.5451
0.8391520854	979580.0622726950	-973520.2863	342.2374	-120.8145	-973641.1007
0.8391525129	979580.0636521290	-973527.4028	331.7450	-117.1105	-973644.5133

0.8391516580	979580.0608932630	-973523.106	345.3234	-121.9039	-973645.0099
0.8391516580	979580.0608932630	-973517.6037	363.2222	-128.2224	-973645.8261
0.8391525129	979580.0636521290	-973515.6785	362.6050	-128.0045	-973643.6830
0.8393354314	979580.6540820030	-973520.4033	340.3858	-120.1608	-973640.5641
0.8391469557	979580.0457195270	-973514.4928	370.9372	-130.9459	-973645.4387
0.8391499481	979580.0553755360	-973515.3754	362.6050	-128.0045	-973643.3799
0.8391490931	979580.0526166750	-973515.4442	360.1362	-127.1330	-973642.5771
0.8392059441	979580.2360840460	-973518.6646	359.5190	-126.9151	-973645.5797
0.8392093634	979580.2471198780	-973523.9035	341.6202	-120.5966	-973644.5001
0.8391516580	979580.0608932630	-973515.293	358.9018	-126.6972	-973641.9902
0.8391503755	979580.0567549670	-973513.6284	357.6674	-126.2615	-973639.8899
0.8391499481	979580.0553755360	-973518.6198	353.6556	-124.8452	-973643.4651
0.8392089360	979580.2457403970	-973518.5249	345.0148	-121.7949	-973640.3199
0.8392072263	979580.2402224800	-973520.4087	342.2374	-120.8145	-973641.2232
0.8393341496	979580.6499432500	-973520.3991	340.3858	-120.1608	-973640.5600
0.8393350041	979580.6527024180	-973520.4019	340.3858	-120.1608	-973640.5627
0.8382023815	979577.0021851520	-973510.7994	377.7264	-133.3426	-973644.1419
0.8382036670	979577.0063210880	-973510.1015	377.4178	-133.2336	-973643.3351
0.8382023815	979577.0021851520	-973509.7219	378.6522	-133.6694	-973643.3913
0.8382023815	979577.0021851520	-973509.3386	381.4296	-134.6498	-973643.9884
0.8382606527	979577.1896841330	-973507.2188	384.5156	-135.7392	-973642.9580
0.8382602243	979577.1883054400	-973509.3944	381.1210	-134.5409	-973643.9353
0.8382572252	979577.1786545990	-973508.3639	383.2812	-135.3035	-973643.6674
0.8382550830	979577.1717611520	-973507.1384	383.8984	-135.5214	-973642.6597
0.8382537977	979577.1676250880	-973505.3834	386.9844	-136.6108	-973641.9942
0.8382589390	979577.1841693630	-973506.5634	390.3790	-137.8091	-973644.3725
0.8382580821	979577.1814119800	-973504.278	395.6252	-139.6611	-973643.9391
0.8382006675	979576.9966705750	-973503.9099	391.9220	-138.3538	-973642.2637
0.8382045240	979577.0090783800	-973507.0367	385.7500	-136.1750	-973643.2117
0.8382040955	979577.0076997340	-973508.446	381.7382	-134.7588	-973643.2048
0.8393358587	979580.6554615880	-973520.4047	340.3858	-120.1608	-973640.5655
0.8383184871	979577.3758109490	-973509.947	377.1092	-133.1247	-973643.0717
0.8383184871	979577.3758109490	-973506.577	385.1328	-135.9571	-973642.5341
0.8383172019	979577.3716747280	-973506.3645	390.3790	-137.8091	-973644.1736
0.8383154885	979577.3661597700	-973505.0571	390.9962	-138.0270	-973643.0840
0.8383202005	979577.3813259170	-973502.7312	399.6370	-141.0773	-973643.8085
0.8383197722	979577.3799471750	-973500.0697	405.5004	-143.1472	-973643.2168
0.8383741715	979577.5550503040	-973496.7832	421.2390	-148.7031	-973645.4863
0.8383728866	979577.5509139440	-973498.7396	407.0434	-143.6919	-973642.4315
0.8383716016	979577.5467775860	-973503.6469	395.0080	-139.4432	-973643.0901
0.8383707450	979577.5440200170	-973506.7513	387.6016	-136.8286	-973643.5800
0.8383711733	979577.5453988010	-973508.3493	382.3554	-134.9767	-973643.3259
0.8383720300	979577.5481563720	-973508.9882	380.5038	-134.3230	-973643.3112
0.8384264222	979577.7232650090	-973510.7841	375.8748	-132.6889	-973643.4730
0.8384242809	979577.7163708590	-973507.6785	381.1210	-134.5409	-973642.2194
0.8384255657	979577.7205073480	-973507.2327	384.5156	-135.7392	-973642.9719
0.8384268505	979577.7246438400	-973503.925	393.4650	-138.8985	-973642.8235
0.8384838044	979577.9080315180	-973502.1387	401.1800	-141.6220	-973643.7607
0.8384825198	979577.9038948840	-973506.2171	388.5274	-137.1555	-973643.3726
0.8384816634	979577.9011371300	-973509.6791	379.2694	-133.8873	-973643.5663
0.8384825198	979577.9038948840	-973511.318	373.4060	-131.8174	-973643.1354

0.8393354314	979580.6540820030	-973520.4033	340.3858	-120.1608	-973640.5641
0.8393345769	979580.6513228340	-973520.4005	340.3858	-120.1608	-973640.5613
0.8385279061	979578.0500578730	-973501.6075	409.2036	-144.4544	-973646.0619
0.8384692455	979577.8611498590	-973498.8434	418.4616	-147.7226	-973646.5660
0.8384135743	979577.6819002470	-973499.2167	417.5358	-147.3958	-973646.6125
0.8383548970	979577.4930052320	-973490.965	433.2744	-152.9518	-973643.9167
0.8382987815	979577.3123892320	-973493.7603	428.0282	-151.0998	-973644.8601
0.8382413727	979577.1276433010	-973499.0759	411.0552	-145.1081	-973644.1840
0.8382418012	979577.1290219780	-973503.7041	396.5510	-139.9879	-973643.6920
0.8383000667	979577.3165254080	-973502.0985	405.8090	-143.2561	-973645.3546
0.8383578953	979577.5026566400	-973502.3531	418.7702	-147.8316	-973650.1847
0.8384127178	979577.6791426070	-973496.5789	427.1024	-150.7730	-973647.3518
0.8384546861	979577.8142686110	-973493.7361	440.0636	-155.3484	-973649.0845
0.8385313312	979578.0610892040	-973498.7397	419.0788	-147.9405	-973646.6802
0.8385874142	979578.2417304830	-973503.9536	400.2542	-141.2952	-973645.2488
0.8393350041	979580.6527024180	-973520.4019	340.3858	-120.1608	-973640.5627
0.8388394761	979579.0540020770	-973518.1744	359.5190	-126.9151	-973645.0895
0.8388351979	979579.0402103600	-973512.9325	370.3200	-130.7280	-973643.6605
0.8388908105	979579.2195054500	-973509.2965	385.7500	-136.1750	-973645.4715
0.8389459875	979579.3974272750	-973519.5101	353.9642	-124.9542	-973644.4643
0.8390045781	979579.5863894780	-973514.0362	364.1480	-128.5492	-973642.5854
0.8390092821	979579.6015619150	-973520.4809	347.1750	-122.5575	-973643.0384
0.8390084268	979579.5988032860	-973519.9255	353.9642	-124.9542	-973644.8797
0.8389481260	979579.4043235890	-973513.2687	370.3200	-130.7280	-973643.9967
0.8389464152	979579.3988065370	-973521.2741	348.7180	-123.1022	-973644.3763
0.8388938048	979579.2291599710	-973516.3979	359.5190	-126.9151	-973643.3130
0.8388950880	979579.2332976280	-973515.5086	363.2222	-128.2224	-973643.7310
0.8393341496	979580.6499432500	-973520.3991	340.3858	-120.1608	-973640.5600
0.8393345769	979580.6513228340	-973520.4005	340.3858	-120.1608	-973640.5613
0.8388377648	979579.0484853850	-973510.5813	381.4296	-134.6498	-973645.2311
0.8388360536	979579.0429687000	-973511.558	373.4060	-131.8174	-973643.3754
0.8388929493	979579.2264015340	-973515.7105	365.0738	-128.8760	-973644.5865
0.8389494091	979579.4084613810	-973514.9789	360.7534	-127.3509	-973642.3298
0.8390127031	979579.6125964410	-973519.4198	351.1868	-123.9737	-973643.3935
0.8390118478	979579.6098378070	-973516.2392	358.5932	-126.5883	-973642.8275
0.8390114202	979579.6084584910	-973512.2109	368.7770	-130.1833	-973642.3942
0.8390165517	979579.6250103100	-973512.3363	367.2340	-129.6386	-973641.9749
0.8389583906	979579.4374260180	-973507.0041	384.8242	-135.8482	-973642.8522
0.8389588183	979579.4388052900	-973512.9759	368.4684	-130.0744	-973643.0503
0.8389566799	979579.4319089320	-973514.9968	362.6050	-128.0045	-973643.0013
0.8388989378	979579.2457106190	-973513.8797	367.8512	-129.8565	-973643.7362
0.8388399039	979579.0553812500	-973510.8293	376.8006	-133.0157	-973643.8451
0.8387830007	979578.8719542700	-973507.8926	388.8360	-137.2644	-973645.1570
0.8387817171	979578.8678168920	-973497.3398	418.7702	-147.8316	-973645.1713
0.8388403317	979579.0567604240	-973503.6811	392.2306	-138.4627	-973642.1438
0.8393358587	979580.6554615880	-973520.4047	340.3858	-120.1608	-973640.5655
0.8389053540	979579.2663990010	-973512.6451	370.3200	-130.7280	-973643.3731
0.8389044985	979579.2636405460	-973506.3103	389.7618	-137.5912	-973643.9016
0.8390182622	979579.6305275940	-973512.3524	372.4802	-131.4906	-973643.8430
0.8390738492	979579.8098424270	-973512.8961	367.5426	-129.7475	-973642.6437
0.8390742768	979579.8112217950	-973514.1425	361.9878	-127.7866	-973641.9291

0.8391029224	979579.9036402660	-973517.1377	357.9760	-126.3704	-973643.5081
0.8391080527	979579.9201929960	-973516.9967	358.5932	-126.5883	-973643.5850
0.8390776973	979579.8222567530	-973519.945	349.9524	-123.5380	-973643.4829
0.8393345769	979580.6513228340	-973520.4005	340.3858	-120.1608	-973640.5613
0.8393345769	979580.6513228340	-973520.4005	340.3858	-120.1608	-973640.5613
0.8390717114	979579.8029455920	-973523.9907	340.3858	-120.1608	-973644.1516
0.8390704287	979579.7988074950	-973523.3933	340.6944	-120.2698	-973643.6630
0.8390695736	979579.7960487660	-973520.383	347.1750	-122.5575	-973642.9405
0.8390700011	979579.7974281300	-973515.0987	372.4802	-131.4906	-973646.5893
0.8390674357	979579.7891519480	-973518.2793	357.6674	-126.2615	-973644.5407
0.8390670082	979579.7877725860	-973520.0525	346.8664	-122.4486	-973642.5010
0.8390674357	979579.7891519480	-973522.0573	347.1750	-122.5575	-973644.6148
0.8390665806	979579.7863932240	-973522.1903	344.0890	-121.4681	-973643.6584
0.8390097097	979579.6029412290	-973514.3039	370.3200	-130.7280	-973645.0319
0.8390088544	979579.6001826010	-973511.1831	374.3318	-132.1442	-973643.3273
0.8390054334	979579.5891481000	-973519.4705	350.8782	-123.8648	-973643.3353
0.8390092821	979579.6015619150	-973518.9954	356.4330	-125.8257	-973644.8211
0.8390084268	979579.5988032860	-973515.9959	366.6168	-129.4207	-973645.4166
0.8393354314	979580.6540820030	-973520.4033	340.3858	-120.1608	-973640.5641
0.8386773017	979578.5313208250	-973507.3775	385.7500	-136.1750	-973643.5525
0.8386751618	979578.5244256350	-973507.3262	384.5156	-135.7392	-973643.0655
0.8386751618	979578.5244256350	-973506.5934	381.1210	-134.5409	-973641.1343
0.8387333642	979578.7119779710	-973512.4426	368.1598	-129.9654	-973642.4080
0.8387325083	979578.7092198000	-973511.2991	371.5544	-131.1638	-973642.4629
0.8387307966	979578.7037034640	-973509.5994	377.4178	-133.2336	-973642.8330
0.8387898466	979578.8940203410	-973511.0704	373.4060	-131.8174	-973642.8878
0.8387851400	979578.8788499070	-973513.2627	366.6168	-129.4207	-973642.6834
0.8387817171	979578.8678168920	-973514.7023	364.1480	-128.5492	-973643.2515
0.8388411874	979579.0595187740	-973513.8961	366.6168	-129.4207	-973643.3168
0.8388411874	979579.0595187740	-973516.0582	358.5932	-126.5883	-973642.6464
0.8388463211	979579.0760688980	-973514.732	363.5308	-128.3313	-973643.0633
0.8389032153	979579.2595028650	-973515.8218	361.0620	-127.4598	-973643.2816
0.8389489814	979579.4070821170	-973517.3247	355.5072	-125.4989	-973642.8236
0.8393337223	979580.6485636660	-973520.3978	340.3858	-120.1608	-973640.5586
0.8393341496	979580.6499432500	-973520.3991	340.3858	-120.1608	-973640.5600
0.8387102554	979578.6375078750	-973501.5309	403.6488	-142.4935	-973644.0245
0.8387115393	979578.6416450750	-973508.0338	389.7618	-137.5912	-973645.6251
0.8387098274	979578.6361288080	-973510.4341	382.6640	-135.0856	-973645.5197
0.8387098274	979578.6361288080	-973505.6138	391.3048	-138.1359	-973643.7497
0.8387081156	979578.6306125480	-973507.0509	386.3672	-136.3929	-973643.4438
0.8387637459	979578.8098939310	-973504.828	392.8478	-138.6806	-973643.5086
0.8387624622	979578.8057566010	-973508.6131	382.3554	-134.9767	-973643.5898
0.8388501713	979579.0884815240	-973507.3368	382.9726	-135.1945	-973642.5313
0.8388514547	979579.0926190730	-973508.5974	383.8984	-135.5214	-973644.1188
0.8389074927	979579.2732951460	-973513.2699	369.3942	-130.4012	-973643.6710
0.8389074927	979579.2732951460	-973511.1674	372.4802	-131.4906	-973642.6580
0.8389622398	979579.4498394820	-973520.4517	371.8630	-131.2727	-973651.7244
0.8389622398	979579.4498394820	-973512.4039	374.3318	-132.1442	-973644.5481
0.8393345769	979580.6513228340	-973520.4005	340.3858	-120.1608	-973640.5613
0.8386982725	979578.5988941580	-973499.5612	406.4262	-143.4740	-973643.0352
0.8386991285	979578.6016522720	-973506.5005	388.8360	-137.2644	-973643.7649

0.8387551879	979578.7823117890	-973507.4058	393.1564	-138.7896	-973646.1953
0.8388163735	979578.9795272260	-973501.3063	422.1648	-149.0299	-973650.3362
0.8388150900	979578.9753897650	-973497.7371	414.1412	-146.1975	-973643.9346
0.8387594669	979578.7961028430	-973501.2727	418.1530	-147.6137	-973648.8864
0.8387081156	979578.6306125480	-973504.6904	400.2542	-141.2952	-973645.9855
0.8387111113	979578.6402660080	-973502.3768	398.0940	-140.5326	-973642.9094
0.8387102554	979578.6375078750	-973500.8177	401.1800	-141.6220	-973642.4397
0.8387705921	979578.8319597470	-973507.3468	386.9844	-136.6108	-973643.9575
0.8387675969	979578.8223059420	-973504.0141	391.9220	-138.3538	-973642.3679
0.8387782940	979578.8567838990	-973507.9856	386.9844	-136.6108	-973644.5964
0.8387641738	979578.8112730420	-973512.4526	374.3318	-132.1442	-973644.5968
0.8387286569	979578.6968080520	-973509.5954	384.2070	-135.6303	-973645.2257
0.8393354314	979580.6540820030	-973520.4033	340.3858	-120.1608	-973640.5641
0.8393345769	979580.6513228340	-973520.4005	340.3858	-120.1608	-973640.5613
0.8385857018	979578.2362146290	-973503.9546	394.0822	-139.1164	-973643.0710
0.8386460574	979578.4306519300	-973503.7389	399.6370	-141.0773	-973644.8162
0.8386387810	979578.4072087610	-973497.6125	414.1412	-146.1975	-973643.8100
0.8385921231	979578.2568991130	-973496.7251	421.2390	-148.7031	-973645.4282
0.8385827052	979578.2265618970	-973494.9719	422.1648	-149.0299	-973644.0018
0.8385801367	979578.2182881410	-973499.4312	411.0552	-145.1081	-973644.5393
0.8385244809	979578.0390265650	-973495.0738	418.4616	-147.7226	-973642.7965
0.8384606812	979577.8335726050	-973491.5914	431.1142	-152.1892	-973643.7806
0.8384512603	979577.8032377890	-973487.1692	445.9270	-157.4183	-973644.5875
0.8385120643	979577.9990382630	-973489.6251	438.8292	-154.9127	-973644.5378
0.8385634408	979578.1645090380	-973499.9481	412.2896	-145.5438	-973645.4920
0.8386023968	979578.2899944520	-973502.7103	401.7972	-141.8399	-973644.5502
0.8386674579	979578.4996030240	-973506.3167	394.6994	-139.3343	-973645.6510
0.8386670299	979578.4982239930	-973498.3032	411.3638	-145.2170	-973643.5202
0.8386550457	979578.4596112810	-973501.5544	401.1800	-141.6220	-973643.1764
0.8393354314	979580.6540820030	-973520.4033	340.3858	-120.1608	-973640.5641
0.8384071502	979577.6612179860	-973491.2886	442.5324	-156.2200	-973647.5086
0.8383613219	979577.5136868430	-973491.9902	435.1260	-153.6054	-973645.5956
0.8383142033	979577.3620235560	-973496.6399	416.6100	-147.0690	-973643.7089
0.8384067219	979577.6598391710	-973502.2981	401.7972	-141.8399	-973644.1380
0.8384692455	979577.8611498590	-973503.2708	401.4886	-141.7309	-973645.0017
0.8385398940	979578.0886676310	-973504.4518	395.6252	-139.6611	-973644.1129
0.8393354314	979580.6540820030	-973520.4033	340.3858	-120.1608	-973640.5641
0.8393345769	979580.6513228340	-973520.4005	340.3858	-120.1608	-973640.5613
0.8386606098	979578.4775385770	-973504.4757	397.1682	-140.2058	-973644.6815
0.8386614658	979578.4802966280	-973507.445	386.3672	-136.3929	-973643.8379
0.8386601818	979578.4761595520	-973504.5116	395.6252	-139.6611	-973644.1726
0.8386584698	979578.4706434560	-973505.4175	392.5392	-138.5717	-973643.9892
0.8386062494	979578.3024052580	-973503.886	397.4768	-140.3147	-973644.2008
0.8386079617	979578.3079211800	-973506.7506	387.6016	-136.8286	-973643.5792
0.8386178070	979578.3396378460	-973508.0143	382.3554	-134.9767	-973642.9910
0.8386199472	979578.3465327980	-973509.6871	378.0350	-133.4515	-973643.1386
0.8386186631	979578.3423958260	-973510.3452	374.3318	-132.1442	-973642.4894
0.8385330438	979578.0666048780	-973508.4171	378.9608	-133.7783	-973642.1955
0.8385407503	979578.0914254810	-973505.1715	388.8360	-137.2644	-973642.4359
0.8385339001	979578.0693627170	-973504.905	391.9220	-138.3538	-973643.2588
0.8384748122	979577.8790751510	-973507.0399	385.7500	-136.1750	-973643.2149

0.8384748122	979577.8790751510	-973506.7625	387.6016	-136.8286	-973643.5912
0.8384829480	979577.9052737620	-973508.479	379.5780	-133.9962	-973642.4752
0.8384242809	979577.7163708590	-973510.2465	378.3436	-133.5604	-973643.8070
0.8384238527	979577.7149920310	-973510.9821	377.4178	-133.2336	-973644.2157
0.8384195700	979577.7012037620	-973508.0136	384.8242	-135.8482	-973643.8618
0.8393354314	979580.6540820030	-973520.4033	340.3858	-120.1608	-973640.5641
0.8393341496	979580.6499432500	-973520.3991	340.3858	-120.1608	-973640.5600
0.8383420468	979577.4516422510	-973497.9937	419.6960	-148.1584	-973646.1521
0.8382850727	979577.2682702210	-973492.7417	437.2862	-154.3680	-973647.1097
0.8382242342	979577.0724964990	-973496.778	421.2390	-148.7031	-973645.4811
0.8382152362	979577.0435446560	-973496.1902	419.6960	-148.1584	-973644.3486
0.8382160931	979577.0463019670	-973503.1681	397.1682	-140.2058	-973643.3739
0.8382225203	979577.0669818500	-973507.4094	382.0468	-134.8677	-973642.2771
0.8382855011	979577.2696489340	-973508.658	376.4920	-132.9068	-973641.5648
0.8382919271	979577.2903296810	-973507.1449	385.1328	-135.9571	-973643.1020
0.8382923555	979577.2917084000	-973501.9247	403.6488	-142.4935	-973644.4182
0.8383557537	979577.4957627760	-973505.3223	394.0822	-139.1164	-973644.4387
0.8383643202	979577.5233382890	-973507.6352	382.3554	-134.9767	-973642.6119
0.8383497570	979577.4764600010	-973510.4903	372.7888	-131.5995	-973642.0898
0.8393354314	979580.6540820030	-973520.4033	340.3858	-120.1608	-973640.5641
0.8385617283	979578.1589932630	-973510.8916	375.8748	-132.6889	-973643.5805
0.8386186631	979578.3423958260	-973509.5545	377.4178	-133.2336	-973642.7881
0.8386704538	979578.5092562480	-973509.3937	378.0350	-133.4515	-973642.8452
0.8387260893	979578.6885335690	-973508.7135	379.5780	-133.9962	-973642.7097
0.8393345769	979580.6513228340	-973520.4005	340.3858	-120.1608	-973640.5613
0.8393341496	979580.6499432500	-973520.3991	340.3858	-120.1608	-973640.5600
0.8389506922	979579.4125991770	-973514.3122	368.7770	-130.1833	-973644.4955
0.8389472706	979579.4015650620	-973508.2257	381.1210	-134.5409	-973642.7666
0.8388967990	979579.2388145090	-973508.6244	379.5780	-133.9962	-973642.6206
0.8388950880	979579.2332976280	-973515.3776	361.9878	-127.7866	-973643.1642
0.8393354314	979580.6540820030	-973520.4033	340.3858	-120.1608	-973640.5641
0.8391525129	979580.0636521290	-973522.6502	350.2610	-123.6469	-973646.2971
0.8392153472	979580.2664326370	-973528.3344	327.1160	-115.4764	-973643.8108
0.8392743255	979580.4568049840	-973521.7812	334.8310	-118.1999	-973639.9811
0.8393324404	979580.6444249170	-973524.7674	337.2998	-119.0714	-973643.8388
0.8393909741	979580.8334310360	-973521.2123	347.7922	-122.7754	-973643.9877
0.8393961007	979580.8499866330	-973515.9149	356.4330	-125.8257	-973641.7406
0.8393986640	979580.8582644510	-973519.8365	351.8040	-124.1916	-973644.0281
0.8393969552	979580.8527459040	-973519.1427	346.5578	-122.3396	-973641.4823
0.8393982368	979580.8568848140	-973502.5457	365.6910	-129.0939	-973631.6396
0.8393952463	979580.8472273630	-973518.6998	347.7922	-122.7754	-973641.4752
0.8393969552	979580.8527459040	-973520.9657	340.6944	-120.2698	-973641.2354
0.8393986640	979580.8582644510	-973511.1303	366.3082	-129.3118	-973640.4420
0.8393986640	979580.8582644510	-973517.1941	351.1868	-123.9737	-973641.1678
0.8393969552	979580.8527459040	-973518.8146	350.8782	-123.8648	-973642.6794
0.8393986640	979580.8582644510	-973520.168	339.4600	-119.8340	-973640.0020
0.8394012273	979580.8665422810	-973521.058	337.2998	-119.0714	-973640.1295
0.8394003729	979580.8637830030	-973519.2923	341.6202	-120.5966	-973639.8889
0.8393986640	979580.8582644510	-973515.5931	344.7062	-121.6860	-973637.2791
0.8393456860	979580.6871921430	-973521.0471	337.2998	-119.0714	-973640.1185
0.8393350041	979580.6527024180	-973520.4019	340.3858	-120.1608	-973640.5627

0.8393341496	979580.6499432500	-973520.3991	340.3858	-120.1608	-973640.5600
0.8380785271	979576.6037716590	-973511.1533	375.5662	-132.5800	-973643.7333
0.8382156647	979577.0449233110	-973508.2853	380.5038	-134.3230	-973642.6084
0.8382315182	979577.0959338200	-973508.4493	382.0468	-134.8677	-973643.3170
0.8382430865	979577.1331580120	-973507.1316	383.5898	-135.4124	-973642.5440
0.8382550830	979577.1717611520	-973506.9157	385.1328	-135.9571	-973642.8729
0.8382610811	979577.1910628260	-973506.4336	386.3672	-136.3929	-973642.8265
0.8382546546	979577.1703824630	-973506.7811	384.5156	-135.7392	-973642.5203
0.8382400874	979577.1235072710	-973507.8956	382.0468	-134.8677	-973642.7633
0.8382272335	979577.0821471480	-973506.3685	382.6640	-135.0856	-973641.4541
0.8382143792	979577.0407873450	-973506.9758	381.4296	-134.6498	-973641.6257
0.8382028100	979577.0035637970	-973506.7706	381.1210	-134.5409	-973641.3115
0.8382156647	979577.0449233110	-973507.2275	382.0468	-134.8677	-973642.0953
0.8382276620	979577.0835258140	-973506.1372	383.5898	-135.4124	-973641.5496
0.8382383735	979577.1179925690	-973505.7169	384.8242	-135.8482	-973641.5651
0.8382507986	979577.1579742840	-973504.4726	386.3672	-136.3929	-973640.8655
0.8393354314	979580.6540820030	-973520.4033	340.3858	-120.1608	-973640.5641

CT (mGal)	L'ANOMALIE DE BOUGUER COMPLETE	FieldCT26	CTproch26 (0-3km)	CTinterm26 (3-10 km)	CTloint26 (10-140 km)
0.169	-973639.6207	0.169	0.38000	0.04900	0.51400
0.046	-973640.1558	0.046	0.35300	0.04900	0.51300
0.04	-973639.5715	0.04	0.42600	0.04900	0.51000
0	-973640.1507	0	0.42100	0.04800	0.50600
0.032	-973641.3991	0.032	0.33900	0.04800	0.50100
0.012	-973640.4564	0.012	0.41800	0.05000	0.49600
0.068	-973639.9615	0.068	0.37200	0.04900	0.48900
0.282	-973635.5808	0.282	0.48700	0.04700	0.48600
0.221	-973640.9002	0.221	0.58800	0.04900	0.48300
0.169	-973639.6335	0.169	0.38100	0.04900	0.51300
0.169	-973639.6193	0.169	0.379	0.049	0.514
0	-973639.3725	0	0.412	0.05	0.52
0.012	-973640.0607	0.012	0.38	0.05	0.524
0.144	-973638.9219	0.144	0.278	0.05	0.527
0.02	-973640.1732	0.02	0.318	0.051	0.528
0	-973640.5924	0	0.403	0.051	0.533
0	-973640.5864	0	0.44	0.051	0.529
0.145	-973640.0638	0.145	0.613	0.051	0.521
0.24	-973641.1628	0.24	0.691	0.055	0.514
0.061	-973641.1679	0.061	0.796	0.05	0.512
0	-973640.4049	0	0.688	0.049	0.512
0	-973641.0120	0	0.579	0.049	0.509
0.35	-973643.3455	0.35	0.633	0.049	0.504
0.105	-973639.4584	0.105	0.557	0.048	0.5
0.264	-973639.6773	0.264	0.465	0.048	0.497
0.174	-973639.6288	0.174	0.568	0.047	0.493
0.384	-973639.0515	0.384	0.454	0.046	0.491
0.16	-973638.6513	0.16	0.376	0.046	0.489
0.169	-973639.6221	0.169	0.379	0.049	0.514

0.169	-973639.6193	0.169	0.379	0.049	0.514
0.305	-973640.9935	0.305	0.832	0.07	0.512
0.033	-973641.8602	0.033	1.009	0.054	0.508
0.16	-973641.5833	0.16	0.916	0.05	0.504
0.394	-973643.6258	0.394	0.483	0.053	0.501
0.02	-973642.4577	0.02	0.749	0.049	0.5
0.032	-973641.0213	0.032	0.602	0.048	0.5
0.3	-973642.8605	0.3	0.762	0.047	0.495
1.502	-973643.4623	1.502	0.773	0.051	0.49
0.323	-973641.8400	0.323	0.658	0.047	0.491
0.334	-973641.8358	0.334	0.513	0.046	0.489
0.054	-973639.5981	0.054	0.408	0.049	0.49
0.115	-973639.9787	0.115	0.58	0.047	0.494
0	-973643.0363	0	0.931	0.048	0.498
0.106	-973643.8529	0.106	0.605	0.053	0.5
0.524	-973644.3261	0.524	0.928	0.071	0.501
0.979	-973642.5810	0.979	0.531	0.066	0.505
0.169	-973639.6251	0.169	0.376	0.049	0.514
0.116	-973643.6727	0.116	1.163	0.09	0.513
0.431	-973642.3329	0.431	0.457	0.073	0.516
0.398	-973641.5431	0.398	0.446	0.07	0.518
0.926	-973644.5347	0.926	0.467	0.062	0.516
0.144	-973643.2331	0.144	0.693	0.053	0.521
0.109	-973640.7982	0.109	0.602	0.069	0.521
0.233	-973638.6039	0.233	0.691	0.07	0.525
2.089	-973642.2411	2.089	0.637	0.062	0.525
0.051	-973639.2019	0.051	0.537	0.053	0.528
0.053	-973639.9492	0.053	0.695	0.052	0.527
0.169	-973639.6190	0.169	0.379	0.049	0.514
0.169	-973639.6207	0.169	0.38	0.049	0.514
0.003	-973643.1389	0.003	0.324	0.121	0.557
0.003	-973642.3501	0.003	0.309	0.117	0.559
0.02	-973642.3873	0.02	0.3	0.137	0.567
0.035	-973643.0214	0.035	0.262	0.135	0.569
0.15	-973641.9580	0.15	0.295	0.14	0.566
0.034	-973642.9883	0.034	0.239	0.14	0.568
0.07	-973642.6874	0.07	0.282	0.133	0.566
0.03	-973641.5877	0.03	0.37	0.135	0.566
0.182	-973640.7732	0.182	0.502	0.144	0.574
0.072	-973642.9695	0.072	0.643	0.168	0.592
0.051	-973642.3851	0.051	0.755	0.189	0.611
0.126	-973640.9917	0.126	0.528	0.162	0.582
0.051	-973642.0307	0.051	0.47	0.14	0.571
0.077	-973642.1298	0.077	0.39	0.125	0.561
0.169	-973639.6235	0.169	0.38	0.049	0.514
0.03	-973642.1167	0.03	0.279	0.116	0.56
0.05	-973641.5651	0.05	0.263	0.139	0.568
0.049	-973643.0866	0.049	0.354	0.156	0.577
0.189	-973641.8540	0.189	0.484	0.159	0.587
0.19	-973642.2375	0.19	0.768	0.195	0.608
0.22	-973641.2518	0.22	1.099	0.224	0.642

0.596	-973642.5143	0.596	1.936	0.321	0.714
0.364	-973640.4235	0.364	1.141	0.225	0.641
0.473	-973641.7161	0.473	0.594	0.18	0.6
0.029	-973642.4640	0.029	0.38	0.155	0.581
0.005	-973642.3079	0.005	0.315	0.134	0.569
0.123	-973642.3672	0.123	0.259	0.124	0.561
0.123	-973642.4930	0.123	0.304	0.119	0.558
0.168	-973641.1294	0.168	0.395	0.13	0.565
0.002	-973641.7289	0.002	0.518	0.146	0.579
0.039	-973641.2155	0.039	0.835	0.168	0.606
0.346	-973641.7947	0.346	1.125	0.21	0.63
0.17	-973641.8616	0.17	0.777	0.149	0.584
0.003	-973642.3403	0.003	0.541	0.122	0.563
0.004	-973642.0514	0.004	0.421	0.109	0.554
0.169	-973639.6211	0.169	0.38	0.049	0.514
0.169	-973639.6193	0.169	0.379	0.049	0.514
0.148	-973643.6809	0.148	1.368	0.314	0.7
0.45	-973643.7930	0.45	1.646	0.391	0.737
0.279	-973644.2775	0.279	1.242	0.345	0.749
0.751	-973640.8127	0.751	1.95	0.402	0.752
1.301	-973641.6651	1.301	2.121	0.354	0.72
0.8	-973641.8860	0.8	1.392	0.246	0.66
0.161	-973642.1060	0.161	0.778	0.191	0.617
0.805	-973642.6086	0.805	1.818	0.258	0.671
0.254	-973647.3457	0.254	1.695	0.397	0.747
0.946	-973644.3258	0.946	1.753	0.457	0.816
1.48	-973644.8925	1.48	2.801	0.54	0.852
0.959	-973643.5442	0.959	1.946	0.414	0.776
0.252	-973643.1678	0.252	1.146	0.264	0.67
0.169	-973639.6207	0.169	0.379	0.049	0.514
0.836	-973642.9055	0.836	1.56	0.086	0.539
0.279	-973642.2795	0.279	0.736	0.103	0.542
0.56	-973643.2665	0.56	1.536	0.137	0.532
0.608	-973642.8673	0.608	1	0.079	0.518
1.043	-973641.2104	1.043	0.796	0.07	0.509
0.231	-973641.5864	0.231	0.888	0.056	0.507
0.437	-973643.6257	0.437	0.672	0.071	0.511
0.525	-973642.7737	0.525	0.623	0.084	0.516
0.485	-973642.6683	0.485	1.132	0.062	0.513
1.623	-973641.6580	1.623	1.06	0.073	0.522
0.307	-973642.3070	0.307	0.81	0.088	0.526
0.169	-973639.6180	0.169	0.379	0.049	0.514
0.169	-973639.6193	0.169	0.379	0.049	0.514
1.52	-973643.4031	1.52	1.143	0.137	0.548
0.613	-973641.7474	0.613	0.958	0.115	0.555
0.234	-973643.2475	0.234	0.713	0.093	0.534
0.267	-973641.0798	0.267	0.654	0.074	0.522
0.027	-973642.1665	0.027	0.65	0.061	0.516
0.103	-973641.6115	0.103	0.618	0.075	0.523
0.35	-973641.0422	0.35	0.724	0.094	0.534
0.252	-973640.4069	0.252	0.92	0.102	0.546

0.41	-973640.7722	0.41	1.35	0.156	0.574
0.189	-973641.5293	0.189	0.877	0.101	0.543
0.459	-973641.6613	0.459	0.73	0.08	0.53
0.12	-973642.2062	0.12	0.888	0.099	0.543
0.505	-973641.8921	0.505	1.245	0.135	0.574
1.312	-973642.8340	1.312	1.501	0.205	0.617
0.884	-973641.2803	0.884	2.87	0.359	0.662
0.739	-973639.4928	0.739	1.816	0.213	0.623
0.169	-973639.6165	0.169	0.386	0.049	0.513
0.237	-973641.4131	0.237	1.291	0.109	0.56
0.666	-973641.2326	0.666	1.852	0.201	0.615
0.123	-973642.2110	0.123	0.975	0.105	0.551
0.059	-973641.4047	0.059	0.612	0.091	0.535
0.153	-973640.7391	0.153	0.582	0.078	0.53
0.014	-973642.5201	0.014	0.402	0.067	0.519
0.029	-973642.5820	0.029	0.418	0.069	0.516
0.256	-973642.3339	0.256	0.578	0.058	0.513
0.169	-973639.6393	0.169	0.359	0.049	0.514
0.169	-973639.6393	0.169	0.359	0.049	0.514
0.066	-973642.8406	0.066	0.752	0.052	0.507
0.03	-973642.3020	0.03	0.807	0.051	0.504
0.313	-973641.4225	0.313	0.958	0.058	0.502
0.718	-973644.2803	0.718	1.72	0.087	0.501
0.256	-973643.1837	0.256	0.791	0.069	0.497
0.905	-973641.1700	0.905	0.786	0.052	0.493
0.49	-973643.1018	0.49	0.955	0.065	0.494
0.137	-973642.1414	0.137	0.97	0.055	0.492
1.048	-973642.7909	1.048	1.612	0.121	0.508
0.923	-973641.4873	0.923	1.248	0.09	0.503
0.506	-973641.9513	0.506	0.829	0.056	0.499
0.53	-973643.5061	0.53	0.735	0.071	0.509
0.672	-973643.7716	0.672	1.024	0.107	0.514
0.169	-973639.6411	0.169	0.36	0.049	0.513
0.052	-973642.3985	0.052	0.439	0.153	0.563
0.06	-973641.9075	0.06	0.467	0.143	0.548
0.349	-973640.0283	0.349	0.444	0.127	0.534
0.122	-973641.3570	0.122	0.428	0.098	0.525
0.311	-973641.3379	0.311	0.473	0.114	0.537
0.178	-973641.7140	0.178	0.431	0.134	0.553
0.291	-973641.6228	0.291	0.603	0.121	0.541
0.102	-973641.5814	0.102	0.489	0.092	0.521
0.057	-973642.2785	0.057	0.377	0.083	0.514
0.098	-973642.2738	0.098	0.447	0.084	0.512
0.096	-973641.4814	0.096	0.579	0.075	0.511
0.317	-973641.7843	0.317	0.666	0.092	0.522
0.246	-973642.1046	0.246	0.597	0.073	0.507
0.248	-973641.5376	0.248	0.722	0.062	0.503
0.169	-973639.6746	0.169	0.322	0.049	0.514
0.169	-973639.6740	0.169	0.324	0.049	0.514
0.39	-973642.0125	0.39	1.134	0.247	0.631
0.322	-973644.0131	0.322	0.811	0.195	0.605

0.169	-973644.1477	0.169	0.64	0.151	0.581
0.213	-973642.4147	0.213	0.593	0.164	0.579
0.018	-973642.2108	0.018	0.478	0.174	0.581
0.074	-973642.0436	0.074	0.713	0.177	0.574
0.112	-973642.3158	0.112	0.563	0.144	0.567
0.413	-973641.1733	0.413	0.675	0.132	0.551
0.393	-973642.4198	0.393	0.975	0.169	0.554
0.33	-973642.2460	0.33	0.78	0.115	0.53
0.158	-973641.2530	0.158	0.751	0.117	0.538
0.434	-973650.4934	0.434	0.625	0.09	0.517
0.413	-973643.0341	0.413	0.899	0.102	0.513
0.169	-973639.6543	0.169	0.344	0.049	0.514
0.369	-973640.8052	0.369	1.33	0.259	0.641
0.292	-973641.8699	0.292	1.157	0.151	0.587
0.633	-973643.8443	0.633	1.56	0.178	0.614
1.711	-973645.9632	1.711	3.373	0.333	0.667
0.344	-973640.6056	0.344	2.334	0.33	0.665
1.256	-973645.1364	1.256	2.788	0.298	0.664
0.306	-973644.0905	0.306	0.996	0.246	0.653
1.204	-973641.0764	1.204	0.98	0.217	0.636
0.41	-973640.5067	0.41	1.056	0.24	0.637
0.305	-973642.4005	0.305	0.813	0.161	0.584
0.657	-973640.8099	0.657	0.787	0.181	0.59
0.511	-973642.9524	0.511	0.915	0.162	0.567
0.293	-973643.2928	0.293	0.612	0.13	0.562
0.166	-973643.7057	0.166	0.774	0.159	0.587
0.169	-973639.6231	0.169	0.379	0.049	0.514
0.169	-973639.5953	0.169	0.403	0.049	0.514
0.291	-973641.2740	0.291	1.047	0.165	0.585
0.421	-973642.6022	0.421	1.409	0.194	0.611
0.04	-973641.2770	0.04	1.579	0.297	0.657
0.3	-973642.0592	0.3	2.411	0.296	0.661
0.012	-973641.3068	0.012	1.624	0.363	0.708
0.051	-973642.5853	0.051	0.922	0.318	0.714
0.08	-973640.5165	0.08	1.182	0.361	0.736
0.379	-973640.3296	0.379	2.358	0.361	0.733
0.326	-973639.8255	0.326	3.334	0.568	0.86
0.287	-973640.7728	0.287	2.479	0.476	0.811
0.301	-973642.9920	0.301	1.434	0.34	0.727
0.156	-973642.6242	0.156	0.991	0.257	0.678
0.294	-973643.8970	0.294	0.882	0.232	0.64
0.253	-973641.4012	0.253	1.131	0.315	0.673
0.305	-973641.2604	0.305	0.965	0.271	0.68
0.169	-973639.6171	0.169	0.385	0.049	0.514
0.31	-973642.8856	0.31	3.296	0.508	0.819
0.212	-973641.7466	0.212	2.71	0.404	0.736
0.283	-973641.2129	0.283	1.554	0.274	0.668
0.197	-973641.9100	0.197	1.27	0.267	0.69
0.145	-973642.8967	0.145	1.192	0.258	0.655
0.089	-973642.3289	0.089	0.915	0.228	0.641
0.169	-973639.6731	0.169	0.329	0.049	0.514

0.169	-973639.5823	0.169	0.416	0.049	0.514
0.093	-973643.1185	0.093	0.747	0.2	0.615
0.027	-973642.3489	0.027	0.725	0.167	0.597
0.159	-973642.7786	0.159	0.607	0.193	0.593
0.167	-973642.6452	0.167	0.576	0.184	0.584
0.054	-973642.7178	0.054	0.66	0.21	0.614
0.007	-973642.2912	0.007	0.522	0.174	0.592
0.027	-973641.8790	0.027	0.398	0.146	0.568
0.02	-973642.0976	0.02	0.358	0.131	0.552
0.116	-973641.5044	0.116	0.331	0.116	0.537
0.002	-973641.1935	0.002	0.321	0.131	0.55
0.076	-973641.2399	0.076	0.462	0.165	0.569
0.033	-973642.0018	0.033	0.489	0.178	0.59
0.108	-973641.8359	0.108	0.623	0.165	0.591
0.098	-973642.4502	0.098	0.423	0.15	0.568
0.025	-973641.4882	0.025	0.302	0.135	0.55
0.046	-973642.8060	0.046	0.335	0.124	0.543
0.093	-973643.0167	0.093	0.512	0.129	0.558
0.178	-973642.2518	0.178	0.836	0.176	0.598
0.169	-973639.6821	0.169	0.32	0.049	0.514
0.169	-973639.6780	0.169	0.319	0.049	0.514
0.454	-973642.9871	0.454	2.014	0.406	0.745
0.771	-973642.4417	0.771	3.441	0.478	0.749
0.47	-973642.4971	0.47	1.983	0.314	0.687
0.396	-973641.3066	0.396	2.004	0.353	0.686
0.171	-973641.4199	0.171	1.109	0.221	0.625
0.073	-973640.9791	0.073	0.601	0.139	0.558
0.073	-973640.2818	0.073	0.615	0.121	0.547
0.237	-973641.4200	0.237	0.923	0.164	0.595
0.316	-973641.8762	0.316	1.596	0.272	0.673
0.138	-973642.4537	0.138	1.139	0.211	0.635
0.004	-973641.2789	0.004	0.619	0.145	0.569
0.053	-973640.9388	0.053	0.497	0.112	0.542
0.169	-973639.6321	0.169	0.369	0.049	0.514
0.016	-973642.3455	0.016	0.565	0.112	0.558
0.02	-973641.3731	0.02	0.738	0.116	0.562
0.014	-973641.1952	0.014	0.966	0.119	0.565
0.059	-973640.6637	0.059	1.336	0.131	0.58
0.169	-973639.6313	0.169	0.368	0.049	0.514
0.169	-973639.6050	0.169	0.393	0.049	0.514
0.472	-973642.9905	0.472	0.904	0.09	0.511
0.134	-973640.9326	0.134	1.193	0.124	0.518
0.106	-973641.1166	0.106	0.877	0.112	0.516
0.28	-973642.0302	0.28	0.553	0.074	0.507
0.169	-973639.5861	0.169	0.416	0.049	0.514
0.767	-973644.7671	0.767	0.99	0.055	0.485
0.007	-973642.6758	0.007	0.597	0.047	0.491
0.044	-973639.0391	0.044	0.408	0.046	0.488
0.224	-973642.9308	0.224	0.38	0.046	0.481
0.108	-973642.9637	0.108	0.494	0.047	0.484
0.316	-973640.2836	0.316	0.924	0.047	0.486

0.225	-973642.7811	0.225	0.704	0.057	0.486
0.052	-973640.6743	0.052	0.269	0.052	0.487
0.186	-973630.6106	0.186	0.48	0.058	0.491
0.04	-973640.6402	0.04	0.288	0.053	0.494
0.012	-973640.2834	0.012	0.408	0.048	0.497
0.696	-973638.8150	0.696	1.068	0.059	0.5
0.288	-973640.2088	0.288	0.402	0.053	0.503
0.238	-973641.6564	0.238	0.464	0.052	0.507
0	-973639.1450	0	0.294	0.049	0.515
0	-973639.2685	0	0.291	0.05	0.52
0.086	-973639.1109	0.086	0.206	0.051	0.521
0.107	-973636.5411	0.107	0.163	0.052	0.523
0	-973639.1955	0	0.354	0.05	0.519
0.169	-973639.6807	0.169	0.32	0.049	0.514
0.169	-973639.6700	0.169	0.327	0.049	0.514
0.029	-973642.8103	0.029	0.272	0.104	0.547
0.015	-973641.5574	0.015	0.364	0.126	0.561
0.027	-973642.2330	0.027	0.388	0.132	0.564
0.039	-973641.4280	0.039	0.412	0.137	0.566
0.02	-973641.7249	0.02	0.436	0.143	0.57
0.028	-973641.6595	0.028	0.45	0.145	0.572
0.039	-973641.3433	0.039	0.462	0.144	0.572
0.021	-973641.6313	0.021	0.428	0.136	0.567
0.073	-973640.3511	0.073	0.407	0.131	0.565
0.028	-973640.5487	0.028	0.388	0.126	0.562
0.02	-973640.2635	0.02	0.367	0.122	0.559
0.006	-973640.9993	0.006	0.404	0.129	0.563
0	-973640.4246	0	0.426	0.133	0.566
0.006	-973640.4091	0.006	0.451	0.137	0.568
0.014	-973639.6585	0.014	0.492	0.143	0.572
0.169	-973639.5861	0.169	0.416	0.049	0.514

CTall26 (sigma)	Boug_Comp_FINAL (-moyenne boug comp.)	ALT_SRTM
0.9420000	1.8090	1095
0.9150000	1.2739	1098
0.9850000	1.8582	1096
0.9750000	1.2790	1094
0.8880000	0.0306	1099
0.9630000	0.9733	1122
0.9100000	1.4682	1123
1.0190000	5.8489	1112
1.1200000	0.5295	1127
0.9430000	1.7962	1096
0.9420000	1.8103	1095
0.9820000	2.0572	1089
0.9540000	1.3690	1089
0.8550000	2.5078	1100
0.8960000	1.2565	1088
0.9870000	0.8373	1090

1.0190000	0.8433	1092
1.1840000	1.3659	1107
1.2600000	0.2669	1135
1.3580000	0.2618	1103
1.2490000	1.0247	1093
1.1370000	0.4177	1087
1.1860000	-1.9158	1105
1.1050000	1.9712	1090
1.0100000	1.7524	1107
1.1090000	1.8009	1094
0.9910000	2.3782	1085
0.9110000	2.7784	1089
0.9420000	1.8076	1095
0.9420000	1.8103	1095
1.4150000	0.4362	1169
1.5720000	-0.4305	1129
1.4700000	-0.1536	1112
1.0370000	-2.1961	1132
1.2970000	-1.0280	1105
1.1490000	0.4084	1086
1.3040000	-1.4308	1090
1.3150000	-2.0326	1135
1.1970000	-0.4103	1079
1.0490000	-0.4061	1095
0.9470000	1.8316	1117
1.1220000	1.4510	1102
1.4770000	-1.6066	1096
1.1570000	-2.4232	1131
1.5000000	-2.8964	1170
1.1020000	-1.1513	1159
0.9390000	1.8046	1094
1.7660000	-2.2430	1198
1.0470000	-0.9032	1171
1.0340000	-0.1135	1166
1.0450000	-3.1050	1149
1.2670000	-1.8034	1119
1.1920000	0.6314	1163
1.2860000	2.8258	1164
1.2240000	-0.8114	1145
1.1180000	2.2278	1115
1.2740000	1.4805	1110
0.9410000	1.8107	1095
0.9420000	1.8090	1095
1.0030000	-1.7092	1230
0.9850000	-0.9204	1224
1.0040000	-0.9576	1242
0.9670000	-1.5917	1241
1.0000000	-0.5283	1246
0.9470000	-1.5586	1246
0.9800000	-1.2577	1240
1.0720000	-0.1580	1241

1.2210000	0.6565	1249
1.4030000	-1.5398	1267
1.5540000	-0.9554	1280
1.2720000	0.4380	1264
1.1810000	-0.6010	1245
1.0750000	-0.7001	1233
0.9420000	1.8062	1095
0.9550000	-0.6870	1222
0.9690000	-0.1354	1245
1.0870000	-1.6569	1258
1.2300000	-0.4243	1260
1.5710000	-0.8078	1286
1.9650000	0.1779	1302
2.9720000	-1.0846	1351
2.0080000	1.0062	1302
1.3740000	-0.2864	1276
1.1160000	-1.0343	1257
1.0180000	-0.8783	1239
0.9440000	-0.9376	1232
0.9800000	-1.0633	1226
1.0900000	0.3002	1237
1.2430000	-0.2992	1249
1.6080000	0.2142	1265
1.9660000	-0.3650	1292
1.5110000	-0.4319	1251
1.2260000	-0.9106	1229
1.0840000	-0.6217	1215
0.9430000	1.8086	1095
0.9420000	1.8103	1095
2.3810000	-2.2512	1346
2.7730000	-2.3633	1382
2.3350000	-2.8479	1360
3.1040000	0.6169	1387
3.1950000	-0.2354	1366
2.2980000	-0.4563	1313
1.5860000	-0.6763	1281
2.7460000	-1.1789	1318
2.8390000	-5.9160	1388
3.0260000	-2.8961	1407
4.1920000	-3.4628	1440
3.1360000	-2.1145	1390
2.0810000	-1.7381	1322
0.9420000	1.8090	1095
2.1840000	-1.4758	1184
1.3810000	-0.8498	1209
2.2050000	-1.8368	1245
1.5970000	-1.4376	1179
1.3750000	0.2192	1164
1.4520000	-0.1567	1134
1.2540000	-2.1960	1169
1.2230000	-1.3440	1187

1.7080000	-1.2386	1151
1.6550000	-0.2283	1169
1.4240000	-0.8773	1191
0.9420000	1.8117	1095
0.9420000	1.8103	1095
1.8280000	-1.9734	1245
1.6280000	-0.3177	1216
1.3390000	-1.8178	1196
1.2500000	0.3499	1171
1.2270000	-0.7368	1145
1.2160000	-0.1818	1172
1.3520000	0.3875	1198
1.5680000	1.0227	1205
2.0800000	0.6575	1254
1.5210000	-0.0996	1204
1.3400000	-0.2316	1180
1.5300000	-0.7765	1203
1.9530000	-0.4624	1238
2.3230000	-1.4043	1286
3.8910000	0.1494	1369
2.6510000	1.9368	1291
0.9490000	1.8132	1095
1.9600000	0.0166	1213
2.6690000	0.1971	1281
1.6320000	-0.7813	1209
1.2390000	0.0250	1193
1.1900000	0.6906	1177
0.9880000	-1.0904	1159
1.0030000	-1.1523	1163
1.1490000	-0.9042	1141
0.9220000	1.7903	1095
0.9220000	1.7903	1095
1.3110000	-1.4109	1123
1.3610000	-0.8723	1115
1.5180000	0.0072	1140
2.3090000	-2.8506	1197
1.3570000	-1.7540	1165
1.3310000	0.2597	1120
1.5130000	-1.6721	1157
1.5170000	-0.7117	1136
2.2410000	-1.3612	1227
1.8400000	-0.0576	1195
1.3840000	-0.5216	1139
1.3150000	-2.0764	1168
1.6450000	-2.3419	1215
0.9230000	1.7886	1095
1.1540000	-0.9688	1253
1.1580000	-0.4778	1246
1.1060000	1.4014	1235
1.0510000	0.0727	1204
1.1250000	0.0918	1220

1.1190000	-0.2844	1236
1.2650000	-0.1931	1225
1.1020000	-0.1517	1198
0.9730000	-0.8488	1186
1.0430000	-0.8441	1188
1.1650000	-0.0517	1175
1.2790000	-0.3546	1195
1.1770000	-0.6749	1171
1.2860000	-0.1079	1150
0.8840000	1.7551	1095
0.8860000	1.7557	1095
2.0120000	-0.5828	1314
1.6120000	-2.5834	1283
1.3720000	-2.7180	1252
1.3350000	-0.9850	1260
1.2330000	-0.7811	1267
1.4650000	-0.6139	1270
1.2740000	-0.8861	1246
1.3580000	0.2563	1235
1.6990000	-0.9901	1264
1.4250000	-0.8164	1220
1.4050000	0.1767	1220
1.2310000	-9.0637	1190
1.5140000	-1.6044	1210
0.9070000	1.7753	1095
2.2300000	0.6245	1320
1.8950000	-0.4402	1252
2.3510000	-2.4146	1269
4.3730000	-4.5335	1357
3.3290000	0.8241	1354
3.7500000	-3.7067	1340
1.8950000	-2.6609	1310
1.8330000	0.3533	1294
1.9330000	0.9230	1306
1.5570000	-0.9708	1258
1.5580000	0.6198	1273
1.6440000	-1.5227	1259
1.3040000	-1.8631	1234
1.5200000	-2.2760	1254
0.9410000	1.8066	1095
0.9660000	1.8343	1095
1.7970000	0.1557	1263
2.2140000	-1.1725	1281
2.5330000	0.1527	1339
3.3690000	-0.6295	1345
2.6950000	0.1229	1371
1.9540000	-1.1556	1348
2.2800000	0.9132	1368
3.4510000	1.1001	1369
4.7620000	1.6042	1449
3.7650000	0.6569	1416

2.5000000	-1.5623	1359
1.9260000	-1.1945	1317
1.7540000	-2.4673	1303
2.1190000	0.0284	1347
1.9160000	0.1693	1324
0.9470000	1.8126	1095
4.6230000	-1.4559	1427
3.8490000	-0.3169	1390
2.4960000	0.2168	1329
2.2280000	-0.4803	1322
2.1050000	-1.4671	1322
1.7840000	-0.8992	1302
0.8910000	1.7566	1095
0.9790000	1.8473	1095
1.5630000	-1.6888	1287
1.4890000	-0.9192	1262
1.3940000	-1.3490	1281
1.3440000	-1.2155	1275
1.4830000	-1.2881	1291
1.2880000	-0.8616	1267
1.1120000	-0.4493	1247
1.0410000	-0.6680	1234
0.9850000	-0.0748	1223
1.0020000	0.2362	1237
1.1960000	0.1898	1264
1.2570000	-0.5721	1272
1.3790000	-0.4062	1262
1.1410000	-1.0205	1253
0.9870000	-0.0585	1240
1.0010000	-1.3763	1232
1.1990000	-1.5871	1236
1.6100000	-0.8221	1270
0.8820000	1.7476	1095
0.8820000	1.7517	1095
3.1650000	-1.5574	1389
4.6680000	-1.0120	1420
2.9840000	-1.0675	1347
3.0420000	0.1231	1372
1.9540000	0.0098	1299
1.2980000	0.4506	1245
1.2830000	1.1479	1230
1.6820000	0.0097	1262
2.5420000	-0.4465	1328
1.9850000	-1.0240	1293
1.3330000	0.1508	1250
1.1510000	0.4909	1222
0.9320000	1.7976	1095
1.2350000	-0.9158	1218
1.4150000	0.0566	1221
1.6500000	0.2345	1224
2.0460000	0.7660	1233

0.9300000	1.7983	1095
0.9550000	1.8247	1095
1.5050000	-1.5608	1194
1.8340000	0.4971	1232
1.5040000	0.3131	1219
1.1340000	-0.6005	1173
0.9780000	1.8436	1095
1.5300000	-3.3374	1142
1.1350000	-1.2461	1075
0.9420000	2.3906	1077
0.9080000	-1.5012	1114
1.0240000	-1.5340	1129
1.4570000	1.1461	1169
1.2470000	-1.3514	1154
0.8080000	0.7553	1124
1.0290000	10.8191	1152
0.8350000	0.7895	1134
0.9520000	1.1462	1106
1.6270000	2.6147	1155
0.9590000	1.2209	1131
1.0230000	-0.2267	1124
0.8570000	2.2847	1096
0.8610000	2.1612	1091
0.7780000	2.3188	1113
0.7380000	4.8886	1113
0.9230000	2.2342	1092
0.8820000	1.7490	1095
0.8900000	1.7597	1095
0.9230000	-1.3806	1214
1.0510000	-0.1277	1233
1.0840000	-0.8033	1239
1.1160000	0.0017	1244
1.1480000	-0.2952	1249
1.1670000	-0.2298	1251
1.1770000	0.0864	1248
1.1320000	-0.2016	1243
1.1030000	1.0786	1238
1.0770000	0.8810	1234
1.0480000	1.1662	1230
1.0960000	0.4304	1236
1.1250000	1.0051	1240
1.1560000	1.0206	1243
1.2070000	1.7712	1247
0.9780000	1.8436	1095

Khalifa ELDURSI

Minéralisations et Circulations péri-granitiques : Modélisation numérique couplée 2D/3D, Applications au District minier de Tighza (Maroc-Central)

Résumé :

L'hydrodynamique et la probabilité de minéralisation (R^2AI) autour des intrusions magmatiques ont été étudiées par modélisation numérique couplant transfert de chaleur et circulation de fluide. L'objectif principal de ce travail est de tester la nature du lien génétique entre l'intrusion et le processus de minéralisation. La première série de résultats s'appuie sur une comparaison avec des exemples naturels de gisements bien connus : i) L'hydrodynamique et la localisation des zones probables de minéralisation sont fortement dépendantes de la profondeur de mise en place du pluton. Au-dessus de 4.5km de profondeur de mise en place, le seuil de perméabilité de 10^{-16} m² est atteint et les cellules convectives peuvent créer des zones de décharge additionnelles où des minéralisations peuvent avoir lieu ; ii) Pour toutes les profondeurs d'emplacement, la zone en dessous du pluton n'est pas favorable à la précipitation minérale ; iii) Les apophyses focalisent les fluides convectifs et les zones de minéralisation autour d'elles ; iv) La phase de refroidissement n'est pas la phase majeure de convection. La zone advective principale et celle de haute favorabilité peuvent se produire avant et pendant la phase la plus chaude d'emplacement, avant que le magma ne cristallise complètement; v) Les détachements sont capables de fortement modifier et de re-localiser les flux convectifs déclenchés par une intrusion syn-tectonique; vi) Les conditions physiques favorables à la minéraliser sont produites pendant une durée courte autour de la phase la plus chaude de l'intrusion. Même si les arguments chimiques sont absents, la circulation de fluide (induite par la mise en place de magma) joue un rôle principal dans la genèse des gisements d'or associés aux intrusions. De plus, la formation de ce type de gisement est favorisée par l'occurrence d'une auréole thermique fracturée autour de l'intrusion.
La seconde série de résultats concerne l'étude du cas naturel de la minéralisation W-Au de Tighza (Jebel Aouam) au Maroc Central. Une campagne d'acquisition de données gravimétriques, l'inversion données et l'utilisation de logiciel 3D, ont permis d'obtenir la géométrie 3D complexe du pluton de Tighza. Les résultats sont les suivants : i) la zone probable de la minéralisation apparaît au début de la mise en place du magma dans la zone perméable (veine W1) et s'étend pour remplir W1 et couvrir la région autour du pluton pendant la phase la plus chaude de mise en place; ii) lors du refroidissement, la zone probable est réduite et limitée à la zone perméable (W1) pendant 0,6 Ma; iii) L'application de la température de fermeture isotopique de la muscovite et de la biotite avec la distribution du R^2AI montre que les âges de refroidissement entre la minéralisation au niveau de la veine W1 et l'intrusion ne sont pas séparés de plus de 0,10 Ma. Ceci est confirmé par la datation absolue de la minéralisation de Tighza et permet de discuter la fiabilité des âges obtenus pour la minéralisation dans la veine W1.

Mots clés : modélisation numérique couplée, circulation de fluide hydrothermal, minéralisation W-Au du Tighza (Jebel Aouam, Maroc), gravimètre, modélisation 3D.

Peri-granitic circulations and mineralization: 2D/3D Coupled Numerical Modeling, applications in the Mining District of Tighza (Central Morocco)

Abstract :

Coupled hydro-thermal numerical modeling has been used to simulate the hydrothermal fluid flow regime and the mineralization probability (R^2AI) around plutons. The main objective behind this work is to test the nature of the genetic link between mineralization and intrusions. The first series of results comes from comparison with well-constrained mineral deposits: i) Fluid circulation and mineralization patterns are strongly dependent of the emplacement depth of the pluton. Deep seated plutons emplaced below 10 km do not induce an advective heat dissipation. For emplacement depth less than 4.5 km, the permeability threshold of 10^{-16} m^2 is reached and second order convection cells may create additional discharge zones where mineralization are expected; ii) For all emplacement depths, the pluton floor zone is not favorable for mineral deposition; iii) The apexes strongly modified the fluid flow patterns by focusing convective fluids and mineralization zones around them; iv) The cooling phase is not the main phase of convection for large pluton often associated with long-lived magma emplacement. Major advective heat dissipation and mineral deposition zone may also occur sometime before and during the hottest phase of emplacement; v) Extensional detachments faults are able to delocalize and strongly modify classical fluid flow patterns induced by coeval intrusion; vi) Favorable physical conditions for mineral deposition are encountered around middle crust pluton, during a short time span bracketing the hottest phase of intrusion. We conclude that, even if chemical arguments are absent, fluid circulation induced by granite emplacement plays a key role in the genesis of granite-related Au deposits. Moreover, formation of this type of deposit is promoted and controlled by the occurrence of a fractured thermal aureole around the intrusion.
The second series of results deals with the W-Au granite related Tighza deposits (Jebel Aouam, Morocco). Based on gravimetric data, inversion, and 3D modeling software, we were able to construct the most probable complex geometry of the Tighza pluton. The 3D geometries of the pluton and major fractures (W1 vein) were injected in the hydro-thermal modeling procedure. The results are: i) the probable zone of mineralization appears at the beginning of magma emplacement within the permeable zone (W1 vein) and extends to fill up W1 and covers the area around pluton at the hottest phase; ii) During the cooling phase, the story was reversed; the probable zone was reduced and restricted in the permeable zone (W1) during 0.6 Myr of cooling; iii) Application of isotopic closure temperature of muscovite and biotite coupled with R^2AI distribution shows that the cooling ages between mineralization in W1 veins and the intrusion are not separated by more than 0.10 Myr. This is confirmed by the absolute dating obtained for Tighza Au mineralization and allows discussing the significance of older ages obtained for the mineralization in W1 veins.

Key words: coupled numerical modeling, hydrothermal fluid flow, intrusion-related ore deposits, W-Au mineralization of Tighza (Jebel Aouam, morocco), gravimetry, 3D modeling.

ISTO 1A, rue de la Férollerie, 45071 ORLEANS Cedex 2, FRANCE